A Numerical Investigation of Periodic Actuation on Bluff Bodies in Ground Proximity

by

Derwin Parkin

A Thesis submitted to Monash University

for the degree of

Doctor of Philosophy

February 2014

Department of Mechanical Engineering

Monash University

For dad.

Statement of Originality

This thesis contains no material that has been accepted for the award of a degree or diploma in this or any other university. To the best of the candidate's knowledge and belief, this thesis contains no material previously published or written by another person except where due reference is made in the text of this thesis.

Candidate: Derwin Parkin

<17/02/2014>

Every honest researcher I know admits he's just a professional amateur.

He's doing whatever he's doing for the first time.

That makes him an amateur.

He has sense enough to know that he's going to have a lot of trouble, so that makes him a professional.

Charles Kettering

Abstract

A detailed numerical study on the drag reduction effects of rear-edge periodic actuation on a flat-back 2.5D Ahmed body (a two-dimensional body extended in the third dimension) is presented, with particular focus on an optimum open-loop configuration. Actuation is applied simultaneously in both perpendicular and parallel directions from the upper and lower rear-edges, in phase. Large Eddy Simulations at $Re = 23,000$ show an optimum drag reduction range between $St_{act} = 0.09$ and $St_{act} = 0.13$.

There is also a region $St_{act} = 0.23 - 0.27$, near the natural Strouhal number, which shows less efficient results. Both results agree with recent experiments completed by Pastoor *et al.* (2008). A thorough transient wake analysis, including Dynamic Mode Decomposition, is conducted for all cases, with special attention paid to the Koopman modes in the flow and vortex progression downstream. Two modes are found to co-exist in the optimum cases: mode N, the natural vortex shedding mode, and mode A, which is characterised by synchronous vortices. The former is shown to be weakened for successful drag reduction cases. This, along with the creation of symmetric vortex shedding in the wake are shown to be the major mechanisms in lowering the drag (with opposite signed vortices annihilating one another and increasing the pressure in the near wake), while antisymmetry returns to the wake further downstream.

Other configurations are also explored, with *shear-layer* actuation (perpendicular to the freestream only) and *base* actuation (parallel to the freestream only) tested. The former is shown to be successful in generating synchronous vortices, while the latter is successful at attenuating the natural instability (and can also create synchronous vortices if the momentum coefficient is large enough). *Dual* actuation (the original actuation method tested which combines the shear-layer and base configurations), is shown to be the most efficient for momentum coefficients under 0.008. At $C_\mu = 0.016$, and likely higher, the base actuation appears to offer potential for even greater drag reduction than is achieved via the dual configuration.

However, when the body is moved towards a moving ground plane, a set up which better approximates flow over a moving vehicle, drag reduction is shown to be negligible. Analysis of the non-actuated flow in ground proximity reveals a far less prominent vortex shedding wake instability, which renders the creation of synchronous vortices through actuation in an effort to delay it redundant. This is once again confirmed through Dynamic Mode Decomposition.

Acknowledgments

I would like to thank both my supervisors, Professor Mark Thompson and Professor John Sheridan, firstly for the opportunity and secondly for their quality guidance (and patience) through my candidature. I would also like to thank the other contributors to the truck project - David Burton, Scott Wordley, Luke Phersson, Matt Corallo and Damien Mcarthur - who all regularly contributed invaluable insights which ended up in this thesis.

I gratefully acknowledge the support of the Department of Mechanical Engineering, for providing the resources and financial assistance (in the form of a Departmental scholarship) throughout my candidature. Stelios Konstantinidis, Helen Frost and Nicole Bodenstaff must not be forgotten for their sound administrative efforts which saw my candidature progress as smoothly as possible.

I would also like to acknowledge the National Computing Infrastructure (NCI) in Canberra for providing the immense computational facilities without which this work would be impossible. I additionally thank LEAP, who provided much assistance in bringing my CFD skills up to scratch.

Others who were a great help at various times around the post-grad office were Stuart Buckingham, Rob Harbig, Andras Nemes, Daniel Tudball-Smith, Timothy Crouch, James Venning, Michael Sherry, David Smith, Justin Leontini, James Bell, Sean Loh, Yogen Padayatchy, Martin Griffith and Tony Vo. I have engaged in many research-related and non-related discussions with these people throughout my candidature, both of which were important in getting me through to this stage.

I would like to let my mother know how grateful I am for her parenting skills. I appreciate the fact that I was encouraged to explore any avenue I chose, and that I would be supported no matter what. This has truly been the ultimate gift...

I am also eternally grateful to my fiancé, Vivienne. Her daily encouragement, love and support have kept me far removed from any possibility of the PhD blues ever setting in.

Finally, I'd like to dedicate this thesis to my late father.

Publications during candidature

Journal papers

Parkin, D.J., Thompson, M.C. & Sheridan, J. 2014 Numerical analysis of periodic open-loop flow control on bluff bodies in ground proximity. *J. Wind Eng. & Industrial Aerodynamics* **Submitted**

Parkin, D.J., Thompson, M.C. & Sheridan, J. 2013 Numerical analysis of bluff body wakes under periodic open-loop control. *J. Fluid Mech.* **739**, 94–123.

Conference papers

Parkin, D.J., Thompson, M.C. & Sheridan, J. 2014 Numerical analysis of periodic open-loop flow control on bluff bodies in ground proximity. *First International Conference In Numerical And Experimental Aerodynamics of Road Vehicles and Trains*, **Submitted**, Bordeaux, France, June 2014.

Burton, D., Nazarinia, M., Sheridan, J. & Parkin, D.J. 2011 Optimisation of Boat-Tails for Heavy Vehicles. *In proceedings of ASME-JSME-KSME Joint Fluids Engineering Conference*, Hamamatsu, Shizuoka, Japan, July 2011.

Parkin, D.J. 2010 Research poster entitled "Optimisation of Boat-Tails for Heavy Vehicles". *Intl. Conference for HPC, Networking, Storage and Analysis (SC10) Early Adopters PhD Workshop* New Orleans, USA, November 2010.

Nomenclature

Greek symbols

Symbol	Description
β_i	log-law additive constant
Γ	circulation
Δ	change in a given variable or grid size/filter width
δ	boundary layer thickness
ϵ	strain rate
η	Kolmogorov length scale
κ	Kármán constant (log-law)
λ	wavelength
λ_k	eigenvalue in DMD analysis
λ_T	Taylor length scale
μ	fluid dynamic viscosity
∇	vector gradient operator (grad)
∇^2	del squared (or div grad) operator
ν	fluid kinematic viscosity
ν_t	eddy viscosity
ρ	fluid density
σ	mode growth rate in DMD analysis
$\sum_{i=a}^{b}$	sum of arguments with i incrementing from a to b
τ_w	shear stress at surface
θ	momentum thickness
ϕ	phase lag between two signals
$\|\|\phi\|\|$	mode magnitude in DMD analysis

Continued on the next page.

Continued from previous page.

Symbol	Description
ψ_k	eigenvector in DMD analysis
ω	vorticity

Roman symbols

Symbol	Description
A	actuation signal amplitude
C_μ	momentum coefficient
C_P	pressure coefficient
C_{pb}	base pressure coefficient
C_{pbu}	uncorrected base pressure coefficient
C_μ	momentum coefficient
C_D	drag coefficient
$C_{D,0}$	drag coefficient for natural flow
C_L	lift coefficient
C_S	Smagorinsky coefficient
d'	wake width
E	kinetic energy
f_{act}	actuation frequency
H	height of bluff body
k	wavenumber
L	length of bluff body
P	pressure
$P\{D_{act}\}$	magnitude of spectra at actuation frequency in drag signal
$P\{D_{nat}\}$	magnitude of spectra at Kármán shedding frequency in drag signal
$P\{L_{act}\}$	magnitude of spectra at actuation frequency in lift signal
$P\{L_{nat}\}$	magnitude of spectra at Kármán shedding frequency in lift signal
$P\{P_{act}\}$	magnitude of spectra at actuation frequency in base pressure signal
$P\{P_{nat}\}$	magnitude of spectra at Kármán shedding frequency in base pressure signal

Continued on the next page.

Continued from previous page.

Symbol	Description
q_a	R.M.S. value of fluid velocity imparted by actuator
R	correlation coefficient
Re	Reynolds number
Re^*	wake Reynolds number
Re_H	Reynolds number based on height
Re_L	Reynolds number based on largest scales in flow
Re_θ	momentum thickness Reynolds number
Re_x	Reynolds number at position x along boundary layer
S	actuator slot width
S_{ij}	large-scale strain-rate tensor
St	dimensionless frequency of vortex shedding (Strouhal number)
St^*	universal Strouhal Number
St_L	Strouhal number based on body length
St_{act}	dimensionless frequency of actuation
t	time variable
u	streamwise velocity component
u_τ	friction velocity
$u_{act,rms}$	RMS actuator velocity
U_{SL}	mean separation velocity
U_{vortex}	streamwise velocity of vortex
U_∞	freestream velocity
$U_{\infty,c}$ & U_c	freestream velocity adjusted for blockage
$\langle u'u' \rangle$	streamwise Reynolds stress component
$\langle u'v' \rangle$	shear Reynolds stress component
v	transverse velocity component
V	collection of instantaneous data snapshots used in DMD
$\langle v'v' \rangle$	normal cross flow Reynolds stress component
w	spanwise velocity component
W	width of bluff body
X	streamwise Cartesian coordinate
X_r	re-attachment point

Continued on the next page.

Continued from previous page.

Symbol	Description
Y	transverse Cartesian coordinate
Z	spanwise Cartesian coordinate

Other symbols

Symbol	Description
$\int$	integration
§	thesis section
$\tilde{.}$	filter or discrete approximation
$.^+$	quantity normalised by the viscous scales ν and u_τ
$\bar{.}$	average
$.'$	fluctuation around the average
$\approx$	"similar to", or "scale with"

Abbreviations

Symbol	Description
AR	aspect ratio (ratio of length to height)
DES	detached eddy simulation
DNS	direct numerical solution
FFT	fast Fourier transform
LES	large eddy simulation
NCI	National Computer Infrastructure (Canberra, Australia)
PSD	power spectral density
$RANS$	Reynolds averaged Navier-Stokes
RMS	root mean square
SAS	scale adaptive simulation

Contents

Introduction

With diesel prices at an all time high and increased public environmental awareness, long-haul ground transport companies are devoting increased attention to fuel efficiency. Recent Australian Bureau of Statistics figures indicate 20% of Australia's fuel consumption can be attributed to truck-trailers. Improvements in the efficiency of truck-trailers may save companies large amounts of money on fuel, while also reducing their carbon footprints. It is estimated that a 15% improvement in fuel consumption applied to Australia's truck fleet would save over 3% of the nations total transport CO2 emissions through 2020 (and 0.36% of total emissions). A significant portion of truck-trailer losses are caused by aerodynamic resistance. Unfortunately, due to the rectangular shape of truck-trailers (which must be maintained to maximise cargo space efficiency), traditional drag friendly streamlined shapes one might find on a car are not possible. This is why the appearance of trailers has changed little over the years, while the standard car has experienced ongoing shape modifications. However, as our knowledge of fluid dynamics continues to grow, it is becomingly increasingly clear that other practical methods of drag reduction exist. In fact, the large flat surfaces available on a trailer allow for many alternative techniques that would simply not be possible on a car's body.

The goal of these, and indeed all bluff-body drag reduction techniques, is to decrease the pressure difference between the front and rear ends of the body. The region at the front of a truck is typically characterised by a high local pressure as the fluid is forced to decelerate. A more streamlined (or less bluff) front will allow the fluid to maintain its momentum, decelerating less and thus decreasing local pressure. As such, many shape-altering devices have been proposed for truck-tractors which help the flow navigate over the undesirable areas and on to the trailer. The most common of these is the deflector, which is now installed on most new trucks. While work still continues in tractor design to reduce the local pressure rise, there is an ever increasing focus on the rear of the

truck.

The area at the rear of a truck trailer is characterised by a large wake of recirculating flow. The pressure in this dead air region is therefore significantly lower than in the freestream. Furthermore, vortices are shed off the rear edges of the trailer, transporting high regions of energy downstream and establishing additional pockets of low pressure in the wake. Reducing the size of the wake and strength of these vortices can substantially lower the drag force exerted on the vehicle. Diminishing the wake can be achieved through shape modification – for example, boat tails have been shown to be highly effective at the rear of truck-trailers – however, the aforementioned shape restrictions on the trailer mean other methods need to be found. Recent research has shown that the formation of vortices can be controlled through small devices such as actuators which blow or suck small streams of fluid into the boundary layer of a body. Appropriately located constant blowing or sucking has been shown to achieve significant drag reduction for particular cases. It has also been shown that pulsed blowing or sucking can yield similar amounts of drag reduction with far less far energy expended. However, the physical mechanisms in play are still not yet fully understood. Optimum actuator location is still being examined, and the effect of leading-edge separation has also not yet been studied. Reynolds number effects are still only qualitatively understood. In fact, full understanding of the natural, unaltered flow over a bluff body is still developing, especially in regards to the interaction of vortices shed off the rear edges.

0.1 Overview of the study

This study investigates the performance of an open-loop control approach based on sinusoidal forcing at the rear edges of a two-dimensional elongated cylinder with the same cross-section as a flat-back Ahmed body, effectively a simplified two-dimensional model with some broad features of a truck cross-section. Of course, trucks are fully three dimensional, with geometrical complexity and three-dimensional flows including drag-inducing trailing vortices originating close to the trailing-face corners. Thus, this research only focuses on one of the wake flow components contributing to variations in the drag, i.e., the rollup of the separating shear layers from the top and bottom edges, and side edges, into large-scale (predominantly two-dimensional) vortices, which form a von Kármán wake. The impact of ground proximity on this process, which has not previously been addressed, is also analysed. The work is expected to aid in

the development of successful flow control techniques, both open- and closed-loop, for three-dimensional bluff bodies.

0.2 Structure of thesis

The thesis is separated into seven chapters excluding the present. Chapter 1 is a review of relevant previous literature. Chapter 2 covers the numerical methods used to both simulate the required flows and process the results, while chapter 3 provides a thorough validation of these methods. The next three chapters present and discuss the results; chapter 4 focuses on the natural flow and its response to actuation at different frequencies, chapter 5 explores the effect of actuation momentum coefficient and orientation, and chapter 6 investigates the changes invoked by ground proximity on both the natural and actuated flow. The findings are then summarised in chapter 7, with recommendations for future work given.

Chapter 1

A Review of the Literature

1.1 Bluff body aerodynamics and vortex shedding

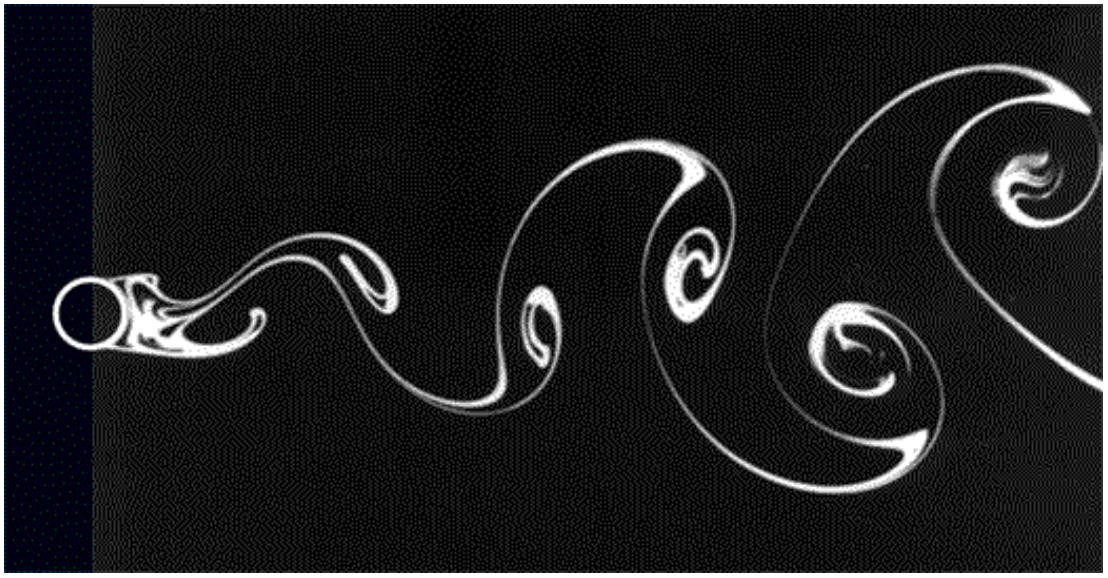

FIGURE 1.1: Unsteady laminar vortex shedding behind a circular cylinder ($Re = 250$). Source: Dyk (2002)

Unlike streamlined flows where the fluid stays fully attached to the body, bluff body flows are characterised by regions of separation. Be it a vehicle's movement through air or wind blowing around a skyscraper, bluff body flows occur in all manner of engineering instances. Vortex shedding behind bluff bodies is an undoubtedly beautiful naturally-occurring phenomenon, as can be seen in Figure 1.1. This beauty is rooted deep in physics and mathematics. While it has been observed for centuries (von Kármán streets have been observed in 14th century paintings), von Kármán & Rubach (1912) were the first to recognise the stability of the asymmetric vortex street downstream of a bluff body. Through linear stability analysis, they established a ratio a/b of 0.28 (see Figure

1.2) was necessary for a stable vortex street. This finding eventually led to the familiar asymmetric vortex wake pattern downstream of bluff bodies, later to be termed Kármán vortex streets.

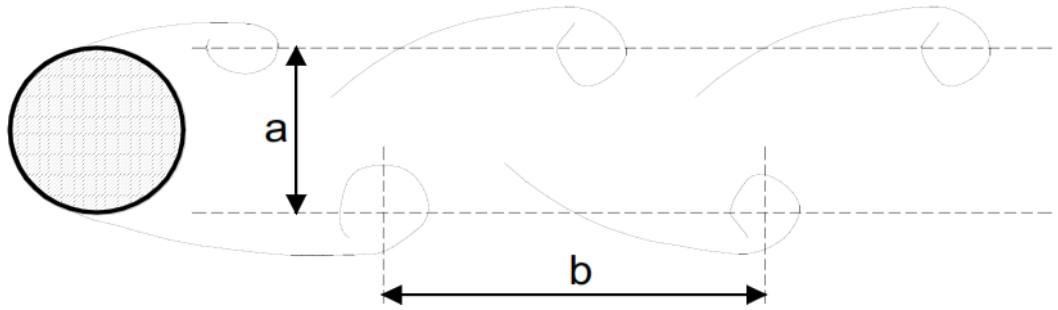

FIGURE 1.2: Characterisation of the ratio of width a and length b in a von Kármán wake, where $a/b = 0.28$. Source: Mills (1998).

1.2 Instabilities and the circular cylinder

While vortex shedding occurs for bluff bodies of many geometries, the circular cylinder has historically been the most researched due to its simple and easily reproduced shape. The instabilities that develop in these flows have been extensively studied through experimental, numerical and mathematical means (Williamson 1996; Zdravkovich 1996). The Kármán wake behind circular cylinders is a globally unstable flow, meaning it features a region of absolute instability. Absolutely unstable systems differ to convectively unstable systems, in that a disturbance grows exponentially in time at its source for the former, while the disturbance convects away from the source for the latter (allowing the system to eventually return to its original state). In addition to the absolute region of instability, the shedding from a circular cylinder has two separated shear layers that are locally convectively unstable. Many bluff bodies, including the elongated bluff bodies this thesis will cover, feature at least these three instabilities. Circular cylinder flow is therefore a useful starting point to understand bluff body flow over more complicated shapes.

1.2.1 The Kármán instability

For circular cylinders, the flow first transitions to laminar two-dimensional vortex shedding in the wake at $Re_c \simeq 46 - 47$ (Dusek *et al.* 1994) . The shedding is periodic,

meaning this critical point is technically a Hopf bifurcation. Provansal *et al.* (1987) showed that this transition is due to a temporal global instability in the wake, and not connected to spatial responses to upstream disturbances. This allows the bifurcation to be modelled by the Stuart-Landau equation (shown in equation 1.1, truncated at the cubic term), commonly used to describe weakly nonlinear dynamics near bifurcation points – so long as the instability mechanism is solely temporal.

$$\frac{dA}{d\tau} = \sigma_c A - \beta A|A|^2 \tag{1.1}$$

For two-dimensional cylinder flow A is taken as the transverse fluid velocity v. σ_c is a complex number $(\lambda + i\omega)$ describing an infinitesimal oscillation with amplification rate (λ) and angular frequency (ω) – both of which are global. β is also complex, comprising of $(C_r + iC_i)$ where $|v| = (\lambda/C_r)^{\frac{1}{2}}$. When λ switches from negative to positive, the base state loses stability and a Hopf bifurcation forms. C_r is positive, and responsible for saturation. The interval of shedding is most commonly given in non-dimensional form as the Strouhal number $St = fL/U_\infty$, where f is the frequency of shedding, L is the cylinder diameter and U_∞ is the freestream velocity. While initially all facets of the flow remain strictly two-dimensional, the Kármán instability persists to varying degrees through the onset of flow three-dimensionality at higher Reynolds numbers.

1.2.2 Shear layer instabilities

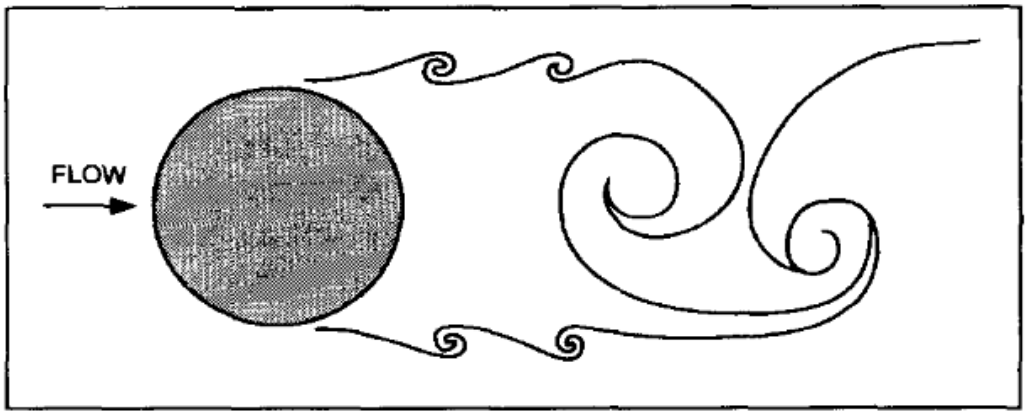

FIGURE 1.3: Diagram showing the development of the von Kármán instability due to interacting upper and lower shear layer instabilities. Source: Wu *et al.* (1996).

For circular cylinders the separated shear layer has become known as the Bloor-Gerrard instability due to the pioneering work of Bloor and Gerrard (in the more

general case it is often termed the Kelvin-Helmholtz instability). Gerrard (1966) showed that the presence of two separated shear layers is instrumental in the development of the Kármán instability. He proposed that the vortices develop alternately through entrainment of the two shear layers into the vortex which eventually grows so large it breaks off and is shed from the body. Bloor (1964) assumed the instability was governed only by boundary-layer properties at separation, and arrived at a relationship of $\frac{f_{SL}}{f_K} \propto Re^{1/2}$ where f_{SL} is the frequency of the shear layer waves and f_K is the Kármán frequency. Her theory and, in particular, exponent value of 0.5 were subsequently discussed in many studies with other numbers ranging from 0.87 (Wei & Smith 1986) to 0.69 (Prasad & Williamson 1997) suggested. More recently Thompson & Hourigan (2005) argued that a global relationship was not valid, and there are two distinct Reynolds number ranges that each have their own relationship. For $1000 < Re < 4000$ the mean separation bubble is much larger than for $Re > 10^4$, with a rapid change between ($4000 < Re < 10^4$). It becomes clear then, that at higher Reynolds numbers the shorter formation length means the separated shear layers are directly affected by the Kármán instability (which causes severe flapping of the shear layers), whilst at lower Reynolds numbers and longer formation lengths the shear layers are unaffected. This proves that Bloor's assumption holds for all but the transition region $4000 < Re < 10^4$. The final relationships, which they also proved theoretically, are $\frac{f_{SL}}{f_K} \propto Re^{0.57}$ for the lower Reynolds number range, and $\frac{f_{SL}}{f_K} \propto Re^{0.52}$ for the higher range.

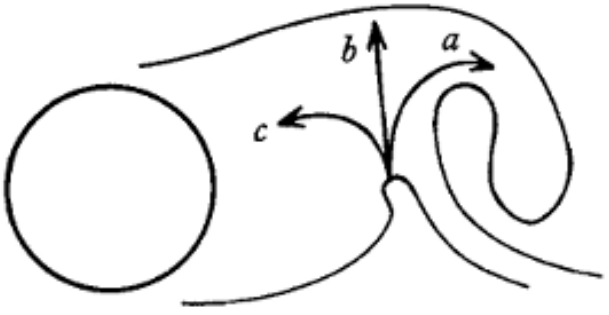

FIGURE 1.4: Sketch of the formation region behind a cylinder. (a) and (b) represent regions of entrainment, with (c) showing reverse flow. Source: Gerrard (1966).

1.2.3 Reynolds number effects

Many flow control strategies, including those covered in this research, target the aforementioned Kármán shedding. Confirming that the shedding persists at higher Reynolds

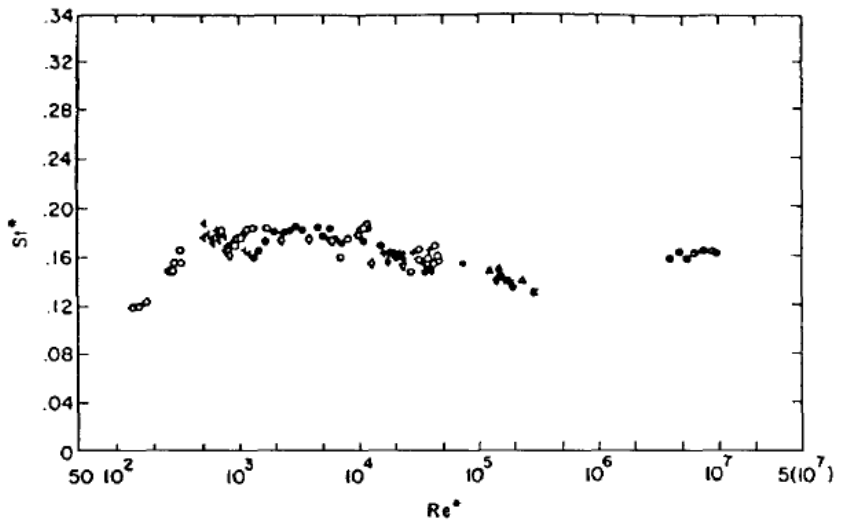

FIGURE 1.5: Universal Strouhal number St^* dependence on wake Reynolds Number Re^*. Source: Griffin (1981), Figure 5.

numbers is therefore a crucial prerequisite before exploring such flow-control techniques in more detail. While testing at practically-relevant Reynolds numbers is often difficult and expensive, it appears that Kármán shedding does indeed continue at higher Reynolds numbers for circular cylinders despite the higher levels of turbulence present in the flow. Tombazis & Bearman (1997) reported Kármán shedding at $Re > 2X10^4$ while Roshko (1961) observed Kármán shedding at Reynolds number of the order 10^7.

The shedding frequency also changes little for the circular cylinder at higher Reynolds numbers. Roshko (1954) observed that bluffer bodies feature larger recirculation regions and thus lower shedding frequencies. He suggested that the width d' of the wake and mean fluid velocity at separation just outside the shear layer U_{SL} were therefore the primary controlling factors in the shedding frequency and devised a universal Strouhal number $St^* = fd'/U_{SL}$ based on these parameters. Figure 1.5 shows St^* changes little regardless of the wake Reynolds number Re^* (calculated using d' and U_{SL}) or shape for short bodies (longer bodies with significant boundary layer thickness do not follow his free streamline-based theory). Gerrard (1966) demonstrated that increasing the freestream turbulence increases the thickness of the shear layers behind a bluff body, delaying their interaction with one another and lowering the Strouhal number. Thus, he proposed that a second length scale, the diffusion length, was also necessary in developing a universal Strouhal number. Nakamura (1996) conducted a thorough investigation of short 2D shapes, and concluded that afterbodies (for example, a rear blunt face) are

able to significantly influence the wake, and that the universal Strouhal number holds only for shapes with no afterbodies.

1.3 Elongated bluff bodies

Elongated bluff bodies are representative of many practical shapes, such as bridges, buildings and road vehicles, where fluid flow is important. Flow over such shapes is characterised by separation at the leading edge before reattachment and separation again at the trailing edge. The boundary layers over the body are therefore not as thin as for shorter bluff bodies, leading to wider wakes and lower shedding frequencies. The aspect ratio ($AR = B/H$ where B is length and H is height), leading edge geometry, trailing edge geometry and incidence angle have all been shown to have significant effects on the flow. Of these many parameters, the rectangular cylinder has received the greatest interest, where the leading and trailing edges are blunt and the effect of Re and AR explored.

1.3.1 The Rectangular cylinder

Parker and Welsh (1983) provided a thorough analysis of vortex shedding frequency and structures in both natural and externally amplified rectangular cylinder flow. For natural flow at $Re_H = 23,700$ they found four clear regimes relating AR and St, between each of which discontinuities occurred. All regimes begin with leading edge flow separation, however the length of body greatly influences what happens thereafter. Regime "a", at $AR < 3.2$, sees no reattachment of the leading edge shear layers, which interact directly further downstream of the trailing edge to form a familiar vortex street. Nakamura & Hirata (1989) later showed that shear layer/edge interaction was also possible above $AR = 0.6$ in this regime. Regime "b", at $3.2 < AR < 7.6$, showed an intermittent reattachment of the leading edge shear layers on the trailing edge, once again resulting in a regular vortex street. Regimes "c" and "d", at $7.6 < AR < 16$ and $AR > 16$ respectively, see the separated shear layers always reattaching to the body. In these regimes the separation bubble length was observed to shorten at irregular intervals, resulting in the bubble breaking away and travelling downstream in the form of a vortex, which diffuses as it approaches the trailing edge. The lone difference between regimes "c" and "d" is that the longer downstream body length of the latter allows the leading edges vortices to completely diffuse, allowing a non-related vortex

shedding process at the trailing edge and dominant peaks to appear in the spectra, while the former shows none. These surprisingly discontinuous regimes confirmed earlier observations by Nakaguchi *et al.* (1968) and Okajima (1982).

Nakamura & Nakashima (1986), working independently of Parker and Welsh, attributed the impinging shear layer instability (ISLI) introduced by Rockwell & Naudascher (1978) to the vortex shedding exhibited in regime "b". The ISLI occurs when the leading edge shear layer encounters the trailing-edge corner and becomes unstable due to the sudden disappearance of the boundary layer. The two unstable shear layers then interact and form a regular vortex street. It was thought that the ISLI was also involved for regimes "c" and "d", and three years later (Nakamura *et al.* 1991) confirmed this. In the regions around each AR discontinuity, they detected two dominant frequencies intermittently occurring in the flow. Furthermore, they found the Strouhal number St_L, here based on body length rather than height, jumped by a constant 0.6 at each regime change, indicating that the wavelength of the velocity fluctuation is related to fractions of the body's length. For each regime the length-based Strouhal number remained locked-on to the body's length through some non-linear processes until the next limit was reached. This led to the possibility of an integer representation of the shedding frequency: St_L=0.6n, with n indicating the number of vortices formed on each side of the body's surface. At the aforementioned AR stepwise regime changes, n would have two values (for example, at $AR = 8$ vortex shedding with both $n = 2$ and $n = 3$ is seen). This confirmed that both regimes "c" and "d" were also characterised by the impinging-shear-layer instability. They concluded that vortex shedding with $n >= 5$ is likely for aspect ratios above 16.

Rockwell & Naudascher (1994) later revisited this area and pointed out that for higher aspect ratios it is the vortices shedding from the leading edge separation bubble that impinge directly on the trailing edge, not the leading edge shear layer itself. They therefore reasoned that the term Impinging Shear Layer Instability (ISLI) was inappropriate and instead used the term Impinging Leading Edge Vortex (ILEV) instability. They shed further light on this process through reference to earlier analysis of a free jet (an efflux of fluid projected into a surrounding non-moving fluid from a nozzle) impinging on a normal flat plate by Ho & Nosseir (1981), who found an upstream propagating pressure wave was responsible for separating the shear layer originating at the jet exit. A similar mechanism is in play for rectangular cylinders: the shear layer instability is

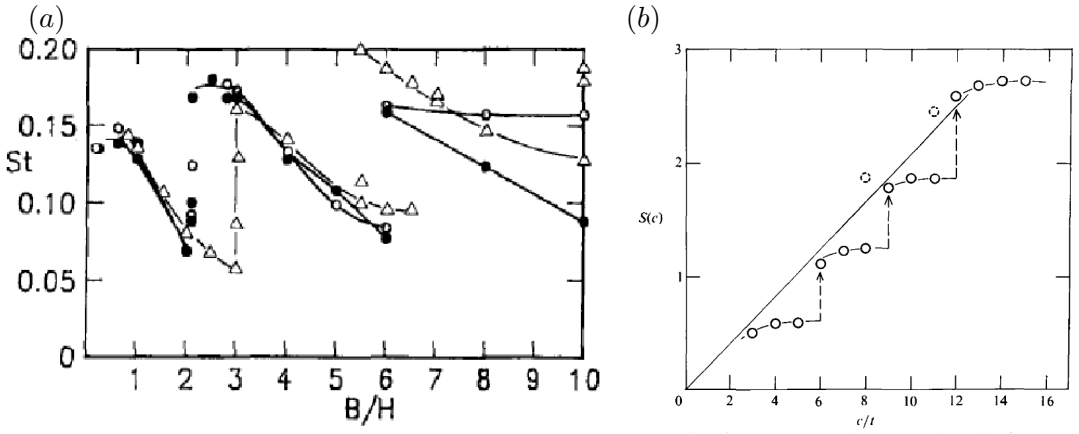

FIGURE 1.6: (a) The effect of Aspect Ratio (B/H) on height-based Strouhal number (St). The results reveal three distinct regimes, while also indicating Roshkos universal Strouhal number hypothesis does not hold for elongated bluff bodies. Source: Okajima *et al.* (1992). (b) When Aspect Ratio (here denoted as c/t) is plotted against cord-based Strouhal number ($S(c)$), a step-wise relationship is observed. Source: Nakamura *et al.* (1991), Figure 4.

enhanced by the pressure-wave feedback of the trailing edge separation point (where a discontinuity of vortex production exists). When the pressure pulse interacts upstream with the still-forming leading edge vortex, it is then shed. This hydrodynamic mechanism explains why the leading edge vortex creation occurs at the same rate as the trailing edge vortex shedding. Nakamura *et al.* (1991) showed the ILEV is suppressed at Reynolds numbers above 2000, confirming observations by Stokes & Welsh (1986). For these Reynolds numbers the trailing edge vortex shedding is still present at a weak periodicity, while the leading-edge vortex shedding has been shown to occur at irregular intervals (Taylor 2011b).

Hourigan *et al.* (2001) focussed on this trailing-edge vortex shedding (TEVS) in more detail. By comparing numerical simulations of elliptical leading-edge rectangles with square leading-edge rectangles, they found that TEVS has more of an influence on the self-sustained oscillations than first thought. While they acknowledged that the ILEV instability is likely to be the dominant instability for flows with no trailing edge vortex shedding and low Reynolds numbers, they concluded that for rectangular cylinders the preferred shedding frequency is that of the trailing-edge shedding, which completes the feedback loop to the leading-edge vortices (rather than the pressure pulse of the leading edge vortices being responsible). The global instability is therefore a combination of the ILEV and TEVS instabilities. As has been discussed above, at higher Reynolds numbers the instability is the combination of randomly shed leading-edge vortices and the TEVS mechanism.

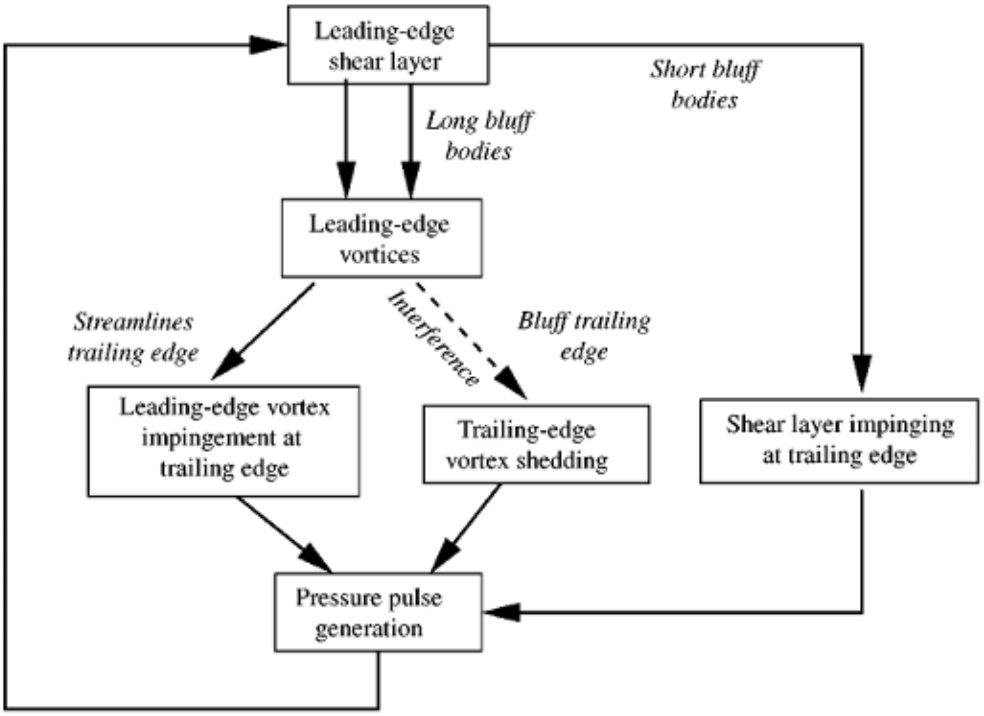

FIGURE 1.7: Flow chart showing the connections between mechanisms in various bluff body flows. Source: Hourigan *et al.* (2001), Figure 8.

1.3.2 Elliptical and semi-circular fronts

From the above it is clear that previous research has shown there is a strong connection between the leading edge vortices (in these studies referred in short hand as L vortices) and trailing edge vortices (T vortices) for rectangular cylinders. The global instability is such that both leading- and trailing-edge geometry can strongly influence the flow. Most heavy vehicles require blunt rear-edges, but it is worthwile focussing here on the leading edge geometry. By replacing the square leading edge with an elliptical shape, the L vortices can be almost completely eradicated, leaving regular trailing edge vortex shedding only. The resulting thinner boundary layer leads to a narrower wake and higher base pressure than observed for regular rectangular cylinders. The uninterrupted boundary layer also allows a stronger streamwise vorticity component to develop (Robinson 1991). While increasing AR still has a slight effect (a thicker boundary layer leads to slightly lower base pressure and shedding frequency (Mills 1998)), the removal of the ILEV simplifies the flow greatly compared to rectangular cylinders.

Of course, these are not the only leading-edge geometries possible: there are a

great variety of front end shapes that leave the flow somewhere in between the two extremes depending on their bluffness. The leading edge separation angle, introduced by Roshko (1954), is the most effective way of characterising this bluffness. The related re-attachment point, X_r, is defined as the point at the wall where shear stress is zero (Tritton 1988). Roshko & Lau (1965) and Cherry *et al.* (1984) have agreeable measurements for square leading-edge bodies of $X_r \simeq 4.3t$. Triangular front end studies have reported $X_r \simeq 2.2t$ (Djilali & Gartshore 1991), with circular leading edges lower again at $X_r \simeq 0.95t$ (Hazarika & Hirsch 1994)). Reynolds number dependence on these values has not yet been thoroughly investigated. The re-attachment length is a good indication of the bubble's size when it is shed downstream. It is clear that a lower leading edge separation angle (less bluff front end) will lead to a smaller leading-edge vortex and hence a less influential ILEV mechanism. It has also been shown that the convection speed of the shed leading-edge vortices holds at $0.6U_\infty$ (Cherry *et al.* 1984). This ratio has proven valid for many different types of leading edges.

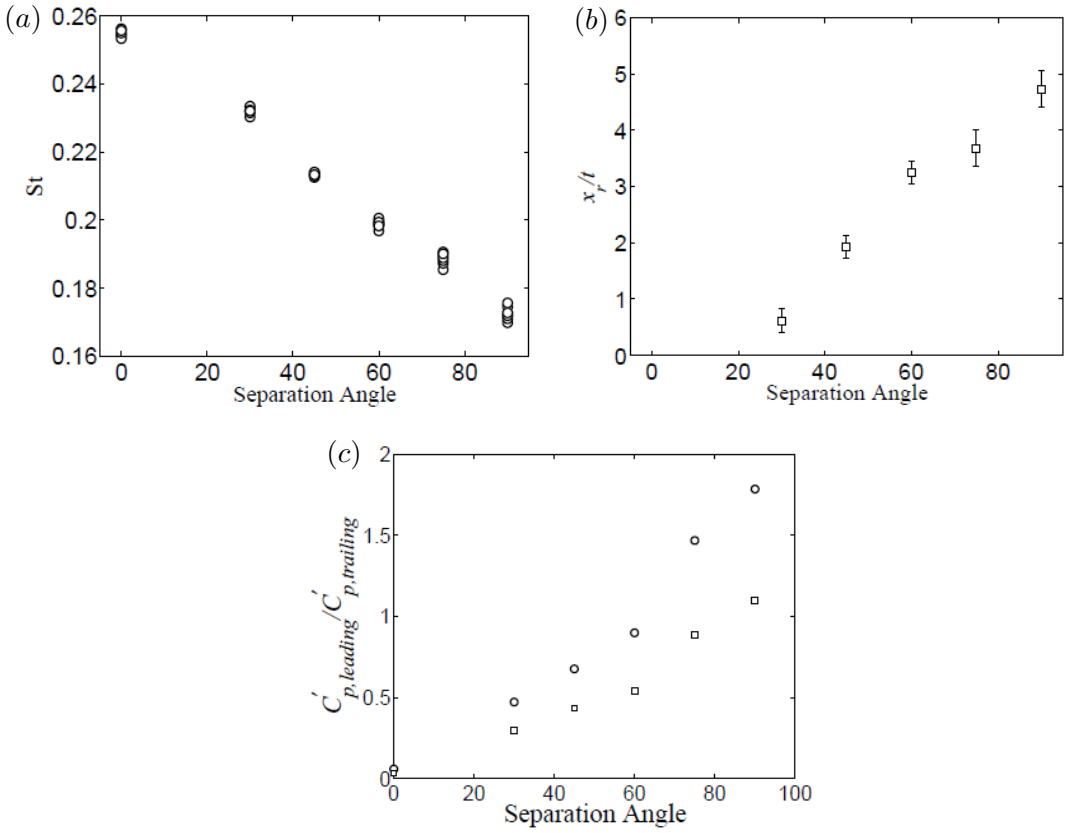

FIGURE 1.8: (a) Lower St due to higher separation angle. (b) Higher X_r due to higher separation angle. (c) Higher fluctuating pressure ratio due to higher separation angle. Source: Taylor (2011a)

Taylor (2011a) completed a thorough analysis on the effect of the leading edge separation angle on the flow over elongated bluff bodies. By taking the ratio of pressure fluctuation slightly upstream of the re-attachment location to the pressure fluctuation at the trailing edge, Taylor established a measure of whether the flow was leading edge dominated or trailing edge dominated. Values above unity indicate leading-edge domination, with values under unity indicating trailing-edge domination. Taylor hypothesised the mechanism as follows: for leading-edge dominated flows, the irregularly shed vortices are of sufficient size to impact the trailing edge shedding, while for trailing-edge dominated flows the vortices are not large enough to achieve this. As such, the trailing-edge dominated flows show more consistent trailing edge shedding and sharper wake velocity spectral peaks.

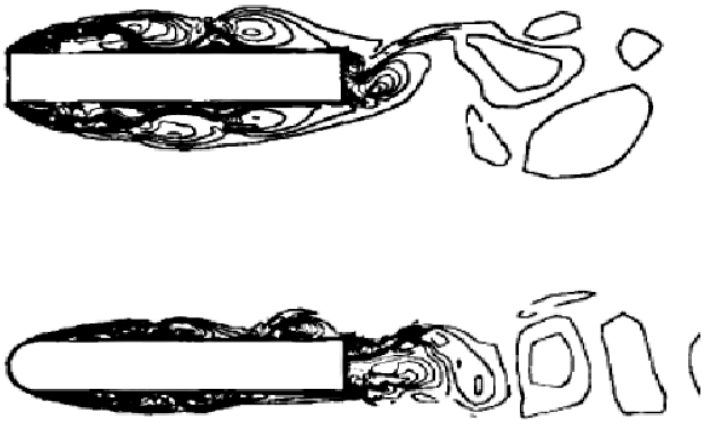

FIGURE 1.9: The effect of a rounded front edge on vorticity contours at $B/H = 6$ and $Re = 4 \times 10^6$. Source: Okajima *et al.* (1992)

The semi-circular leading edge used in this research, which features a blunt surface with rounded edges, is bluffer than the fully circular leading-edge cases mentioned above, but not so bluff as a sharp-edged rectangle. The flow is therefore expected to be somewhere between leading and trailing edge dominated. Okajima *et al.* (1992) provided some excellent visualisations of a semi-circular leading edge bluff body, one of which is shown above in Figure 1.9. As one would expect, the size of the L vortices along the body are much reduced for the rounded front shape (although not completely eradicated). The leading edge vortices are able to reattach sooner, and are smaller. The visualisation also shows the large effect this has on the wake, it is much thinner and correspondingly less drag is observed than for square leading-edge rectangles. Pastoor

et al. (2008) also used the shape in their flow control experiments, observing periodic shedding with $St = 0.23$ at a Reynolds number of 23,000.

Stankiewicz *et al.* (2005) recently completed a 2D stability analysis of the Ahmed body shape, which is very similar to the semi-circular leading edge bluff body. He showed the first pair of eigenmodes becomes negative at $Re > 300$, leading to unstable flow. He also showed the eigenmode values change less with increasing Re. However, the analysis was not possible above $Re = 400$. This again highlights the great gap between practical bluff body flow Reynolds numbers and those which are capable of being accurately solved.

1.3.3 Reynolds number effects

While Reynolds number effects have been studied in great detail for the circular cylinder (showing a high variability due to the non-fixed separation points), less work has been carried out for elongated bluff bodies. From the limited research, however, it appears Reynolds number effects are modest for high Reynolds numbers. Mannini *et al.* (2009)'s recent work on $AR = 5$ rectangular cylinders has extended to $Re = 1 \times 10^6$, an order of magnitude higher than previous studies at similar aspect ratios (Okajima 1982; Hwang & Sue 1997; Obasaju 1983). Analysing the results of these different studies together (see Figure 1.10) makes it clear that St changes minimally with Re for moderate aspect ratios. Mannini *et al.* (2009) also showed other variables, such as drag coefficient and base pressure, changed little with Reynolds number.

The magnitude of these changes suggests there are no further instability changes after the ILEV mechanism weakens at $Re \equiv 2,000$. As Re rises, TEVS remains the dominant mechanism. However, the growth of more turbulent structures masks this behaviour increasingly.

1.3.4 Ground proximity

It has been shown that when an aircraft flies close to ground, a "cushion" effect develops where the lower surface of the aircraft's wing experiences a higher pressure than it would otherwise. Furthermore, the ground interrupts downwash and wingtip vortices behind the wing. The result is a much improved lift to drag ratio. This effect is exploited in the current development of Wing-in-Ground (WIG) boats, which can achieve better efficiency than planes and higher speeds than boats – a compromise which could prove useful in many transport scenarios. Much ground proximity research

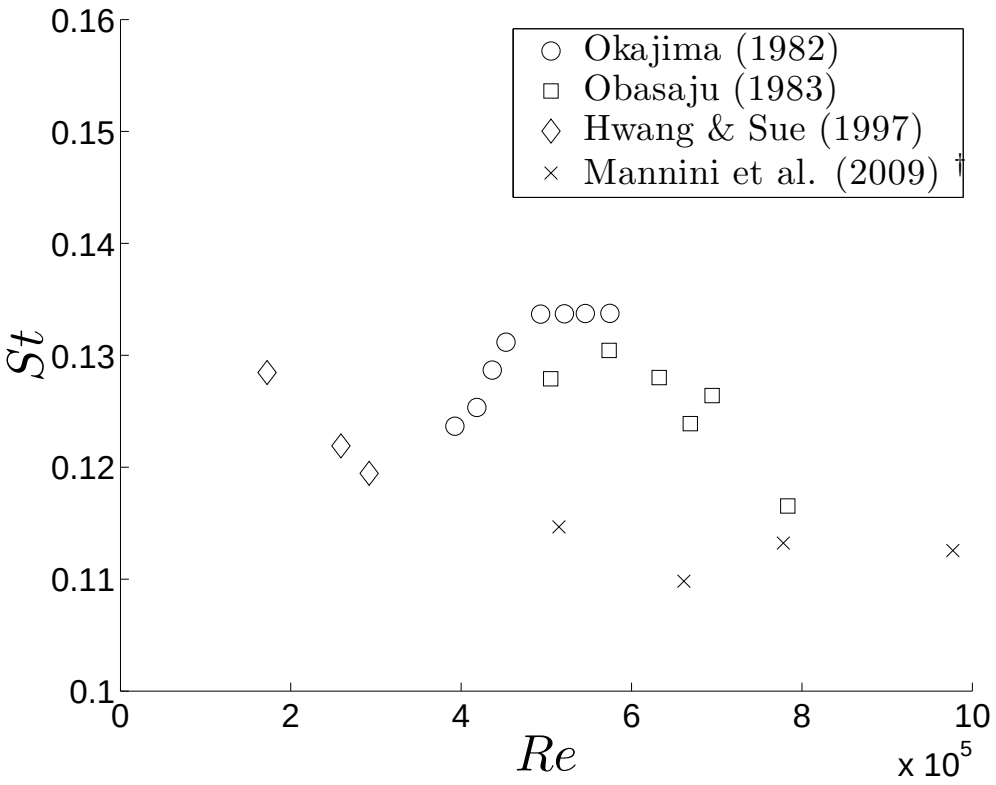

FIGURE 1.10: Reynolds number effect on Strouhal number of a rectangular cylinder ($AR = 4$) for various studies. † Indicates $AR = 5$.

has been completed in the field of motor racing, where the front and rear wings produce downforce.

The ground effect for bluff body flows, and in particular the wake of these flows, is not as well understood. A detailed characterisation of the transient wake structure behind bluff bodies at different heights is only now emerging, with the 3D Ahmed body (discussed in §1.4.1) receiving most attention. Literature on the effect of ground proximity on 2D bluff bodies is less developed, but Kim & Geropp (1998) provide a a sound starting point. For a variety of shapes at $Re_D = 2.2 \times 10^4 - 1.3 \times 10^5$, they found a larger pressure difference between the upper and lower surfaces with decreasing ground clearance – another observation of the "cushion" effect. They also observed a lower drag and longer wake for decreasing ground clearance and showed that ground proximity dampens periodic flow behind the body. This makes sense as the two shear-layers are no longer equal, which hinders the instability mechanism. The reported accompanying decrease in Strouhal number is also expected – as we have discussed, the vortex shedding process slows down when it becomes more "difficult".

The study also highlights the importance of a moving ground plane. A moving ground plane is often used in automotive wind-tunnel testing to neutralise the ground boundary layer that would otherwise develop (in the real world, of course, the ground is stationary and has no boundary layer). Unfortunately, this is an expensive practice and not always possible. Kim's research shows substantial differences between moving and non-moving cases in the body pressure distribution, with the non-moving ground exaggerating the pressure differences between lower-front and lower-rear. They also show that for a car-like shape the lift magnitude is exaggerated by a non-moving ground, especially at higher Reynolds numbers (although, fortunately, differences in measured drag are minimal). Finally, the non-moving ground significantly shortens the dead-water wake region, and moves its centre closer to the ground.

1.3.4.1 Current work

Many recent studies explore the ground effect on wakes behind 3D objects, such as Ahmed bodies, revealing a highly complex flow structure (more detail is given in §1.4.1). It is believed that a more thorough understanding of the infinite-width 2D case, where only an upper and lower shear layer are present, would benefit our understanding of the more complicated structure behind 3D bodies. Section §4.3 of this thesis is devoted to filling this gap. Full characterisation of the flow will be completed for different ground displacement cases: X/H=0.4, X/H=0.2, $X/H = 0.1$ and $X/H = 0$ (which is similar to a backward facing step problem). The difference between upper and lower shear layer development, and the effect this has on the von Kármán instability, are key areas of interest. Better understanding here will also help to develop open-loop control systems for bluff bodies in ground proximity. This topic itself is subsequently explored in §1.5.

1.4 3D bluff bodies

Ground vehicles, unlike the previous bluff bodies discussed in this literature view, are of course not "infinitely wide'. A finite spanwise dimension elicits a number of additional flow features not seen for the infinite-width case. Most importantly, the flow is not constricted to either travelling above or below the body – it can travel around the sides also. This introduces another pair of opposing shear layers at the rear, and regions where non-aligned vorticity streams can interact both along the body corners and downstream, further complicating the flow. Of further consideration is the ground

plane, which is inherently present every time a ground vehicle is analysed – whether its effect is isolated or not.

Bearman (1997) provided a thorough description of some of these with his experimental analysis of flow past a car-like shape. He noted that flow behind a 3D body features more streamwise vortices than the transverse vortices found for 2D bodies, and that the strength of vortex shedding is less pronounced. The time-varying nature of the flow was also highlighted – an instantaneous visualisation of velocity vectors in the wake revealed many streamwise vortices while the time averaged vector field indicated only two counter-rotating vortices exist at all times. Bearman also presented a region of flow where transverse vortex shedding existed. While this shedding was relatively weak, it illustrates coherent transverse vortex shedding associated with two-dimensional bodies still exists behind three-dimensional shapes.

1.4.1 The square-back Ahmed Body

The flow around 3D bluff bodies has been shown to be extremely sensitive to the body shape, making a general discussion of ground vehicle flows difficult. The Ahmed body (pictured in Figure 1.11) has become a commonly used standardised geometry that, thanks to its variable rear slant angle, can approximate numerous ground vehicle shapes. With a rear slant angle of zero degrees, for example, the Ahmed body resembles a short truck, van or bus. As the angle increases, different car shapes such as hatchbacks and notchbacks are approximated. It was introduced by Ahmed & Ramm (1984), who discovered that the inclination of the slant at the rear of the body significantly affects drag. For high Reynolds numbers, they showed that between an angle of 12.5 and 30 degrees the flow may detach from the body, forming a recirculation zone. This induces a large pressure gradient difference between the slant and the non-angled side walls, which produces two strong counter-rotating vortices along the upper side slant corners (as previously highlighted in discussion the study of Bearman (1997)). When the slant angle increases past 30 degrees, full flow separation reduces the pressure gradient and inhibits the formation of the counter-rotating vortex pair, lowering drag. This was an important result, as traditional bluff body aerodynamics would call for a lower slant angle in an effort to minimise sudden changes in the path of the flow.

The zero-angle rear slant case, also known as a square-back Ahmed body, is the geometry of interest here. While not as long as a traditional semi-trailer truck, the

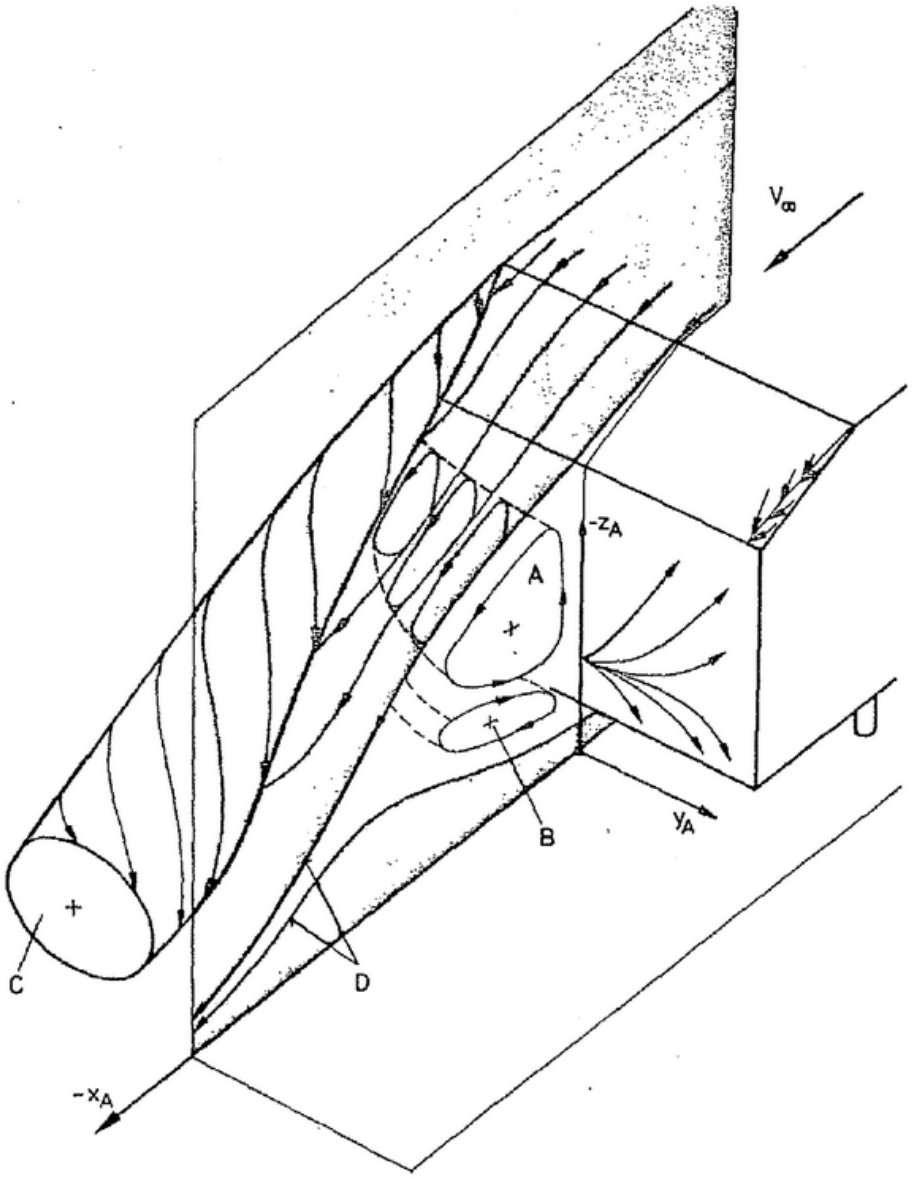

FIGURE 1.11: The Ahmed body shown with counter rotating vortices off rear slant corners. Source: Ahmed & Ramm (1984), Figure 6.

two shapes share many features, such as fixed separation points at the rear and leading edge separation/re-attachment.

Understanding flow around square-back Ahmed bodies (and, indeed, all Ahmed body shapes) is an active area of research and continues to develop with the help of numerical analysis and improved flow measurement techniques. Recent studies have revealed a complex flow structure, with a large number of frequencies present in the wake and force signals. A low frequency at $St \approx 0.07$ has been widely reported in experimental works by Duell & George (1999); Khalighi *et al.* (2001, 2012). Bayraktar

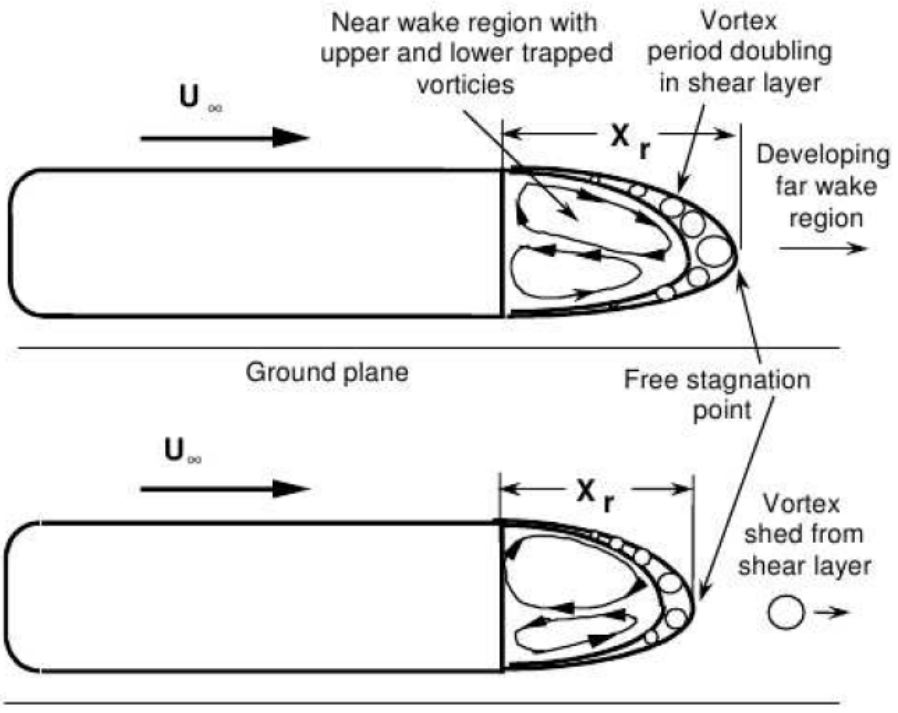

FIGURE 1.12: Schematic of the upper and lower shear layer developments in the wake of a square-back Ahmed body. A similar process exists for the side shear layers. Source: Duell & George (1999), Figure 5.

et al. (2001) identified two frequencies at $St = 0.106$ and 0.086 in the lift and side force signals respectively. Khalighi *et al.* (2012) found a clear peak frequency at $St = 0.17$ downstream of the recirculation region near the symmetry plane, while Duell & George (1999) observed a high-frequency motion at $St = 1.157$, proposing a pseudo-helical shedding structure.

Using these results and their own from experiments at $Re_H = 9.2 \times 10^4$ with non-moving ground, Grandemange *et al.* (2013) were recently able to propose a complete global characterisation of the flow. Their mean and dynamic flow analysis yielded the following conclusions:

- The time-averaged streamlines (see Figure 1.13) reveal two separation regions: one at the front due to the adverse pressure gradient imposed by the geometry, and the other at the rear fixed-separation points. The front re-attachment is reported to occur at $X/H \approx 0.65$ downstream of the front face on the side and top surfaces, and slightly earlier on the bottom face. This re-attachment length

seems to remain constant for all high Reynolds number flows, with Krajnovic & Davidson (2005b) and Spohn & Gillieron (2002) reporting similar lengths at far higher Reynolds numbers.

- The time-averaged pressure distribution around the body in the X-Y plane (viewing the body from the side) is similar to that in the X-Z plane (viewing the body from above). In the Y-Z plane, however, the ground effect does seem to play a significant role (see Figure 1.13).

- The boundary layers are fully turbulent at the trailing edges. The boundary layer on the bottom surface is roughly 65% the height of those on the top and side surfaces.

- A prominent recirculation region exists behind the body, with a length of $X/H \approx 1.47$. The shape of the recirculation region has a shape roughly similar to the square-back, with the ground having seemingly little effect. This seems to be further evidence of the toric recirculation organization suggested by Duell & George (1999) and Khalighi *et al.* (2001).

- Downstream separation on the ground is not observed, despite a strong adverse pressure gradient observed on the ground at $1 < X/H < 2$ which induces significant momentum losses.

- Reynolds stresses over the bottom and top surfaces are more intense than over the sides, with the ground causing a slight asymmetry in the Y-direction. The recirculation bubble is a force balance of the shear stresses, normal stresses and pressure forces – the importance of the Reynolds stresses on the rear base pressure should not be forgotten.

- Frequency peaks are observed at $St = 0.127$ and 0.174 downstream of both the top and lateral shear layers. These are associated with the interactions of both pairs of opposing shear layers, showing the conclusions of Kiya & Abe (1999) for elliptical and rectangular flat plates in cross flow carry over to the square-back Ahmed shape. Here the higher frequency is associated with the top/bottom shear layer interaction, as the height is smaller than the width. The presence of the ground results in a diminished energy of this mode, and also causes a phase shift between upper and lower parts of the wake.

- The lateral shear layers also exhibited a significant low frequency behaviour. These relate to a bi-stability identified in the wake through PIV snapshots: while the centre of the wake remains steady in the z-direction at $Z/H \approx 0.58$, it's location in the y-direction (laterally) randomly alternates between either $Y/H \approx +0.06$ or -0.06. The phenomenon is shown to be a global mode which occurs at ground clearances above $X/H = 0.10$ and not due to disturbances or asymmetry occurring upstream. This may be related to the bi-stability mode observed behind a double backward facing step by Herry *et al.* (2011).

- All frequencies picked up contain only 5-6% more energy than the surrounding turbulent fluctuations. The instabilities, while definitely present, do not dominate the flow as much as observed in other bluff body cases, such as low Reynolds number infinite-width cylinder flow.

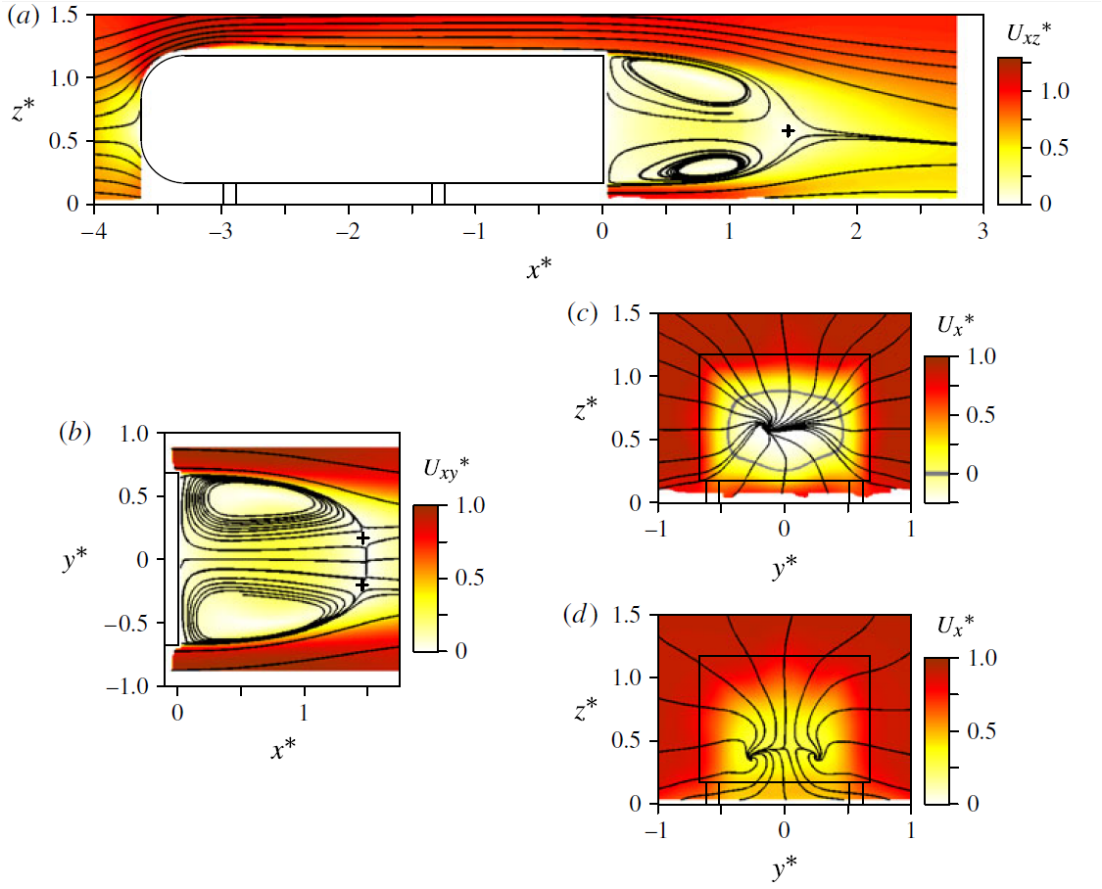

FIGURE 1.13: Streamlines coloured by velocity at the planes $\frac{Z}{H} = 0$ (a), $\frac{Y}{H} = 0.6$ (b), $\frac{X}{H} = 1$ (c) and $\frac{X}{H} = 2$ (d). Crosses are saddle points. Source: Grandemange *et al.* (2013)

While this recent study has brought a degree of confidence to many of the mech-

anisms of square-back bluff body flow, there still remain many unknowns. Further understanding of the bi-stability in the wake, for example, would be of both fundamental and practical importance.

1.4.2 Relevance of current work to truck-trailer aerodynamics

Truck-trailers are a further step up in complexity from the square-back Ahmed body, and are the ultimate target vehicle of this research. Total length, front cabin shape, the addition of fairings, truck-trailer gap width and under-carriage features are just a few of the extra variables that can influence turbulence regions over the body and have significant effect on drag (see Figure 1.14).

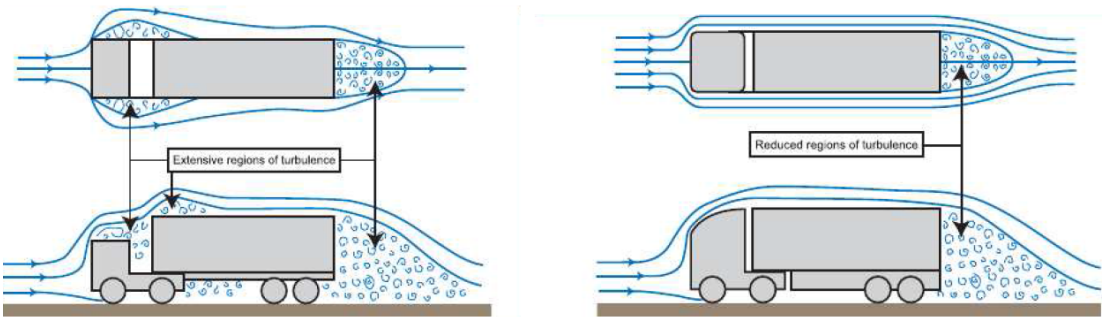

FIGURE 1.14: Schematic of typical airflow over non-aerodynamic truck (left) and aerodynamic truck (right). Source: UK Dept Transport (2010), Figures 2 and 3.

The Generic Conventional Model (GCM), pictured in Figure 1.15, has emerged as the most popular standardized model in truck aerodynamic research. It can be described as a moderate-fidelity model, as it includes many features of a full-scale truck such as the truck-trailer gap, wheels and the familiar conventional cabin shape, but not finer details like side windows. The GTS model (shown in Figure 1.16), a low-fidelity model similar to the square-back Ahmed body, but longer, with 10 wheels and a more truck-like front, has also received recent attention.

The time-averaged flows around medium- and high-fidelity truck models have been recently well-documented. However, the large Reynolds numbers and scales involved make both numerical and experimental transient analysis expensive. Investigation of key wake dynamics therefore remains the domain of the simpler, low-fidelity models, such as the square-back Ahmed and GTS models.

Of particular interest in this study is the continued presence of von Kármán shedding as a primary mechanism behind truck-trailers travelling at highway speeds (if it were

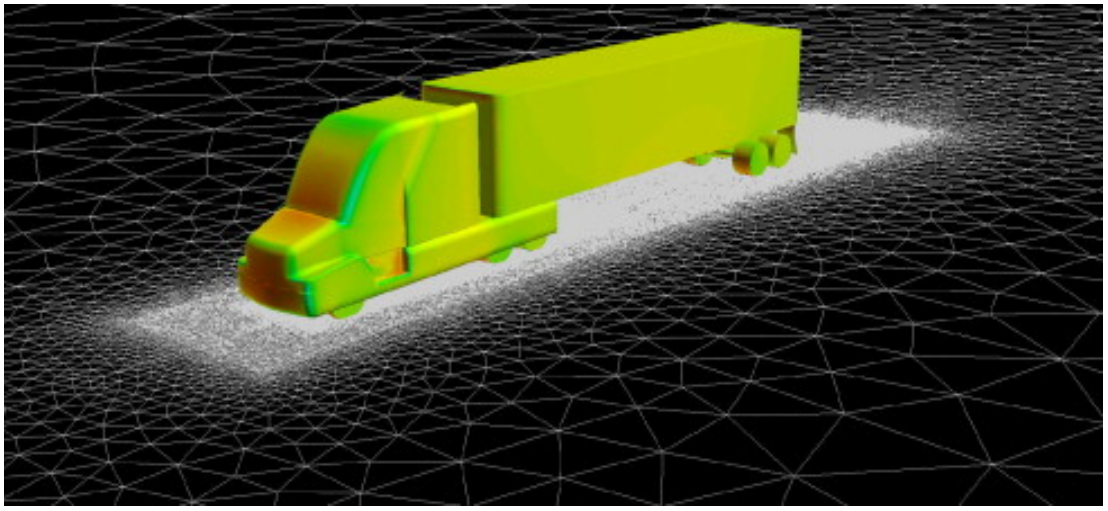

FIGURE 1.15: The Generic Conventional Model: a medium-fidelity truck-trailer model. Source: Pankajakshan *et al.* (2008), Figure 1.

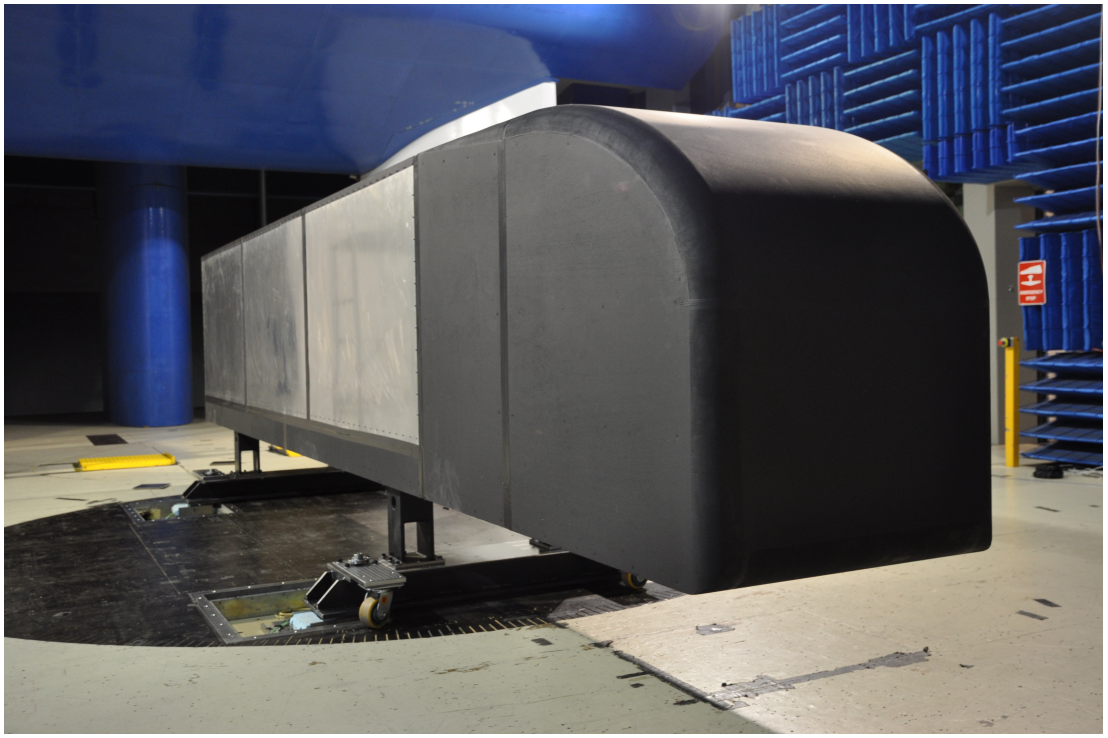

FIGURE 1.16: The GTS model: a low-fidelity truck-trailer model. Source: Damien McArthur, Monash Wind Tunnel (2012)

not present in such real-life scenarios, the method of control proposed below would be misguided). As just discussed, dynamic wake information on actual truck-trailers is sparse. Still, there seems to be substantial evidence from the low-fidelity model research suggesting that the instability does indeed persist at high Reynolds numbers. In addition to those mentioned in section §1.4.1, von Kármán shedding was observed

by:

- Andrus, whose numerical study noted the strong presence of shedding at high Reynolds numbers.
- Krajnovic & Davidson (2002), who have also shown the existence of vortex shedding behind bluff bodies, and found the recirculation zone is accompanied with increased turbulent stress due to the creation of small scale structures related to the Kelvin-Helmholtz instability.
- Menter & Kuntz (2004), whose Detached Eddy Simulation work showed a large unsteadiness due to a spanwise instability creating large scale structures.
- Maddox *et al.* (2003) whose Detached Eddy Simulations showed shear layer interactions and a Strouhal number of 0.2.
- Vino *et al.* (2005), who observed strong vortex shedding behaviour behind an Ahmed body with 30 degrees slant angle.

With this in mind, it would appear that von Kármán shedding is present behind truck-trailers at highway level Reynolds numbers, although the energy of the instability is still debatable. It therefore remains unclear whether targeting this instability in flow control strategies is worthwhile. This study is a crucial step on the road to answering this question. While the Reynolds number of 23,000 is two orders of magnitude lower than highway-truck-travel Reynolds numbers, it is high enough for a turbulent boundary layer to develop over the body, and therefore will yield relevant results. Furthermore, with full understanding of 3D bluff body flow still incomplete, it is hoped the reduced complexity of a 2D geometry will help reveal more information on the major flow mechanisms present in the 3D case.

1.5 Bluff body flow control

The possible target zones for bluff body flow control directed at minimising drag are the boundary layer and the wake. Boundary layer control has proven effective for shapes with moveable separation points, such as circular cylinders: if tripped to turbulence, the boundary layer separation is delayed and hence a narrower wake and lower drag are observed. However, delaying separation is not beneficial in the case of an elongated bluff

body with blunt trailing-edge, where flow (often re-attached and turbulent) separates at fixed points at the rear of the body.

The usual goal of flow control for these bodies is therefore to manipulate the wake in such a way that the rear base pressure is increased (i.e. made a less negative value). Suppressing the Kármán vortex wake instability, which we have now established as responsible for a large component of the base suction, is the most effective way of achieving this.

1.5.1 Kármán shedding suppression

There are at least four possibilities in suppressing the instability, which Pastoor *et al.* (2008) describes as:

- direct opposition control of vortices
- mitigating the evolution of large scale vortex formations by high-frequency forcing
- breaking large scale vortex formations by forcing 3D structures
- enhancing the initial symmetry by forcing synchronous shedding.

These can be attempted through passive, active open-loop and active closed-loop control approaches, to varying degrees of success.

A well-known example of direct opposition control of vortices is the splitter plate, which extends from the base surface downstream. The splitter plate does not allow the alternate vortices to interact until further downstream, which weakens their strength and thus increases pressure in the near wake region. This has been shown often (Anderson & Szewczyk 1997; Bearman 1965; Hwang *et al.* 2003; Kwon & Choi 1996; Ozono 1999; Roshko 1955), however such a large geometric addition is rarely possible practically. A similar effect can be achieved actively through base bleed, as has been shown by Arcas & Redekopp (2004); Bearman (1967); Delaunay & Kaiktsis (2001); Wood (1964); Yao & Sandham (2002); Wassen *et al.* (2010) or base suction (Leu & Ho 2000). However, as these methods target the global wake instability rather than the more receptive convective shear-layer instabilities, a great deal of input power is required. The whole process ends up inefficient, usually requiring more energy to operate than the energy saved through drag reduction (Choi *et al.* 2008).

The shear layer instability seems a more efficient target zone for wake control. Energising both shear layers through high-frequency forcing results in less well-developed

large vortical structures, which enlarges the dead water region and lifts base pressure. Park *et al.* (2006) achieved this on a 2D blunt-rear body through rear-mounted tabs and achieved an impressive drag reduction of 33% with optimised tab spacing and size. This effect has also been successfully implemented on other shapes by Yoon (2005) and (Darekar & Sherwin 2001) and actively by Kim *et al.* (2004) and Protas & Wesfreid (2002) who used rotating circular cylinders. Beaudoin *et al.* (2006) also used a rotating cylinder in his closed-loop investigation of this method on a backward facing step, where extremum-seeking feedback control was applied.

The third item, also known as "3D forcing", has generally been approached with passive solutions such as 3D geometric modification near the rear separation point on 2D bluff bodies. This has proven successful at low Reynolds numbers, with the normally 2D shear layers becoming more three-dimensional and less prone to rolling up to form the characteristic von Kármán vortex street (Petrusma & Gai (1994), Rodriguez (1991) and Tanner (1972)).

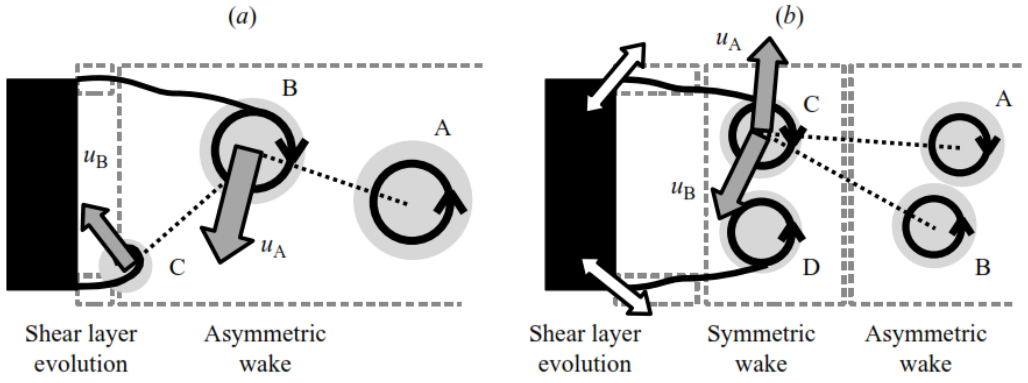

FIGURE 1.17: Schematic showing the standard von Kármán vortex shedding (a) compared to the synchronous vortex shedding mechanism created by periodic forcing (b). In the natural case, the downward velocity imposed by vortex A triggers the roll up of the upper shear layer into vortex B. The velocity imposed by vortex B then triggers the roll up of the lower shear layer, and so on. In the actuated case, the creation of synchronous vortices delays the appearance of asymmetries. Now, opposite velocities are imposed by both vortex A and B on the new vortices C and D, which almost annihilate one another. This attenuates the natural wake instability. Source: Pastoor *et al.* (2008) Figure 9.

However, the three aforementioned wake-control strategies become less successful as the Reynolds number is increased and three-dimensional effects, such as oblique shedding and vortex dislocation, begin to appear at random locations along the span (summarised eloquently in Tombazis & Bearman (1997)). As noted by Pastoor *et al.* (2008), "turbulent flows tend to elude suppression strategies by forming new struc-

tures". Fortunately, the fourth method listed above and first demonstrated by Pastoor *et al.* (2008) – forcing synchronous shedding – seems to bypass these difficulties. They attribute the drag reduction to synchronous vortex shedding from either side of the body, promoting cross-annihilation of the vortices in the near wake and thus increasing base pressure. This is achieved by perturbing the separating shear layers in-phase at the rear top and bottom edges, so that they resist forming a von Kármán vortex street immediately after separation. Increasing the amplitude of these shear-layer vortices makes it more difficult for such instabilities to break the initial symmetry. Pastoor *et al.* (2008) found that this process was most effective between actuation frequencies of $St_{act} = 0.10$ and $St_{act} = 0.20$, with an optimum close to $St_{act} = 0.15$.

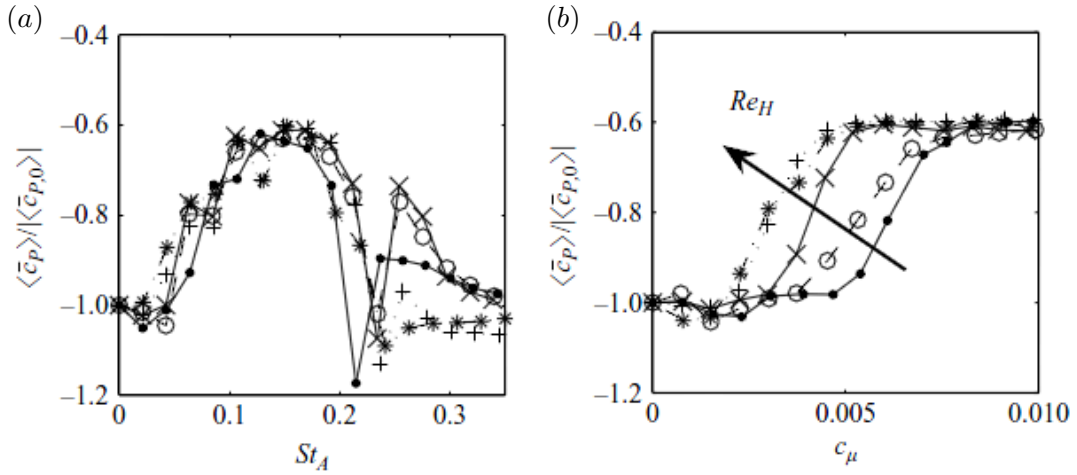

FIGURE 1.18: The effect on base pressure of actuation Strouhal number on (left) and momentum coefficient (right). Source: Pastoor *et al.* (2008) Figure 4.

Krajnovic & Fernandes (2011) completed a numerical replication of the study at a single actuation frequency with Large Eddy Simulations. They obtained good agreement in many of the output variables, including the drag reduction obtained and wake velocity profiles under actuation. The numerical approach also allowed for some excellent visualisations not possible experimentally (Figure 1.19). The images show a "busy wake" with an upper and lower vortex created by the blowing, temporarily lowering the base pressure, followed by a wake with less coherent structures during the sucking phase, leading to a higher base pressure. Even though the base pressure associated with blowing is lower than would be expected without actuation, the incredibly high base pressure associated with sucking more than compensates for this, resulting in a higher mean base pressure, and lower mean drag.

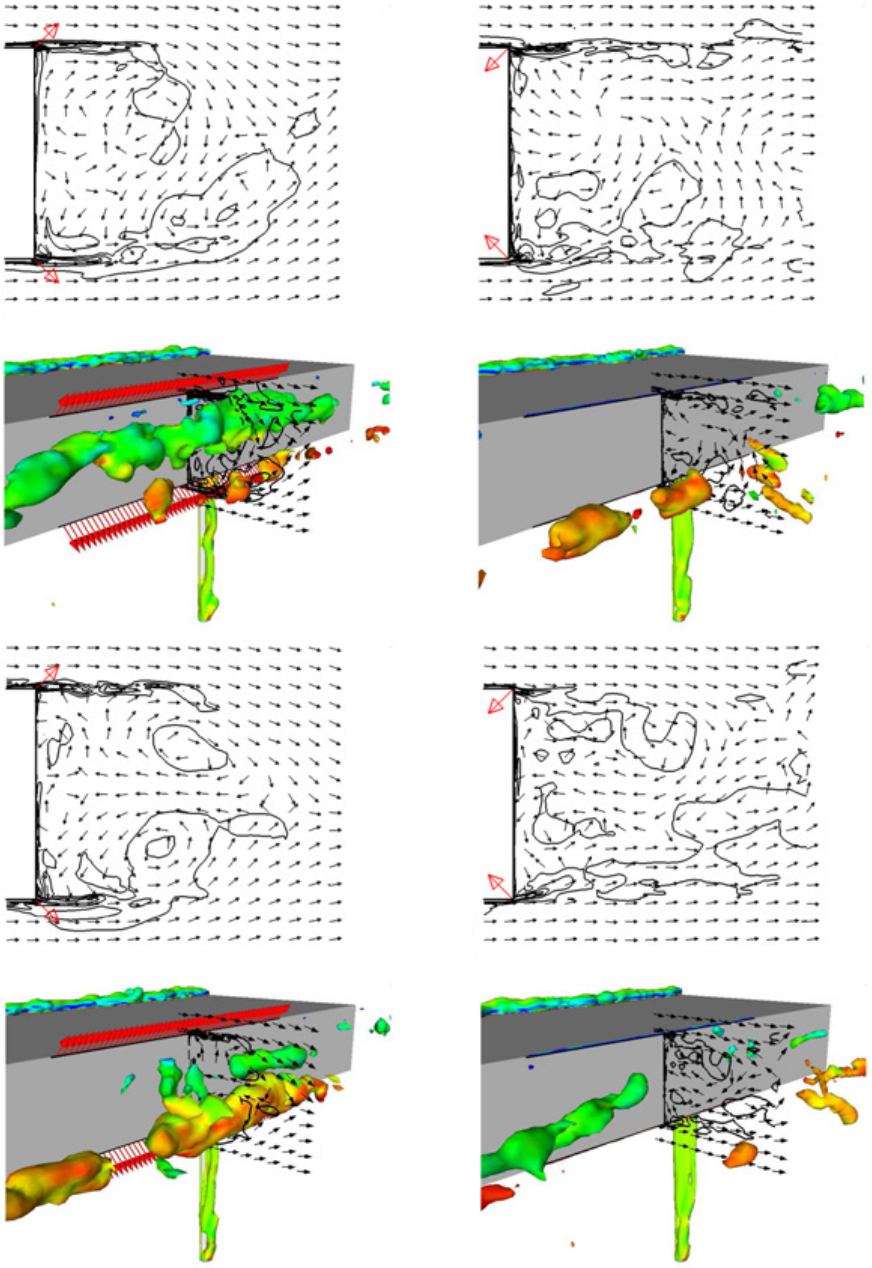

FIGURE 1.19: Velocity vector fields and spanwise vorticity (upper figure) and isosurface of p=-12, coloured with spanwise vorticity (lower figure). The first and third pictures (top left and bottom left) represent maximal blowing and correspond to maximum drag, while the second and fourth pictures (top right and bottom right) represent maximal suction and correspond to minimum drag. Source: Krajnovic & Fernandes (2011) Figure 12.

1.5.2 Current work

Chapter 4 in this study is devoted to numerically repeating the Pastoor *et al.* (2008) study (with an actuation sweep and momentum coefficient sweep) in order to confirm their analysis and yield further information on how the forcing influences the flow

dynamics in the near wake and leads to increased base pressure. It also seeks to answer the question – why does this frequency range most effectively influence the flow dynamic? The resolved time-dependent numerical simulations capture the velocity and pressure fields as a function of time and hence can substantially supplement the limited information available from the physical experiments of Pastoor *et al.* (2008), providing substantially more insight into the underlying flow physics. It is also planned to explore the effect of other variables, such as the angles of actuation and steady blowing and suction.

This is followed by a study of the effect of ground proximity on the flows and their capacity to effect change. This is examined in chapter 5. It is not known how ground proximity will affect the optimum actuation strategies, if at all. A thorough transient investigation of this will be beneficial to both the bluff body and flow control communities.

1.5.3 Closed-loop control

Away from the ideal conditions of the laboratory, open-loop approaches have been found to be unable to deal with external effects such as gusts and upstream turbulence, which apply in practical situations. These issues can, however, be tackled with closed-loop control, where real-time measurements of the flow can be actively fed back to actuators controlling their output to modify the downstream flow. While closed-loop control may provide the crucial link of successful open-loop methods to the real world, a better understanding of these open-loop control methods is still a required precursory step. The research presented in this thesis therefore focusses exclusively on open-loop control but is conscious of its importance in the further development of sophisticated closed-loop control strategies, be they gradient-based feedback schemes (Henning *et al.* 2007; Beaudoin *et al.* 2006), black-box models (Henning *et al.* 2007) or POD models (Noack *et al.* 2004).

1.6 Summary

In this chapter the role of fluid mechanics in the research of bluff body flow control has been demonstrated. The primary instabilities of bluff body wakes and the effect of aspect ratio were first explored before the complexities of three-dimensional bluff body flow and ground proximity were highlighted. Finally, a review on bluff body drag

reduction control techniques was presented.

This thesis explores the performance of an open-loop control approach based on sinusoidal forcing at the rear edges of a two-dimensional elongated cylinder with the same cross-section as a flat-back Ahmed body (Ahmed & Ramm 1984), effectively a simplified two-dimensional model with some broad features of a truck cross-section. Of course, trucks are fully three dimensional, with geometrical complexity and three-dimensional flows including drag-inducing trailing vortices originating close to the trailing-face corners. Thus, this research only focuses on one of the wake flow components contributing to variations in the drag, i.e., the rollup of the separating shear layers from the top and bottom edges into large-scale (predominantly two-dimensional) vortices, which form a von Kármán wake. The impact of ground proximity on this process is also analysed.

The following chapter outlines the various numerical techniques used to analyse the flows investigated in this thesis.

Chapter 2

Numerical Method

2.1 Domain and geometry details

Figure 2.1 shows the geometry studied in this work, together with the computational domain. The same dimensions and geometry used in the previously mentioned Pastoor *et al.* (2008) and Krajnovic & Fernandes (2011) studies are used here, with three exceptions. Firstly, the width of the domain is reduced from 550mm to 125mm to reduce computation time, noting that decreasing the width further resulted in significant differences in the flow statistics and flow structure. Secondly, the supports under the body are not modelled, in an effort to better understand the primary flow features associated with only the isolated bluff body. Finally, the trip-wires placed just downstream of the nose (Krajnovic & Fernandes 2011), which were added to trip the boundary layer at lower Reynolds numbers, were removed here—Krajnovic and Fernandes hypothesised they would not be required at $Re = 20,000$ because of natural minor flow separation on passing over the nose, and initial tests in this study confirmed that this was the case.

In regards to the actuation modelling, only one difference exists for this study. While Pastoor *et al.* (2008) chose only to apply actuation across the middle section of the rear edges and Krajnovic & Fernandes (2011) duplicated this for their numerical simulations of the same setup, they both recommended actuation across the entire span. Such an approach has been taken in this study. Not only does it potentially offer even greater drag reduction, but it also provides a better understanding of the wake structure—since all areas of the wake are influenced equally by the actuation.

Note that the actuation frequency was chosen as the main independent variable of interest for this study, with a momentum coefficient C_μ (as described in equation 2.1) held constant at 0.008, which was the optimum value found by Pastoor *et al.* (2008) for $Re_H = 23,000$. However, the effect of the momentum coefficient was investigated later,

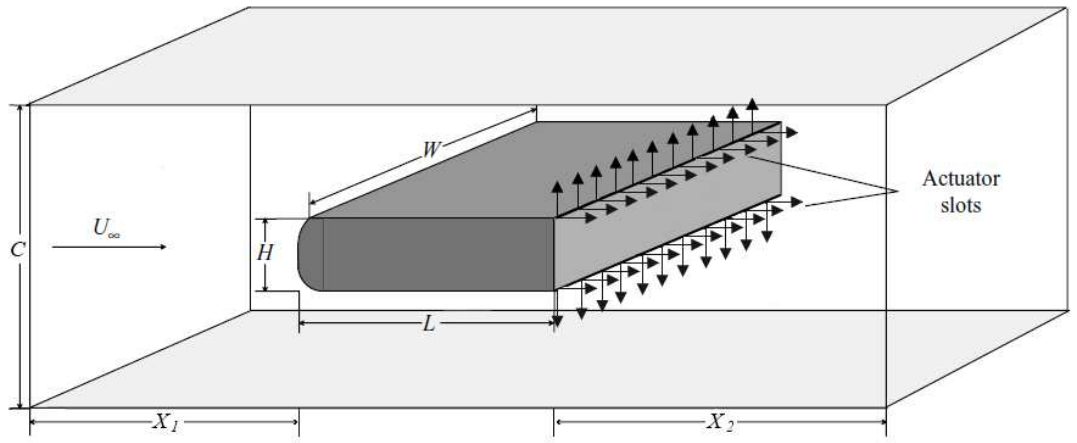

FIGURE 2.1: Sketch of the 3D flow domain showing the problem setup. The cylinder consists of an elongated rectangle with rounded leading edges, consistent with the Ahmed body geometry. The aspect ratio is $L/H = 3.64$. The computational domain dimensions are: $X_1 = 6.61H$, $X_2 = 24.47H$ and $C = 7.71H$. The domain extends into the third dimension a distance $W = 1.74H$. The blockage ratio is 13.0%. The origin $(0, 0, 0)$ is at the centrepoint of the body's rear face. The positive x-direction is downstream parallel to U_infty, positive y-direction upwards parallel to C and positive z-direction into the page, parallel to W.

showing a similar trend on the drag reduction to that observed by Pastoor *et al.* (2008), confirming the choice of $C_\mu = 0.008$ for the actuation frequency sweep as appropriate.

2.1.1 Actuation signal

The actuation signal is sinusoidal, and prescribed as a velocity at the actuators of $u_{act} = Asin(\omega t)$, where A is the amplitude of oscillation and $\omega = 2\pi f_{act} = \frac{2\pi St_{act} U_\infty}{H}$ defines the frequency. This signal results in an outlet RMS velocity $u_{act,rms} = A/\sqrt{2}$. The momentum coefficient is expressed as

$$C_\mu = N_a \frac{S}{H} \frac{u^2_{act,rms}}{U^2_\infty}, \tag{2.1}$$

where N_a is the number of actuators (four for the dual slot actuation case) and S/H the ratio of the slot width (1 mm) to the height of the body (72 mm). This is just the ratio of the momentum flux through the slots to the momentum flux passing through the region occupied by the body.

The total energy required to supply such a signal is relatively low: for the $Re_H = 23,000$ case, Pastoor *et al.* (2008) showed actuators at $c_\mu = 0.009$ require 0.094 W to operate, markedly lower than the power drag savings of 0.482 W obtained.

2.2 Code selection

The commercial software package ANSYS CFX was chosen as a suitable code to solve the Navier-Stokes equations for this geometry. Because of the long computation times and significant memory requirements for this parameter study, the large number of High Performance Computing (HPC) licenses held by Monash University was one reason for this choice.

2.3 Turbulence model selection and numerics implementation

Computational Fluid Dynamics is used to obtain approximate numerical solutions to the Navier-Stokes equations, which, derived from Newton's second law, describe the motion of fluids. Equation 2.2 shows the equations in an inertial frame of reference for incompressible flow of Newtonian fluids. In the form presented, the origin of Newton's second law is apparent, with the left side of the equation describing the total acceleration of the fluid packet and the right side the summation of body forces (f) and the divergence of the stress tensor (contributed by the pressure gradient, $-\nabla p$, and the viscous stress term, $\mu\nabla^2\boldsymbol{v}$):

$$\rho(\frac{\partial \boldsymbol{v}}{\partial t} + \boldsymbol{v}\cdot\nabla\boldsymbol{v}) = -\nabla p + \mu\nabla^2\boldsymbol{v} + f. \tag{2.2}$$

The vector momentum equation is solved in conjunction with the continuity equation which, when constant density is assumed, is a statement of volume conservation. That is,

$$\nabla\cdot\boldsymbol{v} = 0. \tag{2.3}$$

The nonlinear convective acceleration term $\boldsymbol{v}\cdot\nabla\boldsymbol{v}$ makes solving these equations difficult. While it is believed that the Navier-Stokes equations accurately describe fluid flow even in the highly turbulent case, the wide range of length and time scales associated with turbulence make this extremely resource intensive for high Reynolds numbers. The grid cell size and timestep used must be able to resolve eddies down to the Kolgmogorov microscale (or the order thereof, according to Kim, Moser and Moin 1987), η, below which the energy dissipates as heat. The ratio of largest (L) to smallest scales is proportional to $L/\eta = Re_L^{0.9}$ (where $Re_L = L\,V_\infty/\nu$). With this constraint applied in all three dimensions, the number of grid points required for Direct

Numerical Simulation (DNS) grows quickly with increasing Reynolds number. The estimated number of grid points for fully resolved DNS at various Reynolds numbers is shown in Table 1. With top-range desktop computers currently capable of working with grids of around 6×10^7 elements, and the world's top supercomputers capable of using grids up to around 1×10^9, it is clear that DNS is not yet possible for most bluff body flows of practical interest. With recent studies predicting future CPU transistor counts and densities to double only every 3 years, rather than every 1.5 years as per Moore's law, fully resolved DNS for highway-speed truck flow ($Re_L \approx 10^6 - 10^7$) may be over 100 years away.

Re_L	Grid Points Required	Bluff body example
$6,600$	2×10^6	Small marble rolling at $\sim$ 25 kph
$20,000$	4×10^7	1:43 scale matchbox car at $\sim$ 12 kph
$100,000$	3×10^9	Cricket ball bowled by Shane Warne ($\sim$ 90 kph)
$1,000,000$	1.5×10^{12}	Golf cart at average cruising speed ($\sim$ 25 kph)

This leaves fluid dynamicists with two options: avoid the resolution of the turbulent scales altogether through time-averaging and attempting to approximately account of the effects of turbulence on the time-averaged flow, or resolve only the turbulent structures above a certain size limit (filtering).

2.3.1 Reynolds-averaged Navier-Stokes approaches

Reynolds-averaged Navier-Stokes (RANS) approaches involve solving time-averaged Navier-Stokes equations. In a process first described by Reynolds (1895), the equations are decomposed into time-averaged and fluctuating components. Once time-averaged, the fluctuating terms become zero, leaving the time-averaged Navier-Stokes equations describing the mean flow. The time-averaged equations feature non-linear Reynolds-stress terms, which describe the effect of turbulence on the mean flow. There exist a great variety of turbulence models which attempt to approximate these Reynolds-stress terms. While no RANS turbulence model can claim universal accuracy or applicability, different models have been tailored for different flow situations over the years, and reasonably accurate mean-flow solutions can be obtained with appropriate model selection and implementation. This is especially true for flows with minimal separation regions.

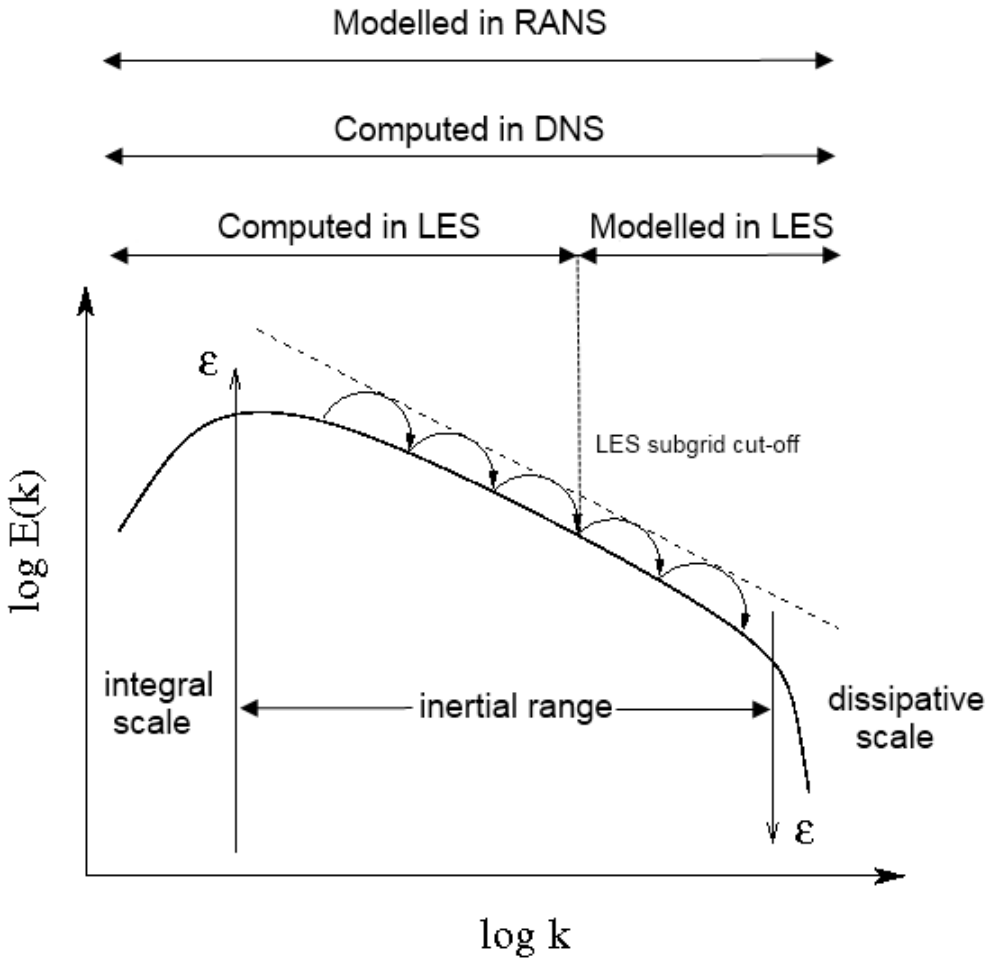

FIGURE 2.2: Schematic showing the turbulence energy cascade and differences between RANS, DNS and LES approaches. Image adapted from University (2012).

RANS techniques can be applied to obtain transient solutions also by leaving in the time-dependent terms: a process known as Unsteady Reynolds-averaged Navier-Stokes (URANS). In this case, the averaging can be considered over a set of ensembles at the same time, rather than a set of snapshots at different times. Traditional URANS methods can provide transient information on a single large-scale mode of unsteady behaviour, but still will not return smaller turbulent structures, which are essential in much flow analysis. A relatively recent approach, Scale Adaptive Simulation (SAS), is a new method of URANS modelling formulated by Menter and Egorov (2010) that partially overcomes this problem. By including the second velocity derivative, the model is able to automatically adjust its length scale to the structures already resolved in the flow. Thus turbulent structures down towards the size of the grid are better able to be

resolved, whereas traditional URANS solutions returned only transient structures on a single scale. This appears to allow solutions of similar accuracy to LES with much reduced computational power. The recent ANSYS 13.0 release is the first commercial software to feature the method in non-beta form, indicating the relative infancy of the method. It seems likely that SAS represents a significant breakthrough in the world of CFD, and will likely be a useful tool for transient bluff body flow analysis in coming years, however, its development and refinement was a few years too late to be used with confidence in this research.

2.3.2 Large Eddy Simulation

For flows with large separation zones, RANS and URANS approaches are unable to provide crucial temporal scales such as Kevin-Helmholtz frequencies, which can significantly alter the downstream development of a flow. For such flows, filtering approaches such as Large Eddy Simulation (LES) are required. The idea behind LES is to employ DNS for the important spatial and temporal scales in a flow, while modelling the effect on the flow of even smaller scales, which are assumed of negligible importance. Adequately deciding this cut-off point is the first vital step, and considering the energy cascade of turbulence is helpful in this regard. Figure 2.2 shows the approach schematically: it is clear that selecting an appropriate cut-off point will recover the majority of energy in the flow. Unfortunately, this is where difficulty arises—this size becomes progressively smaller as the Reynolds number rises, leading to a greater number of grid points being required. Thus, LES is still computationally expensive—but not so much as DNS, while still capable of recovering all the important flow information that DNS can.

The initial step of LES requires a low-pass filter to remove the small-scale motions. A convolution filter is typically employed for this task, taking a quantity ϕ and returning a filtered representation $\tilde{\phi}$ over the entire domain D as follows

$$\tilde{\phi}(x;\Delta) = \int_D G(x-x';\Delta)\phi(x')dx'. \tag{2.4}$$

G is the convolution kernel of the filter, and has a cutoff scale Δ. While this filter can be explicitly defined, in most practical finite-volume LES implementations, it is implied by the spatial discretisation (i.e., the grid cell size). This amounts in local volume averaging, which can be described as a box or top-hat filter (equation 2.5)

$$G(x-x') = \begin{cases} \frac{1}{\Delta} & \text{if } \mid x-x' \mid \leq \frac{\Delta}{2} \\ 0 & \text{otherwise.} \end{cases} \tag{2.5}$$

If G were only a function of $x-x'$ (which is the case for uniform grids), the filtering operation and differentiation would commute. However, more practically relevant non-uniform grids return commutation errors of $O(\Delta)$ (described by Ghosal & Moin (1995)).

Once filtered, we can represent the total quantity as the sum of a resolvable scale component and a subgrid scale component, as such:

$$\phi(x,t) = \tilde{\phi}(x,t) + \phi'(x,t). \tag{2.6}$$

We can express the velocity $U_i = \tilde{U}_i + U_i'$ and pressure $P = \tilde{P} + P'$ in this way, and derive a set of equations for the resolved field. In tensor form, the resolved field equations are thus

$$\frac{\partial \tilde{U}_i}{\partial x_i} = 0. \tag{2.7}$$

$$\frac{\partial \tilde{U}_i}{\partial t} + \frac{\tilde{U}_i \tilde{U}_j}{\partial x_j} = -\frac{1}{\rho}\frac{\partial \tilde{P}}{\partial x_i} + \nu \frac{\partial^2 \tilde{U}_i}{\partial x_j^2} - \frac{\partial \tau_{ij}}{\partial x_j}. \tag{2.8}$$

These are in fact similar to the RANS equations, with filtered components in place of the averaged components. It should be noted, however, that this is by appearance only, and the filtered quantities are substantially different in character to those in the RANS equations. Table 2.1 shows the fundamental differences between the two processes. The

Property	RANS	LES
$\bar{\phi}' = 0$	true	false
$\frac{\partial \bar{\phi}}{\partial x_i} = \overline{\frac{\partial \phi}{\partial x_i}}$	true	grid and filter dependent
$\bar{\bar{\phi}} = \bar{\phi}$	true	false

TABLE 2.1: Filter properties.

final term on the right hand side of equation 2.8 represents the residual stress left over from the filtering operation of $\widetilde{U_i U_j}$. Thus, the residual or sub-grid stress tensor is simply $\tau_{ij} = \widetilde{U_i U_j} - \tilde{U}_i \tilde{U}_j$. This must be modelled to close the equation—this is the greatest challenge facing Large Eddy Simulation practitioners.

The main role of the sub-grid model is to remove energy from the resolved scales such that the energy cascade is appropriately mimicked. Eddy viscosity models work on the molecular transport analogy, which relate the sub-grid scale stresses to the rate of strain in the fluid as follows:

$$\left(\tau_{ij} - \frac{\sigma_{ij}}{3}\tau_{kk}\right) = -2\nu_t \tilde{S}_{ij}, \tag{2.9}$$

where $S_{ij} = \frac{1}{2}\left(\frac{\partial \bar{U}_i}{\partial \tilde{x}_j} + \frac{\partial \bar{U}_j}{\partial \tilde{x}_i}\right)$ is the large-scale strain-rate tensor, ν_t the eddy viscosity and τ_{kk} is the trace of τ_{ij}, and represents the kinetic energy of the residual stress. These models fail to account for the energy dissipated due to other effects such as vorticity, and are therefore not theoretically perfect. However, with proper case-to-case modification using *a priori* knowledge, an appropriate amount of large-scale energy can be removed and desirable results achieved.

The original and most popular eddy viscosity model is the Smagorinsky model. It leans on the assumption that the small scales are in equilibrium and dissipate all energy received from larger scales instantaneously (production balances dissipation). This simplifies things greatly, leaving us with the following algebraic expression for the eddy viscosity ν_t:

$$\nu_t = \left(C_s \bar{\Delta}\right)^2 |\bar{S}| \bar{S}_{ij}, \tag{2.10}$$

where the grid length $\bar{\Delta}$ is approximated as the cube root of the element volume, and $\bar{S} \equiv \sqrt{2\bar{S}_{ij}\bar{S}_{ij}}$. The Smagorinsky constant C_s, which dampens the viscosity, must be specified and usually varies between 0.1 and 0.2 depending on the physics of the problem. Homogeneous turbulence fields such as those in channel or pipeline flow have been shown to require greater damping and typically employ a C_s value of around 0.2. For bluff body flows, with larger regions of shear and near-wall flow, the literature suggests 0.1 as a more appropriate value (Krajnovic & Fernandes 2011). The algebraic approach allows for relatively fast solutions times, and has made the Smagorinsky model the most popular LES method to date. However, three major weaknesses exist. Firstly, the lack of a universally applicable C_s value is an obvious problem. Secondly, the Smagorinsky model encounters difficulty with laminar and transitional flows, as it cannot produce zero eddy viscosity. Thirdly, the equilibrium assumption breaks down in near-wall and shear regions, requiring the application of ad-hoc damping (the Van Driest damping function being the most popular). The *Wall-Adapting Eddy-Viscosity* (WALE) model overcomes the latter problem by modifying $\bar{S}$ to adapt to near-wall flow structure. The *Dynamic* Smagorinsky model overcomes all three issues by dynamically adjusting C_s using the idea of scale-similarity, which allows the sub-grid scales to be modelled from information from the resolved velocity field (Germano *et al.* 1991; Lilly 1992). Of course, these models enforce extra mathematical relationships, often hindering stability, and results have been known to vary for anisotropic grids and complex geometries (Scotti *et al.* 1997).

While the filter width Δ and type of filter do not appear in the filtered equations, it must be remembered they are inherently present through the modelled τ_{ij} term. The end result is a method where the filtering, modelling, and numerical techniques are all interrelated to some extent. The result of the interplay between these factors is difficult to predict. A standard grid resolution analysis is therefore not sufficient in analysing resolution and *a posteriori* comparison with experimental results is recommended for full confidence.

Krajnovic and Davidson (Krajnovic & Davidson 2002, 2005a,b) have been instrumental in the development of Large Eddy Simulation for bluff bodies. They estimated that a computational grid of 6×10^8 nodes would be required to accurately perform Large Eddy Simulations on real-world Reynolds numbers for road vehicles (Krajnovic & Davidson 2002). Fortunately they have also shown a large similarity of flows in lower Reynolds numbers approaching the real-world levels, meaning lower Reynolds number simulations are still beneficial for at least a semi-quantitative understanding of the flow. LES is currently at the forefront of 3D bluff body analysis, with its ability to model the time-variant features so common in 3D flow a major advantage. *Detached Eddy Simulation* (DES) , which switches between the LES and Reynolds Averaged Navier-Stokes equations based on the location of turbulence in the flow, is a hybrid form of LES, which has also proved increasingly popular in recent years.

2.3.3 Details of final turbulence model and numerics used

For the element-based finite-volume (FV) commercial code ANSYS CFX, quantities at the face between two control volumes are approximated from nodal values via shape functions for the non-advection terms. For the advection term a blended scheme or central-differencing scheme can be used. The former uses a weighted combination of a first and a second-order scheme: when the blend factor (β) is zero the scheme is first-order, and when it is set to one, the scheme is second-order accurate. In this work, as with Krajnovic & Fernandes (2011), $\beta = 1$ was chosen, returning 2nd-order accuracy in space. This scheme features more numerical diffusion than the alternative 2nd order central-differencing scheme available (perhaps a downside, considering sub-grid modelling in LES already over-predicts diffusion), but it is also more stable. Further validation for the selection of the blend scheme is discussed in § 3.1.5.

The diffusion and pressure gradient terms are also calculated from shape functions,

and are 2nd-order. The 2nd-order (iterative) backward Euler-type scheme was used for temporal discretisation.

In line with the standard large-eddy simulation approach, the implicit LES technique in CFX filters out eddies smaller than the grid spacing, resolving the larger structures, which contain the bulk of energy in the flow. However, energy needs to be removed from the resolved scales such that the energy cascade is appropriately mimicked, and this is the job of the sub-grid scale model, the types of which are discussed in § 2.3.2. The standard Smagorinsky model was the final model used in this work, with C_s held constant at 0.1—a value leading to moderate damping of the sub-grid eddy viscosity dissipation and often used for bluff body flows (and also used in the Krajnovic & Fernandes (2011) study). This model performed well, showing good agreement with the experimental results of Pastoor *et al.* (2008). Further validation on the selection of the Smagorinsky model is discussed in § 3.1.4.

2.4 Mesh generation

2.4.1 Requirements

Generating an acceptable mesh is often one of the most difficult tasks involved in CFD. While the simple geometry involved in this study lessened this difficulty somewhat, challenges remained. A key issue with simulations involving actuation is the high ratio of fluid speed to inlet velocity in the narrow actuated regions, which can easily lead to high local Courant-Friedrich-Lewy numbers. Nevertheless, care must be taken when meshing around these areas, with both a high quality and high quantity of mesh elements to resolve these regions. In addition, dimensionless wall values (i.e., y^+, but also Δx^+ and Δz^+) need to be kept in an acceptable range for accurate Large Eddy Simulations. For efficient solving, all these requirements must be met without allowing the mesh point count to become too high.

After a period of trial-and-error testing, a mesh generation procedure was developed to best achieve these requirements. This is shown in table 2.2. Steps 1–5 and 8 are discussed in more detail below. Differences between the standard and ground proximity model procedure are outlined where required.

	Step	Description
1	Geometry creation	Draw the geometry, splitting domain into numerous wake-boxes
2	Import geometry	Import the geometry into ANSYS Workbench
3	Edge/Face meshing	In ANSYS Meshing create the 2D mesh by selecting the number of intervals required on the body and wake-box edges
4	Sweep to create volume mesh	Sweep the 2D mesh a certain number of intervals in the spanwise dimension
5	Examine the mesh	Check mesh for unacceptable elements through quality measures such as aspect ratio and skewness
6	Naming	Apply named selections to appropriate regions such as "inlet", "outlet", etc.
7	Export mesh	Save and export the mesh to the CFX solver
8	Repeat for grid resolution study	The process is repeated with different edge sizings, and key flow statistics are compared to judge grid independence

TABLE 2.2: Mesh generation procedure.

2.4.2 Geometry creation

The model was built "bottom up" using the commercial software NX 7.5. An initial sketch of the 2D geometry was extruded in the spanwise dimension, with the body region then subtracted to create the fluid volume. The domain was split in to numerous regions to allow for greater control of mesh density according to the local flow. Figure 2.3 shows the regions and corresponding numbers for identification in this section. The result was saved as a .prt file, which has strong associations with ANSYS.

Figure 2.5 shows the geometry created for the ground proximity case. The body is $0.2H$ above the ground. Extra zones were required to gain complete control of the mesh elements in the ground regions.

2.4.3 Edge/Face Meshing

Hexahedral elements were chosen for regions 1–6. They exhibit less diffusion and are generally more accurate than tetrahedral cells of the same size. The weakness of hexahedral elements, that they provide less control for capturing complex geometries, is not applicable for the parallelogram shapes of these regions (region 6 is equivalent to a rectangle if the bottom half is twisted up to be parallel with the top half). For the non-parallelogram regions 7 and 8, coarse triangular-prism elements were used. Extremely fine resolution was generated at the rear edges of the body and in the near wake, with

the elements slowly growing downstream. Figures 2.3 and 2.5 show the final mesh edge sizings used for the away-from-ground and ground proximity cases, respectively, Further information on the final mesh sizings is given in § 2.4.7.

2.4.4 Sweep to create volume mesh

The 2D mesh was swept in the spanwise dimension a certain number of elements. The sizing was uniform across the span.

2.4.5 Examine the mesh

Element skewness and aspect ratio values are examined for the mesh. For the final mesh, aspect ratio averaged 5.5, with a maximum of 35. This is far below the maximum recommended aspect ratio of 100, above which significant round-off errors occur. The average skewness is 0.05, which is very low. There exist a few highly skewed elements in the far field, although they are still under the 0.85 maximum value recommended. The average orthogonal quality is 0.99.

2.4.6 Grid and timestep resolution studies

The dependence of the flow on grid and timestep sizes was analysed in some detail, the results of which are summarised in §3.1.

2.4.7 Final mesh details

The mesh shown in Figure 2.4 demonstrated acceptable grid independence in the grid resolution study, and adheres to the dimensionless wall value recommendations of Krajnovic (2009). It consists of 7,600,600 elements and features dimensionless wall values $\Delta x^+ \approx 10\text{–}20, y^+ \approx 0.5\text{–}4, \Delta z^+ \approx 5\text{–}50$. The average y-plus value is $y^+_{ave} = 3$.

Figure 2.3 shows the number of elements along each zone edge. The numbers in brackets represent the bias factor associated with each edge. The direction of bias can be considered to always be towards the rear corners of the body. For example, the green lines have more elements on the left side of the lines, while the black lines have more elements at the outer extremities. The blue line features bias towards the centre of the line. Face sizings of 5 mm and 15 mm were imposed in zones 7 and 8, respectively. The 2D mesh was swept 70 cells over 0.125 m into the third dimension. This gives a uniform size of 0.0018 m in the 3rd dimension.

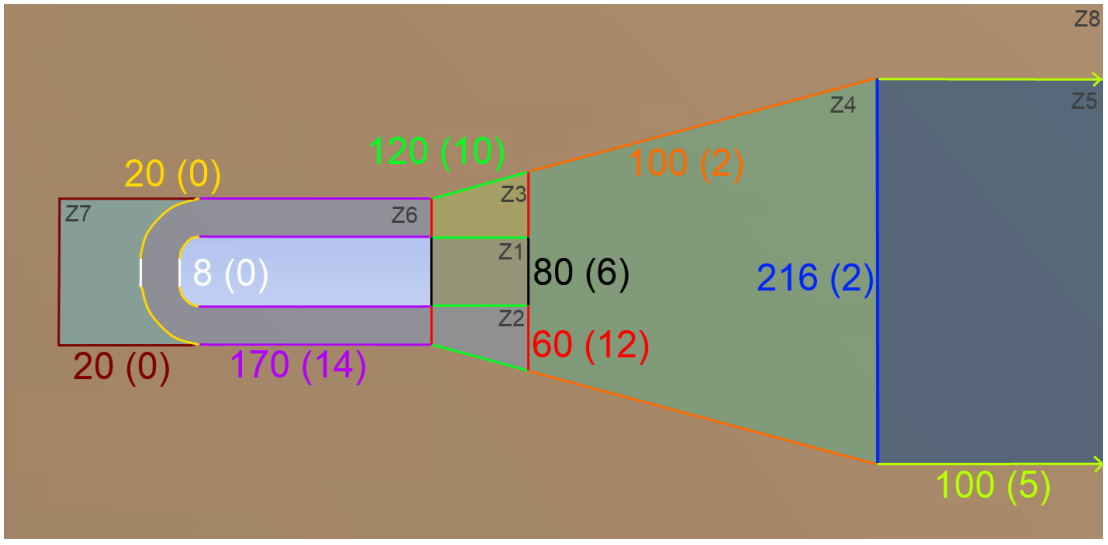

FIGURE 2.3: Wake boxes showing the number of elements along each zone edge (the numbers in brackets represent the bias factor associated with each edge).

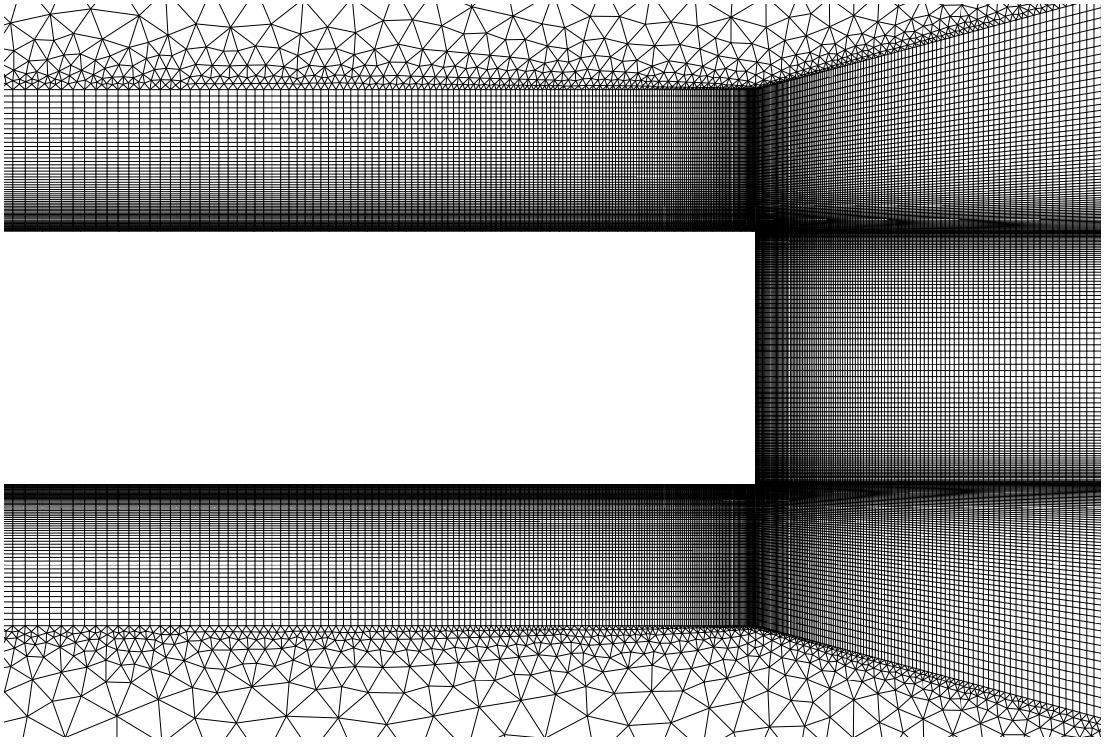

FIGURE 2.4: Cross-section of the mesh used for away-from-ground study (the 2D mesh was swept 70 elements into the Z-dimension).

Figure 2.6 shows the mesh for the ground proximity model. The mesh was kept identical to the away-from-ground model wherever possible, however this, of course, was not achievable in the ground region. In order to capture the ground proximity flow properly, a high mesh density was required in this region, increasing the final mesh to 8.6 million elements compared to 7.5 million elements for the away-from-ground case.

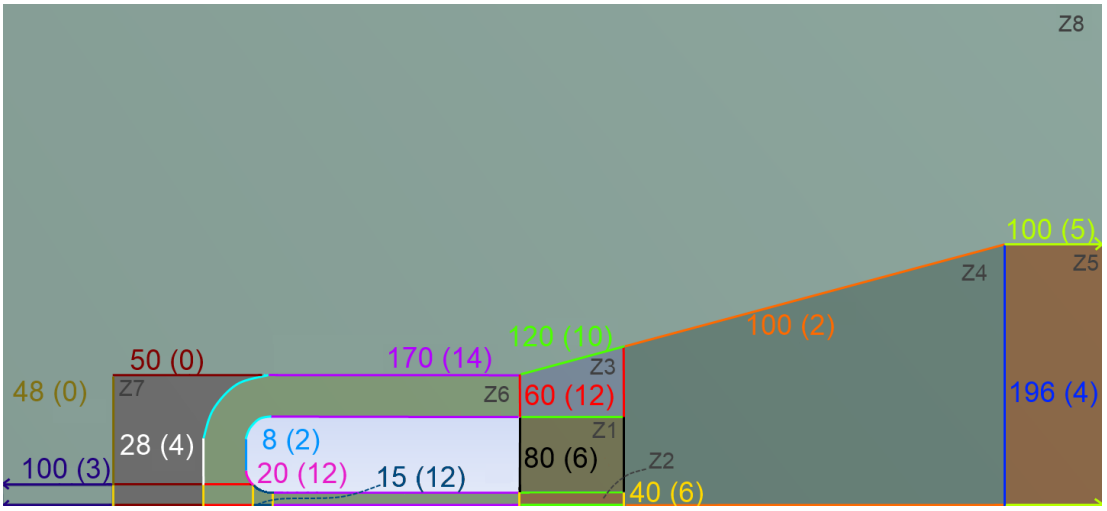

FIGURE 2.5: Wake boxes for the ground-proximity case.

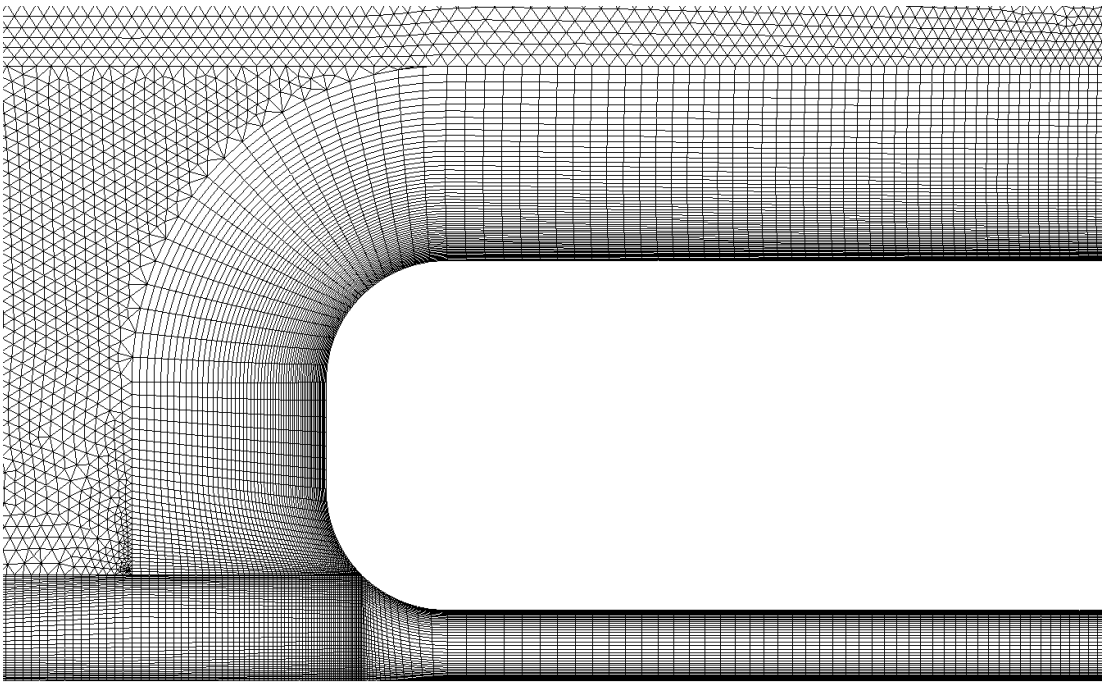

FIGURE 2.6: Cross-section of the mesh used for ground proximity study (the 2D mesh was swept 70 elements into the Z-dimension).

Dimensionless wall values for the ground proximity case are $\Delta x^+ \approx$ 10–20 and $\Delta z^+ \approx$ 5–50. With more of the fluid travelling over the body, the y-plus value reaches 10 over the upper leading edge, but is limited to $y^+ \approx$ 0.5–5 over the rest of the body. The average y-plus value is $y^+_{ave} = 2.75$.

Monitor Point	X/H	$\pm Z/H$
B	-1.40	0.70
S	0.21	0.50
$W1$	1.00	0.80
$W2$	3.00	0.90
$W3$	5.00	1.00

TABLE 2.3: Monitor point locations for away-from-ground case. The origin $(0, 0, 0)$ is situated at the centre of the rear surface of the body. All points are on the spanwise centreplane $(Y/H = 0)$.

2.5 Monitor points

A full time history of certain variables was obtained at the locations displayed in Figure 2.7 and Table 2.3 for each case. This allowed for thorough frequency analyses at multiple points in the flow, information which is crucial in developing a proper understanding of the mechanisms in place.

All shear layer and wake points were velocity monitoring positions, while the remaining points and surfaces (including the actuator surface, not pictured) were pressure monitors.

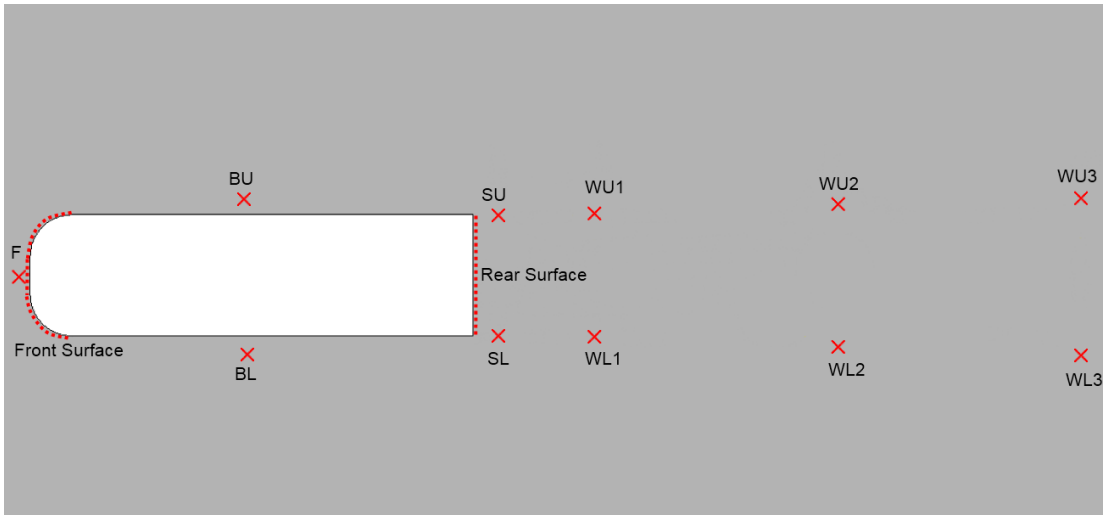

FIGURE 2.7: Monitor point locations. The acronyms follow the labelling code where "B" represents "Body", "S" is "Shear Layer", "W" is "Wake", "U" is "Upper", "L" is "Lower" and "F" is front. All points are located on the centre plane. Stations W1, W2 and W3 occur at H, $3H$ and $5H$ downstream of the rear face, respectively. Note also the dotted red lines, which indicate line monitors of surface pressures. Exact locations are displayed in Table 2.3.

A similar set of monitors was set up for the ground proximity model. As can be seen in Figure 2.8 and Table 2.4, variations occur in the placement of the wake monitor

Monitor Point	X/H	$\pm Z/H$
B	-1.67	0.60
S	0.21	0.60
$W1$	1.00	0.50
$W2$	3.00	0.50
$W3$	5.00	0.50

TABLE 2.4: Monitor point locations for ground-proximity case. The origin $(0, 0, 0)$ is situated at the centre of the rear surface of the body. All points are on the centreplane ($Y/H = 0$).

points—the slight gradient outward for the away-from-ground monitor points is not able to be replicated here, due to the ground obstruction. Instead, the wake monitor points are all at the same height with increasing downstream distance.

2.6 Collection of transient results

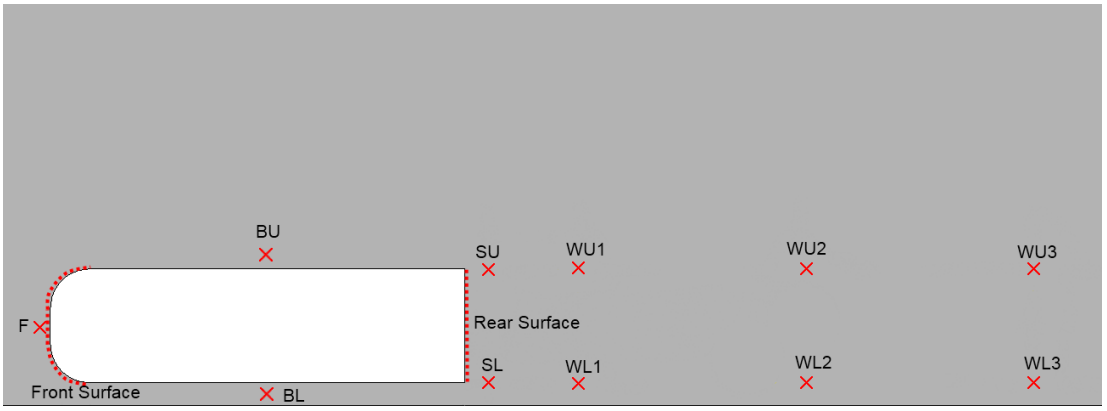

FIGURE 2.8: Monitor point locations for the ground proximity model.

While monitor points return a time history for every iteration at certain locations, this is not possible for the whole domain due to computational storage constraints. Thus, a full set of the field variables can only be saved at a certain interval of time. Here, results were saved every 50 timesteps (0.005 seconds of flow). This relates to a non-dimensional time of 0.29—the freestream fluid travels a distance of approximately $0.29H$ between each saved time. More important is the relationship between the saving interval and the characteristic period of von Kármán shedding. The wake Strouhal number, measured at 0.22, relates to a frequency of approximately 13 Hz or period of 0.08 s. The 0.005 s saving interval is therefore 0.005/0.08 or approximately one sixteenth

of the wake shedding period. Importantly this allows enough resolution for accurate Dynamic Mode Decomposition (discussed later) and smooth video reconstruction of the wake.

2.7 Domain size and blockage correction

The computational domain size, or equivalently the wind tunnel size for experiments, has been shown to have a substantial effect on the flow field for both experimental and numerical bluff body tests. Closed wind tunnels, those usually replicated numerically, return higher drag values than would be the case in infinitely large domains. A major reason is the decrease in available flow area around the body, which causes an increase in velocity as the flow passes over the body (akin to a the convective acceleration experienced by a parcel of fluid travelling through a converging nozzle). For cases with leading edge separation, this effect is even greater. To be able to compare with other results obtained for different blockage ratios, this increase in fluid speed around the body must be accounted for when calculating non-dimensional values such as drag coefficient or Strouhal number. Using the appropriate method is vital in this situation, where the blockage is a relatively high 13%.

Maskell (1963) was the first to devise blockage correction formulae for bluff-body flows in closed wind tunnel test sections. He proposed that the pressure field and therefore flow separation behaviour was invariant under constraint, and Farell *et al.* (1977) have since shown this is true for $S/C < 0.21$, where S is the cross-sectional area of the model, and C is the cross-sectional area of the test section.

Maskell also described the constraining effects of the test section walls, which reduce the expansion of the wake, distorting the drag value. This is known as the wake constraint effect, and is separate to the increase in freestream velocity. His momentum-based derivation of a dynamic pressure correction equation includes this wake constraint consideration. For bluff bodies with no support rig and negligible skin-friction drag, his proposed correction equation is approximately:

$$q_c/q_u = \left[1 + \theta \left(\frac{S}{C}\right) C_{Du}\right], \tag{2.11}$$

where C_{Du} is the uncorrected drag coefficient and $\theta = -1/C_{bpc}$. C_{bpc} is the corrected base pressure coefficient and must be obtained by iterating

$$(1 - C_{pbc})_i = \frac{(1 - C_{pbu})}{1 + (-1/C_{pbc})_{i-1}(C_{Du}S/C)},$$

where C_{pbu} is the uncorrected base pressure coefficient, and the initial value of C_{pbc} is simply C_{pbu}.

This method combines the dynamic pressure and the incremental drag blockage components into a single dynamic pressure adjustment. While this results in an accurate drag correction, it leaves the dynamic pressure over-corrected. Hackett *et al.* (1979) eliminated this problem by splitting the correction into a dynamic pressure component, and a drag blockage component. He proposed a two-step method, the first step of which finds the drag corrected for blockage only $C_{D\infty}$:

$$C_{D\infty} = (C_{DcM1} - \Delta C_{DM}) = \frac{C_{Du}}{q_c/qu} = \frac{C_{Du}}{1 + \theta(C_{DcM1} - \Delta C_{DM})(S/C)}, \tag{2.12}$$

where C_{DcM1} is the drag corrected by Maskell's method (equation 2.11). Next Hackett computes the drag corrected for both blockage *and* wake constraint C_{DcM2}:

$$C_{DcM2} = \frac{C_{Du} + \Delta C_{DM}}{(q_c/q_u)} = \frac{C_{Du} + \Delta C_{DM}}{1 + \theta(C_{DcM1} - \Delta C_{DM})(S/C)}.$$

Now the corrected dynamic pressure term q_c/q_u does not include the wake constraint effect (which is solely represented in the ΔC_{DM} term), as desired. ΔC_{DM} is found via the quadratic equation

$$\Delta C_{DM}^2 - \left(\frac{1}{\theta(S/C)} + 2C_{DcM1}\right)\Delta C_{DM} - C_{DcM1}(C_{Du} - C_{DcM1}) = 0.$$

This method has shown strong performance in a variety of situations, and is used in this study. In this case, the freestream corrected velocity $U_{\infty,c}$ was calculated as 4.91 m/s according to Hackett's method, compared to the inlet value of 4.36. All non-dimensional values are calculated using $U_{\infty,c}$. For example, the corrected velocity lifts the Reynolds number from $20,000$ to $23,000$ and drops the Strouhal number from 0.248 to 0.220. The corrected drag coefficient according to equation 2.12 is 0.72 compared to 0.89 uncorrected. For brevity, U_∞ instead of $U_{\infty,c}$ will be used to indicate the corrected freestream velocity hereafter.

2.8 Ground proximity changes

For the ground proximity case, aside from the different geometry and mesh already discussed, all numerics, turbulence model details and boundary conditions were maintained from the away-from-ground case, with one exception: the stationary, free-slip lower domain wall was replaced with a no-slip wall moving at the inlet velocity. The effect of a moving ground plane is discussed in § 1.3.4.

2.9 Data processing

Data processing was exclusively conducted using the software package MATLAB. The program allows for efficient processing of large data structures through Matrix operations.

2.9.1 Data management

Two types of data are returned from each simulation: the monitors data recorded at every timestep, and full domain solutions recorded at designated timesteps (in this case, every 50 timesteps). The former are exported at the conclusion of the solution stage from the CFX Solver into a *.csv file with each column holding the time history for each monitor point. The latter must be exported one timestep at a time from within the CFX-Post module. This can of course be tedious, and scripts are therefore used to progress through each timestep and extract the required information (again, to a *.csv file).

2.9.2 Averaging

Both instantaneous and time-averaged data are useful in fluid flow analysis. CFX has the ability to average certain variables "as it goes", so long as this is requested during the problem set up. Here, all velocity components, vorticity components, wall shear components and pressure variables were time-averaged, according to

$$\langle f(t) \rangle = \frac{1}{\Delta T} \int f(t')\, dt',$$

where ΔT is the total time for the average to be taken over.

2.9.3 Frequency analysis

Accurately identifying key frequencies in the flow is vital in constructing a complete understanding of the flow. The Fast Fourier Transform (FFT) is the most recognised method of achieving this, and is used in this research. The FFT computes the Discrete Fourier Transform (DFT) in a more computationally efficient manner than the standard form of the DFT. The DFT is defined as

$$X_k = \sum_{n=0}^{N-1} x_n e^{-i2\pi k \frac{n}{N}} \quad k = 0, ..., N-1,$$

where $x_0, ..., x_{N-1}$ represents the set of complex numbers describing the signal at discrete times, and N is the number of terms. In this research the popular Cooley-Tukey

algorithm (Cooley & Tukey 1965) is used to compute this in a "fast" manner. The algorithm recursively breaks down a DFT of any size into many smaller DFTs, and as such is able to deal with large data sets. Importantly the operation count is reduced from order N^2 to $N \log N$.

Approaches based on wavelets provide information on the time-varying nature of the frequencies in the flow, something not possible with FFTs. A wavelet is a short wave-like oscillation with amplitude of zero at beginning and end, and will mathematically "resonate" if its frequency exists in a signal. This unique capability can be utilized in the continuous wavelet transform (CWT) operation to provide a time-frequency representation of a signal with superb time and frequency localization. The CWT projects a signal $x(t)$ on a continuous family of frequency bands. The bands, $X_w(a, b)$ where a and b are the scale and translational value respectively, are built around scaled versions of a mother wavelet function ψ as follows (the * indicates the complex conjugate operation):

$$X_w(a,b) = \frac{1}{\sqrt{|a|}} \int_{-\infty}^{\infty} x(t)\psi^* \left(\frac{t-b}{a} \right) dt.$$

In this research the Morlet mother wavelet (Goupillaud *et al.* 1984) is used in this process. This wavelet, shown in Figure 2.9, offers the best balance between spatial and frequency resolution. A MATLAB script developed by the United Kingdom National Oceanography Centre (see Appendix B) flow, with the x-axis giving the time evolution of the signal, the y-axis the frequency spectrum and the z-axis the magnitude of frequency. For the results displayed in the thesis, these are visualised in colour contour format, with the z-component represented by a rainbow spectrum.

2.9.4 Model Reduction Techniques

Developing an understanding of high-order systems based solely on observed data, such as those involving turbulent fluid flow, is difficult. For the fluid flow example, a wide range of both spatial and temporal scales exist, which makes a traditional global stability analysis close to impossible. By reducing the system to a lower-order model, where the important features can be analysed separately and in more detail, a greater understanding of the system can be gained.

Consider we have a set of N flow fields obtained experimentally or numerically with constant timestep Δt and n variables of interest. This can be represented as one data

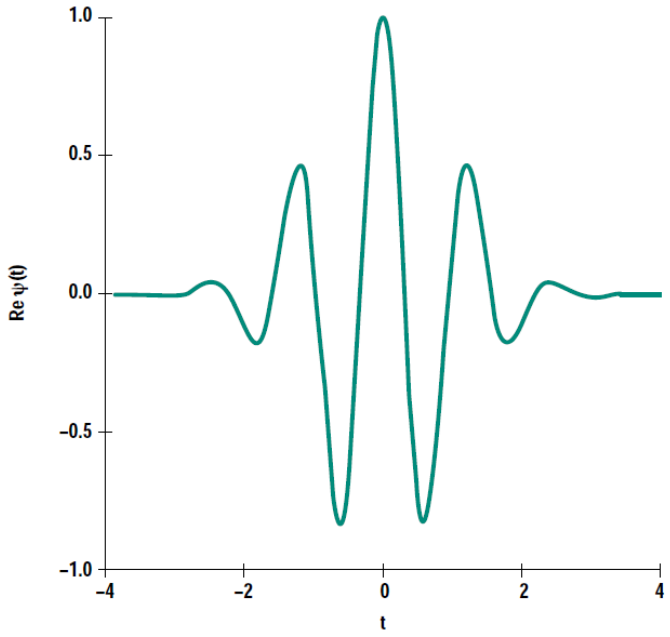

FIGURE 2.9: An example of a Morlet Wavelet. Source: Lee & Yamamoto (1994).

matrix with the columns containing the snapshots,

$$V = [v_1 \quad ... \quad v_{N-1} \quad v_N], \tag{2.13}$$

where $v_j = v(x_i, t_j)$ is each snapshot. This data can be approximated as a superposition of M modes

$$v(x_i, t_j) \approx \sum_{m=1}^{M} b_m(x_i) a_m(t_j). \tag{2.14}$$

We can express the temporal amplitudes $a_m(t_j)$ as T, and the spatial modes $b_m(x_i)$ as X, giving the alternate matrix form

$$V \approx XT. \tag{2.15}$$

Finding the basis functions X and T mathematically is not difficult, however our motivation here is to find such functions from raw data only. Proper Orthogonal Decomposition (POD) and Dynamic Mode Decomposition (DMD) are two popular methods of achieving this with data snapshots alone. Both will be explored below in the context of fluid flow.

2.9.4.1 Proper Orthogonal Decomposition

Proper Orthogonal Decomposition (POD) extracts spatial or temporal correlation of the measured variables V. The goal is to compute the set of basis functions in 2.14 so that

the error between the original and reconstructed data is minimized. The technique begins by computing a weighted correlation matrix C of the data matrix V as per equation 2.16

$$C = V^* W V, \tag{2.16}$$

where * denotes the transpose. Here, W, the weighting matrix, is diagonal with weights equal to the local cell volumes for each grid point. The correlation matrix is able to describe the covariance of any two snapshots. For example, $C_{2,5} = u_2^* W u_5$ would return the global covariance of the second and fifth snapshots. The next step is to find the eigenvalues λ_k and eigenvectors ψ_k of C. That is,

$$C\psi_i = \lambda_i \psi_i, \qquad i = 1, \ldots, N. \tag{2.17}$$

We are left with real and nonnegative eigenvalues which describe the energy content of the flow structure represented by the corresponding eigenvectors. The eigenvectors are orthogonal, meaning each mode is decorrelated statistically from any other. We now express the temporal amplitudes T introduced in equation 2.14 as scaled versions of the eigenvectors ψ_i,

$$T = \begin{bmatrix} a_1(t_j) \\ \vdots \\ a_N(t_j) \end{bmatrix} = \begin{bmatrix} \psi_1^T \sqrt{\lambda_1} \\ \vdots \\ \psi_N^T \sqrt{\lambda_N}. \end{bmatrix} \tag{2.18}$$

Finally, the modes X can be obtained by inversion of equation 2.14.

$$X = VT^{-1} = V \left[\frac{\psi_1}{\sqrt{\lambda_1}} \cdots \frac{\psi_N}{\sqrt{\lambda_N}} \right]. \tag{2.19}$$

There are two limitations of POD which are well known:

- the structures are ranked on variance or energy contained, which is physically not always appropriate
- the modes are based on averages, thus losing key phase information

Whilst the first of these is usually not an issue with turbulent fluid fields (the most energetic modes are generally the most relevant), the second most definitely is: the transient evolution of a fluid flow structure can describe extra information not possible statically.

2.9.4.2 Dynamic mode decomposition

Dynamic Mode Decomposition (DMD) is a technique recently introduced by Rowley *et al.* (2009) and Schmid (2010) which aims to extract dynamic information, specifically the time-based evolution of spatial structures, from a set of observed snapshots. The process involves decomposing the flow into modes through spectral analysis of the linear Koopman operator, K. Here the modes are separated by the motion frequency of each structure, rather than spatial information (which is the case for POD).

Once again, we begin with the global data matrix V of observed measurements M over N timesteps—here we also express the range of V with the subscript and superscript denoting the first and final timesteps considered, respectively. The matrix is of size $M \times N$, which typically is a *tall* rectangular matrix as the number of measurement points M is generally much larger than the number of snapshots N. From here forward we will assume the measurement being made is velocity—the most common measurement for such analyses. We have

$$V_1^N = \{v_1, v_2, ..., v_N\}. \qquad \text{where} \quad v_j = \begin{bmatrix} \text{velocity at point 1} \\ \text{velocity at point 2} \\ \vdots \\ \text{velocity at final point} \end{bmatrix}. \tag{2.20}$$

Next a linear-tangent approximation is used to allow for linear mapping from one snapshot (v_j) to the next (v_{j+1}). While the progression is of course in reality nonlinear for fluid flow, the linear Koopman operator K is infinite dimensional, and can thus can capture the full information of the nonlinear system. This is represented as

$$v_{j+1} = Kv_j, \tag{2.21}$$

and if considering the global data matrix V, we therefore have

$$V_2^N = KV_1^{N-1}. \tag{2.22}$$

Using only the observed velocity fields, we are able to analyse the flow dynamics using the eigenfunctions ψ_j and eigenvalues λ_j of K. Finding these, however, is not straightforward. DMD uses a technique similar to the Arnoldi method where the large K matrix is approximated by a companion matrix S, which shifts the snapshots from 1 to $N-1$ and leaves a residual error vector r.

$$V_2^N = KV_1^{N-1} \approx V_1^{N-1}S + r. \tag{2.23}$$

The final column of S, which holds the linear representation of the last sample v_N, is represented in terms of all the preceding samples, according to Ruhe (1984). This is possible due to our assumption that there is a linear dependence of recent snapshots on previous ones (Schmid 2010). We therefore have

$$S = \begin{bmatrix} 0 & & & & a_1 \\ 1 & 0 & & & a_2 \\ & \ddots & \ddots & & \vdots \\ & & 1 & 0 & a_{N-2} \\ & & & 1 & a_{N-1} \end{bmatrix}.$$

The a values are determined from the snapshot matrices V_1^{N-1} and V_2^N by a least-squares procedure which minimises the Frobenius norm (equation 2.24) of the residual vector from equation 2.23:

$$\min ||V_2^N - V_1^{N-1}K||_F^2. \tag{2.24}$$

The matrix division of V_1^{N-1} by the final snapshot v_N solves this equation with relative ease.

However, while solving equation 2.23 is often sufficient for smaller datasets, performing a singular value decomposition (SVD) of V_1^{N-1} is an option for larger datasets to improve robustness and convergence. We begin with

$$V_1^{N-1} = A\Sigma B^*, \tag{2.25}$$

where A and B are unitary matrices of size $M \times N$ and $N \times N$ respectively, while Σ is an $N \times N$ diagonal matrix whose main diagonal has non-zero singular values $\{\sigma_1, \ldots, \sigma_N\}$. Substituting into equation 2.25 we now have

$$KA\Sigma B^* \approx A\Sigma B^* S + r, \tag{2.26}$$

which can be re-arranged to give

$$A^*KA \approx \Sigma B^* S B \Sigma^{-1} + A^* r B \Sigma^{-1}. \tag{2.27}$$

Thus we are left with S_T, the transformed version of the companion matrix S,

$$S_T = \Sigma B^* S B \Sigma^{-1}. \tag{2.28}$$

Returning to the Frobenius norm (equation 2.24), we finally have

$$\min_{S_T} ||(A^* V_2^N B \Sigma^{-1} - S_T)\Sigma||_F^2. \tag{2.29}$$

We are left with L, a low-dimensional representation of the Koopman mapping companion matrix S.

$$L = A^* V_2^N B \Sigma^{-1}. \tag{2.30}$$

2.9.4.3 DMD modes

Within L (or S if SVD has not been performed) is information on the spectrum and associated structures of the flow. We again have a similar eigenproblem as encountered in equation 2.17. The eigenvectors y_j and eigenvalues λ_j (known as Ritz values) of L are found through

$$Ly_j = \lambda_j y_j, \qquad j = 1, 2, \ldots. \tag{2.31}$$

The Ritz values are a subset of the K eigenvalues, while the corresponding eigenvectors y_j contain the coefficients for the reconstruction of dynamic modes. The final DMD modes are then constructed individually via

$$\Psi_j = U y_j, \tag{2.32}$$

where U is the right singular vectors of V_1^{N-1}.

Represented as a whole, the DMDs modes are

$$\Psi = UY. \tag{2.33}$$

2.9.4.4 Reconstructing the snapshots

The measured values at any time v_j can now be approximated by superposition of any number of DMD modes Ψ via

$$v_j = \sum_{i=1}^{N} \alpha_i \lambda_i^{j-1} \Psi_i. \tag{2.34}$$

For example, if we were reconstructing the flow field using the first two dynamic modes, the fourth timestep would be approximated by $v_3 = \alpha_1 \lambda_1^3 \Psi_1 + \alpha_2 \lambda_2^3 \Psi_2$. The global representation of the reconstructed flow fields, at all timesteps is

$$[v_1 v_2 \ldots v_{N-1}] = [\Psi_2 \Psi_3 \ldots \Psi_N] \begin{bmatrix} \alpha_1 & & & \\ & \alpha_2 & & \\ & & \ddots & \\ & & & \alpha_N \end{bmatrix} \begin{bmatrix} 1 & \lambda_1 & \ldots & \lambda_1^{N-1} \\ 1 & \lambda_2 & \ldots & \lambda_2^{N-1} \\ \vdots & \vdots & \ddots & \vdots \\ 1 & \lambda_N & \ldots & \lambda_N^{N-1} \end{bmatrix}. \tag{2.35}$$

The amplitudes α can be found by inversion of Ψ or other standard methods.

Unlike with POD, the final dynamic modes are non-orthogonal. The Koopman eigenvalues λ_j, which lie on a unit circle, characterise the temporal dynamics of the mode Ψ_j. The frequency f_j and growth rate σ_j are computed by

$$f_j = \mathrm{Im}\{\log(\lambda_j)\}/\Delta t/2\pi, \tag{2.36}$$

$$\sigma_j = \mathrm{Re}\{\log(\lambda_j)\}/\Delta t. \tag{2.37}$$

The time-averaged flow field is returned for the mode corresponding to $f_j = 0$.

DMD has been shown to be more effective at decoupling different transient features and their corresponding frequencies compared to the POD method (Rowley *et al.* 2009). It is therefore ideal for this study, where an actuation frequency will be imparted onto the flow field.

2.9.5 Phase averaged instantaneous data analysis

Often we are interested in the flow at certain moments in the vortex shedding cycle. For example, we may wish to visualise the wake at the maximum point of each drag signal fluctuation. Unfortunately, analysing just one instance of this occurrence is rarely sufficient, as turbulence or other random events may be influencing the wake. Instead, a collection of these occurrences needs be averaged before a meaningful representation of the flow can be visualised. This process is known as phase-averaging.

In this study phase-averaging is completed in MATLAB via a simple for loop, summing the required data for each flow field, before dividing by the total number of timesteps. The timesteps to be averaged are pinpointed manually by analysing the time history signal.

2.9.6 Circulation calculation and vortex identification

Circulation, Γ, is a macroscopic measure of rotation for a finite area of the fluid and defined as the line integral around a closed curve of the fluid velocity. Vorticity, a microscopic measure of rotation at any point in the fluid, is the circulation per unit area. The circulation is the most appropriate measure of vortex "strength", as it returns the net vorticity of the vortex, not the maximum found in the vortex,

$$\Gamma = \oint_C V \cdot dl. \tag{2.38}$$

While calculating the circulation of a vortex is not difficult, identifying the vortex in the first place often is. In this study nine planes of spanwise vorticity across the

domain are averaged before being analysed. This process leaves a plane with very coherent circular structures, and therefore many of the issues encountered by vortex identification algorithms are bypassed. Here, the vortex is identified using the *vortex core identification algorithm*, described in Graftieaux *et al.* (2001). The method requires the calculation at all points in the field of Γ_2, a local function dependent on Ω, the rotation rate corresponding to the anti-symmetrical part of Δu, and ν, the eigenvalue of the symmetrical part of Δu. The ratio $|\Omega/\nu|$, then, indicates whether the flow is locally dominated by strain ($|\Omega/\nu| < 1$) or rotation ($|\Omega/\nu| > 1$), with pure shear occurring at $|\Omega/\nu| = 1$. Graftieaux *et al.* (2001) showed a consistent relationship between $|\Gamma_2|$ and $|\Omega/\nu|$, with $|\Gamma_2| < 2/\pi$ indicating flow dominated by strain and $|\Gamma_2| > 2/\pi$ indicating flow dominated by rotation. Thus, all points where $|\Gamma_2| > 2/\pi$ can be described as regions where the flow is rotation-dominant, and if numerous such points are clustered together, the presence of a vortex can be assumed. In this study a minimum threshold value of 0.75, slightly higher than $2/\pi$, was used as the threshold value. This helps the algorithm avoid the less obvious vortices, but is low enough to always capture the large Kármán vortices.

Once the vortex is identified, circulation Γ is calculated by summing the vorticity at each point within. The area A_v of the vortex is also measured, allowing the total vorticity of the vortex to be computed via $\omega_v = \Gamma/A_v$.

2.10 Summary and validation of methodology

The intention of this chapter has been to present an outline of the numerical techniques used to both simulate the flow accurately, and process the data appropriately. Validation of the methodology outlined above is discussed in § 3.

Chapter 3

Results validation

3.1 Natural flow

In §2.3.2 the complexities of Large Eddy Simulation were highlighted. The interplay of filtering, modelling and numerical techniques used in the method makes standard (RANS methods) grid resolution analysis difficult. There are varying recommendations in correctly analysing resolution for Large Eddy Simulations. Pope (2004), for example, suggests the LES is well resolved if the ratio of resolved turbulent kinetic energy to the total is above 80%. However, he also states this number is difficult to acquire in practice. Davidson (2009) showed this is not always an appropriate measure in any case, and proposed other methods such as analysing the two-point correlations of the fluctuating velocity components, information which can relate the largest resolved scales to cell size. He proposes a minimum of around 8 cells to encompass the largest scales, with preferably double that if possible for extra confidence.

Fortunately, comparison with experimental results *a posteriori* is also possible in this study, allowing for a greater level of confidence in the numerical technique. Time-averaged velocity profiles are available from the published experimental work of Pastoor *et al.* (2008), in addition to traditional bluff body statistics such as mean drag coefficient, C_D, and Strouhal number, St. These are also available from previously published numerical work by Krajnovic & Fernandes (2011).

In summary, validation here consists of a thorough yet subjective analysis of the effects of grid and timestep refinement, and comparison with previous experimental and numerical results. This step was exhaustive, and work on new areas such as angled-actuation and the near-ground case did not proceed until full confidence was obtained in the numerical technique. Of course, with no experimental results to compare with, these new areas can only be validated *a priori*. While future experimental work is

Elements (million)	$C_{D,0}$	GCI %	St	$P\{C_{D,max}\}$
2.42	0.604	-	0.24(5)	0.59×10^{-5}
5.28	0.707	4.3	0.22(5)	4.61×10^{-5}
7.60*	0.720	2.0	0.22(5)	3.60×10^{-5}

TABLE 3.1: Grid resolution analysis results for natural flow (all statistics taken from a sample of flow starting at 0.5 seconds and finishing at 2.0 seconds, with a timestep of 1×10^{-4} s). * denotes the final mesh used.

required before full confidence in these results is achieved, they can nevertheless be treated with cautious optimism.

3.1.1 Grid resolution study

A grid resolution study was completed with three different relative mesh sizings for natural flow. Table 3.1 summarises the change in mean drag force and Strouhal number for each mesh sizing. The statistics show that increasing the mesh resolution would likely have no impact on the Strouhal number returned and negligible impact on the mean drag coefficient. Of extra interest is the peak spectral frequency magnitude in the drag signal, $P\{C_{D,max}\}$, which increases an order of magnitude between the 2.42 and 5.28 million element cases, before dropping slightly for the 7.60 million element case. This indicates the periodicity of the flow is not well represented at lower mesh densities.

The time-averaged wake velocity profiles also trend towards a final shape with increasing resolution. Figure 3.1 shows that in the near wake $0.5H$ downstream of the rear the streamwise velocity profile is near identical for the medium and fine mesh, while the vertical velocity profile does change slightly with the extra resolution. Further downstream at $1.4H$ the differences between the two resolutions are negligible. It seems likely that further resolution would result in negligible change in the profiles.

The velocity profiles for the fine mesh agree well with the experimental results of Pastoor *et al.* (2008)[1]. The streamwise profile at $0.5H$ exhibits a slightly overpredicted peak negative velocity in the recirculation region. This is most likely related to the Large Eddy Simulation method, considering the results of Krajnovic & Fernandes (2011) also show this behaviour. The low Smagorinsky constant of 0.1 used here and by Krajnovic may be underdissipative in this area of the flow—the more expensive dynamic

[1]The original experiments, it should be noted, were first presented by Henning *et al.* (2007). The later paper of Pastoor *et al.* (2008), which features many of the same authors and includes a more extensive discussion on the original results, is referenced throughout this Thesis.

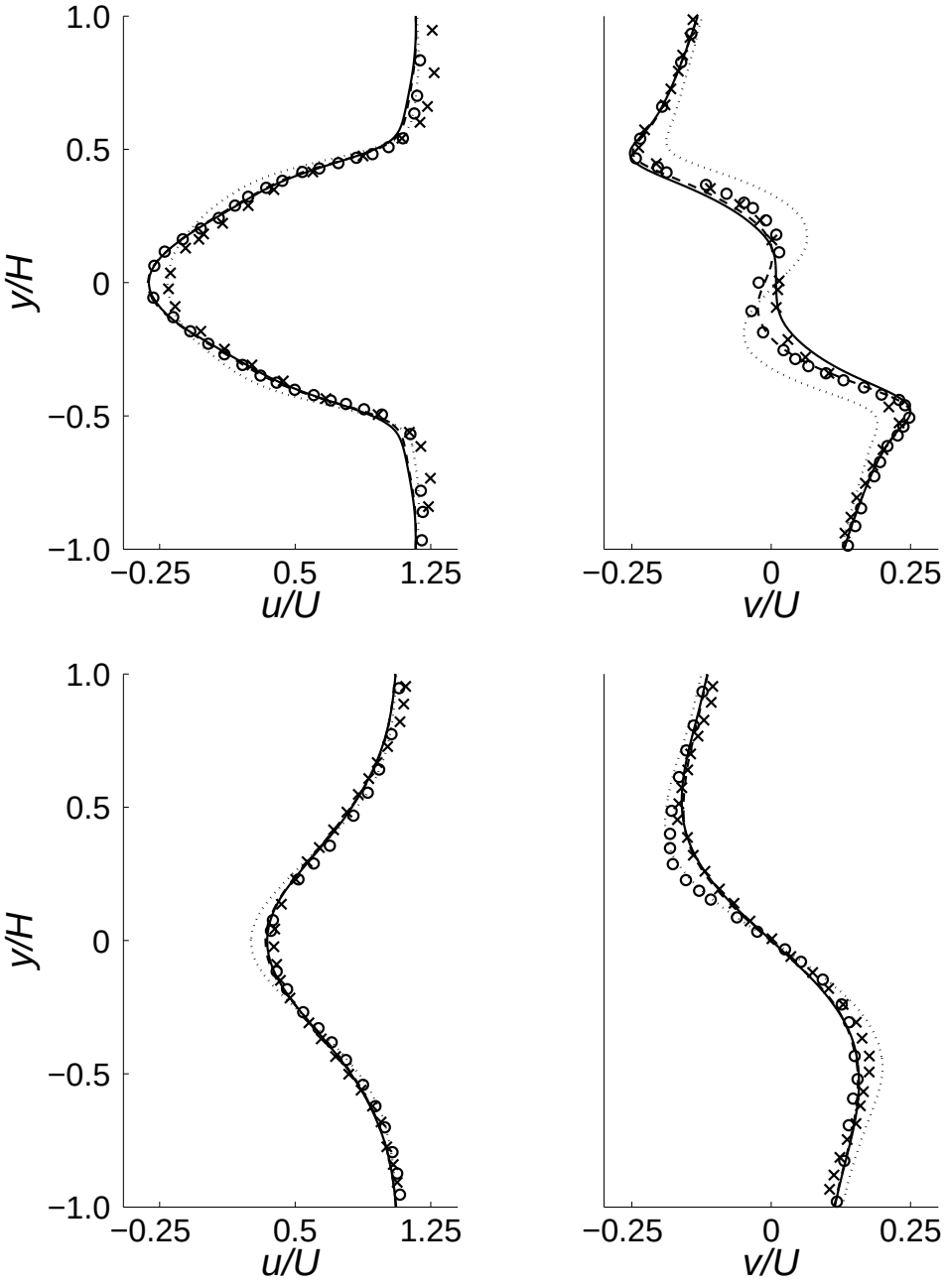

FIGURE 3.1: Span- and time-averaged streamwise (left) and vertical (right) velocity profiles $0.5H$ (top) and $1.4H$ (bottom) downstream of the base. Lines represent coarse (dotted line), medium (dashed line) and fine (solid line) meshes. Previous experimental results of Pastoor *et al.* (2008) (crosses) and numerical results of Krajnovic & Fernandes (2011) (circles) are included for comparison. The profile velocities in all three studies are normalised with inlet velocity U (not the corrected freestream velocity).

Smagorinsky model would likely alleviate this discrepancy. The streamwise profile also shows a slightly lower freestream velocity than observed in the previous studies. This is most likely due to the free-slip boundaries employed here—simulations run at lower mesh resolutions but with no-slip boundaries resulted in higher velocities in the

	Δy_w (m)	y^+	Δx_w^+	Δz_w^+	θ/H	$\delta*/H$	$S = \frac{\delta*}{\theta}$
Coarse	2.4×10^{-4}	3.7	50	46	0.0266	0.0401	1.5047
Medium	1.85×10^{-4}	3.4	44	41	0.0274	0.0375	1.3689
Fine	1.5×10^{-4}	2.4	36	29	0.0280	0.0377	1.3477

TABLE 3.2: Average non-dimensional wall units, non-dimensional momentum thickness (θ), displacement thickness ($\delta*$) and Shape Factor (S) for the three meshes.

freestream regions overlaying the values of Pastoor *et al.* (2008). Further downstream at $1.4H$, these disparities are less apparent.

The vertical velocity profile at $0.5H$ is almost identical to Pastoor's results, and an improvement on Krajnovic's results. Further downstream the slight asymmetry in the vertical profile recorded by both Pastoor *et al.* (2008) and Krajnovic & Fernandes (2011) are not observed in our results. It is unclear whether the slight asymmetry observed by Pastoor and Krajnovic is due to the supports under the body or randomness in the time-averaging window. The latter seems most likely, considering the Pastoor results show a higher peak magnitude in the lower half of the wake, while for Krajnovic the higher peak appears in the upper half of the wake.

3.1.1.1 Boundary layer

The average non-dimensional wall unit value normal to the wall, y^+, on the upper and lower surfaces of the body is 2.4. This is slightly outside the recommended range for attached boundary layers of $y^+ < 1$ (Davidson 2010; Chapman 1979; Jiang & Lai 2010). However, plots of u^+, the velocity normalised with the friction velocity $u_t = \sqrt{\frac{\tau_w}{\rho}}$, against y^+ show the viscous sublayer to be well resolved, and only a slight difference in the boundary layer profiles between the medium and fine meshes. Moreover, the number of grid points encompassing $0 < y^+ < 10$ is 3, within the range of 3–5 recommended by Jiang & Lai (2010). Thus, despite y^+ being slightly larger than the ideal value of 1 or less, it appears that the resolution in the boundary layer is adequate.

In the streamwise and spanwise directions the average wall units of the final mesh are $\Delta x_w^+ = 36$ and $\Delta z_w^+ = 29$ respectively. A universally appropriate range for these values is more difficult to define: Jiang & Lai (2010) recommends $50 < \Delta x_w^+ < 150$ and $10 < \Delta z_w^+ < 40$. The optimum value varies from case to case, depending on the velocity gradients encountered in the flow. Δx^+ is slightly lower than necessary in this case due to the presence of the four very narrow actuation slots at the rear of the body

which require high resolution—smooth mesh transition to these regions requires extra streamwise resolution all over the body.

Pastoor *et al.* (2008) obtained boundary layer measurements just upstream of separation at $X/H = -0.01$, and found $\theta/H = 0.017$ (which Bearman (1967) and Park *et al.* (2006) also obtained at $Re_H = 41,000$ and $Re_H = 40,000$ respectively). Our results compare favourably at this location, with $\theta/H = 0.0188$. The shape factor $S = 1.31$ also falls between Pastoor's value of 1.19 and Bearman's of 1.47. This suggests the adverse pressure gradient at separation is stronger than Pastoor's, and weaker than Bearman's. These are reasonable agreements, considering the difficulty of boundary layer measurements.

The boundary layer is discussed in further detail in §4.2.1.

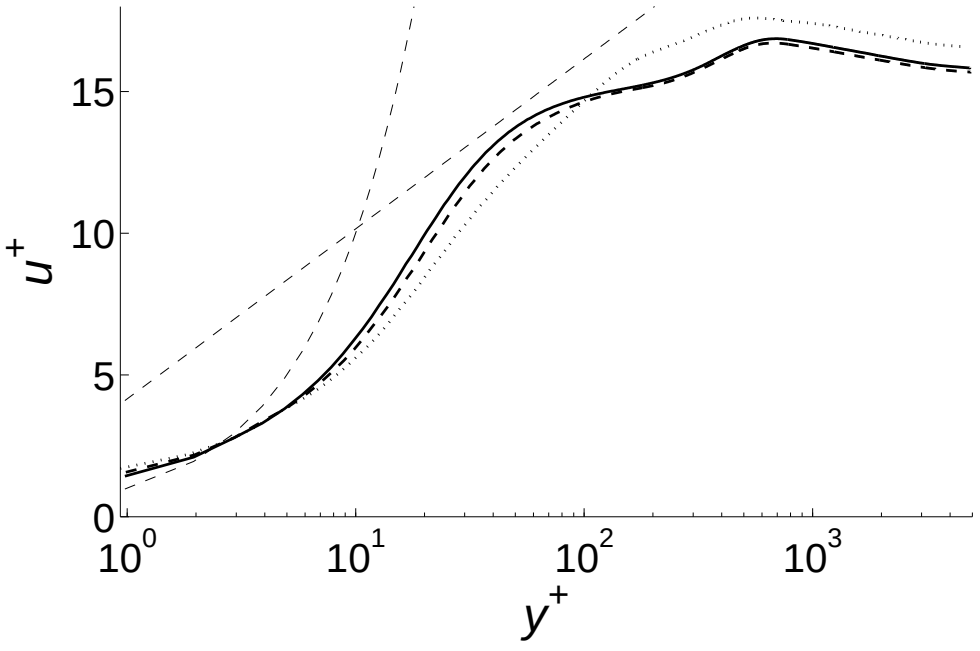

FIGURE 3.2: Time-averaged boundary layer profiles at $X/H = 0.3$ for coarse mesh (dotted line), medium mesh (thick dashed line) and fine mesh (thick solid line). The thin dashed lines represent the theoretical relationships $\frac{1}{\kappa}log(y^+) + B_i$ (the linear line, with $\kappa = 0.384$ and $\beta_i = 4.16$ as per Österlund *et al.* (2000)) and $y^+ = u^+$.

3.1.1.2 Energy spectrum

The velocity energy spectrum was the final consideration in the grid resolution decision. Singh & Mittal (2004) showed that for a 2D cylinder, the spectra of velocity fields at one point in time yielded similar plots to the spectra of temporal descriptions of velocity at a single point. In other words, the spectra of a velocity monitor should be sufficient

to analyse the energy scales in the flow. Of course, the spectra will change depending on grid size and dynamics at the measurement point. Here the six wake monitor point velocity signals ($W1 - W6$ as described in §2.5) are averaged to obtain a more global representation of the wake (while this is not advisable when analysing the lower frequencies in the flow, here we are more interested in the decay in the higher frequency range). The FFT operation described in §2.5 is applied to the signals, squared to obtain the power spectra, and normalised by dividing by the number of timesteps in the signal. The resulting spectra are plotted for each grid in Figure 3.3, with the circular wavenumber $k = \frac{2\pi}{\lambda}$ (where $\lambda = V_c/f$) along the x-axis. It should be remembered when analysing this plot that increasing grid resolution will always result in an improvement at the higher wavenumbers until the Kolmogorov limit is reached and the Large Eddy Simulation method is effectively Direct Numerical Simulation. Obtaining grid independence in this measure is therefore an unrealistic goal—the Figure does, however, still allow us to gauge the performance of each grid at the higher wavenumbers.

Figure 3.3 also shows that the higher resolution grids better achieve the desired energy decay rate of $E \propto k^{-5/3}$ in the inertial range, delaying the onset of high dissipation brought on by the previously discussed deficiencies in the Smagorinsky eddy viscosity model (see §2.3.2). The dissipation is observed to be at its greatest over the medium wavenumbers, as has been shown by Davidson (2009).

The superior performance of the fine mesh is, of course, expected for LES – further increases in resolution will yield improved performance again and again until the Kolmogorov scales are reached. Most important is deciding when these extra gains are of no further value, with the main features of the flow already accurately represented. In this case, the similarity of the time-averaged vertical velocity profile at $X/H = 0.5$, velocity gradients in the near-wall region and energy spectra for the medium and fine meshes suggests that sufficient accuracy has been achieved, and no further iterations in increasing the grid resolution are required.

3.1.2 Timestep resolution study

The timestep resolution is often overlooked in Large Eddy Simulation studies due to computational expense. However, the importance of the time step size is clear: turbulent structures have not only a length scale but also a time scale which must be appropriately considered for accuracy. Here a timestep study was completed at the fi-

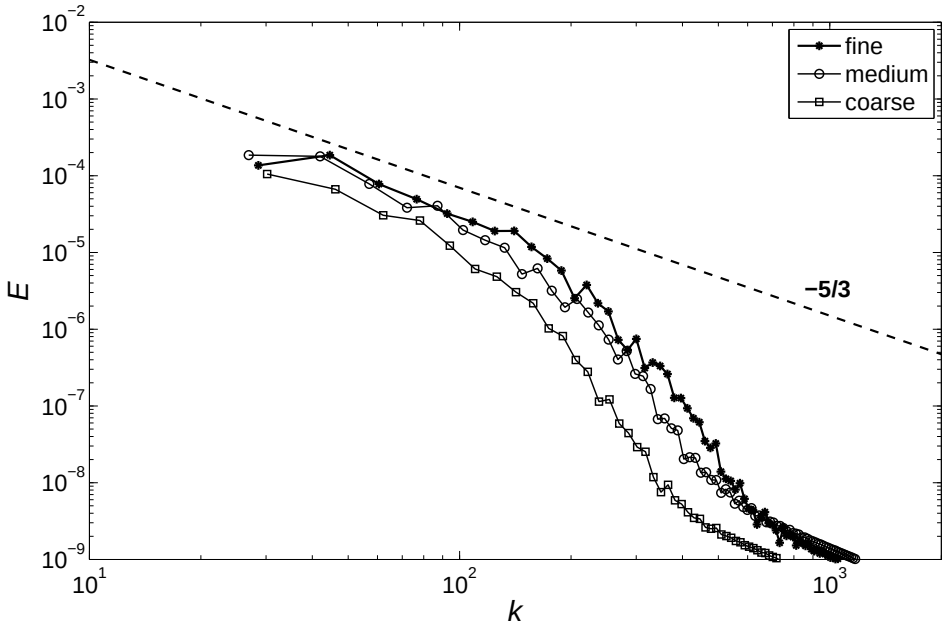

FIGURE 3.3: Grid resolution analysis of the spectra. Lines have been smoothed to aid comparison.

Timestep (s)	Δt^+	$C_{D,0}$	St	$P\{C_{D,max}\}$
2×10^{-4}	1.14	0.645	0.23(1)	0.19×10^{-4}
1×10^{-4}*	0.57	0.72	0.22(5)	1.00×10^{-4}
5×10^{-5}	0.29	0.72	0.22(5)	1.44×10^{-4}

TABLE 3.3: Timestep resolution analysis results for natural flow (all statistics taken from a sample of flow starting at 3.0 seconds and finishing at 4.0 seconds, with the 7.60 million element mesh). * denotes final timestep used.

nal mesh resolution, the results of which are shown in Table 3.3. Ultimately a timestep of 1×10^{-4} seconds was chosen: a larger timestep produced a slightly lower mean drag and substantially lower peaks in the drag spectra, whilst a smaller timestep showed acceptable small changes in the solution. Once again, as for the grid resolution study, the $P\{C_{D,max}\}$ values show a high dependence on resolution. These results remind us of the importance of resolution studies for LES: to properly capture the key flow periodic features, for example the shear-layer and von Kármán flow structures, the time and length scales must be appropriately fine. These are difficult to estimate *a priori*, and hence a trial-and-error approach must be used.

A noticeable change is observed between the 2×10^{-4} s and 1×10^{-4} s cases, with the lower timestep yielding velocity profiles somewhere between the results of Krajnovic & Fernandes (2011) (who used a timestep of 1×10^{-4} s) and Pastoor *et al.* (2008). A

slight asymmetry is observed for the finest timestep 5×10^{-5} s, but this is most likely due to the relatively short sampling period of 1 s. As was the case for the different grid sizes, the errors diminish further downstream. They are therefore not plotted here.

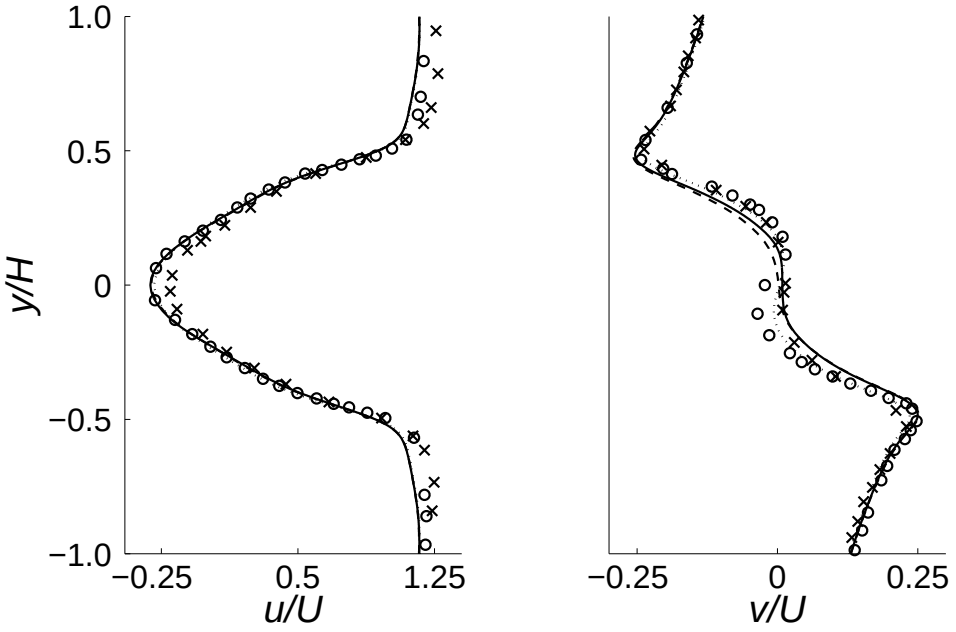

FIGURE 3.4: Span- and time-averaged streamwise (left) and vertical (right) velocity profiles $0.5H$ downstream of the base. Lines represent timesteps of 2×10^{-4} s (dotted line), 1×10^{-4} s (solid line) and 5×10^{-5} s (dashed line) meshes. Previous experimental results of Pastoor *et al.* (2008) (crosses) and numerical results of Krajnovic & Fernandes (2011) (circles) are included for comparison. The profile velocities in all three studies are normalised with inlet velocity U (not the corrected freestream velocity).

The boundary layer profiles at $X/H = -0.3$ are near identical for each timestep – the average velocity difference between the 2×10^{-4} s and 5×10^{-5} s cases is 0.01% from the body wall to the outer domain wall and 0.15% in the boundary layer. They are therefore not plotted here.

The wake energy spectra of each timestep case (the process by which it is found is described in §3.1.1) confirm the importance of the timestep on the wake dynamics. It is clear that the timestep of 2×10^{-4} s results in high dissipation at relatively low wavenumbers and should be avoided. The difference between the two smaller timesteps is less extreme, although still evident.

Making the final timestep decision was not as straightforward as for the grid resolution. The 5×10^{-5} s timestep size admittedly returns slightly more faithful spectral information than the 1×10^{-4} s case, especially at higher wavenumbers. However, all other measurements are near identical. The latter offers a vastly improved simulation

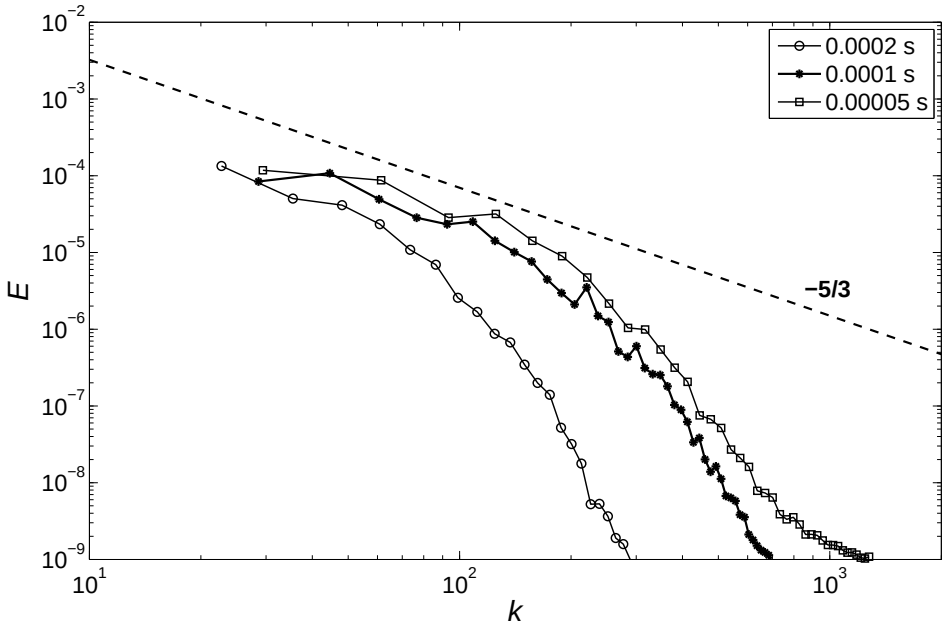

FIGURE 3.5: Timestep resolution analysis of the spectra. Lines have been smoothed to aid comparison.

turnaround time, potentially allowing nearly twice the number of simulations to be run. Given the relative insensitivity of the velocity profile predictions, this was deemed too great an advantage to overlook, and the 1×10^{-4} s timestep was therefore chosen. This timestep is also suitable for the actuation cases, as they feature relatively low frequencies of the same order of magnitude as the natural Strouhal number. The chosen timestep corresponds to a non-dimensional timestep $t^* = \frac{U}{H}$ of 0.0058.

One final confirmation that the selected timestep is appropriate comes from Choi & Moin (1993), who introduced the viscous time step $\Delta t^+ = \Delta t U_\tau / \upsilon$ (which is included on table 3.3). They found a viscous time step comfortably less than the Kolmogorov time scale was required for accurate turbulence statistics prediction – preferably around half ($\Delta t^+ \approx 0.5$). The final Δt^+ selected here gives an average $\Delta t^+ = 0.57$ over the upper and lower surfaces, in good agreement with this recommendation.

3.1.3 Further measures of final resolution

3.1.3.1 Grid size in relation to turbulent length scales

While the preceding measures have provided confidence in the final resolution, they do not reveal the extent of physical scalings captured. This is worth knowing for the sake of comparison with previous and future LES studies. Howard & Pourquie (2002)

and Minguez *et al.* (2008) estimate the Kolmogorov μ and Taylor λ_T length scales as $A^{-0.25}Re_L^{-0.75}L$ and $15^{0.5}A^{-0.5}Re_L^{-0.5}L$ respectively (where A is a constant of the order unity, here assumed to be 0.5, Re_L is the Reynolds number based on body length, and L is the length of the body). In this case this leads to theoretical estimates $\mu \approx 7\times10^{-5}$ m and $\lambda_T \approx 0.005$ m or in non-dimensional terms $\frac{\mu}{L} \approx 2.7 \times 10^{-4}$ and $\frac{\lambda_T}{L} \approx 0.020$. The ratio of the mesh cell size $\Delta = (\Delta x \Delta y \Delta z)^{(1/3)}$ to these scales is dependent on location – near the body walls, where the LES technique is less accurate, the grid is purposely constructed to be finer whereas further downstream in the wake, where the LES technique better estimates the subgrid stresses, the grid is coarser.

Figure 3.6 and the corresponding table 3.4 show these ratios at various points in the wake. The values confirm that the solution in the immediate shear layer is far closer to DNS than in the wake. This compares favourably with Minguez *et al.* (2008), who had a minimum Δ/λ_T of 0.37 (although their Reynolds number was an order of magnitude larger, and they used a Chebyshev and Fourier spectral method solver).

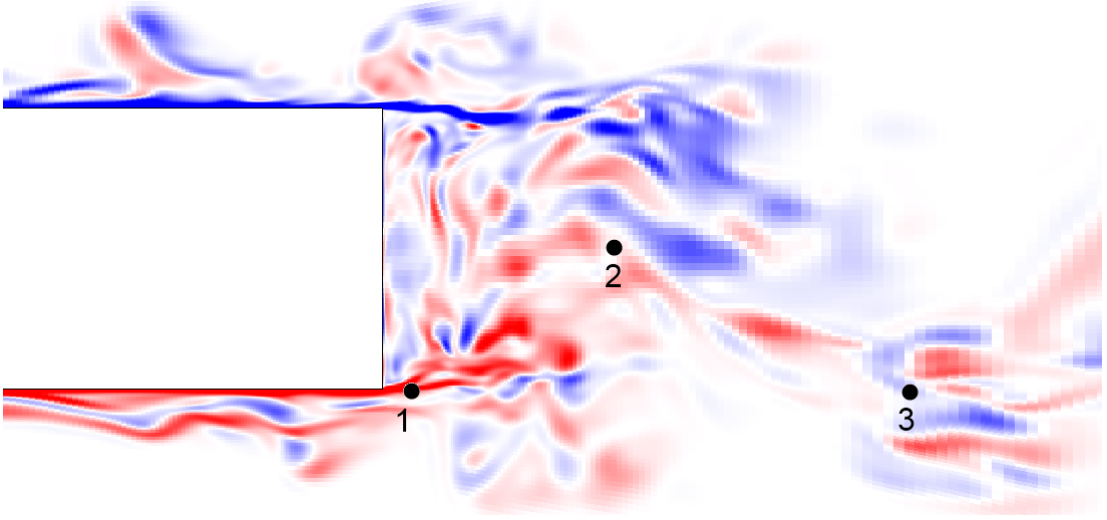

FIGURE 3.6: Locations of points described in Table 3.4, over an instantaneous snapshot of vorticity contours along the centre plane.

	x	y	Δ (m)	Δ/λ_T	Δ/μ
Point 1	$0.01L$	$0.5H$	4.4×10^{-4}	0.08	6
Point 2	$0.15L$	0	1.6×10^{-3}	0.30	23
Point 3	$0.5L$	$0.5H$	1.5×10^{-3}	0.28	21
Point 4*	L	0	2.0×10^{-3}	0.38	29

TABLE 3.4: Grid size compared to theoretical length scales λ_T (Taylor scale) and μ (Kolmogorov scale) at points denoted in Figure 3.6. *Point not pictured.

3.1.3.2 Two-point correlations

Two-point correlations give a final indication of the resolution for the fine mesh (unfortunately these measurements were not recorded for the coarse and medium meshes). Figure 3.7 shows the two-point correlations over a line inserted in the shear-layer directly behind the body. Accordingly to the recommendation of Davidson (2009), the largest structures (defined as the distance where the two-point correlation remains above 0.5) in the x direction span roughly 30 cells—well above the 16 minimum limit recommended by Davidson.

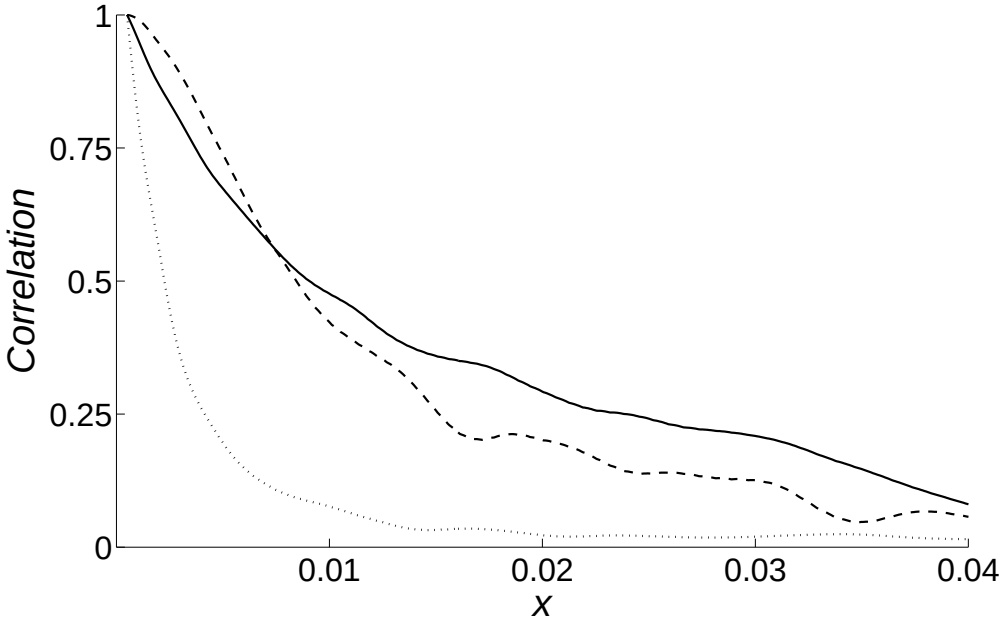

FIGURE 3.7: Two-point correlations of the three velocity components along a streamwise line in the shear layer. The correlation coefficient is computed between the velocity signal at each point and the origin of the line, over the total duration of the simulation. Solid line: $\langle u'u' \rangle$, dashed line: $\langle v'v' \rangle$, dotted line: $\langle w'w' \rangle$.

3.1.4 Effect of eddy viscosity model

The dynamic Smagorinsky model was also tested for the natural flow and one actuated case, to provide a comparison with results from the standard Smagorinsky model. For the natural case the drag coefficient and Strouhal number are within 5% of the Smagorinsky model values. The velocity profiles also show good agreement, with a slight improvement in the shear-layer regions using the dynamic model. Under actuation, when the flow is strongly forced, a near-identical drag reduction (within 1%) was returned compared with the standard Smagorinsky case, with differences in wake

Turbulence Model	$C_{D,0}$	St	$P\{St_{act}\}$	$\overline{\epsilon_u}/U_\infty$	$\overline{\epsilon_v}/U_\infty$
Smagorinsky*	0.72	0.22	-	-	-
Dynamic	0.69	0.23	-	0.7%	0.3%
Smag. (actuation) *	0.62	0.19	0.011	-	-
Dyn. (actuation)	0.60	0.19	0.012	0.7%	1.0%

TABLE 3.5: Predicted mean drag ($C_{D,0}$) and Strouhal number (St) for both turbulence models tested. The * indicates the final model used. All statistics taken over approximately 80 non-dimensional time units. Actuation case tested: $St_{act} = 0.19$. $P\{St_{act}\}$ is the magnitude of the drag spectra peak at the actuation frequency. Windowing was not used for the quoted St.

velocity profiles negligible. The similar performance of the two models is most likely due to the C_s of 0.1 chosen for the Smagorinsky model: for the dynamic model, the mean C_s values in the shear layers were also approximately 0.1. Perhaps not surprisingly, it seems that under actuation, when the flow is artificially regulated in the shear regions, the differences between the two models appear to be minimised. These *a posteriori* comparisons, along with the validations against experimental data, indicate the Smagorinsky model performs reliably, but also show that the dynamic model is capable of replicating the experimental results well for this type of flow. (As a reminder, the dynamic model was not used for this research because the implemented version in initially used version of CFX was unstable. These problems were rectified in subsequent versions).

3.1.5 Effect of advection scheme

A central differencing advection scheme was also tested for the natural flow case. The scheme returns a slightly higher drag value, with a slightly shorter wake (the velocity profiles at $X = H$, shown in Figure 3.9, shows a higher minimum velocity at the centre of the wake). The dynamics of the flow, however, show a negligible difference between cases, with the Strouhal number consistent across both and the magnitude of the spectral peak also nearly identical. The results are summarised in table 3.6.

3.1.6 Effect of blockage

Aside from the previously discussed traditional blockage effects (see § 2.7), other behaviour appeared to be influenced by the domain size. A pair of pressure bubbles over the leading edges show a subtle but distinctive pulsing behaviour, and a PSD analysis of the front pressure signal identifies this frequency as $St = 0.44$, i.e. double the Strouhal

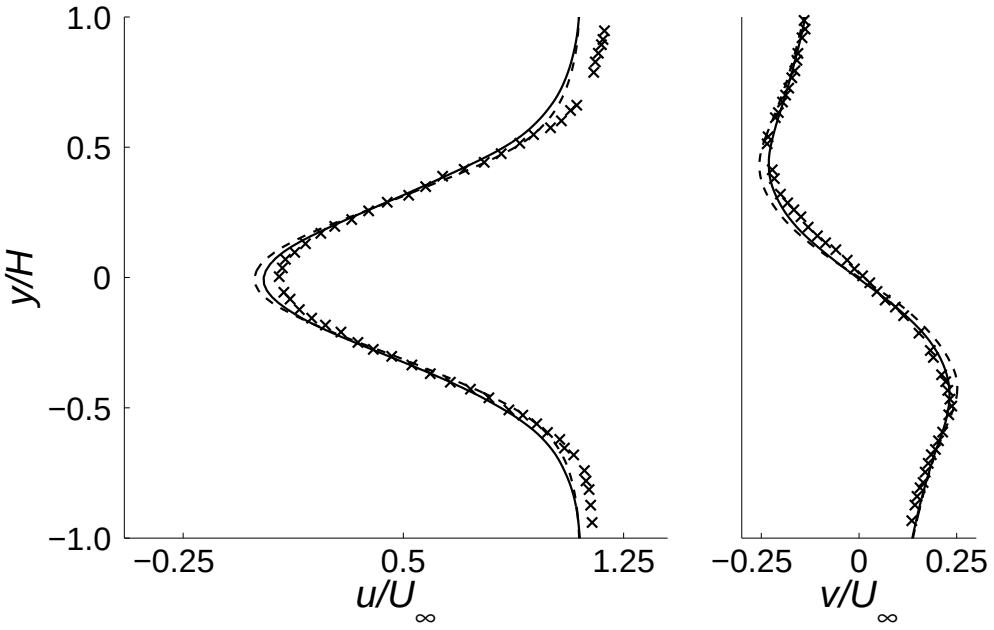

FIGURE 3.8: $X = H$ velocity profiles. Solid line: Smagorinsky model, dashed line: Dynamic model, crosses: Pastoor *et al.* (2008) experimental results.

Advection scheme	$C_{D,0}$	St	$P\{St_{act}\}$	$\overline{\epsilon_u}/U_\infty$	$\overline{\epsilon_v}/U_\infty$
Blend, $\beta = 1$*	0.72	0.22	2×10^{-5}	-	-
Central Differencing	0.74	0.22	2×10^{-5}	1.3%	0.6%

TABLE 3.6: Predicted mean drag ($C_{D,0}$) and Strouhal number (St) for both advection schemes tested. The * indicates the final model used. All statistics taken over approximately 80 non-dimensional time units. Actuation case tested: $St_{act} = 0.19$. $P\{St_{act}\}$ is the magnitude of the drag spectra peak at the actuation frequency. Windowing was not used for the quoted St.

frequency. Closer inspection reveals the front pressure and base pressure signals are almost perfectly out-of-phase. Furthermore, when the rear base pressure reduces to lower values, the front pressure signal appears to increase higher, and vice-versa. This behaviour is most likely due to the high blockage ratio used (13%), which amplifies all pressure changes in the wake both upstream and downstream.

To explore this issue further, both natural and actuated flow were tested in a domain with half the blockage ratio (achieved by doubling the domain height, giving a blockage ratio of 6.5%) of the original tests. Indeed, in this domain the amplitude of the front pressure oscillations was greatly minimised (from $\Delta C_P \approx 0.06$ to $\Delta C_P \approx 0.03$), which in turn reduced the amplitude of the drag signal. The mean pressure at the front, however, was unchanged, meaning the amplification had no negligible effect on the

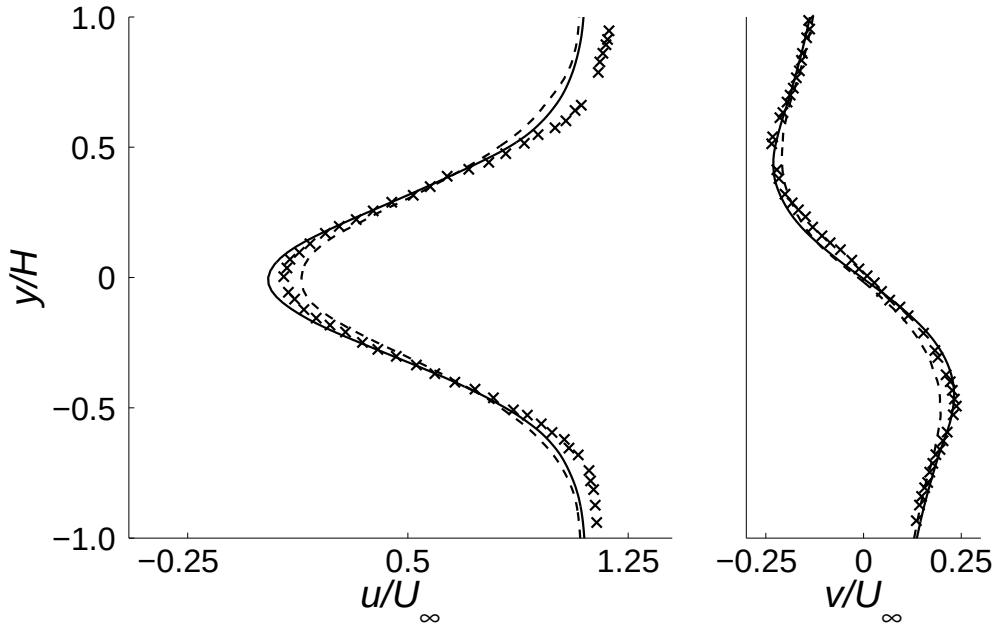

FIGURE 3.9: $X = H$ velocity profiles. Solid line: Blended scheme, dashed line: central differencing scheme, crosses: Pastoor *et al.* (2008) experimental results.

mean drag value. The same was observed under actuation. This effect was likely to have occurred experimentally also, and the original smaller domain was therefore chosen for consistency. However, this undesirable effect of a high blockage ratio should be noted.

Figure 3.10 shows the time-averaged profiles in the wake, however, differ little between the two cases.

3.1.7 Overview of key findings

Table 3.7 gives a final comparison of selected fine-mesh predictions against those from previous relevant studies. It should be noted that the domain size and boundary conditions are not consistent from study to study. The experimental study of Bearman (1967) featured a blockage ratio of 3% (with no blockage correction applied), whilst the studies of Pastoor *et al.* (2008) and Krajnovic & Fernandes (2011) featured 13% blockage, as was the case here (no blockage correction was applied in the Krajnovic study). The non-dimensional numbers in this paper (Re, St, C_D, C_L, C_P and C_μ) were calculated using the corrected freestream velocity $U_{\infty,c} = U_\infty\sqrt{B_c}$ where B_c is the blockage correction factor applied. Due to the leading-edge separation, B_c was calculated using the general approach for bluff bodies in closed test section wind tunnels

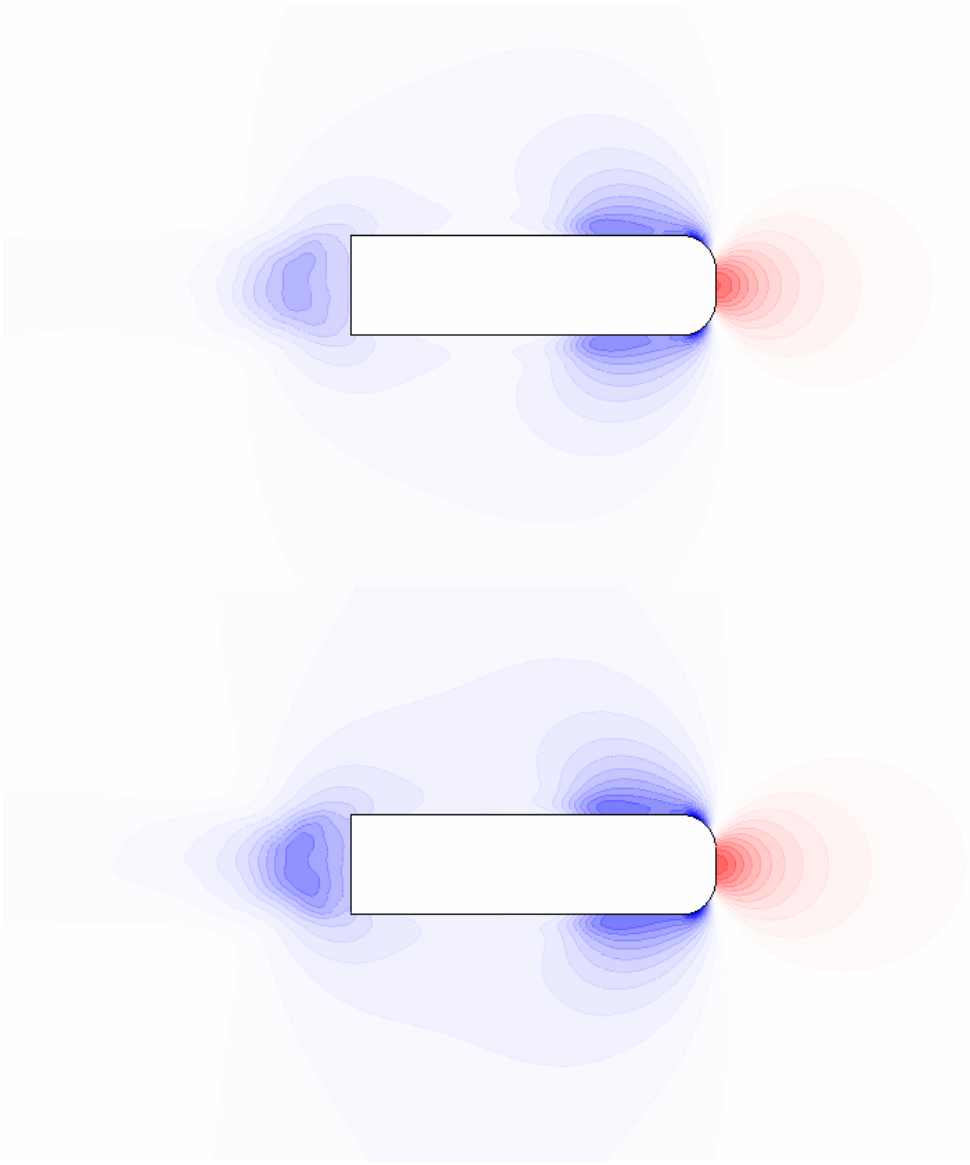

FIGURE 3.10: Comparison of pressure profiles between natural flow with .

described by Hackett *et al.* (1979) (adapted from Maskell (1963)) as opposed to other techniques (such as that described by Mercker (1986)) which are designed for cases with no leading-edge separation. Comparisons with previous time-averaged wake velocity profiles are also available in § 3.1.1. The profiles agree favourably with previous experimental and numerical results.

Furthermore, this study features free-slip domain walls to remove the effect of wall boundary layers, compared with no-slip walls for the other studies. This choice was dictated by the desire to avoid wasting grid points in attempting to resolve the wall boundary layers, to allow better resolution of the flow in the vicinity of the bluff body.

Study (year)	Re_H	$C_{D,0}$	$C_{P,0}$	St	B_c
Bearman (1967)*†	41,000	-	-0.57	0.24	1.03
Pastoor (2008)*	23,000	0.89	-0.53	0.23	1.32
Krajnovic (2010)†	20,000	0.79	-	0.27	1.32
Parkin (2013)#	23,000	0.72	-0.53	0.22(5)	1.27

TABLE 3.7: Comparison of natural flow results over a D-shaped bluff body: * experimental results, †no blockage correction applied in initial study: B_c values have been estimated here and blockage correction applied retroactively, # mounts and no-slip domain walls not modelled.

In addition, the no-slip spanwise boundaries of previous studies (Krajnovic & Fernandes 2011; Pastoor *et al.* 2008) will affect the flow in the neighbourhood of the wall and for some distance inward. All these are likely contributing factors to the discrepancy in mean drag coefficient. For this reason, the base pressure coefficient (taken in the middle portion of the base region away from the end effects) seems a better point of comparison; and here the agreement with the experimental results of Pastoor *et al.* (2008) is very good (within 5%). The Strouhal number also agrees to within 5%, and appears to agree with other experimental St measurements on similar bodies, as shown in Figure 3.11. Given the differences in the details between these cases, this degree of agreement seems satisfactory.

3.2 Ground proximity case

While the above results encourage confidence in the methodology for the ground proximity case (as all numerics and meshing method are maintained as far as possible), no experimental data is available for comparison. Thus, until experimental investigations have been carried out on a similar geometry and flow, the level of confidence in the ground proximity results cannot reach the levels of the away-from-ground simulations.

Nonetheless, a grid resolution study and energy spectrum analysis are possible, and are helpful in validation.

3.2.1 Grid resolution study

Three grids were constructed: a coarse grid with 1.20 million elements, a medium grid with 4.53 million elements and a fine grid with 8.56 million elements. Table 3.8 summarises the changes in drag coefficient with increasing grid resolution. No dominant frequencies occur in the wake, so a comparison of the St number is not included. The

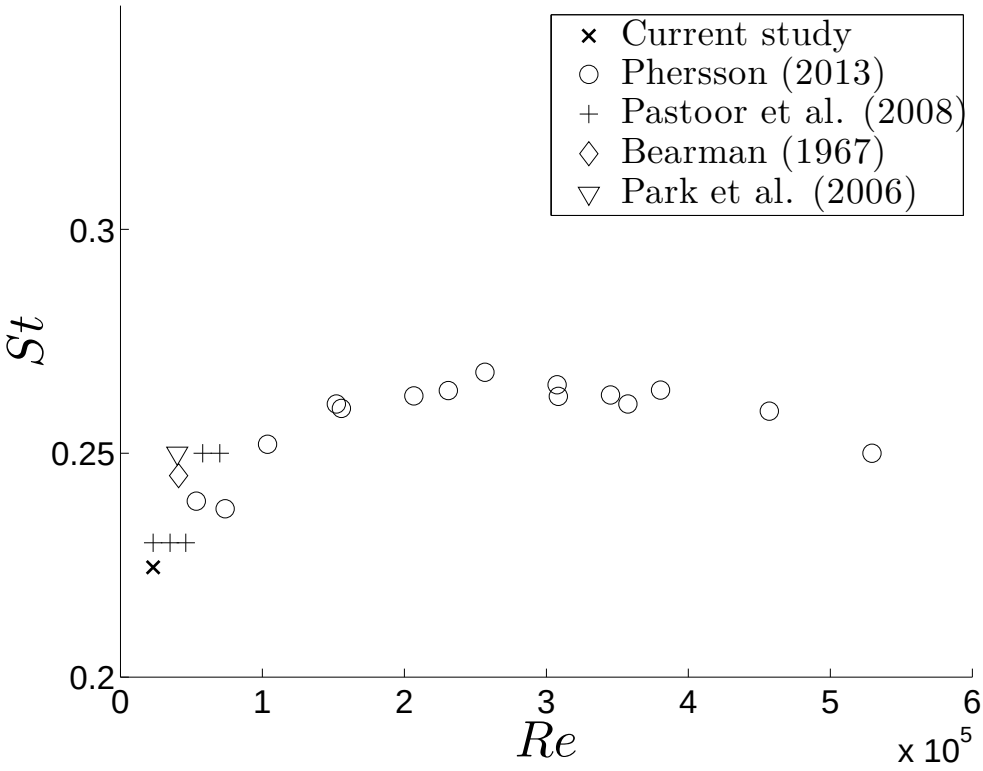

FIGURE 3.11: St number comparison of various studies with rounded leading edge bluff bodies. Phersson (2013) refers to as yet unpublished experimental results obtained from private correspondence.

Elements (million)	$C_{D,0}$	GCI %
1.20	0.557	-
4.53	0.593	0.5
8.56*	0.590	0.2

TABLE 3.8: Grid resolution analysis results for natural flow (all statistics taken from a sample of flow starting at 0.5 seconds (34 non-dimensional time units) and finishing at 1.35 seconds (92 non-dimensional time units), with a timestep of $1 \times 10^{=4}$ s). * final mesh used.

velocity profiles suggest extra resolution would have little effect on the results: $X = H$ the streamwise and vertical velocity rms error between medium and fine meshes are 2.0% and 1.1% respectively; at $X = 5H$ (pictured in Figure 3.12) they are 1.1% and 0.23%.

The boundary layers also change little between the medium and fine meshes. The various measurements of the upper fully turbulent boundary layer, shown in table 3.9, show negligible changes between the two cases, and also indicate the coarse mesh has far too low of a resolution to accurately resolve the boundary layer.

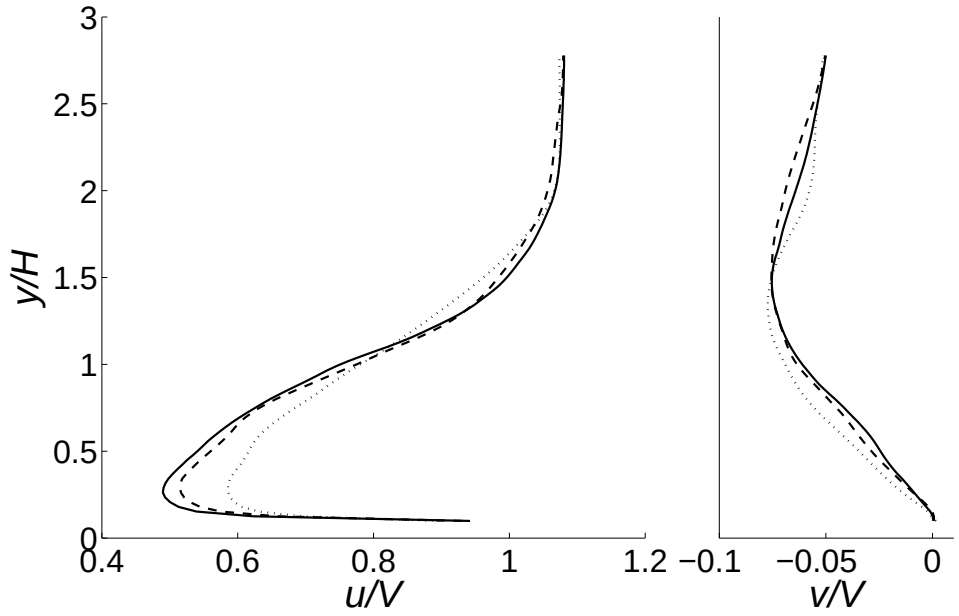

FIGURE 3.12: Span- and time-averaged streamwise (left) and vertical (right) velocity profiles $5H$ downstream of the base. Lines represent coarse (dotted line), medium (dashed line) and fine (solid line) meshes. Velocity components here are normalised with inlet velocity U (not the corrected freestream velocity).

	$\Delta y_{w,top}$ (m)	$\Delta y_{w,bottom}$ (m)	y^+_{top}	y^+_{bottom}	θ/H	$\delta*/H$	$S = \frac{\delta*}{\theta}$
Coarse	3.10×10^{-4}	2.45×10^{-4}	4.8	5.3	0.13	0.16	1.20
Medium	1.95×10^{-4}	1.60×10^{-4}	3.3	3.0	0.46	0.52	1.14
Fine	1.55×10^{-4}	1.25×10^{-4}	2.6	2.3	0.46	0.52	1.15

TABLE 3.9: Average dimensional and non-dimensional wall units perpendicular to the flow for the three meshes.

3.2.2 Energy spectrum

Figure 3.13 shows the energy spectra of the upper (WU1, WU2 and WU3 monitor points, as described in § 2.5, summed) and lower (WL1, WL2 and WL3 monitor points summed) velocity monitors show negligible changes between fine and medium meshes. Once again, however, the coarse mesh deviates greatly from the two finer meshes. The mesh is too diffusive, dropping away from the expected $k^{-5/3}$ decay rate at relatively low wavenumbers.

These results also indicate that for a ground proximity model, monitor points in both the upper and lower wake return a similar energy cascade.

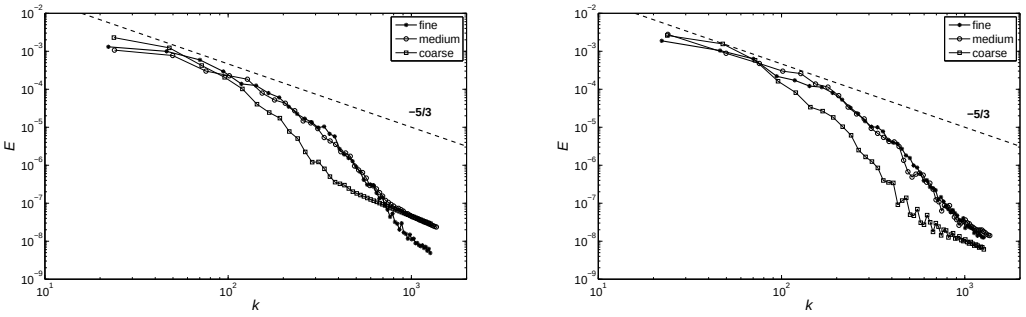

FIGURE 3.13: Resolution analysis of the spectra for (a) upper wake monitor points and (b) lower wake monitor points. Lines have been smoothed to aid comparison..

3.3 Summary

This chapter has presented the basis behind the selection of the numerical parameters/characteristics used in this study. With the accuracy of bluff body flow simulations at high Reynolds numbers dependent on so many variables, multiple measures of validation have been provided to ensure a high level of confidence in the methodology and the application to actuated flows. This includes both numerical considerations and comparison with experimental results, where possible. Whilst it would have been preferable to use even higher resolution meshes, the already high computational resource requirements (simulations are performed on 64 nodes in parallel and typically run for several thousand cpu hours), the desire to undertake several large parameter studies, and the apparent good prediction of global and local flow characteristics (St, C_D, velocity profiles), support the final turbulence model, mesh and timestep choices.

The next chapter begins a discussion of the results obtained by using the numerical techniques outlined in this and the previous chapter.

Chapter 4

Effect of actuation frequency

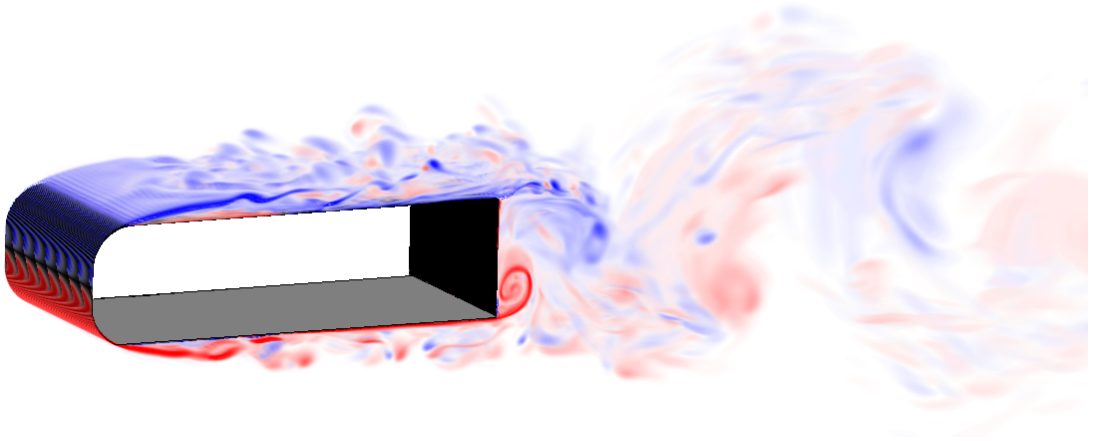

FIGURE 4.1: A snapshot of a perspective view of the instantaneous absolute spanwise vorticity for the natural flow over the body at $Re_H = 23,000$. The flow is characterised by separation at the leading edges to form turbulent boundary layers, which separate at the rear edges to form a von Kármán wake further downstream. The blue-white-red colour map depicts spanwise vorticity from negative (clockwise) to positive (counter-clockwise) levels.

4.1 Natural flow statistics

The natural flow is characterised by weak separation over the leading edge with predominately spanwise aligned coherent flow structures forming as the flow convects towards the trailing edge as shown in Figure 4.1. An absolute instability in the wake (Huerre & Monkewitz 1990) results in large-scale von Kármán shedding from the rear separation points.

The wake shows considerable 3D motion at smaller scales. The lift and drag coefficient history are shown in Figure 4.2 together with power spectra for both signals at the right-hand side of the figure. The drag signal shows consistent fluctuations at the vortex shedding frequency. There are periods where these fluctuations grow in amplitude,

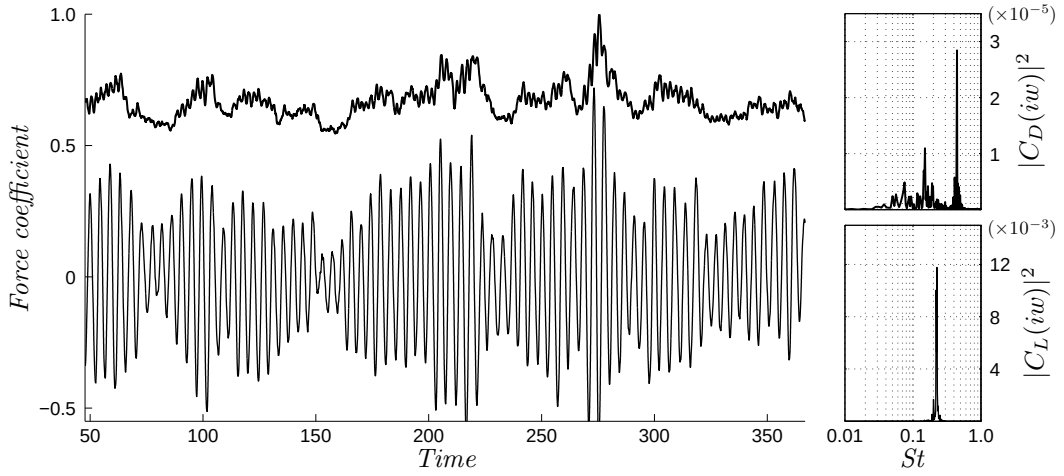

FIGURE 4.2: Time history of drag (thick line) and lift (thin line) signals for natural flow. The frequency spectrum for each signal is displayed on the right. The drag spectra amplitude (top) is displayed at a scale two orders of magnitude lower than the lift spectra amplitude (bottom). The lift signal returns a much clearer peak at the natural frequency than the drag signal.

indicating stronger vortex shedding, which coincide with an increase in the local mean drag value. These periods are followed by periods of lower amplitude vortex shedding, which results in a sharp drop in the local mean drag value. This is likely related to the circular cylinder findings of Lehmkuhl *et al.* (2000), who attribute a low frequency instability to shrinkage and enlargement of the recirculation zone. This can be seen as two different modes of wake configuration—a high-energy mode with larger shear layer fluctuations and shorter recirculation region, and a low-energy mode with smaller fluctuations and longer recirculation zone. Here we observe an average recirculation zone of $1.1H$ in the low-energy mode (for example, between $t \equiv 70$–90 in Figure 4.2) and $0.8H$ in the high-energy mode (between $t \equiv 90 - 110$.) The mechanism behind this behaviour has yet to be explained. The mean downstream distance of the centre of the recirculation zone from the base is $0.43H$.

The large difference in the drag value between these two phases of flow adds noise in the low-frequency range to the Power Spectral Density calculations used to identify the vortex shedding and other key frequencies. This noise, which occurs at $St < 0.06$, dominates the other frequencies of interest and therefore is removed from the signal with a high-pass filter before applying the PSD. This is not as large a problem in the lift signal, but the high-pass filter is still used for consistency.

Other considerations are also required: while the frequencies of the spectral peaks change little with increasing sampling time (Figure 4.4), the corresponding magnitudes

vary noticeably (Figure 4.3). These magnitudes, which give an indication of the energy of the frequency in the signal, are useful to compare later with other cases. To account for this variation, which also occurs to a lesser extent in the actuation and ground simulation signals, the average magnitude over the final 20 von Kármán shedding periods is used. This technique is also used to arrive at the final St values.

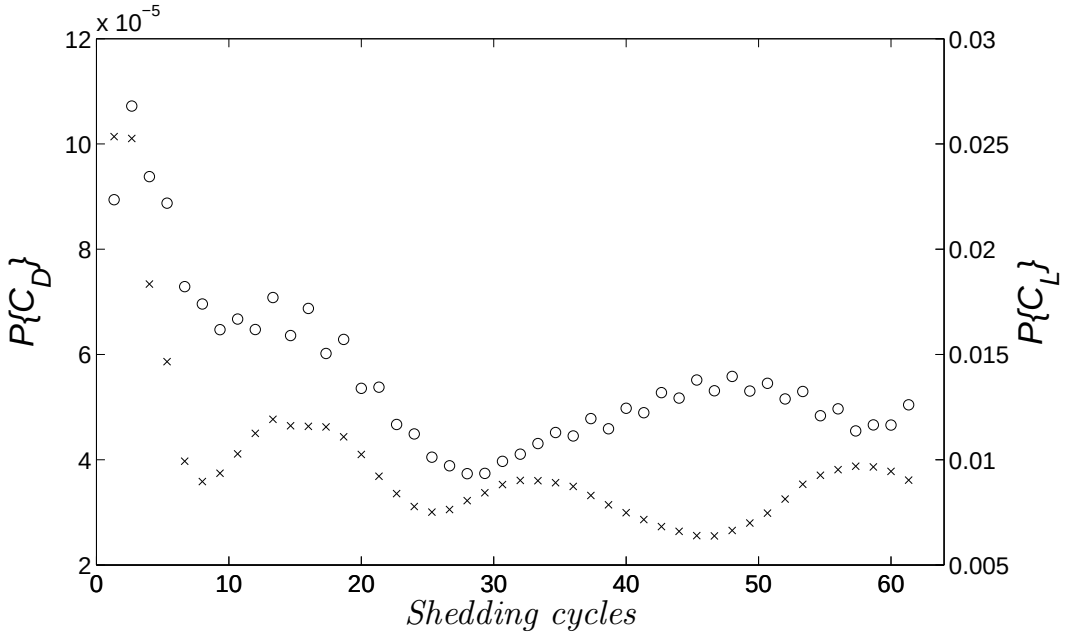

FIGURE 4.3: Variation of the spectral peak magnitudes in the drag (crosses, left axis) and lift (circles, right axis) signals.

The dominant lift signal frequency is 0.22(2), while in the drag signal it is double this value, 0.44(4). (The drag peak frequency is double the lift peak frequency because each drag signal period represents one shed vortex, while each lift signal period represents two). While occasional periods of slightly higher shedding frequency are observed, we conclude that the predicted natural Strouhal number is 0.22, in good agreement with the experimental value obtained by Pastoor *et al.* (2008) of 0.23.

A secondary peak occurs at $St = 0.15$ in the drag signal. The peak is broader than the von Kármán peak and surrounded by other smaller peaks, suggesting it is related to a secondary mechanism in the flow. While a secondary peak at a similar frequency has been observed (but not explained) in three-dimensional blunt trailing-edge flows (summarised in Grandemange *et al.* (2013)), this has not been reported in the previous two-dimensional studies. The mechanism behind this remains unclear.

The values presented in table 4.1 are time-averaged from $t = 0.7$ s (approximately

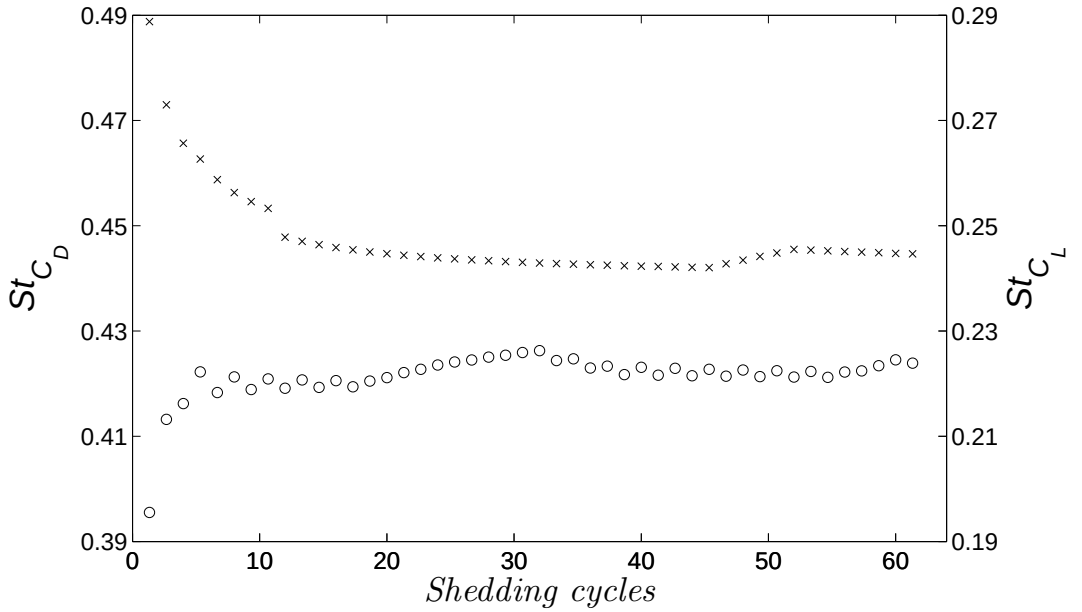

FIGURE 4.4: Variation of the spectral peak frequencies in the drag (crosses, left axis) and lift (circles, right axis) signals.

50 non-dimensional time units) onwards. The flow from the inlet at $t = 0$ first detaches from the rear of the body at $t = 0.17$ s. Thus, 0.53 seconds, or approximately 7 vortex shedding cycles, have occurred before averaging begins. The initial bulk of inlet fluid first reaches the outlet at $t \approx 0.6$ s. Defining the exact moment when the flow can be considered to have reached its asymptotic state is of course an ambiguous task, however it is reasonably safe to assume the flow has settled by $t = 0.7$ s. There are approximately 63 von Kármán shedding periods sampled from this point onward.

Re_H	C_D	$C_{L,rms}$	C_{pb}	St_D	$P\{D_{max}\}$	St_L	$P\{L_{max}\}$	t_{total}
23,000	0.72	0.29	-0.51	0.444	1.2×10^-2	0.222	2.8×10^-5	367 (5.38 s)

TABLE 4.1: Natural flow statistics. St_D and St_L refer to the dominant frequencies in the drag and lift signals respectively, while $P\{D_{max}\}$ and $P\{L_{max}\}$ are the magnitudes of these spectral peaks.

4.2 Natural time-averaged flow structure and topology

Figures 4.5 and 4.6 show the time-averaged streamwise velocity and pressure fields through the centreplane. The first notable observation is a striking acceleration of fluid over the convex curved leading edges (a maximum velocity of $U/U_\infty = 1.3$ occurs in these regions), accompanied by a favourable pressure gradient ($\frac{dP}{dX} < 0$). This

acceleration is so large that the total front face pressure coefficient is actually negative (-0.175). However, as the curved surface flattens out, the low pressure begins to rise and an adverse pressure gradient ($\frac{dP}{dX} < 0$) is formed. This results in separation and eventual reattachment as the pressure gradient returns to zero.

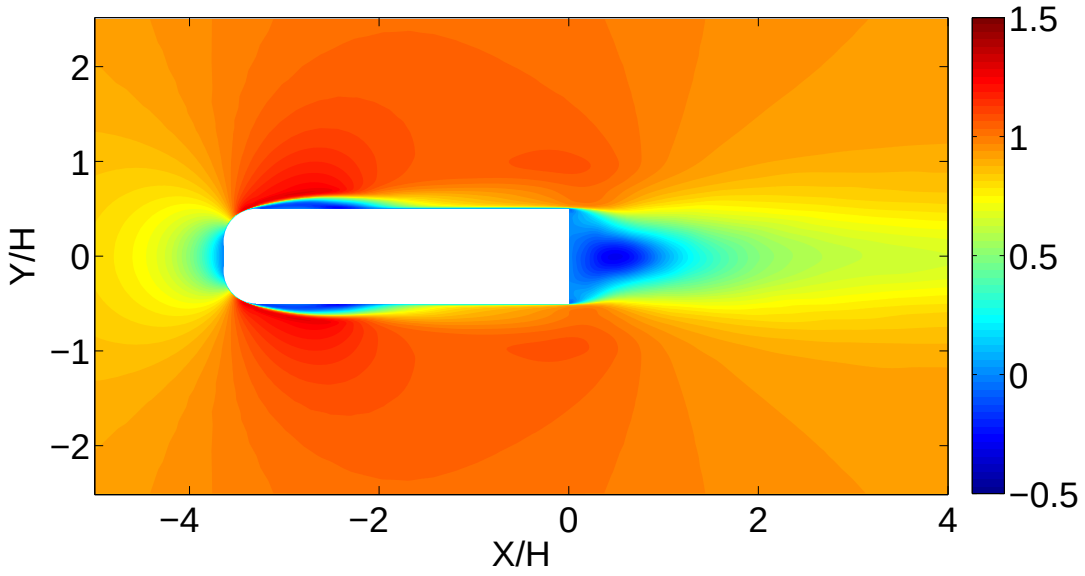

FIGURE 4.5: Time-averaged u velocity along the centreplane.

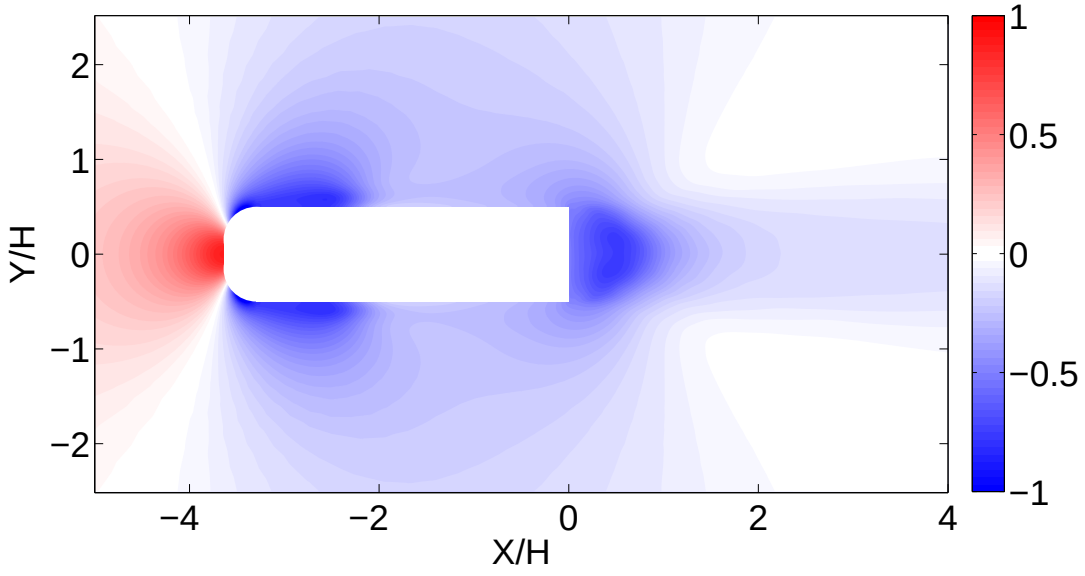

FIGURE 4.6: Time-averaged pressure coefficient contour through the centre plane.

Separation occurs once again, of course, further downstream at the fixed rear corners. This leads to another sharp drop in pressure—the minimum pressure coefficient in

the wake is -0.78, occurring approximately at $X/H = 0.5$, $Y/H = \pm 0.15$. The minimum velocity in the wake also occurs $= 0.5H$ behind the rear, measuring $U/U_\infty = -0.3$. The rear base pressure coefficient is -0.51, as expected markedly lower than the front face coefficient.

Recirculation regions relating to both the leading edge and trailing edge shedding are apparent on the time-averaged centreplane velocity streamline plot (Figure 4.7). The re-attachment point occurs at $X/H = -2.01$, which is $X/H = 1.63$ downstream of the leading edge. When the wake is analysed closer, a "pocket" recirculation region can also be seen directly behind both the upper and lower rear separation points.

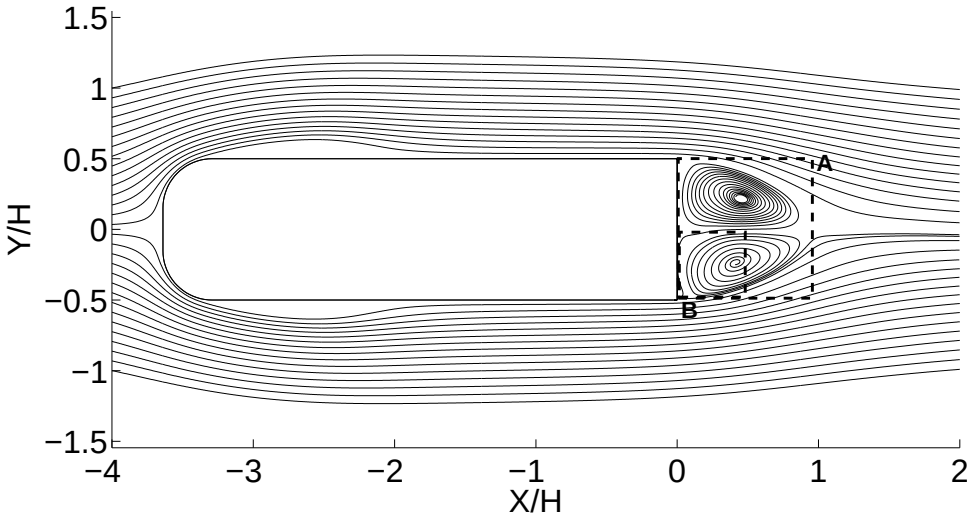

FIGURE 4.7: Time-averaged velocity streamlines through the centre plane (recirculation zones at front of body are not shown). Figure 4.8 shows regions "A" and "B" in greater detail.

4.2.1 Boundary layer

The leading edge separation and re-attachment creates a boundary layer different from those of the widely studied flat plates. Thus, despite the Reynolds number over the surfaces being below the critical value of $Re_x = 5 \times 10^5$ (Schlichting & Gersten 2000) for turbulence on flat plates, the boundary layers here have some turbulent properties and are highly unsteady. Due to the non-zero pressure gradient along the body's upper and lower surfaces, the boundary layer profile (averaged over both time and the span) is highly dependent on location. The momentum thickness at separation is $0.019H$, and the displacement thickness is $0.025H$, giving a shape factor of 1.30. The momentum thickness Reynolds number $Re_\theta = \frac{\theta U_{99}}{\nu}$ is approximately $2,000$. This is above the

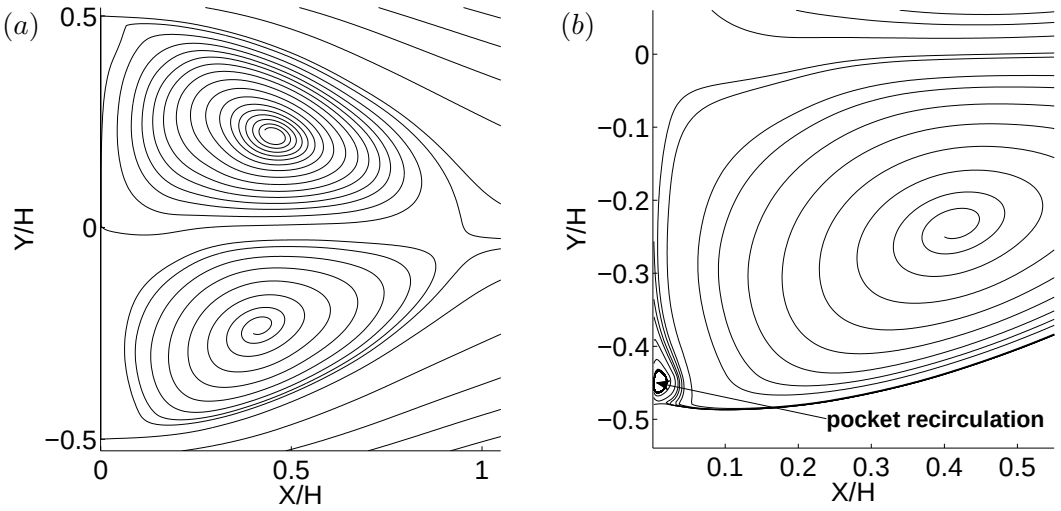

FIGURE 4.8: (a) Centreplane time-averaged streamlines zoomed on region "A" outlined in Figure 4.7 (b) Region "B" showing the smaller pocket recirculation regions.

critical value $Re_{\theta,c1} \approx 1,000$ where George (2007) suggests a log-layer begins to develop, but below $Re_{\theta,c2} \approx 10,000$, where it is able to reach a significant size (a decade in space)[1].

In addition to this, the upstream separation and re-attachment further complicates the boundary-layer behaviour. Thus, the time-averaged boundary-layer shape recovered here will be different from those found in boundary layer text books. However, at $X/H = -0.3$ (where the pressure gradient is close to zero), there are some similarities with a zero pressure gradient turbulent boundary layer (ZPG TBL) over a flat plate. The viscous sub-layer, as expected, is evident at $y^+ < 10$, where velocity scales linearly with height. A narrow log-layer region seems to be present at $200 < y^+ < 0.15\delta$, as predicted by Österlund *et al.* (2000) for ZPG TBL (the log-layer best-fit line overlaid on the Figure is constructed from Österlund's recommended values of 0.38 and 4.16 for the von Kármán and displacement constants—in agreement with values a thorough review of the ZPG TBL literature by George (2007) also recently recommended).

While a typical flat plate turbulent boundary layer transitions smoothly from the viscous sublayer to the log-layer, here the velocity rises higher than anticipated before transitioning to the log-layer region. As we continue further from the wall, the velocity gradually falls to the freestream value, whereas a traditional ZPG TBL would gradually

[1]George also argues that the true inertial layer actually exists for $300 < y^+ < 0.1\delta_{99}$, rather than the often quoted range $30 < y^+ < 0.1\delta_{99}$. This means that current experimental and numerical boundary layer work is even further from the structure of real-world turbulent boundary layers, which feature a significantly larger log-layer.

rise to the freestream value.

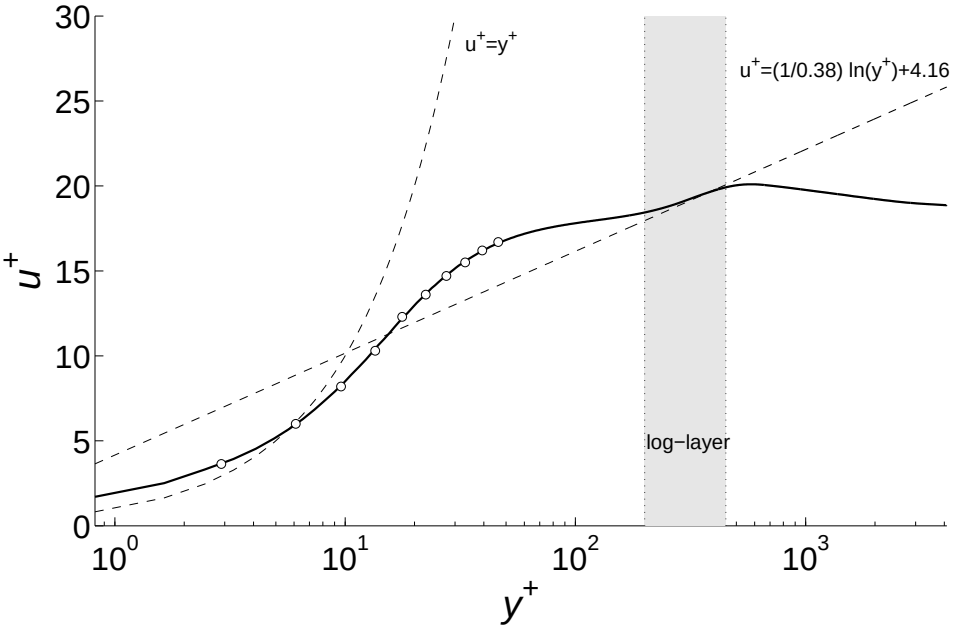

FIGURE 4.9: Spanwise- and time-averaged boundary layer profile $X/H = -0.3$ (IE: 0.3 upstream of the rear). The average pressure gradient along the span at this location is $\frac{\partial C_P}{\partial X/H} \approx -1.2$. The pressure gradient is zero at $X/H \approx -1.7$ (equivalent to 1.9 downstream of the front nose).

4.2.2 Wake

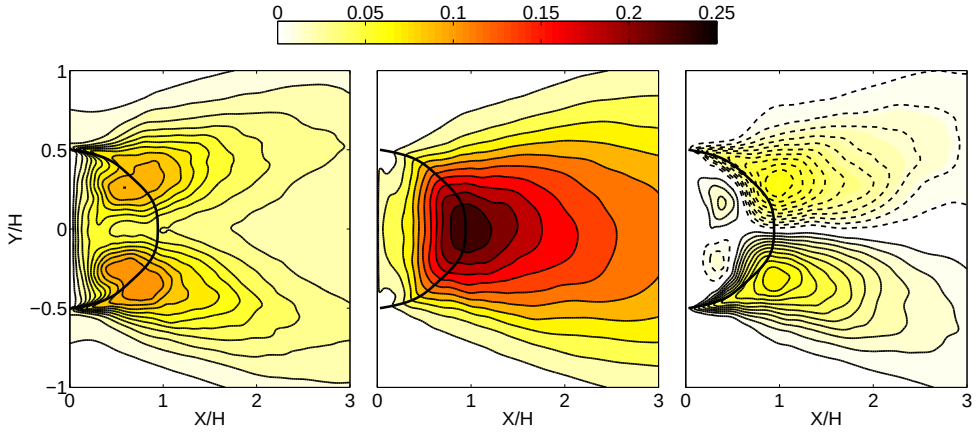

FIGURE 4.10: Reynolds stress averages along the centreplane in the wake. From left to right: $\langle u'u' \rangle / U_\infty^2$, $\langle v'v' \rangle / U_\infty^2$, $\langle u'v' \rangle / U_\infty^2$. Dashed contour lines indicate negative magnitudes. Thick line indicates separatrix (mean separation line).

The normal Reynolds stress components are shown in Figure 4.10. The normal cross-flow stress $\langle v'v' \rangle$ is by far the highest component in this case, peaking in the

centre wake around $X/H = 1$ behind the rear face at the edge of the recirculation regions. The peak streamwise normal fluctuations $\langle u'u' \rangle$ occur in the centre of the recirculation region at approximately $X/H = 0.5$. The spanwise fluctuations $\langle w'w' \rangle$, by comparison, are less substantial. The shear stresses involving w' are also negligible.

The shear-stress $\langle u'v' \rangle$ plot reveals two distinct zones – one inside the recirculation region and one outside. The Reynolds stresses in the wake contribute to the equilibrium of the recirculation region.

The time-averaged rear base pressure profile, which can be thought of as an "output" parameter of the wake activity and directly responsible for drag, is shown on Figure 4.11(b) (the outer edges $0 < X/H < 0.1$ and $0.9 < X/H < 1$, where mild end effects occur, are not shown). The pressure is shown to be slightly higher at the upper and lower edges, and relatively uniform over $-0.3 < Y/H < 0.3$. This pressure profile is dependent on the wake pressure profile (figure 4.11a). The minimum pressure occurs at the centre of each recirculation region—slightly above and below the centreline $Y/H = 0$, at $X/H \approx 0.5$). It is clear that, by either increasing this minimum wake pressure, and/or pushing its location further downstream, the rear base pressure will increase.

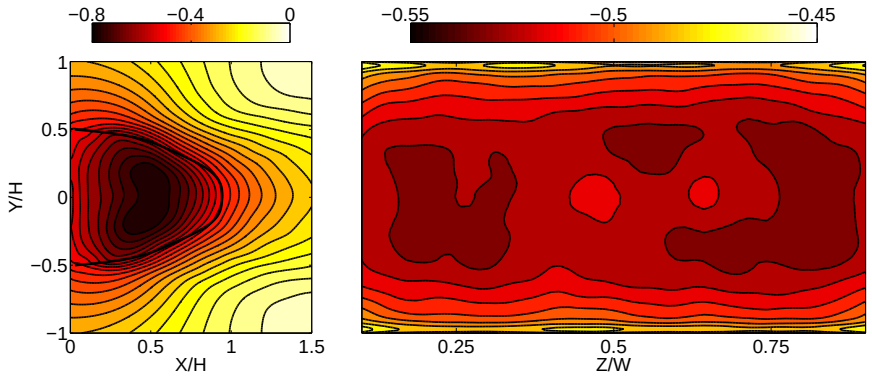

FIGURE 4.11: (a) Time-averaged pressure coefficient along the centreplane in the wake and (b) on the rear base surface over $0.1 < Z/W < 0.9$. The thick line represents the separatrix.

4.3 Natural transient flow characteristics

4.3.1 The von Karman and Kelvin-Helmholtz instabilities

The Strouhal number obtained from the drag and lift signals—$St = 0.22$—is also dominant in the velocity spectra throughout the wake (Figure 4.13). Both upper and lower monitor points return similar PSDs, indicating an acceptable length of sampling time has transpired. The out-of-phase nature of upper and lower-slot pressure signals

shown in Figure 4.12 confirms the vortex shedding process is the dominant mechanism throughout the wake. However, visualising this process is challenging, as countless turbulent structures with small time and length scales are present at all times and no two shedding cycles are ever exactly the same. Figure 4.14, for example, shows the spanwise vorticity from multiple $X - Y$ planes in the middle portion of the span overlaid on one another. The general shape of a vortex street is evident, but the large amount of turbulent "noise" in the wake makes further anaylsis difficult. Despite this noise, the corresponding pressure contours (Figure 4.15), reveal just how influential the larger vortex structures are on the rear base pressure, and consequently drag. It can be seen that the minimum drag in each cycle occurs when both the new and previous vortices are moderately sized (the former is still growing in size, while the latter has begun to diffuse), and relatively close to one another in the wake. The maximum drag occurs when a new vortex has reached it largest size, and the previous vortex has convected downstream.

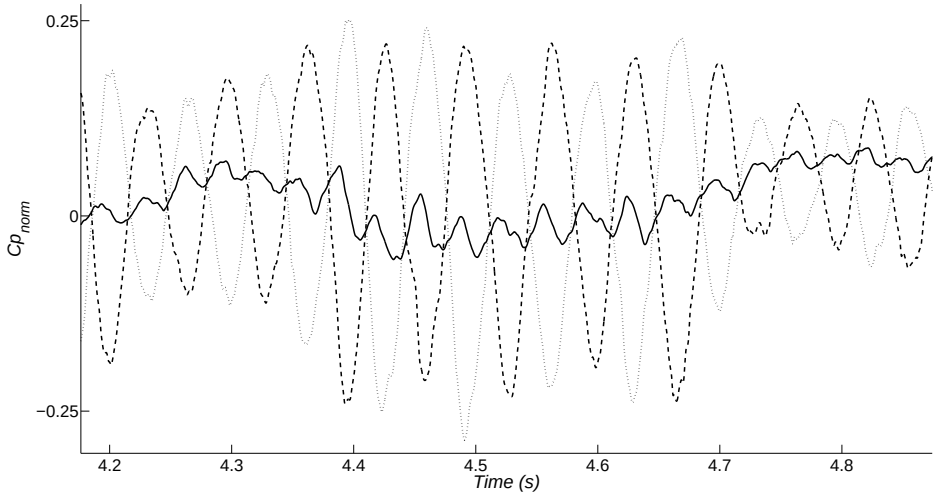

FIGURE 4.12: The normalised base, upper- and lower-slot pressure coefficient signals show alternate vortices are being shed at regular intervals.

Through phase averaging, the essentially random fluctuations of the smaller eddies are filtered away, and an idealised representation of the shedding cycle can be formed. Thus, more specific details of the average shedding cycle can be surmised (see § 2.9.5 for details on the phase-averaging process used here). Figure 4.16 shows the spanwise vorticity at four equidistant points in the shedding cycle. By the time a new vortex is formed with centre at $X/H \approx 0.5$, the previous vortex of same sign is at $X/H \approx 2.75$

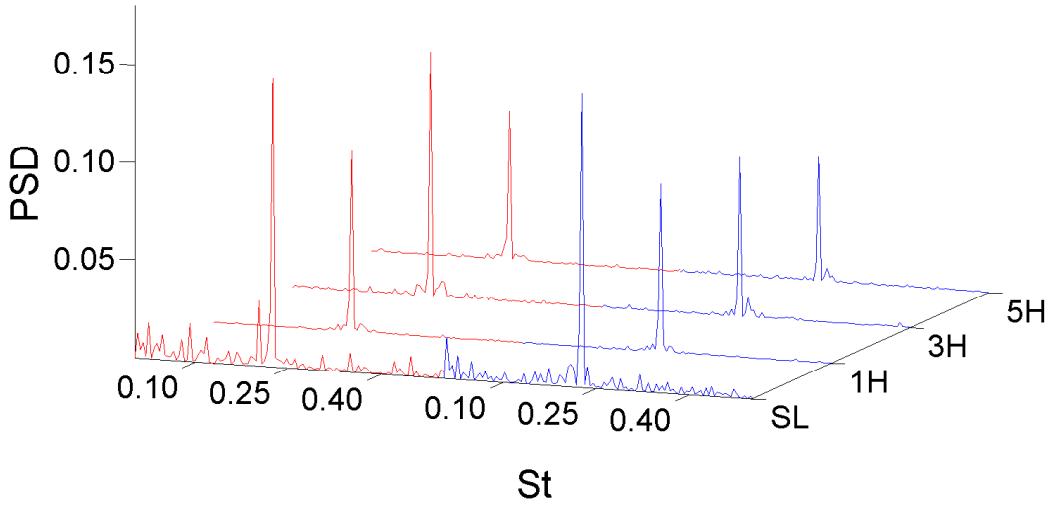

FIGURE 4.13: Spectra of velocity monitors in shear layer, 1H, 3H and 5H downstream of rear. The red line represents the lower-wake monitors, while the blue line represents the upper-wake monitors. All peaks occur at $St = 0.224$. See § 2.5 for exact locations of monitor points

.

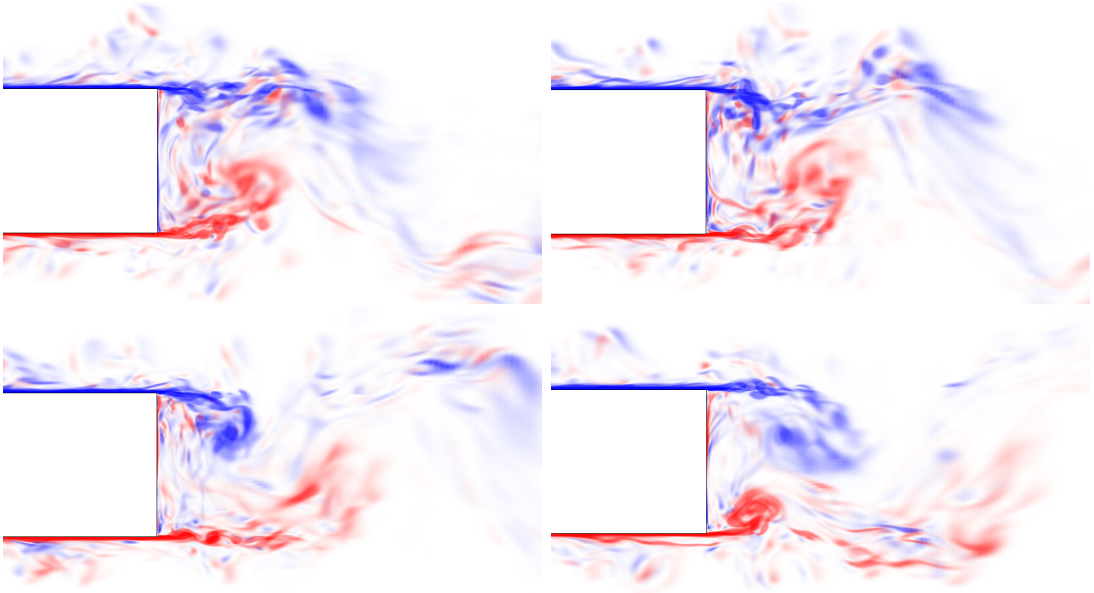

FIGURE 4.14: Spanwise vorticity snapshots for a typical vortex shedding cycle. Data from multiple X-Y planes placed at $Z = 0, \pm 0.08W, \pm 0.16W$ is overlaid on one another. Left snapshots: local maximum in drag; right snapshots: local minimum in drag.

(not pictured). The previous vortex of opposite sign, on the other hand, remains at $X/H \approx 1.25$, far closer than halfway between the two same-signed vortices. This shows the tendency for each vortex to travel slower while in the near wake and growing in size

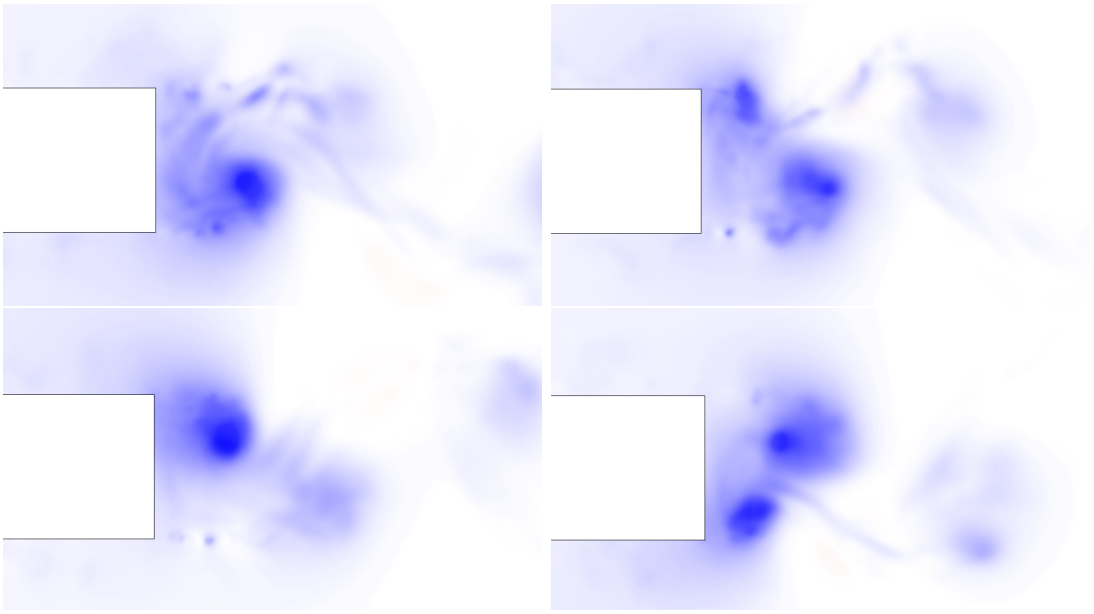

FIGURE 4.15: Pressure snapshots for a typical vortex shedding cycle. Data from multiple $X-Y$ planes placed at $Z = 0, \pm 0.08W, \pm 0.16W$ is overlaid on one another. Left snapshots: local maximums in drag; right snapshots: local minimums in drag.

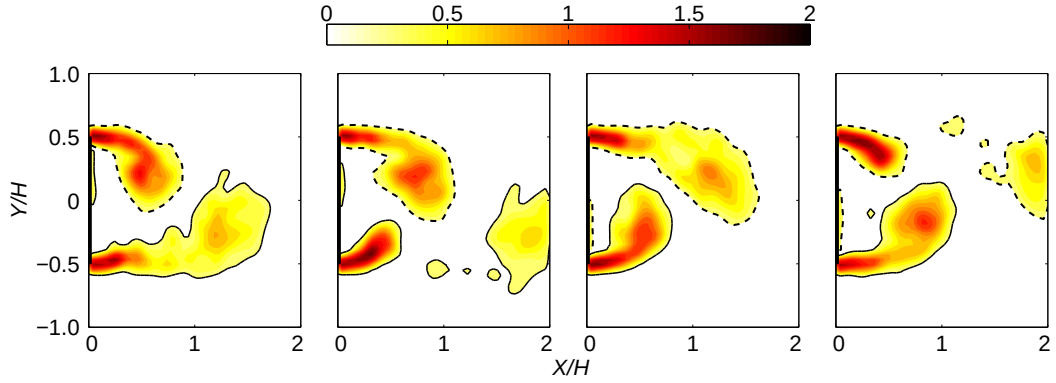

FIGURE 4.16: Natural flow: Vorticity contours of one complete cycle of phase-averaged observed flow field. A similar wake evolution is observed to that of the Koopman reconstruction using only modes M and N (Figure 4.25).

– once large enough, it breaks free and convects downstream. The local maximum in drag occurs when each new vortex is around $X/H \approx 0.5$ downstream.

The much smaller and weaker shear-layer instability, which develops due to the Kelvin-Helmholtz mechanism, is not apparent in the phase-averaged contour figures. However, it does appear in instantaneous snapshots of the shear layer preceding the formation of a new vortex. Figure 4.17 shows a collection of small low pressure regions in the shear-layer region, which represent the shear-layer instability (the darker contours represent vortex structures). The corresponding vorticity contour reveals the "wavy"

shape associated with the instability. The instability has been explored in depth for circular cylinder flows, as outlined in §1.2.2, however analysis for fixed rear separation point flows is more sparse (it has recently been observed by Pun & O'Neill (2007); Almeida *et al.* (2008)). Thus, while a global relationship $f_{SL}/f_{VK} \propto Re^{0.69}$ has been well established for the former (Prasad & Williamson 1997; Thompson & Hourigan 2005; Khor *et al.* 2010), an estimate of f_{SL}/f_{VK} for the latter does not exist. Brun *et al.* (2008) showed that the relationship is similar for the leading edge separation of a square cylinder, however it is unclear whether this holds for the shear-layers at the rear of an extended D-shape body such as that studied here. The thickness of the shear layer is far larger in this case, which may result in a lower shear layer frequency as linear stability theory for a mixing layer suggests $f_{SL} \propto U_{SL}/\theta$ (Michalke 1965). Were this theory to hold in the present case, a predicted value for f_{SL} would be $0.033U/\theta$ (Brun *et al.* 2008), which gives $St \approx 0.80$. This is much smaller than the aforementioned circular cylinder work which for $Re = 23,000$ would predict a frequency of $20 \times f_{VK} \approx 4.4$. These two values are used as a lower and upper limit respectively in the search for the shear layer frequency outlined below.

While no noticeable peaks in this range appear in the drag and lift power spectra of Figure 4.2, the shear-layer monitor point (SU and SL) velocity spectra are expected to provide some frequency information on the instability. However, Prasad & Williamson (1997) have shown that the intermittency of the shear layer instability causes drastically lower and broader peaks in the velocity spectra than would occur if the instability were continuous – and this appears to be the case here. When the spectra is smoothed and viewed on a log-log plot, a slight hump is observed at $St \approx 1.1$. This may be related to the shear-layer frequency, but could of course be due to other motions or randomness.

Further insight is gained from wavelet analysis, which is an ideal tool in this scenario due to its ability to identify intermittent frequencies (the technique is described in § 2.9.3). Figure 4.19 shows that higher frequencies are, despite being intermittent, very prevalent in the shear layer monitor signal SL. The velocity monitor $WL3$, which is $5H$ downstream, shoes less activity at these higher frequencies. When viewed over a shorter time range, as is shown in Figure 4.20, the frequencies evident in the shear layer signal alone are around $St \approx 2.2$. These frequencies appear more intermittent than the frequency of $St \approx 1.1$ that was located in the PSD analysis, which is expected for parallel shear layers (Prasad & Williamson 1997). It is therefore likely that the shear

layer frequency is somewhere in this frequency range, around $St \approx 2.2 \pm 0.5$. With so many high frequency turbulent structures in the flow at this Reynolds number, however, this is merely speculation. In any case, the shear layer frequency has once again been shown here to be difficult to identify through statistics, despite its straightforward identification visually. Due to the importance of the instability in the development of the wake, continued research in this area is recommended.

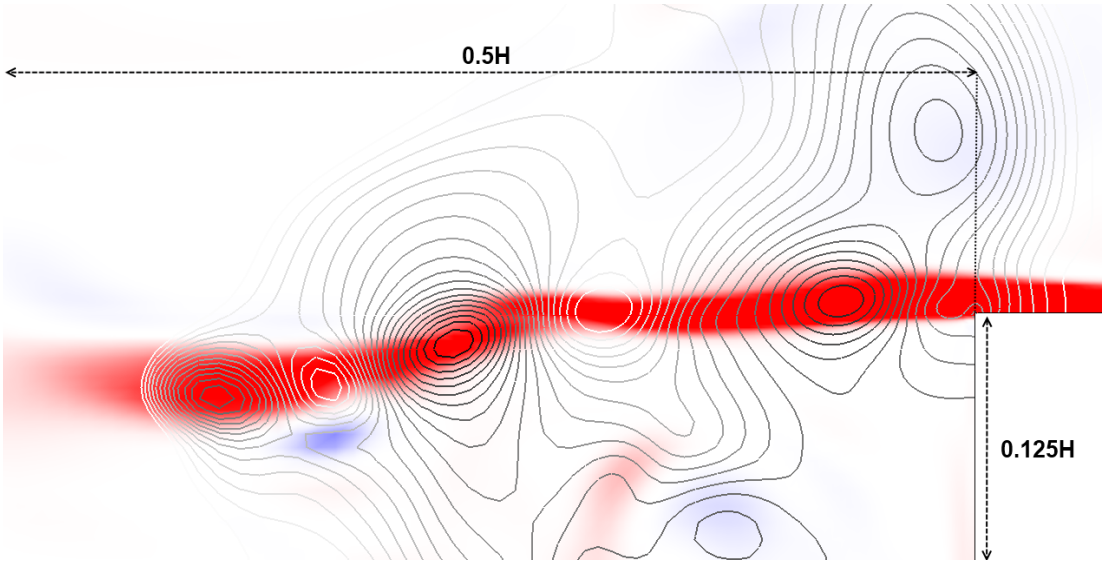

FIGURE 4.17: Centreplane non-dimensional instantaneous spanwise vorticity contour (blue-white-red indicating $\omega = -2000$, 0, and 2000 s^{-1} respectively) with low pressure contours overlaid (black lines indicate $C_P = -0.47$, white lines $C_P = -0.32$).

4.3.2 Transience in the drag and lift signals

A wavelet analysis on the drag and lift signals reveals further information on the transience of the instabilities highlighted in § 4.1 (no higher frequencies are returned in these signals, as expected). The drag signal shows the dominant Strouhal frequency ($St \approx 0.44$ or in dimensional terms $f \approx 32$ Hz) is intermittent. Furthermore, the secondary instability, which occurs at $St \approx 0.15$, and the long-wave instability frequency at $St \approx 0.06$ (which was removed with a high-pass filter for the PSD calculations but not here) are also intermittent, and appear to grow and shrink in prevalence concurrently (for example, between 3 and 4 seconds). This is further evidence of the aforementioned theory of Lehmkuhl *et al.* (2000), with the wake in either a high-energy or low-energy mode.

The lift signal, by contrast, is influenced more by the shear layer development than the wake, and therefore returns a far more consistent Strouhal frequency – however

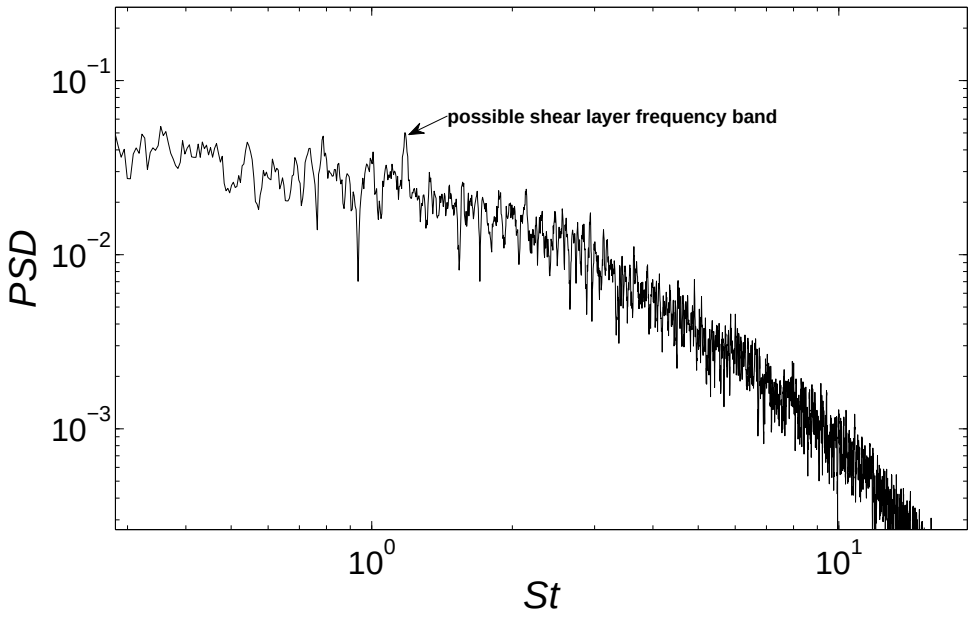

FIGURE 4.18: High-frequency spectra of shear layer velocity monitors at the lower (bottom) shear layer.

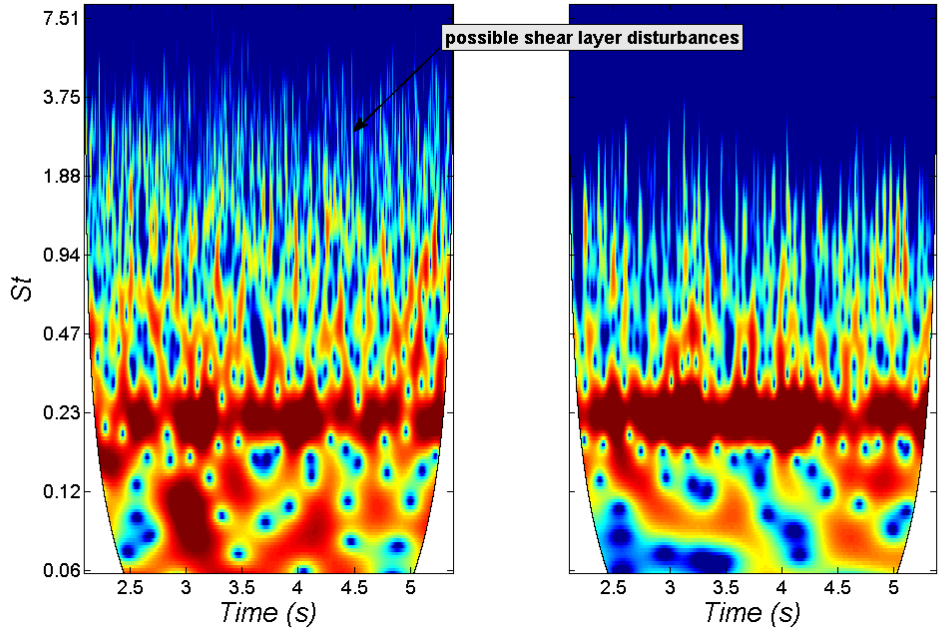

FIGURE 4.19: Wavelet analysis for velocity signals in shear layer (left) and $5H$ downstream (right).

there are still occasional periods of variance (for example, at the 2.4 second mark).

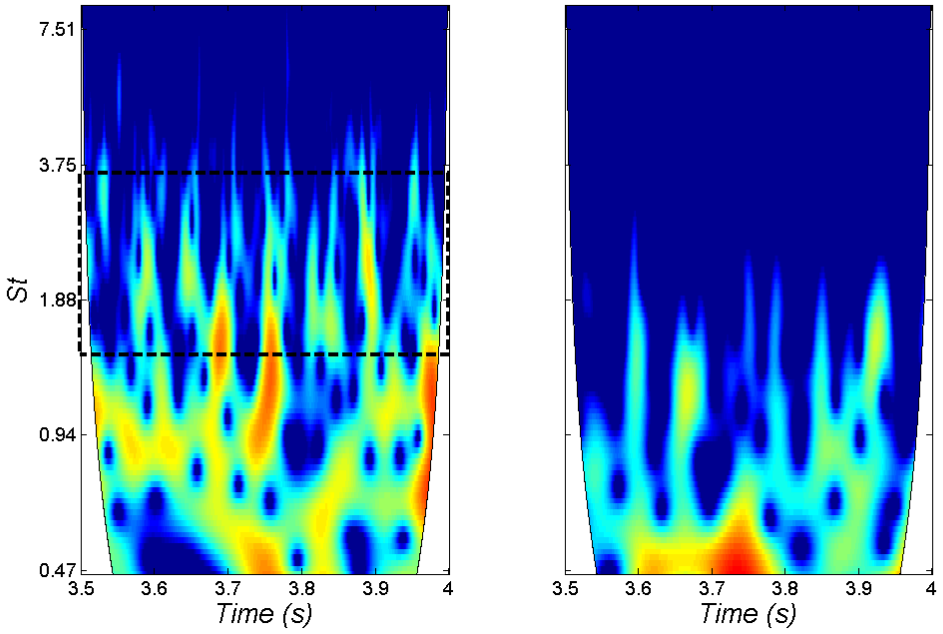

FIGURE 4.20: Zoomed wavelet analysis for velocity signals in shear layer (left) and $5H$ downstream (right). The dashed box indicates possible shear layer frequency disturbances.

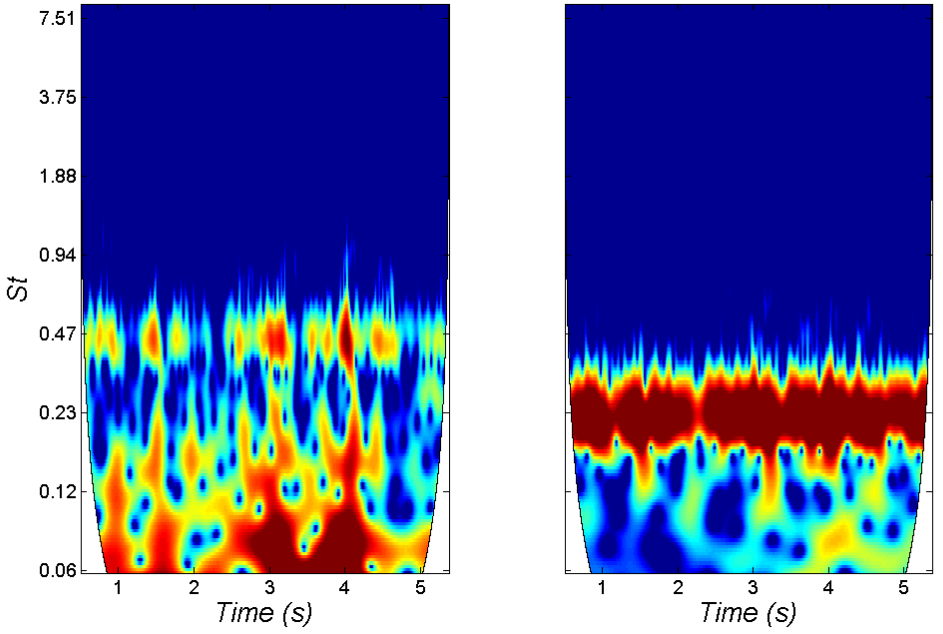

FIGURE 4.21: Wavelet analysis of the drag (left) and lift (right) signals.

4.3.3 Dynamic Mode Decomposition

To analyse the wake further in terms of the dominant wake flow structures, a Dynamic Mode Decomposition (DMD) was performed on the 2D velocity flow fields obtained at

regular time intervals from the midplane of the wake. For those readers not familiar with this relatively new analysis tool, §2.9.4.2 contains a background, with a specific outline of the method used also therein.

DMD was applied to the natural flow span-averaged velocity fields over $0 < X/H < 4$ and $-1 < Y/H < 1$ (divided into a grid with 20,000 measurement locations and $\Delta x = \Delta y = 0.02H$) with the number of samples $m = 117$, which covers a period of 9 complete vortex shedding cycles. The time between each sample was $\Delta t_s = 0.005$ seconds, equating to approximately 13 samples per shedding period. It was confirmed that these numbers obtained effectively a complete vector space (completing the analysis with a higher amount of timesteps produced near identical results).

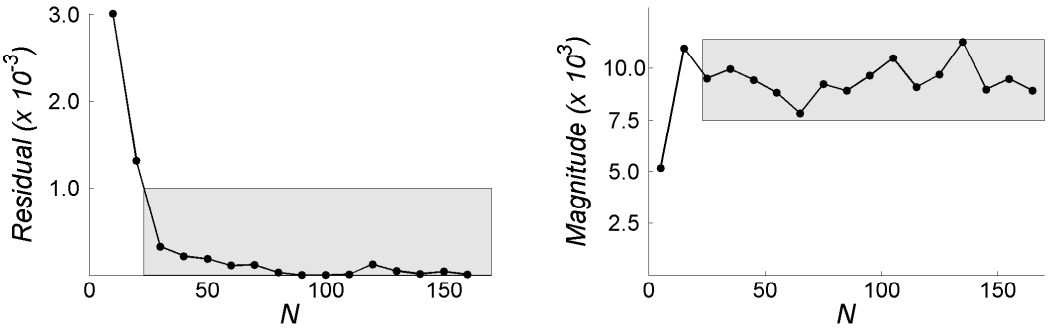

FIGURE 4.22: Convergence analysis for the natural flow case. (a) The DMD residual $\overline{V_N^2 - V_{N-1}^1}$ against number of flow field samples used in the decomposition N. (b) The magnitude of the first dynamic mode against N. Grey boxes show the range where averaging was completed.

The convergence of the decomposition is monitored via analysing the progression of the mean residual $\overline{V_N^2 - V_{N-1}^1}$ and the fluctuation of the first dynamic mode magnitude with increasing N timesteps. It should be emphasised that, due to the high levels of turbulence and non-linear physics involved with this flow, the magnitude of the modes recovered by the DMD do not converge ideally to a final value, despite the residual nearing zero. This behaviour is shown in Figure 4.22, where the magnitude of mode N (introduced below) never approaches a truly steady value with increasing timesteps. To account for this fluctuation, the magnitude is measured by taking the average over all timesteps where the residual is below 10^{-3}. This process will be completed for all actuated cases also, allowing for a reliable comparison measurement between cases. This also allows for the calculation of standard deviation, which reveals further information on the time-varying nature of the modes.

The results, shown in Figure 4.23, indicate that the wake is dominated by only

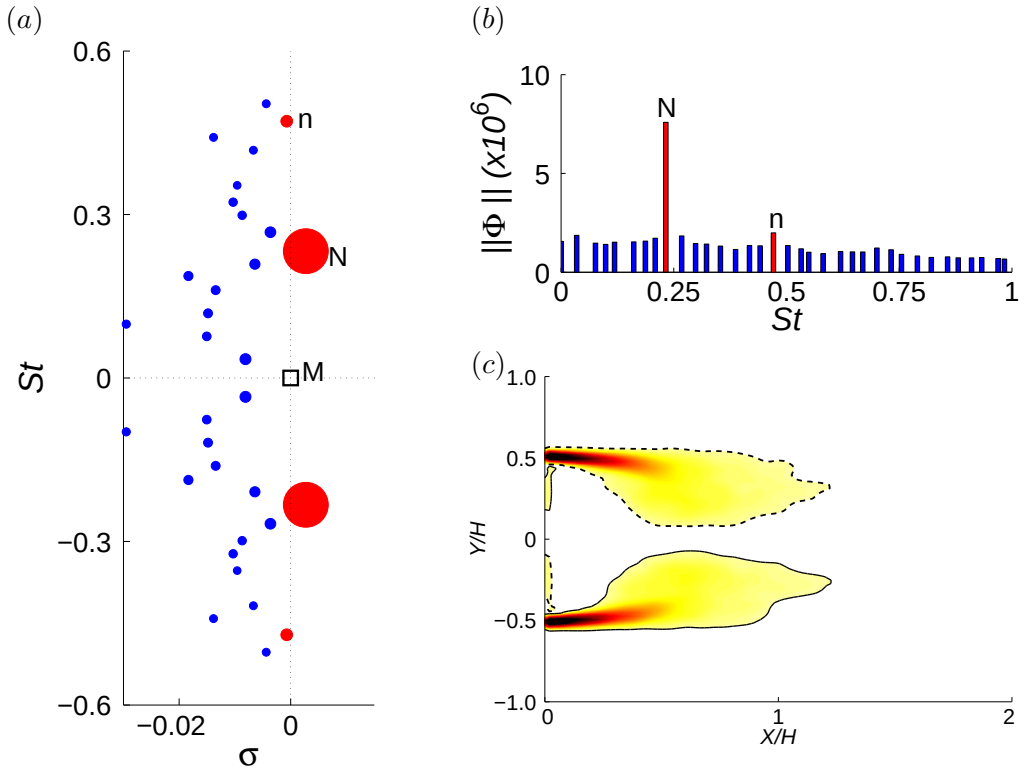

FIGURE 4.23: Natural flow dynamic mode decomposition: (a) spectrum showing the growth rate (σ) of each mode. The red dots are the most relevant modes, with the size of each dot showing its relative magnitude. The mean mode (M) is indicated with an open square. Mode N occurs at the natural Strouhal number and mode n at the first harmonic of N; (b) The relative magnitude of each mode is plotted against frequency; and (c) vorticity contours for the mean mode.

one dynamic mode, together with the mean mode. Not surprisingly, the frequency of this mode corresponds to the observed (uncorrected) shedding frequency of $St = 0.22$. Notably the spectrum at the top right shows that the first harmonic of that mode is also discernible. Even so its relative low amplitude indicates that the wake flow associated with the dominant mode (N) together with its harmonics is not too far from sinusoidal.

Figure 4.3.3 shows the vorticity evolution over a cycle for the dominant time-dependent Koopman mode (N). This mode shows a pair of co-rotating vorticity perturbations form from each trailing edge of the body, with each new pair having the opposite direction of rotation to the previous pair. These two vortices quickly come together to form one large vortex, which proceeds downstream. While the co-rotating nature of the vortices in this mode may seem unexpected, it should be recalled that this mode exists superimposed on the mean mode (M), which features two counter-rotating regions of

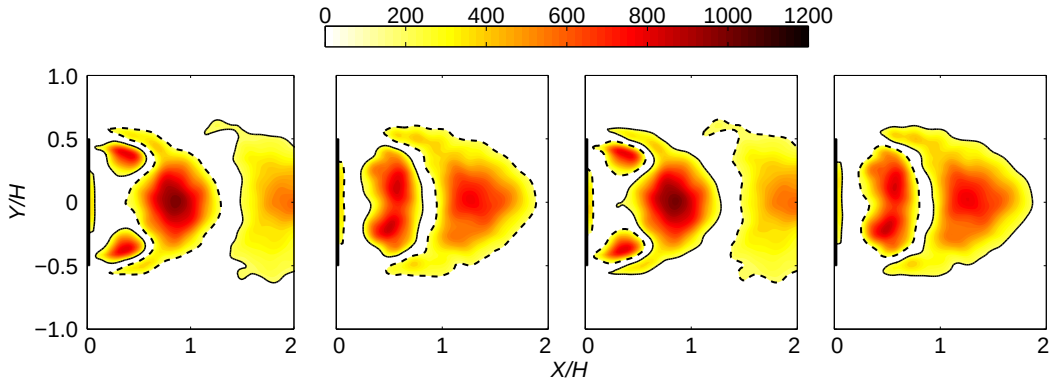

FIGURE 4.24: Natural flow: Vorticity contours (dashed line indicates clockwise vorticity, solid line indicates anti-clockwise vorticity) of one complete cycle of the first Koopman mode (also referred to as the actuation mode), i.e., mode N. The sequence progresses left to right, with each image progressing one quarter step through the cycle from the previous image). Flow is from left to right.

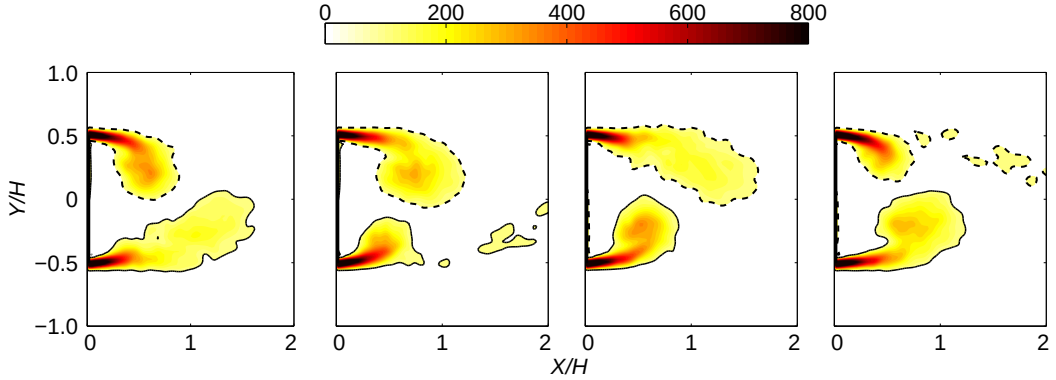

FIGURE 4.25: Natural flow: Reconstruction of the vorticity evolution for the natural flow using just the Koopman mean mode M and the larger amplitude DMD mode N.

vorticity, as shown in figure 4.23(c), and does not change with time. Thus, when the first dynamic mode N and mean mode are added together in figure 4.25, it can be seen that one of the mode N co-rotating vortices is amplified by the similarly-signed vorticity region in the mean mode, whilst the other is nullified by the opposite-signed vorticity region. We therefore end up with traditional von Kármán shedding—asymmetric vortex shedding resulting in a von Kármán vortex street progressing downstream. This accounts for the dominant time-dependent features of the unsteady wake, as can be seen from a comparison with the phase-averaged evolution shown in figure 4.16.

4.4 Natural flow upstream analysis

Figure 4.26 reveals shear-layer vortices develop synchronously from both upper and lower leading edges. However, as they travel downstream, the vortices break down and asymmetry develops. By the time they reach the trailing edge, they have diffused and only random pockets of vorticity remain. At this stage, they are much lower in vorticity and pressure magnitude than the trailing-edge structures, and appear to impact the trailing-edge shedding process little.

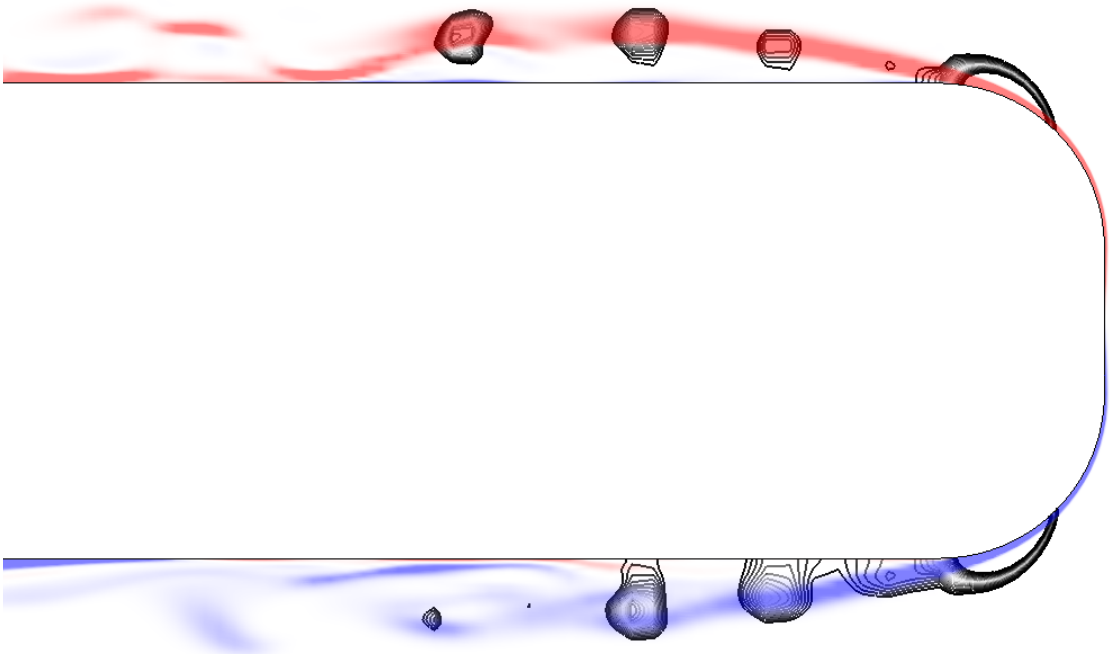

FIGURE 4.26: Leading edge vortices indicated with black contour lines (highlighting areas where pressure is between $C_P = -0.77$ and $C_P = -0.91$), over an instantaneous spanwise vorticity snapshot (blue and red regions indicating $\omega = -1500s^{-1}$ and $\omega = 1500s^{-1}$ respectively).

Visual inspection of the instantaneous pressure and vorticity snapshots of Figure 4.26, reveals shear-layer vortices developing at somewhat regular intervals. Once again, however, the spectra of the velocity monitors placed above and below the body do not show a clear frequency peak (Figure 4.27). The shear-layer instability is clearly present, but difficult to establish with statistics. However, due to the more regular intervals observed here than at the trailing edge, the frequency can be estimated visually. With an average distance of approximately $0.28H \approx 0.02$ m between each structure, and the average shear-layer velocity at approximately $0.5U_\infty \approx 2.5$ m/s, the frequency of this process appears to be approximately 125 Hz or $St = 1.8$. Of course, this is just an

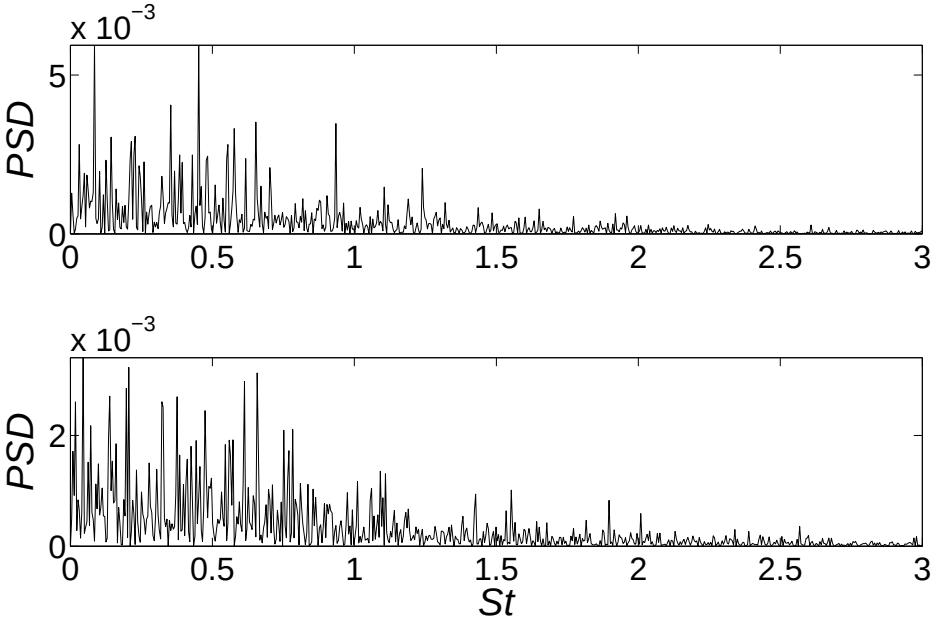

FIGURE 4.27: Velocity spectra of monitor points BU (top) and BL (bottom).

average, and the frequency varies throughout.

Aside from the slight pressure pulse discussed in section 3.1.6, an undesirable effect of the high blockage ratio, the pressure profile at the front remains relatively constant. In other words, the major contribution to the varying component of drag experienced by the body is due to wake activity. Furthermore, in relation to the concept of leading-edge dominated and trailing-edge dominated flows discussed in 1.3.2, this flow can be categorized as a trailing-edge dominated flow. The pressure fluctuations at re-attachment are approximately five times lower than those at the trailing edges, suggesting the leading-edge vortices have little effect on the flow downstream.

4.5 Natural flow downstream circulation analysis

The behaviour of the Kármán vortices as they progress downstream is a further point of interest in the flow. The vorticity and circulation of each vortex, in particular, are key measures which have a direct effect on the base pressure. Comparing the characteristics of downstream vortices for both the natural and actuated cases will provide confirmation of whether or not the actuation technique is achieving its goal.

Vortices were identified using the method described in § 2.9.6, with a Γ_2 threshold value of 0.75. For the natural case, seven span-averaged Kármán vortices were tracked downstream, with their position, total vorticity, area, circulation and estimated speed

recorded. The progression of total vorticity with downstream position varied the least from vortex to vortex, as Figure 4.28 (a), the scatter plot with all measurements, shows. The downstream distance and vorticity of the vortex appear to have a power-curve relationship, with exponent -0.60. Figure 4.28 (b) shows both the speed and downstream location of a typical vortex measured as a function of time. The typical vortex is calculated by averaging the measurements of all seven vortices at each measurement location. As a fresh vortex is created, it begins with a relatively low velocity as it grows in area. However, by the time the vortex reaches $X/H \approx 3$ downstream, its velocity has approached the freestream. This results in each pair of vortices being closer to one another initially, before becoming further spaced apart downstream.

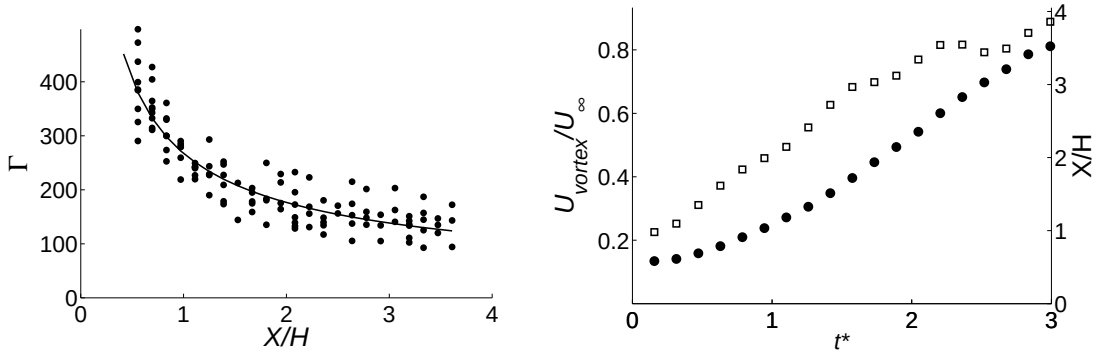

FIGURE 4.28: (a) Scatter plot of total vorticity of each vortex as a function of downstream location. Plot includes all measurements from seven tracked vortices. (b) Time elapsed (non-dimensionalised by the average time between the shedding of each vortex) from initial vortex identification at $X/H = 0.5$ versus vortex velocity (open squares, left axis) and downstream location (closed circles, right axis).

While at inception the area and therefore the circulation (circulation is simply the product of vortex area and vorticity) of each vortex tracked changes little from case to case, further downstream there is more variability. This is apparent in the circulation scatter plot shown in Figure 4.29 (a). However, if the typical vortex is once again plotted, as in Figure 4.29 (b), a clear trend in the progression of vortex circulation and area can be seen. The circulation briefly grows to a maximum value, before reducing slightly and then remaining approximately steady for $X/H > 2$ according to Kelvin's law. The area of the typical vortex, on the other hand, continues to grow until $X/H \approx 3$. These results suggest a strong relationship between the vortex velocity (Figure 4.28b) and area: the vortex increases velocity as it grows in size and, once it reaches maximum size, it is travelling close to the freestream velocity.

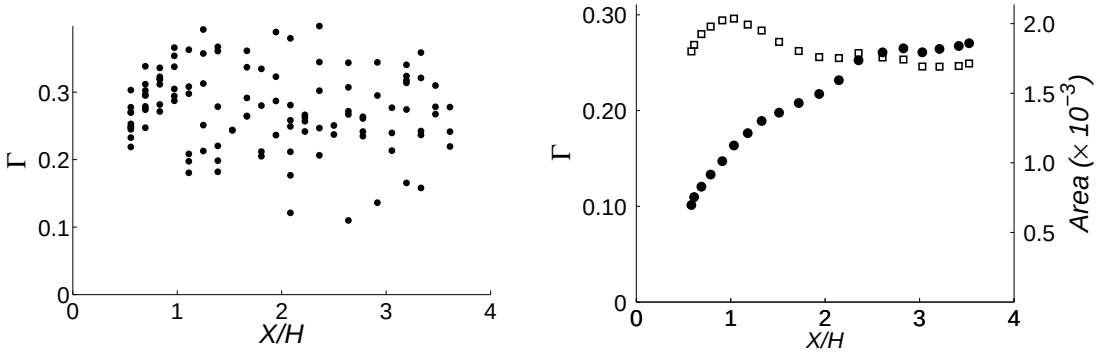

FIGURE 4.29: (a) Scatter plot of circulation of each vortex as a function of downstream location. Plot includes all measurements from seven tracked vortices. (b) Circulation (open squares, left axis) and area (closed circles, right axis) of a typical vortex as a function of downstream location .

4.6 Actuated flow statistics

Periodic actuation was applied from the rear slots after the natural flow had settled into a consistent transient response pattern ($\sim$ 140 non-dimensional time units). The progression of the drag and lift coefficients for $St_{act} = 0.11$ can be seen in Figure 4.30. As found for all actuated cases, settling time is relatively short ($\sim$ 10 time units or less), with the actuation regulating the drag signal almost instantly. However, figure 4.31 reveals the fidelity of the signal differs from case to case. The lowest frequency $St_{act} = 0.04$ drag signal, for example, notably features small perturbations superimposed on the larger amplitude wave (Figure 4.31a). Spectral analysis of this case reveals a weak secondary frequency peak at the Strouhal frequency, indicating two modes may be co-existing in the wake. The next lowest frequency cases shown, $St_{act} = 0.09$ and $St_{act} = 0.11$, also display some semblance of this behaviour. As the actuation frequency is increased, the corresponding drag signal appears to become more periodic.

The lift signal (also displayed on Figure 4.31) also differs from case to case. Perfectly symmetrical shedding would theoretically result in a contribution of zero lift from the wake. It might be expected that the measured RMS lift value follows a similar trend to the mean drag value—and that is precisely the case. At $St_{act} = 0.04$ the signal alternates in a manner similar to the natural case, with a large peak in the power spectrum occurring at $St = 0.22$. As the actuation frequency increases, however, the periodicity of the lift signal appears to break down, before returning when the actuation is close to the natural Strouhal frequency at $St_{act} = 0.22$. At yet higher frequencies, the signal becomes less periodic again, but is not as distorted as observed at the lower

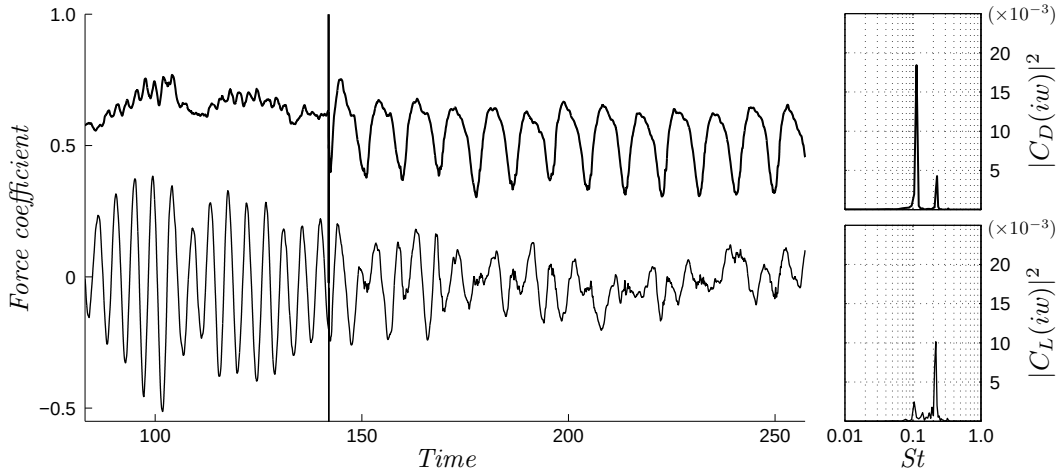

FIGURE 4.30: Time history of drag (upper line) and lift (lower line) signals for $St_{act} = 0.11$. The frequency spectrum for each signal is displayed on the right. The drag spectra amplitude (top) is displayed at the same scale as the lift spectra amplitude (bottom). The drag signal returns a much clearer peak than the lift signal. The discontinuity at $t = 140$ corresponds to the switch from unforced to forced flow.

actuation frequencies.

The power spectra recovered from fast Fourier transforms of the drag and lift signals (Figure 4.32b) quantify this behaviour. The peak response in the drag spectrum occurs at the actuation frequency (we denote this by $P\{D_{act}\}$), while the peak in the lift spectrum occurs very close to the natural Strouhal frequency (this is denoted $P\{L_{nat}\}$). This is expected, as the contribution of actuation to the lift should theoretically be zero, as the actuation is in-phase at upper and lower edges. This also suggests some natural vortex shedding is occurring in conjunction with the synchronous vortices created by actuation (this will be explored more throughout this chapter). A weak secondary frequency, at St_{act}, does appear in the lift signal for some of the lower frequency actuation cases, indicating the pressure fluctuations due to the vortex creation (which are never perfectly synchronous) have a mild feed-forward influence on the pressure of the upper and lower body surfaces. This appears to be a minor effect, however.

As the actuation frequency increases, so does $P\{D_{act}\}$, peaking at $St_{act} = 0.23$. This is consistent with Pastoor *et al.* (2008). However, it appears that this value is not the crucial factor in determining optimal drag reduction: $P\{L_{nat}\}$ closely mirrors the drag reduction (again, also observed by the Pastoor group), and it appears minimising this value is the key. Indeed, $P\{L_{nat}\}$ also correlates strongly with the aforementioned RMS lift signal value, which is indicative of asymmetry in the wake. These lift measurements

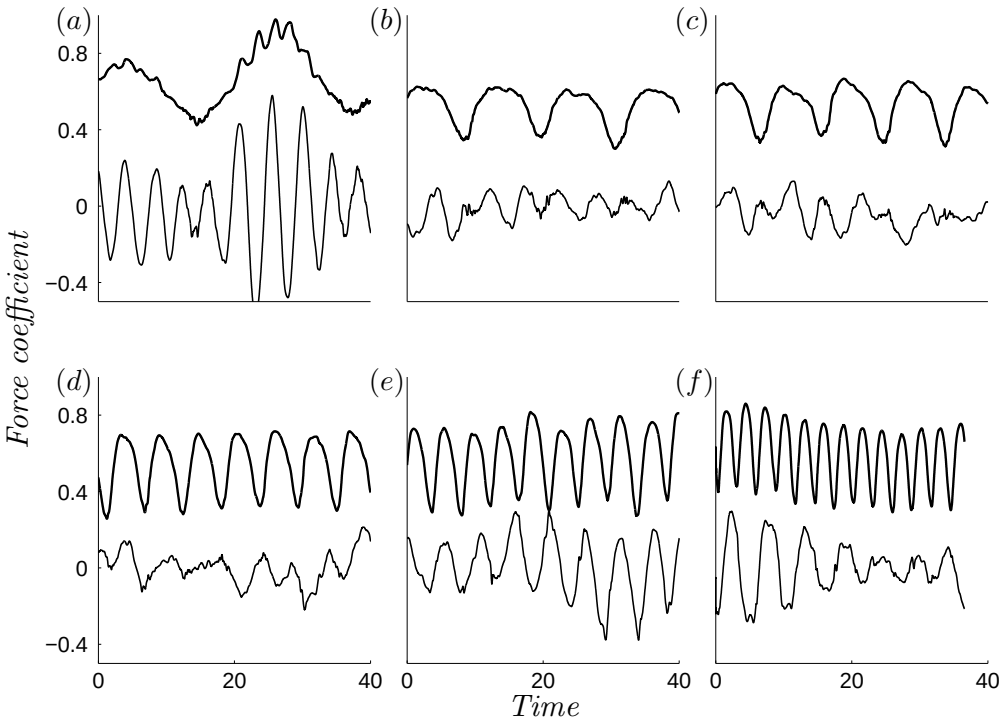

FIGURE 4.31: Sample of drag coefficient (higher, thick line) and lift coefficient (lower, thin line) signals for various actuation signals $u_{act} = Asin(2\pi \frac{St_{act} U_\infty}{H} t)$ where (a) $St_{act} = 0.04$ (b) $St_{act} = 0.09$ (c) $St_{act} = 0.11$ (d) $St_{act} = 0.18$ (e) $St_{act} = 0.23$ (f) $St_{act} = 0.35$.

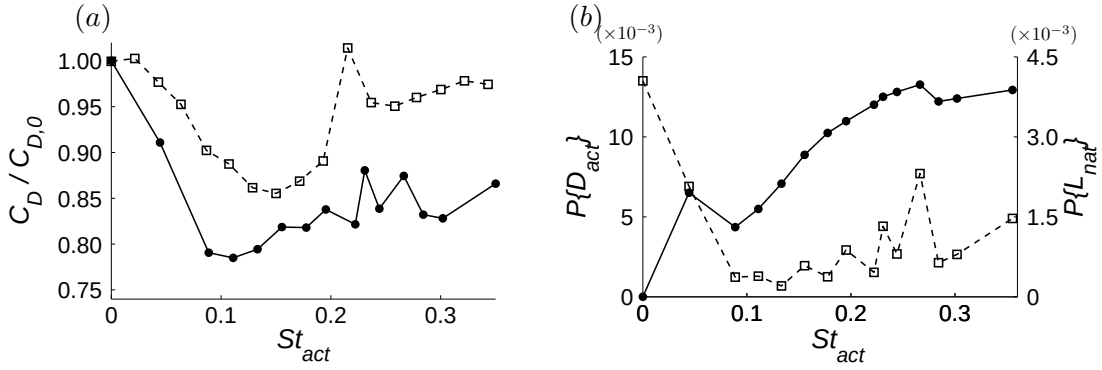

FIGURE 4.32: (a) LES results (filled circles) for mean drag at different actuation frequencies. Minimum drag is obtained at $St_{act} = 0.11$. Experimental results from Pastoor *et al.* (2008) (actuation applied over only half of the span) also shown (open squares). (b) Amplitude of actuation frequency spectral peaks ($P\{D_{act}\}$) for drag signal (closed circles) and Strouhal frequency spectral peaks ($P\{L_{nat}\}$) for lift signal (open squares).

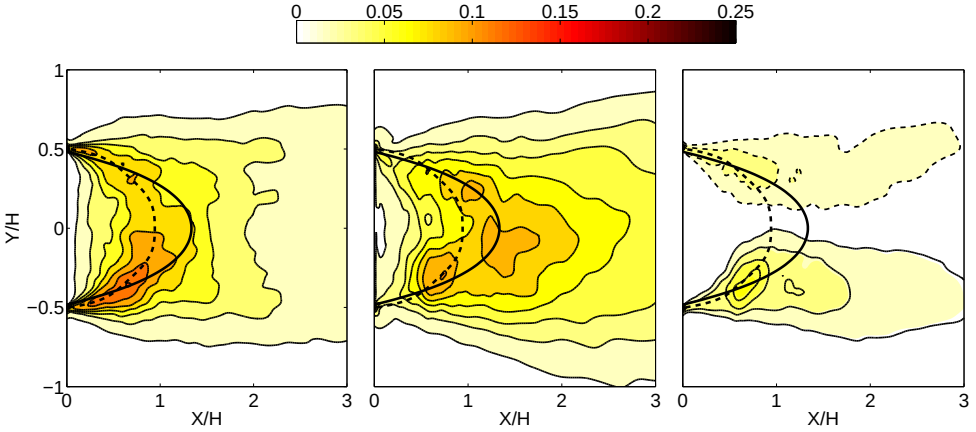

FIGURE 4.33: Reynolds Stress Averages along the centreplane in the wake. From left to right: $\langle u'u' \rangle / U_\infty^2$, $\langle v'v' \rangle / U_\infty^2$, $\langle u'v' \rangle / U_\infty^2$. Dashed contour lines indicate negative magnitudes. Thick line indicates separatrix (mean separation line), dashed thick line indicates the separatrix of unforced case.

make it clear that optimal drag reduction corresponds with reduced asymmetry in the wake.

The final drag reduction results (Figure 4.32a) show there is an optimal actuation frequency range between $St_{act} = 0.09$ and $St_{act} = 0.13$, with the effect slowly decreasing as actuation frequency increases. A maximal drag reduction of 22% occurs at $St_{act} = 0.11$. By comparison, Pastoor *et al.* (2008) found an optimum reduction of 16% at $St_{act} = 0.15$. Again, recall that in the experiments the 7:1 aspect-ratio body extended across the entire working section of the tunnel and hence end effects would not be negligible. In addition, it was only actuated over half the span, thus some difference in the optimal actuation Strouhal number between the simulations and experiments might be expected. A noticeable peak is seen at $St_{act} = 0.23$, where the actuation frequency is close to the natural Strouhal frequency. This peak, not as large as that observed by the Pastoor group, coincides with a moderate strengthening of the natural wake instability, which does not occur for the other cases. At $St_{act} = 0.265$ another peak is observed. The potential cause of these less successful drag reduction cases are discussed in the DMD analysis below (§ 4.8.2).

4.7 Actuated time-averaged flow structure and topology

Analysis of the time-averaged wake reveals the separatrix (marking the mean recirculation bubble) for the optimum case ($St = 0.11$) is noticeably longer than for the unforced case, as shown in Figure 4.33. This longer formation length is due to the suppression of

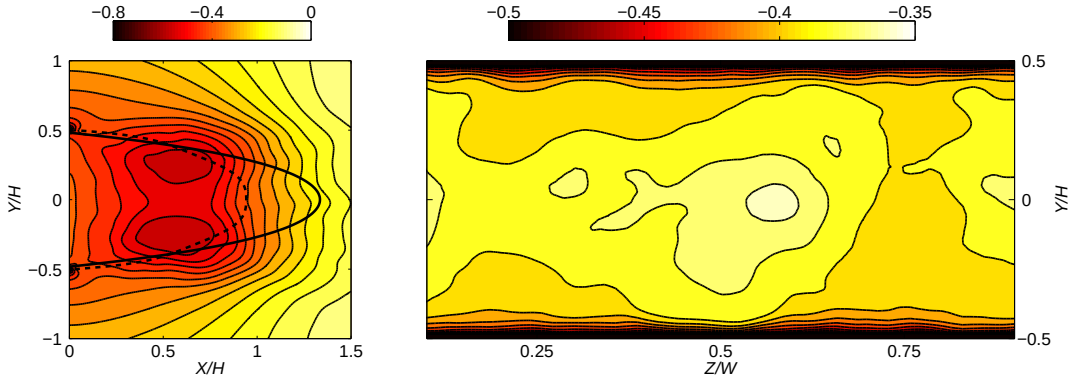

FIGURE 4.34: Time-averaged pressure coefficient along centreplane in wake (left) and on rear base surface over $0.1 < Z/W < 0.9$ (right). Thick line represents the separatrix.

the von Kármán shedding caused by the rear-edge actuation: strong shear-layer perturbation prevents the immediate development of an asymmetric wake. Larger-scale upper and lower shear layer vortices eventually do develop (the vortex roll-up is initiated by the induced velocity of the previously shed vortex pair) and are shed synchronously. Asymmetry eventually returns further downstream. The Reynolds stress contours, also shown in Figure 4.33, reveal a strong reduction in the normal cross-flow stress $\langle v'v' \rangle$. Furthermore, the shear stress $\langle u'v' \rangle$ is much reduced in the near wake. The time-averaged wake pressure is considerably higher than for the natural case. Of further note is the distribution of this pressure—while for the natural case the pressure varies greatly with respect to Y, with a minimum occurring at $Y = 0$—in the actuated case the pressure is relatively uniform over the range $-0.5 < Y/H < 0.5$. This translates to a rear base pressure profile which is uniformly higher over $-0.45 < Y/H < 0.45$. By comparison, the natural case was uniform only over the narrow range $-0.3 < Y/H < 0.3$.

4.8 Actuated dynamic behaviour

While these time-averaged results certainly have use in developing an understanding of the flow, they do not reveal full details of the dynamic mechanisms operating in the wake. The proceeding discussion first analyses the relationship between various signals in the flow, before exploring both the observed transient wake measurements and lower-order representations. Through comparison of Figures 4.12 and 4.35, which show the upper/lower slot pressure signals for the natural and actuated flows respectively, it is immediately clear that vortices are no longer being shed out-of-phase from upper and lower surfaces, but synchronously. Both upper and lower pressure signals almost per-

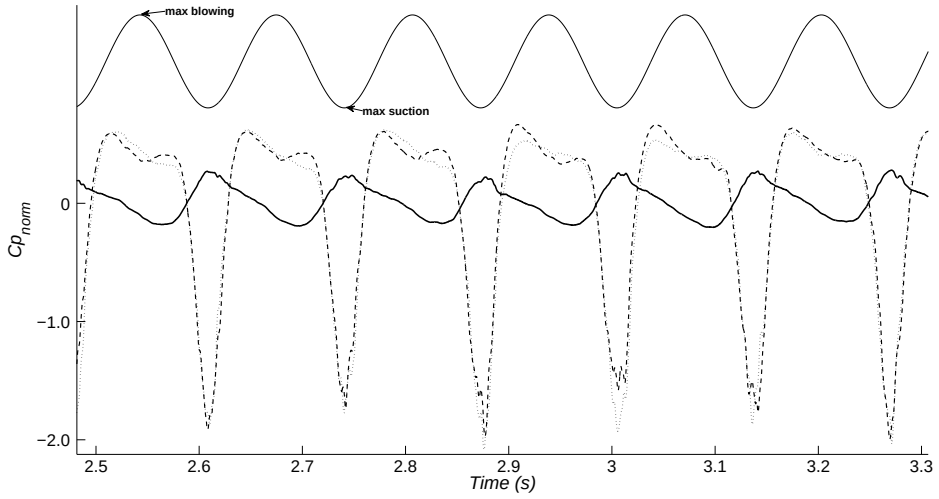

FIGURE 4.35: Normalised pressure coefficient signals measured at the upper slot surface (dashed line), the lower slot surface (dotted line) and the base surface (thick line) for the case $St_{act} = 0.11$. The thin line represents the actuation signal.

fectly overlap, with slight discrepancies only occurring in the peak and trough regions. The pressure on the slots is seen to drop dramatically in unison with an increasing base pressure. This is due to the creation of a new pair of vortices at the slots, which lowers the pressure in these regions, before they have travelled into the wake and influenced the base pressure.

The development of these vortices in the wake is also responsible for the non-sinusoidal nature of the base pressure signal: it rises sharply as the previous vortices convect downstream and the wake dislocates, but falls more gradually as the vortex pair grow and wake vorticity develops. The shed vortices tend to remain in the near wake, until they reach a large enough size to break free from the shear layers and convect downstream. The maximum drag (minimum base pressure) therefore occurs slightly after the point of maximum blowing, while minimum drag occurs very near the point of maximum suction (this can be seen more clearly in Figure 4.36a).

The phase-averaged vorticity progression of a typical actuation cycle, shown in Figure 4.37, elucidates this. The new shear-layer development begins just after the actuation switches from blowing to sucking (between figures 4.37(a) and 4.37c). Meanwhile, the previous vortex pair have detached and begun to interact in the wake. By the time maximal suction has been reached (Figure 4.37c), this cross annihilation has left the wake with considerably reduced vorticity levels, and the new upper and lower shear layers, while still small, begin to be drawn into the wake and roll up into vortices.

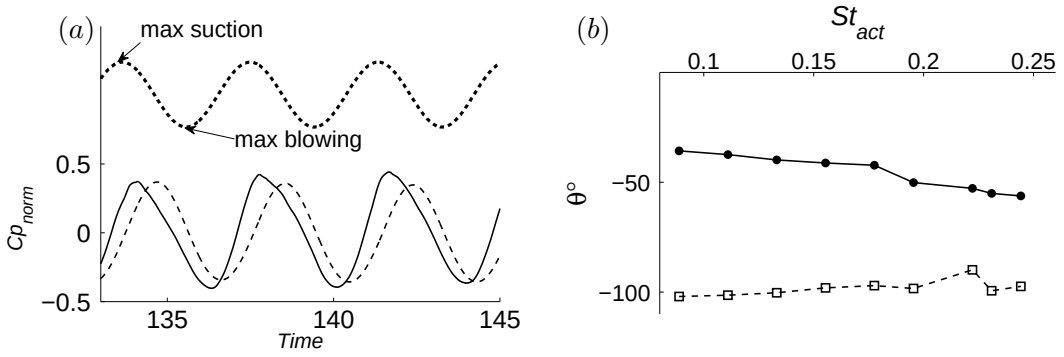

FIGURE 4.36: (a) A comparison of the actuation signal time history (dotted line) with the normalised rear base pressure $C_{pb} - \overline{C_{pb}}$ (solid line) and stagnation pressure response (dashed line) for $St_{act} = 0.23$. (b) The lag in phase between the actuation signal and the rear base pressure (solid line) and stagnation pressure (dashed line) as actuation frequency is varied.

When actuation switches from sucking to blowing (Figure 4.37d), these new vortices have reached a medium size, leading to a steady rise in drag and, once maximal blowing is reached (Figure 4.37b), they have formed large coherent structures, which results in a peak in the drag signal. As the blowing reduces, they travel downstream, with drag decreasing once again, and the process repeats. The large amplitude of the drag signal is due to the combined effect of the vortices both developing together (high drag) and then convecting downstream together *and* destructively interacting with one another (low drag). When compared against the natural progression shown in Figure 4.16, the effect of the actuation is apparent: the vortex shedding is symmetric, extending formation length and raising the pressure in the near wake and lowering drag.

The stagnation pressure at the front of the body interestingly shows strong correlation with the actuation signal. Separation occurs over the leading edge, creating leading-edge vortices that travel downstream before interaction with the trailing-edge vortices. Previous work by Mills *et al.* (2001), Hourigan *et al.* (2001) and Rockwell & Naudascher (1979) (amongst others) has shown that the trailing-edge vortex formations can have a profound feedback effect on the leading-edge vortices. In fact, Mills *et al.* (2001) showed that the rate of leading- and trailing-edge vortex shedding become locked-in together for certain conditions. Here we see a similar effect—the stagnation pressure oscillates significantly at a moderate delay from the rear base pressure, which in turn is slightly delayed from the actuation signal. The small wind tunnel size used by Pastoor *et al.* (2008), and replicated in virtual space here, was found to be amplifying this effect: simulations run at a larger domain size showed a significant drop in the amplitude of the stagnation pressure fluctuation. It remains unclear how large the

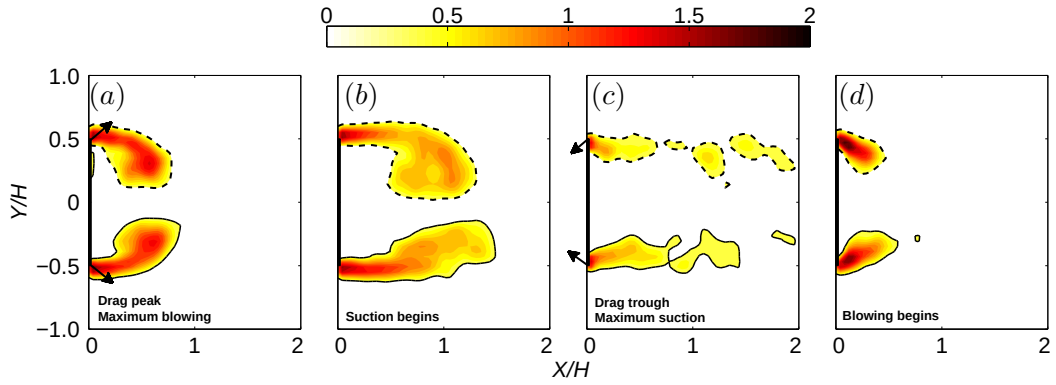

FIGURE 4.37: $St_{act} = 0.11$: Vorticity contours (dashed line indicates clockwise vorticity, solid line indicates anti-clockwise vorticity) of one complete cycle of the phase-averaged flow field. (a) Drag signal peak, (b) Halfway between drag signal peak and trough, (c) Drag signal trough, (d) Halfway between drag signal trough and peak. A rapid decrease in vorticity, presumably due to diffusion and cross-annihilation, is observed once the symmetrically shed vortices interact. Arrow directions are a simplified representation of the actuation at each snapshot (no arrows indicate the actuation is halfway between blowing and sucking or vice-versa). Flow is from left to right.

amplitude would be in an infinitely large domain, although the previously mentioned research by Mills *et al.* (2001) suggests the feedback is expected on some level. This effect does not impact the mean stagnation pressure, meaning its effect on the mean drag measured is negligible (it does, of course, increase the amplitude of the drag fluctuations recorded). Indeed, the drag reduction measured for $St_{act} = 0.135$ at the larger domain size was identical to that measured at the smaller domain size. The stagnation pressure phase difference appears to remain fairly constant for each case at close to a 100° delay. The rear base pressure measurement signal also locks on to the actuation signal for all cases, with a small lag in the phase between the actuation signal and the response gradually increasing with actuation frequency from 35° to 55°, as seen in Figure 4.36(a).

4.8.1 Downstream circulation analysis

The results discussed so far confirm that the lower drag obtained via actuation is due to a reduction of the natural wake instability, the theory of which is discussed by Pastoor *et al.* (2008) and summarised here in the caption of Figure 1.17 (§ 1.5.1). However, the circulation of the vortices created by actuation has not been measured or calculated in any previous work. The theory suggests that circulation in the actuated wake should be lower due to the symmetric shedding and corresponding cross-annihilation of vorticity.

To investigate this the progression of seven vortices were tracked downstream for the optimum case $St_{act} = 0.11$, and compared with the natural results presented in § 4.5. Figure 4.38 (a), the scatter plot with all measurements, shows the vorticity of the vortices decays in a similar manner to the natural case. However, the initial circulation of the vortices appears to be altogether lower for the actuated case, leading to a shallow line-of-best (the exponent is -0.52 compared to -0.60 for the natural case). Figure 4.28 (b) shows the velocity of a typical vortex in the actuated case is slightly lower initially, before rapidly approaching the freestream velocity at $X/H \approx 2$.

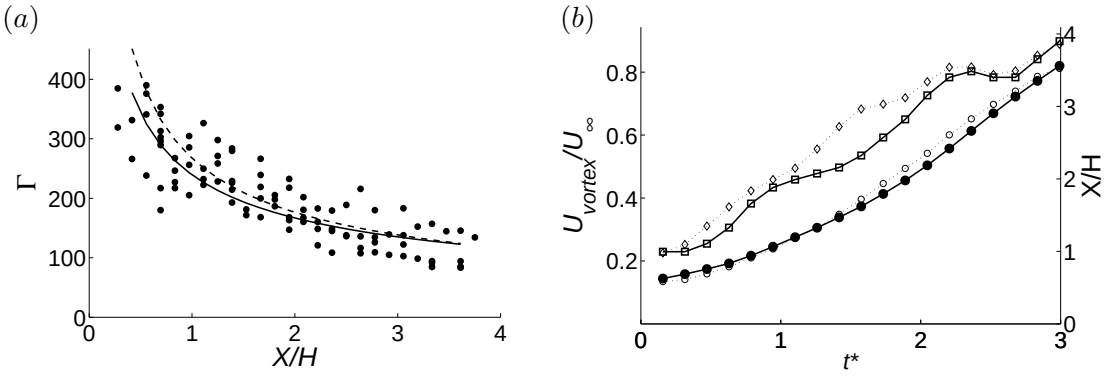

FIGURE 4.38: (a) Scatter plot of total vorticity of each vortex as a function of downstream location. Plot includes all measurements from seven tracked vortices. Thick solid line indicates the line of best fit $239 \cdot (X/H)^{-0.52}$, dashed line indicates line of best fit for natural case $267 \cdot (X/H)^{-0.60}$. (b) Time elapsed (non-dimensionalised by the average time between the shedding of each vortex) from initial vortex identification at $X/H = 0.5$ versus non-dimensional vortex velocity U_{vortex}/U_∞ and downstream location X/H. The open diamonds (dotted line) and open squares (thick line) represent vortex velocity for natural and actuated flow respectively, while the open circles (dotted line) and closed circles (thick line) represent downstream location of the vortex for natural flow and actuated flow respectively.

The circulation measurements, plotted against downstream location in Figure 4.39, reveal further information. The vortices in the actuated case appear to begin their downstream journey with a near identical area to the natural case vortices. However, the vorticity contained within is lower, which results in a lower circulation. At $X/H \approx 1$, the rate of growth of the actuated vortices decreases. In fact, the area of the vortices appears to remain constant at $1 < X/H < 1.5$, before continuing to grow until reaching sizes observed in the natural case at $X/H \approx 3$. This passive vortex growth at $X/H \approx 1$ is perhaps a function of the two synchronous vortices coming together in the near wake and restricting each others space. The lower initial circulation of the vortices persists downstream, and in fact decreases further as the vortices are often observed to break up into multiple smaller vortices, lowering the average circulation calculated by the algorithm used (described in § 2.9.6).

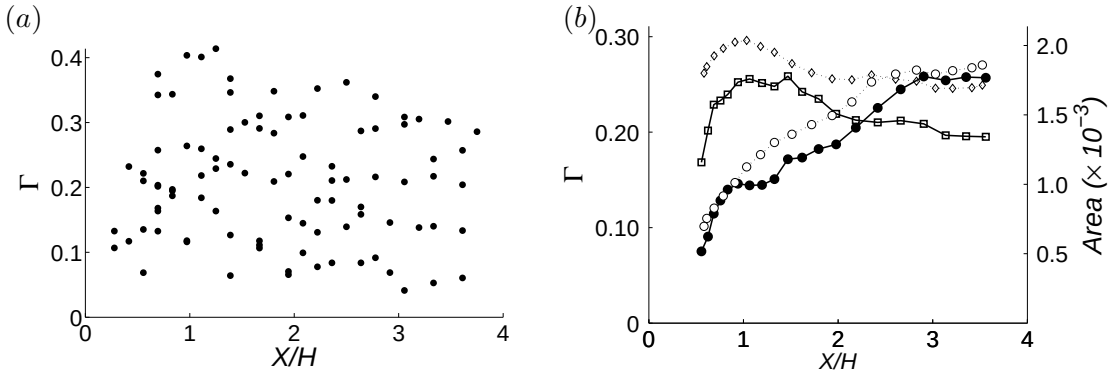

FIGURE 4.39: (a) Scatter plot of circulation of each vortex as a function of downstream location. Plot includes all measurements from seven tracked vortices. The measurements are substantially more varied than those obtained for the natural case. (b) Circulation (left axis) and area (right axis) of a typical vortex as a function of downstream location. The diamonds (dotted line) and squares (thick line) represent vortex circulation for natural and actuated flow respectively, while the open circles (dotted line) and closed circles (thick line) represent vortex area of the vortex for natural flow and actuated flow respectively.

These results conclusively show that the circulation of vortices in the wake is substantially lower for flow under actuation. The weakened natural instability results in a lower average circulation of vortices at all points in the wake, increasing pressure in the wake and reducing drag.

4.8.2 Dynamic Mode Decomposition

Dynamic Mode Decomposition of the spanwise-averaged velocity fields reveal the presence of a new mode in the flow due to actuation (mode A) that is not observed for the natural case. This mode appears to co-exist with mode N of the natural case (the mean mode M is effectively equivalent to that of the natural case). Vorticity contours of mode A (Figure 4.42) show a symmetric structure about $Y = 0$, with two pairs of opposite-signed vortices created and shed per cycle (while the opposite-signed vortices at first glance appear to form an anti-symmetric structure, if we reflect the positive direction of vorticity across $Y = 0$, we can describe the mode as symmetric). Each vortex in this mode first develops on the inside of the shear layer, with the previous vortex of opposite sign still attached in the shear-layer region. Once the previous vortex breaks from the shear layer, the new vortex then grows in this area. When mode A is superimposed on the non-dynamic mode M, each pair of mode A vortices alternately either adds to the mean mode vorticity of each shear layer (creating a large pair of synchronous vortices), or subtracts from it (leaving an "empty" wake), resulting in a significant change in near-wake pressure throughout the cycle. Perfectly symmetric

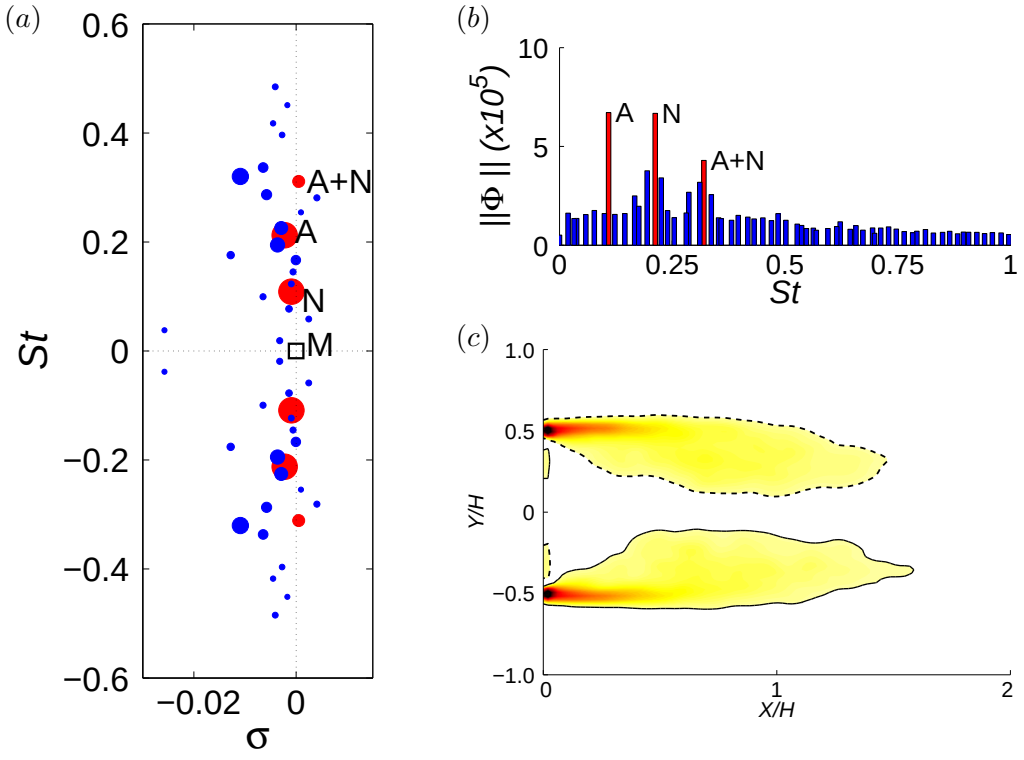

FIGURE 4.40: Dynamic mode decomposition for $St_{act} = 0.11$: (a) spectrum showing the growth rate (σ) of each mode. The red dots are the most relevant modes, with the size of each dot showing its relative magnitude. The mean mode (M) is indicated with an open square. Mode N occurs at the natural Strouhal number and mode $A + N$ at the sum of frequencies N and A; (b) The relative magnitude of each mode is plotted against frequency (top right); and (c) vorticity contours for the mean mode (bottom right).

shedding would be achievable if it were just this dynamic mode in the wake. However, as mentioned above, the symmetric mode N of the natural case is also present. For most cases, this mode operates at a different frequency to mode A, and thus will impact the symmetric shedding process in different ways from case to case, and cycle to cycle. The interplay of these modes—the actuation and natural modes—appears to be a dominant mechanism in the flow. Indeed, for each case a reconstruction using only these modes recovers the majority of features seen in the observed phase-averaged flow (Figures 4.37 and 4.42 show this for the optimal case of $St_{act} = 0.11$).

Figure 4.44, which shows the Ritz values for the low frequency actuation cases, exhibits the large effect that actuation frequency has on the magnitudes and growth rates of the modes in the wake. For $St_{act} = 0.04$, where the drag signal has been shown to not lock-in completely to the actuation signal, mode A is relatively weak. Mode N, meanwhile, is the strongest of any actuation case, although it's magnitude has been

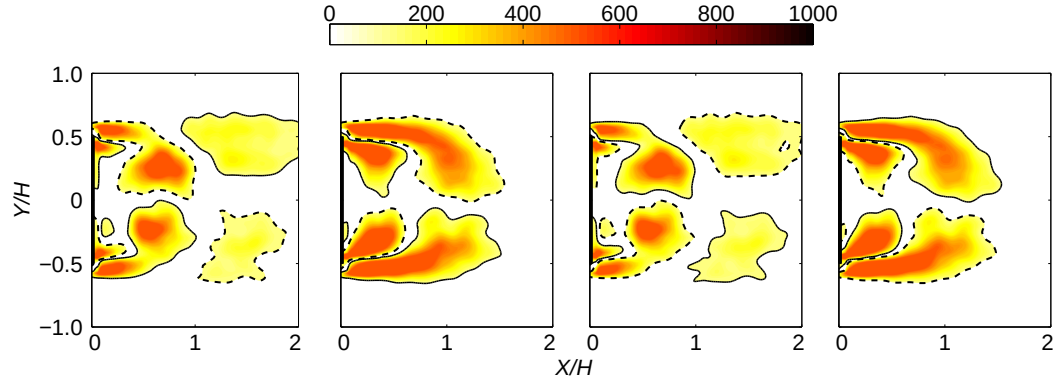

FIGURE 4.41: $St_{act} = 0.11$: Vorticity contours of one complete cycle of first unsteady Koopman mode (mode A).

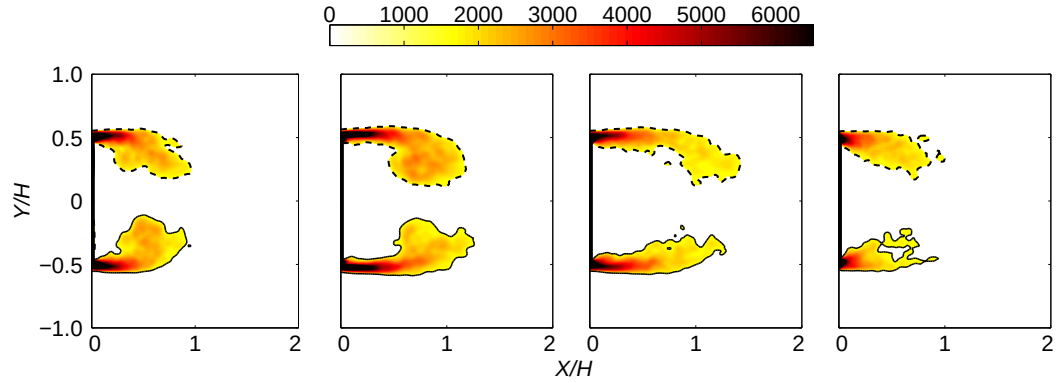

FIGURE 4.42: $St_{act} = 0.11$: Reconstruction of the vorticity evolution over one complete cycle using the Koopman mean mode and the first two unsteady Koopman modes (modes A and N).

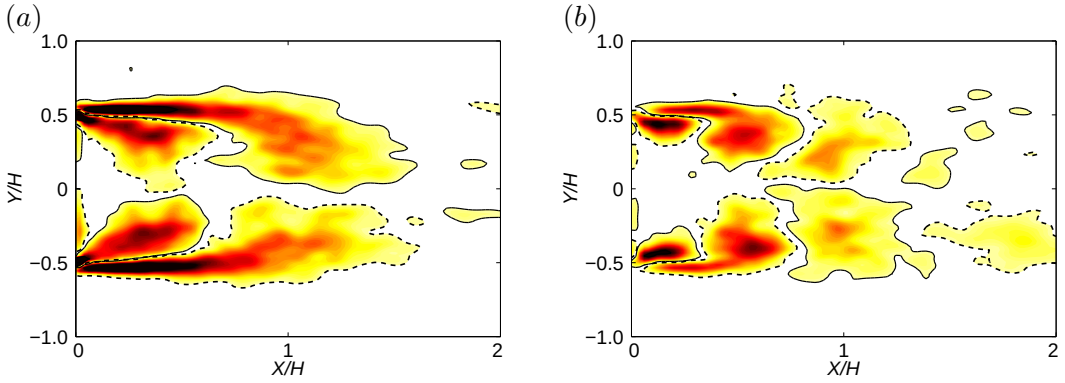

FIGURE 4.43: Vorticity contours of actuation mode for $St_{act} = 0.11$ (left) and $St_{act} = 0.35$ (right). The size of the mode A vortices is significantly less for the higher frequency actuation case.

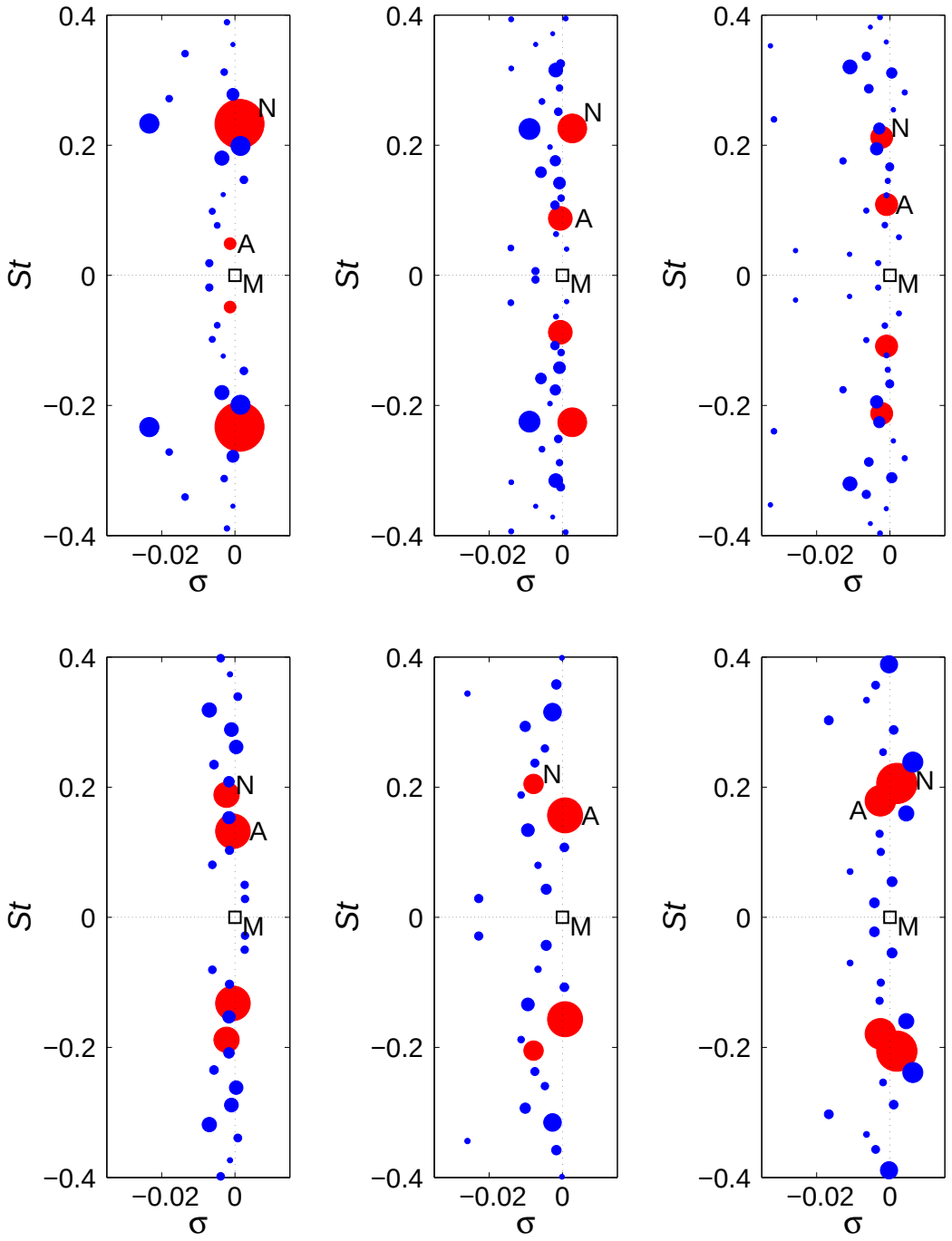

FIGURE 4.44: Dynamic Mode Decomposition spectra for low frequency actuation cases. From left top to bottom right: $St_{act} = 0.04$, $St_{act} = 0.09$, $St_{act} = 0.11$, $St_{act} = 0.135$, $St_{act} = 0.155$ and $St_{act} = 0.175$ showing the growth rate (σ) of each mode. Red dots are the dominant modes, with the diameter of dot showing its relative magnitude. The mean mode (M) is indicated with an open square. Mode A represents the symmetric shedding actuation mode, while mode N represents the natural mode.

reduced by around 25% from the natural case. An additional mode of moderate size appears at the exact same frequency of mode N, but has a large negative growth rate.

This mode shows the same structure of mode N, but with opposite-signed vorticity and in a far less coherent form. The negative growth rate suggests this mode is not permanent: indeed, a series of DMD using multiple temporal ranges confirm the magnitude of this mode is usually negligible. The same is true for the other cases: those modes in Figures 4.44 and 4.45 which appear to have a high magnitude, but also a large negative growth rate, can be discounted.

For the next three frequencies, which all produce low drag, the magnitude of mode N reduces. At $St_{act} = 0.09$ mode A has a larger magnitude, while there is a noticeable band of smaller modes between mode N and mode A. These modes become yet smaller for $St_{act} = 0.11$. At $St_{act} = 0.135$, there is not much room between modes N and A, and only one mode appears between them. The presence and distribution of these smaller modes appears to be inconsequential to the drag reduction result – rather, it is the magnitude of modes A and N that are the main values of interest.

As the actuation frequency approaches the Strouhal frequency, the magnitude of A reaches its largest magnitude, while the magnitude of N becomes less predictable. At $St_{act} = 0.23$ and $St_{act} = 0.266$, the drag deviates from the trend and rises moderately. It was initially thought that the local peak that occurs in this frequency range is due to an excitation of mode N due to actuation being near the Strouhal frequency. However, at $St_{act} = 0.244$, no such excitation of mode N occurs. Furthermore, the mode N frequency under actuation has been shown to be lower than the natural Strouhal frequency, suggesting the original conjecture is perhaps not true.

However, while the presence of mode A appears to fluctuate little with time, the same cannot be said of mode N. Over certain intervals the mode N structure appears close the non-actuation case, while over others it loses coherency. Moreover, the frequency of the mode St_N, fluctuates from case to case; it remains close to the natural value $St = 0.22$ for the low frequency actuation cases but drops to $St = 0.195 \pm 0.015$ for all cases $St_{act} \geq 0.133$. Despite this meandering nature, measuring the magnitude of the mode, $||\Phi_N|| = \Sigma|K_N|$ (the sum of the Koopman eigenvector magnitudes at each point in the wake), for each case does provide some insight, as shown on Figure 4.46.

In the higher frequency range, it appears that $||\Phi_N||$ shows a strong correlation with C_D; the two drag peaks $St_{act} = 0.23$ and $St_{act} = 0.265$ feature substantially higher mode N magnitudes. The natural mode seems to be more excitable in this regime, and whether or not it is excited may be a random phenomenon, more likely

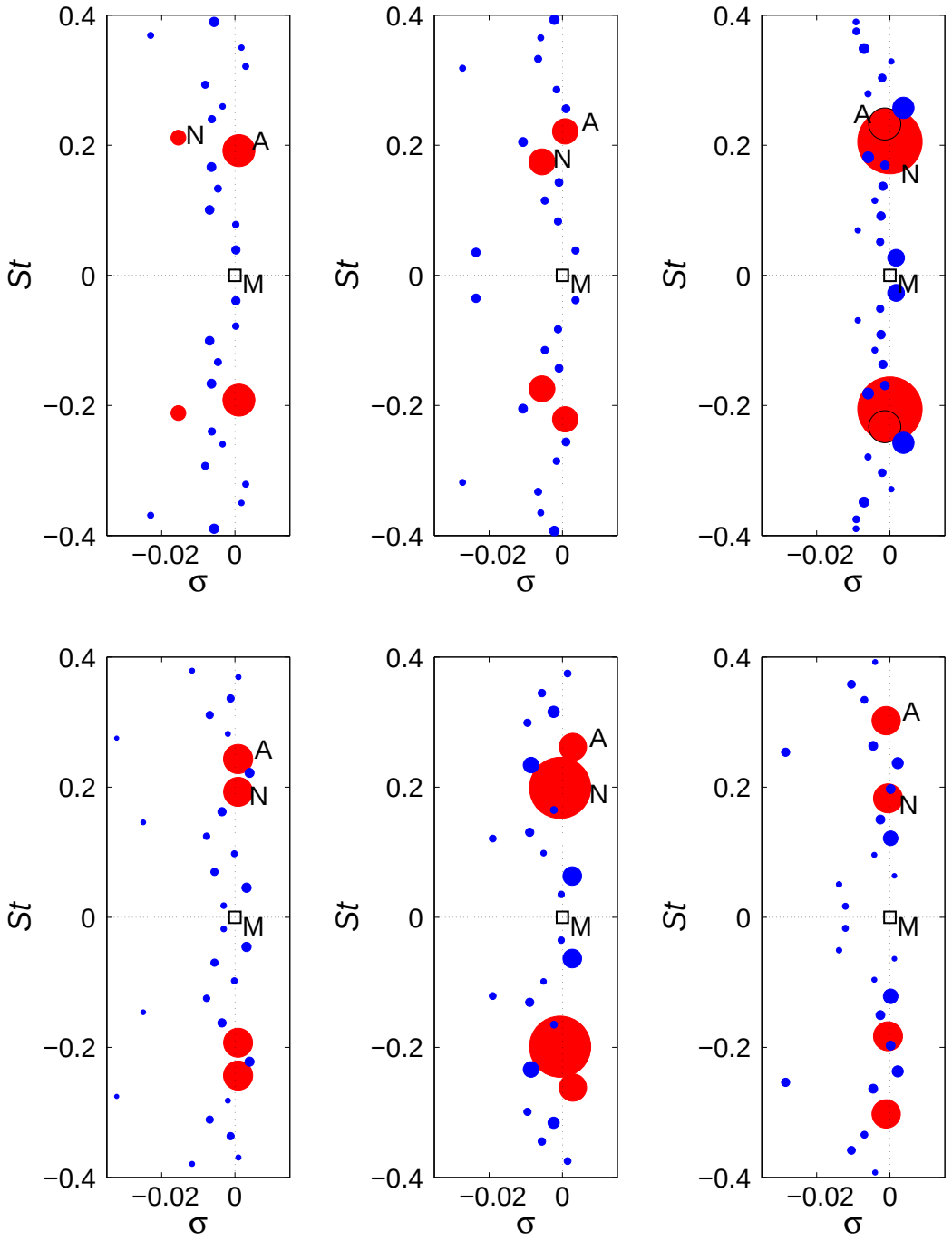

FIGURE 4.45: Dynamic Mode Decomposition spectra for cases with the actuation approaching Strouhal frequency and higher. From left top to bottom right: $St_{act} = 0.195$, $St_{act} = 0.222$, $St_{act} = 0.231$, $St_{act} = 0.244$, $St_{act} = 0.266$ and $St_{act} = 0.302$ showing the growth rate (σ) of each mode. Red dots are the dominant modes, with size of dot showing its relative magnitude. The mean mode (M) is indicated with an open square. Mode A represents the symmetric shedding actuation mode, while mode N represents the natural mode.

to occur with actuation near the original natural frequency. In the lower frequency range, however, the correlation is somewhat less strong, with one of the optimal drag

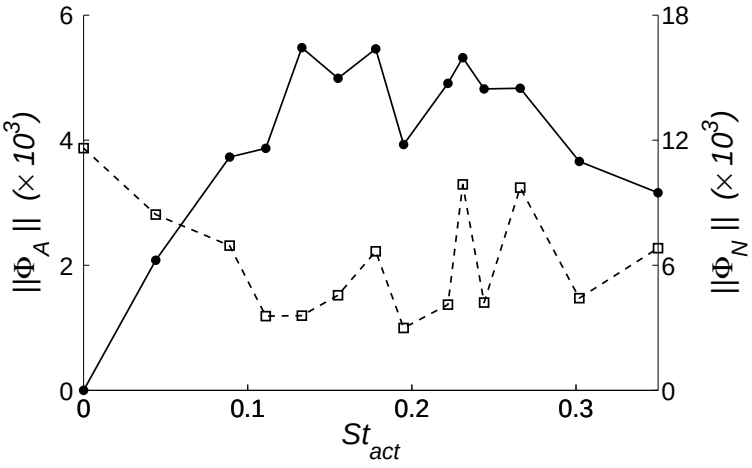

FIGURE 4.46: Magnitudes of Koopman modes A (left axis, closed dots, continuous line) and N (right axis, open squares, dashed line) for each actuation frequency St_{act}.

reduction cases, $St_{act} = 0.09$, still featuring a relatively high mode N magnitude.

The magnitude of mode A, $||\Phi_A||$, also does not appear to be an indicator of drag reduction success: it is seen to be highest both slightly above and below the mode N frequency $St_N \approx 0.195$, yet is relatively lower for two of the optimal drag reduction cases $St_{act} = 0.09$ and $St_{act} = 0.11$. At $St_{act} = 0.195$ the magnitude of both modes A and N drop, suggesting that when the actuation frequency is close to the expected $St_N \approx 0.195$, the two modes are less successful at co-existing. Yet, even for this case, no significant change occurs in drag reduction. It is clear that there is more to achieving optimal drag reduction than simply creating a prevalent symmetric mode A and weakening mode N. But what other mechanism could be responsible?

It appears at least a partial answer lies in the changing characteristics of the mode A vortices at different actuation frequencies, and their superposition with mode N in the near wake. Figure 4.43, which shows a snapshot of mode A for a lower frequency case ($St_{act} = 0.11$) and a higher frequency case ($St_{act} = 0.35$), makes this difference clear—high frequency actuation creates mode A vortices smaller than those created with low actuation frequencies. While both cases appear to generate vortices with a similar *peak* vorticity, the larger area of the lower frequency vortices results in a greater total circulation per vortex, which, of course, is connected to the different times that the shear layer vorticity feeds into the wake vortices.

Furthermore, as shown in Figure 4.47(a), the centres of the low frequency vortices are observed to approach the wake centreline much more closely than the higher frequency vortices. This proximity to the centreline, coupled with their larger area and

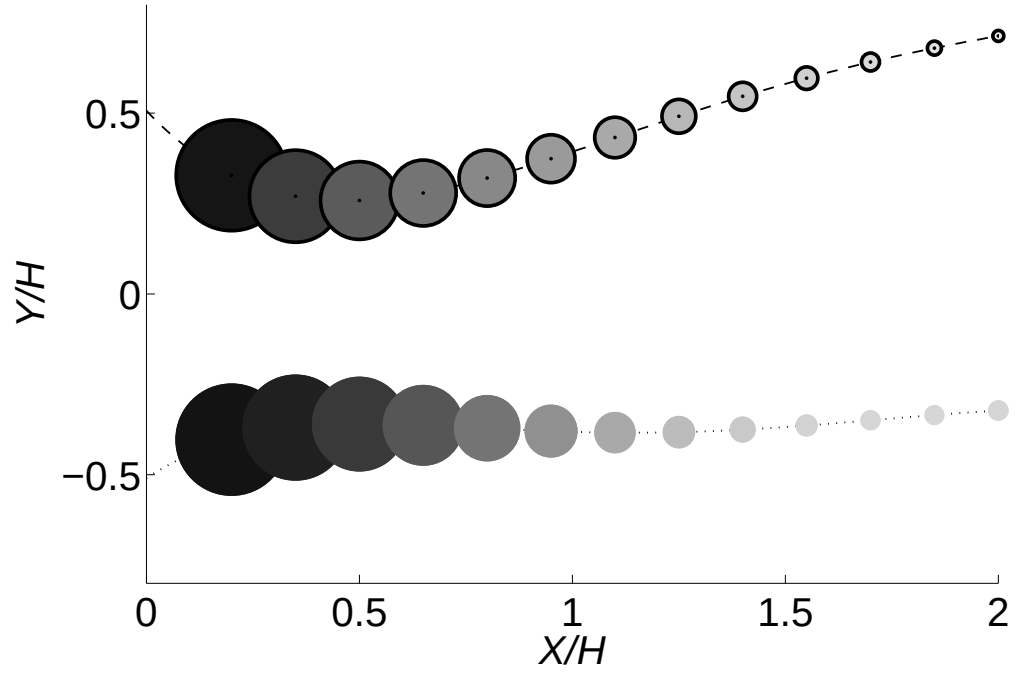

FIGURE 4.47: Comparison of a typical mode A vortex path for cases $St_{act} = 0.09$ (upper circles with thick edges) and $St_{act} = 0.35$ (lower circles with no edges). The size and shading of each circle represents the average vorticity of the vortex (circulation per unit area).

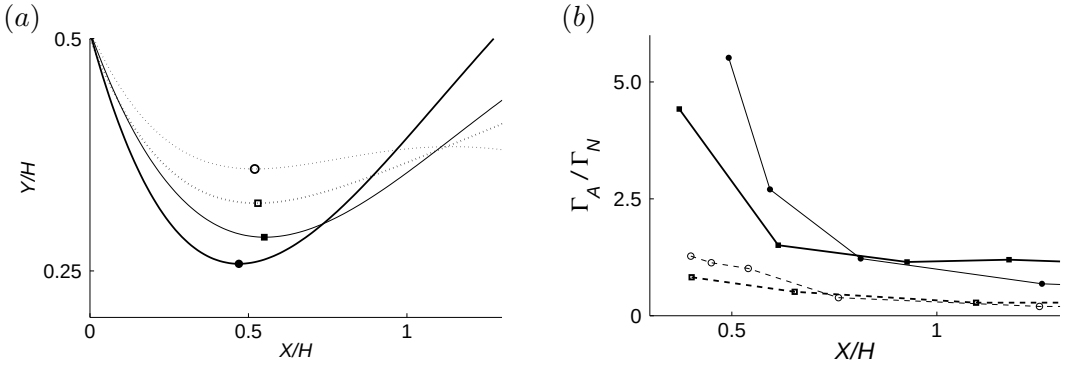

FIGURE 4.48: (a) The near-wake path of a typical mode A vortex for four cases for $St_{act} = 0.09$ (thick solid line), $St_{act} = 0.13$ (thin solid line), $St_{act} = 0.27$ (thick dotted line), and $St_{act} = 0.35$ (thin dotted line). (b) The ratio of mode A vorticity to mode N vorticity as a function of downstream location. Line styles represent same cases as (a).

circulation allow the low frequency mode A vortices to diminish the impact of the coexisting mode N vortices which become prevalent on the centreline of the wake at $X/H \approx 0.6$ and further downstream. At higher frequencies, the smaller circulation of the mode A vortices and greater distance from the centreline weakens their influence on the final wake once the modes are superimposed. This was checked by calculating the

vorticity of numerous mode A and N vortices for each case, and comparing the ratio Γ_A to Γ_N as a function of downstream location. The circulation values were obtained by using the Γ_2 approach, outlined in Graftieaux *et al.* (2001), to identify the vortex and finding the integral of the spanwise vorticity over the area enclosed by the identified contour. Figure 4.47(c) shows a significant drop in the influence of mode N in the near wake for the lower frequency cases. This results in a higher near-wake pressure and lower drag.

4.8.3 Wavelet analysis

Wavelet visualisation was also conducted on the actuated drag and lift signals. While it does not offer any additional insights to the flow, it does provide an alternative way to visualise the effect of actuation. For example, consider Figures 4.49 (a) and (b), which show the wavelet analysis for $St_{act} = 0.04$ and $St_{act} = 0.11$ respectively. The former, which is less successful at achieving drag reduction, shows the drag signal is locked-on to the actuation frequency is at all times, but the Strouhal frequency in the lift signal is barely impacted. Moreover, unwanted higher frequencies appear in the drag signal at irregular intervals. The latter case, the most successful at drag reduction, shows a less predictable presence of the Strouhal frequency in the lift signal, while the actuation frequency strongly regulates the drag signal, with its harmonic $St = 0.22$ the only other frequency observed. Wavelet analysis for all the cases is located in Appendix B.

Once the mechanisms in the flow are understood, this method of visualisation offers an efficient way to compare cases – especially when the frequency is held constant and other variables are altered, such as the momentum coefficient or actuation configuration. These are covered in the next chapter.

4.9 Summary

This chapter has provided new details and perspectives into the wake dynamics of both natural and open-loop periodically controlled flow behind D-shaped bluff bodies. These new insights are possible due to the numerical approach undertaken, allowing for such data processing techniques as dynamic mode decomposition (DMD). DMD has revealed a dominant mode N exists in the natural flow, confirming the Kármán wake mode as the primary wake mechanism, which leads to regions of high circulation in the wake and a low base pressure.

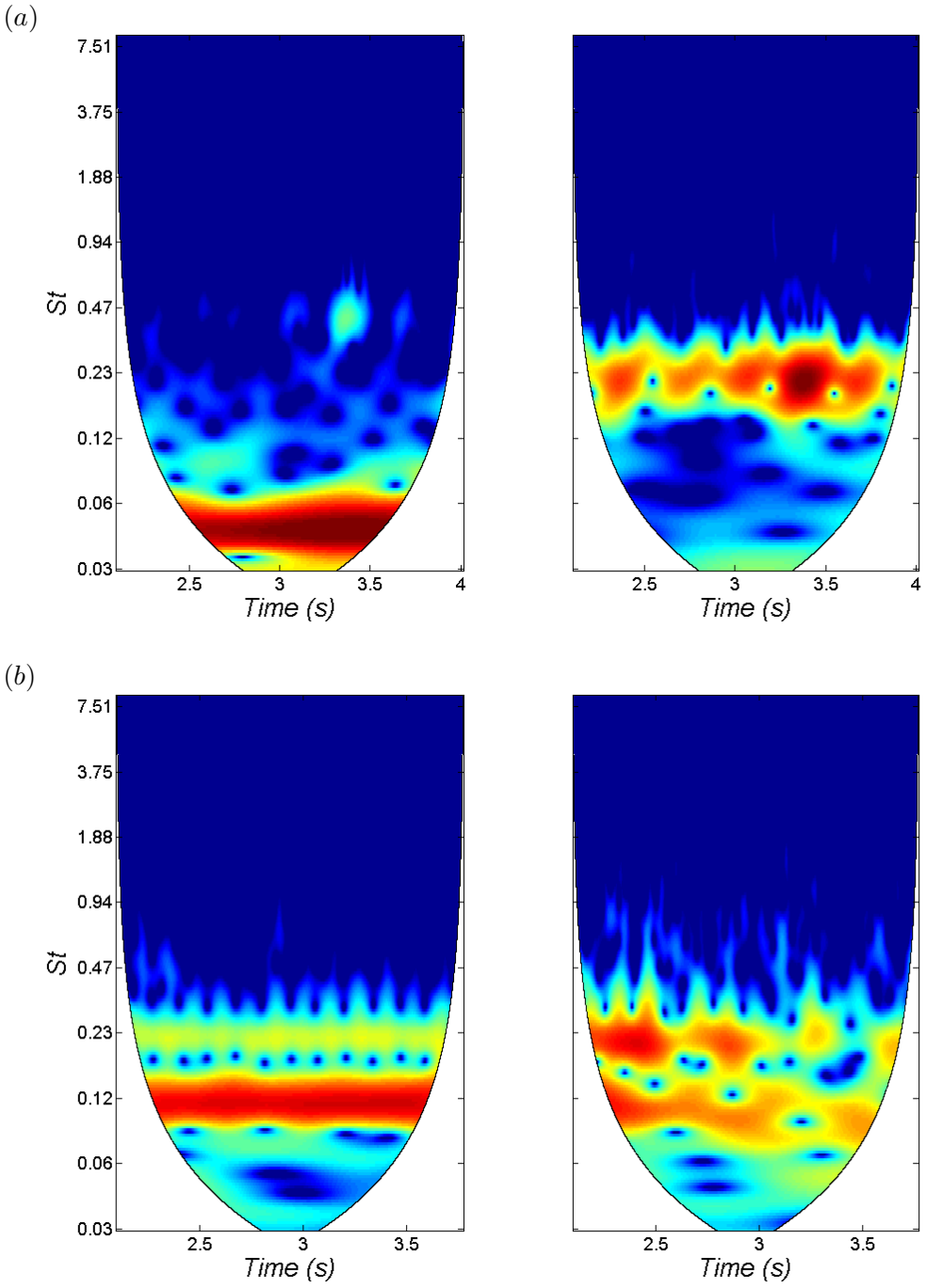

FIGURE 4.49: Wavelet analysis on the drag (left) and lift (right) signals for (a) $St_{act} = 0.04$ and (b) $St_{act} = 0.11$.

One focus has been on the actuation frequency, with an optimum actuation frequency of $St_{act} = 0.11$ found, slightly lower than the $St_{act} = 0.15$ found experimentally for a similar set up by Pastoor *et al.* (2008). Note, however, that the predicted drag reduction at $St_{act} = 0.15$ is only about 2% less. Increased symmetry of vortex shedding,

which leads to a longer formation length and increased cross-annihilation in the near wake, has been observed for all cases of actuation.

Dynamic mode decomposition reveals the actuation produces an additional wake mode, mode A, characterised by synchronous vortex shedding, which co-exists with, rather than displacing, mode N. Actuation frequencies in the range $St_{act} = 0.09$–0.135 allow the actuation mode to remain coherent and successfully co-exist with the natural mode. However, creating successful synchronous shedding is not the only requirement to achieve optimal results: if the shedding is generated at a high frequency, the smaller vortices are not able to dominate the mode N vortices as effectively, resulting in lower drag reduction. Thus, lower frequencies are more effective. Too low a frequency (for example, at $St_{act} = 0.04$), however, and the persistence of the natural flow fluctuations do not allow mode A to properly develop.

New information on the upstream effect of actuation has also been found, with the stagnation pressure shown to oscillate at the actuation frequency with a lag of approximately 100° for all cases. It has been shown that the strength of this effect is likely amplified by the relatively high blockage ratio.

The next chapter explores the effect of other actuation variables, namely the momentum coefficient and actuation orientation.

Chapter 5

Effect of other actuation variables

5.1 Momentum coefficient

In the preceding chapter, the actuation frequency has been shown to significantly affect the drag reduction obtainable behind a bluff body. However, the amplitude of the actuation fluctuations is also clearly an influential parameter. To explore this, tests were run with the actuation frequency held constant and the amplitude of the actuation signal incremented through $A = 0.66, 1.31, 1.90, 2.62$ and 3.70. These values represent the maximal blowing and sucking velocity, in metres per second, produced by the actuators during each sinusoidal cycle. They can also be expressed in terms of momentum coefficient (equation 2.1), giving values of $C_\mu = 5 \times 10^{-4}, 2 \times 10^{-3}, 4 \times 10^{-3}, 8 \times 10^{-3}$ and 1.6×10^{-2}.

This was carried out for both the optimal actuation frequency, $St_{act} = 0.11$, and a higher frequency, $St_{act} = 0.30$. The results are shown in Figure 5.1.

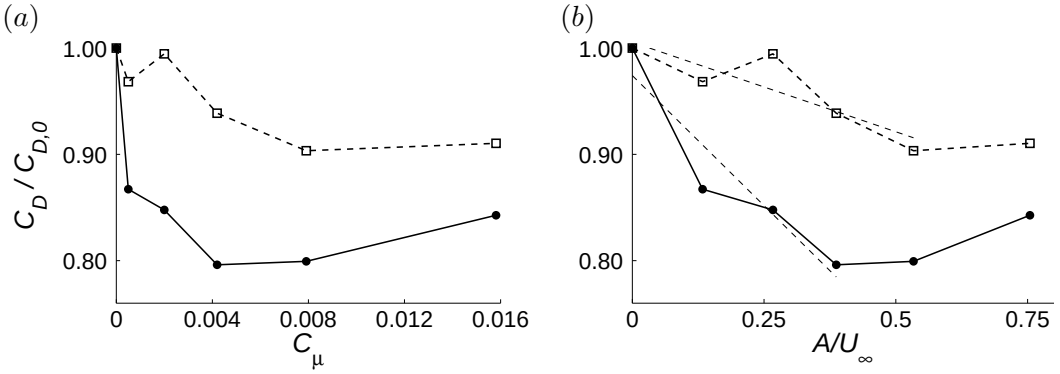

FIGURE 5.1: Effect of actuation strength on drag for $St_{act} = 0.11$ (thick solid lines, filled circles) and $St_{act} = 0.30$ (thin solid lines, open square). Two measures of actuation strength imposed are shown: (a) the momentum coefficient, C_μ, and (b) the maximal blowing and sucking velocity normalised by freestream velocity, A/U_∞ (the thin dashed lines show a line of best fit through the points up to and including the threshold value).

It can be seen from the Figure that once a certain threshold actuation level is reached, no further gains can be expected. The threshold value is also not consistent across frequencies of actuation, as it appears to be around $C_\mu = 4 \times 10^{-3}$ for $St_{act} = 0.11$, but $C_\mu = 8 \times 10^{-3}$ for $St_{act} = 0.30$. This suggests that the optimal actuation frequencies require less energy input to achieve their maximum drag reduction. In fact, for the optimum actuation case a very small momentum coefficient of 5×10^{-4} is able to achieve over 10% drag reduction. When the drag is plotted against the actuator output velocity A/U_∞, a more linear relationship is observed before the threshold value is reached, suggesting the actuator velocity input may be a more appropriate measure of the actuation strength than the actuator energy input. This makes intuitive sense, as the shear layer instability is convective, and receptive to all sizes of velocity perturbations. Thus, while methods which directly target the absolute instability in the near wake require some over/under threshold amount of momentum input, here the effect of instability suppression will be tied in some way to the magnitude of the velocity perturbations. Due to the presence of both an absolute and convective instability in the wake, it is likely that a combination of both the velocity perturbation amplitude and momentum input contribute to the response of the system.

In comparison, Pastoor *et al.* (2008) found a threshold value of 8×10^{-3} at $St_{act} = 0.15$, their optimum frequency. However, their actuation was applied over only half the spanwise width of the trailing edge—effectively halving the true momentum they were injecting to the flow. Thus, the threshold value of 4×10^{-3} obtained here for the optimum frequency $St_{act} = 0.11$ appears to be consistent with their result. However, it should also be remembered that our results suggest each actuation frequency has its own threshold value and response to momentum coefficient, meaning such single frequency comparisons may not be the complete "story".

Pastoor *et al.* (2008) also found a minimum threshold value $C_\mu \simeq 5 \times 10^{-3}$ (which becomes $2 \times 10^{-3}5$ if we correct it as above), below which minimal drag reduction is achieved. This matches well with the $St_{act} = 0.30$ case that showed negligible drag reduction at $C_\mu \simeq 2 \times 10^{-3}$. However, it is clearly at odds with our finding that at $St_{act} = 0.11$ a quite reasonable drag reduction can be achieved with momentum coefficients below 1×10^{-3}. Once again, this difference highlights the unique response of each actuation frequency to momentum coefficient. One possible explanation could be the difference in fidelity of the applied actuation signals. In this numerical work

the signal is perfectly sinusoidal, even at lower amplitudes. In experiments, however, low amplitude noise tends to make the achieving of clean, low amplitude sinusoidal signals especially difficult, while high amplitude signals are able to mask the noise. While this is beyond the scope of the work presented here, it seems plausible to suggest that signal fidelity is likely to be an important consideration for practical actuation. In any case, actuation at $C_\mu \simeq 4 \times 10^{-3}$ seems the appropriate level for peak drag reduction at highest efficiency. This may also help explain why the optimal St_{act} of 0.11 is lower than that observed in the experiments by the Pastoor group (0.15). Just as clean lower amplitude signals are more difficult to generate experimentally, so are lower frequency signals. It is possible that frequencies around $St \simeq 0.11$ are most effective if the actuated signal is clear enough.

The following sections explore the results in greater detail, revealing the main changes in the flow mechanisms with increasing actuator velocity input.

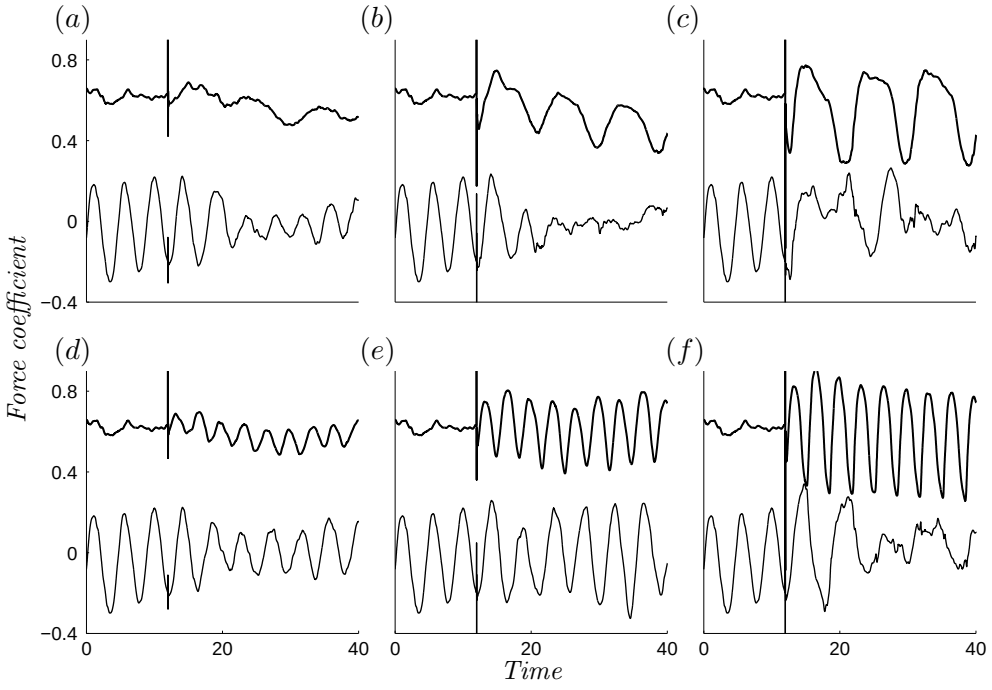

FIGURE 5.2: Drag (thick lines) and lift (thin lines) signals for (a) $St_{act} = 0.11, C_\mu = 5 \times 10^{-4}$, (b) $St_{act} = 0.11, C_\mu = 4 \times 10^{-3}0$, (c) $St_{act} = 0.11, C_\mu = 1.6 \times 10^{-2}0$, (d) $St_{act} = 0.30, C_\mu = 5 \times 10^{-4}$, (e) $St_{act} = 0.30, C_\mu = 4 \times 10^{-3}0$, (f) $St_{act} = 0.30, C_\mu = 1.6 \times 10^{-2}$.

5.1.1 Flow statistics

The influence of momentum coefficient on the drag and lift signals is shown for a select few cases in Figure 5.2. Even at the low momentum coefficient of $C_\mu = 5 \times 10^{-4}$, where

actuator input velocity is a only 13% of freestream velocity, the drag signal locks on to the actuation signal. The amplitude of the drag signal can be seen to grow with momentum coefficient, while the lift signal becomes more disrupted.

Both the mean drag signal amplitude and the spectral peak magnitude $P\{D_{act}\}$ (the latter of which is shown in Figure 5.3(a)) rise in an almost perfectly linear fashion with momentum coefficient. This confirms that, despite the actuator velocity input perhaps being a better predictor of drag reduction, the momentum coefficient is physically the correct measure of energy input. Even when the drag reduction plateaus at $C_\mu > 4 \times 10^{-3}$, $P\{D_{act}\}$ and the drag signal amplitude continue to grow.

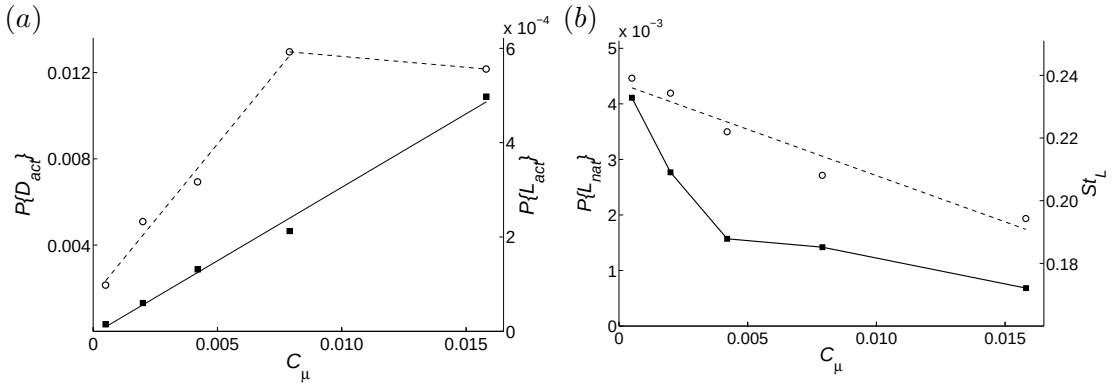

FIGURE 5.3: Momentum coefficient results for $St_{act} = 0.11$. (a) Drag signal spectral peak $P\{D_{act}\}$ (solid squares, left axis) and secondary lift signal peak $P\{L_{act}\}$ (open circles, right axis) against momentum coefficient C_μ. (b) Lift signal spectral peak (solid squares, left axis) and lift signal Strouhal number St_L (open circles, right axis) against momentum coefficient C_μ.

Interestingly, two key momentum coefficient threshold values appear in the lift spectra. $P\{L_{nat}\}$, the PSD magnitude of the natural frequency in the lift signal, falls dramatically for $C_\mu \leq 4 \times 10^{-}3$, before decreasing more gradually at $C_\mu \geq 4 \times 10^{-}3$. The secondary peak magnitude $P\{L_{act}\}$, which occurs at the actuation frequency, grows linearly for $C_\mu \leq 8 \times 10^{-}3$, before plateauing thereafter. It appears the weakening of the former, $P\{L_{nat}\}$, is more critical in the reduction of drag, as the large increase observed in $P\{L_{act}\}$ between $C_\mu = 4 \times 10^{-3}$ and 8×10^{-3} in Figure 5.3(b) is not accompanied by a significant change in the drag results. This confirms the findings of § 4.6, where $P\{L_{nat}\}$ was found to correlate moderately with the drag reduction obtained at different actuation frequencies.

Also adding further support to some of the earlier findings is the decreasing Strouhal frequency in the lift signal, St_L, which decreases with $P\{L_{nat}\}$ (shown in Figure 5.3b). This is expected, as the frequency of vortex shedding is likely to decrease as the process

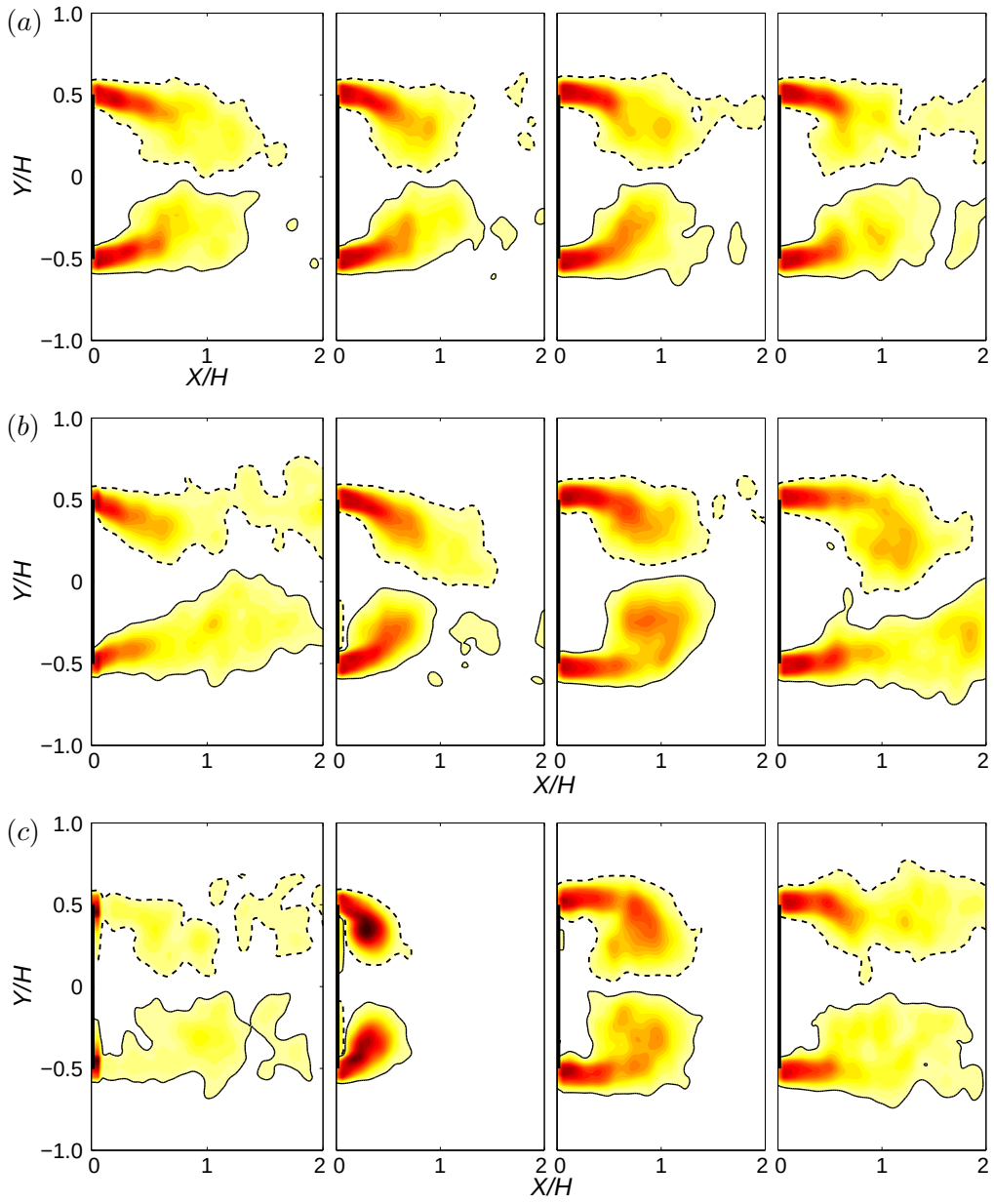

FIGURE 5.4: Phase-averaged vorticity contours for dual actuation at $St_{act} = 0.11$ with (a) $C_\mu = 5 \times 10^{-4}$, (b) $C_\mu = 4 \times 10^{-3}$ and (c) $C_\mu = 1.6 \times 10^{-2}$.

becomes less coherent and increases the formation length (Roshko 1955).

The results for $St_{act} = 0.34$ show a similar trend although, as was discussed in chapter 4, there is no trace of the actuation frequency in the lift signal, leading to $P\{L_{act}\}$ being zero for all cases.

5.1.2 Dynamic behaviour

Phase-averaged analysis reveals that some trace of the symmetric vortex shedding imposed by the actuation remains at the lower momentum coefficients. However, the

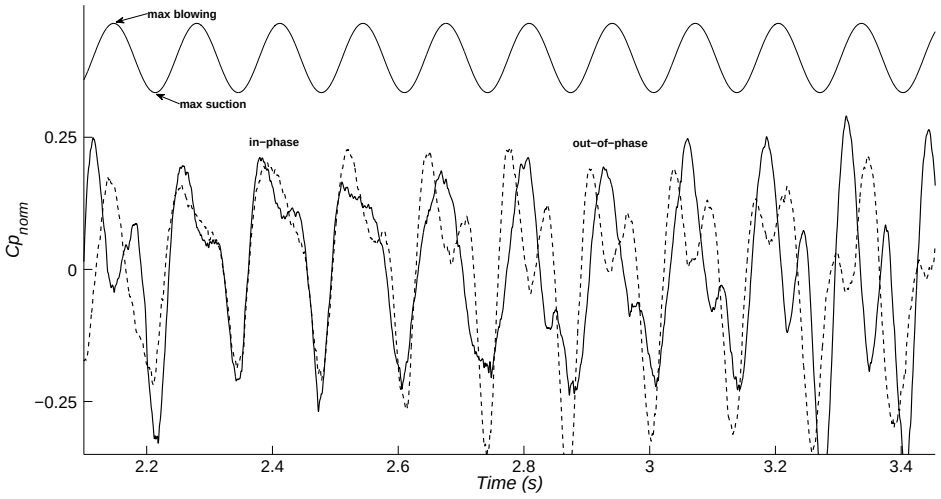

FIGURE 5.5: Normalised pressure coefficient signals measured at the upper slot surface (dashed line) and the lower slot surface (thick solid line) for the case $St_{act} = 0.11$ with $C_\mu = 2 \times 10^{-3}$. The thin line above the plot represents the actuation signal.

process is not as pronounced, and slight asymmetries are observed in the wake. Figure 5.4[1] shows that as the momentum coefficient increases, the mechanism becomes more exaggerated. The lowest momentum coefficient case (Figure 5.4a) shows little change in vorticity through the vortex formation cycle, while the largest case (Figure 5.4c) shows a quieter wake followed by a strong pair of symmetric vortices forming in each cycle.

For the lower momentum coefficient cases, the flow exhibits periods of in-phase upper and lower slot pressure signals, amongst periods with the signals out-of-phase. This suggests that often extra "unwanted" vortices are being shed amongst the synchronous vortices created by actuation. At $C_\mu = 2 \times 10^{-3}$, shown in Figure 5.5, the periods of in-phase and out-of-phase flow are apparent.

At the lower momentum coefficient $C_\mu = 5 \times 10^{-4}$ the period of out-of-phase flow dominates, whilst at $C_\mu \geq 4 \times 10^{-3}$ the flow is mostly in-phase. The amount of time each case spends in-phase can be quantified by a cross-correlation coefficient R between the two signals. This is plotted in Figure 5.6(a), which confirms that the signals become more in-phase at higher momentum coefficients, and negligible correlation occurs at the lowest momentum coefficient. Figure 5.6(b) shows how the spectral peaks in the upper

[1]It should be noted here that these phase-averaged vorticity progressions are an averaged representation of flow which alternates between periods of symmetric vortex shedding and periods of natural shedding (and periods that could be classified as either). As such, the more subtle changes that occur over time – both lower and higher frequency mechanisms – are not observable through this representation. The movie files in the attached CD are instead recommended for an understanding of the complete physical flow.

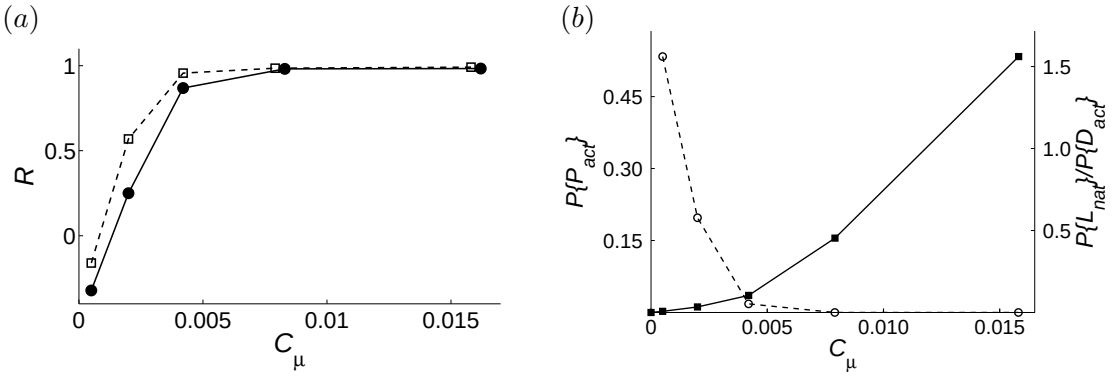

FIGURE 5.6: (a) Cross-correlation coefficient R between upper and lower slot pressure signals (b) Slot pressure signal spectra at $St_{act} = 0.30$. The closed squares with solid line represents the magnitude of the actuation frequency peak $P\{P_{act}\}$; the open circles represent with dashed line represents the ratio of the natural frequency peak magnitude to that of the actuation frequency, $P\{P_{nat}\}/P\{P_{act}\}$.

slot pressure signal vary with momentum coefficient. Here, this is shown for $St_{act} = 0.30$ (this is a better case to analyse than $St_{act} = 0.11$, where the harmonic $2St_{act}$ interferes with the natural Strouhal frequency). The natural frequency is only attenuated from this signal completely at $C_\mu \geq 8 \times 10^{-3}$, while the actuation frequency strength appears to be proportional to C_μ^2. The actuation frequency peak in the base pressure signal spectra $P\{P_{act}\}$, on the other hand, grows linearly with C_μ (not pictured).

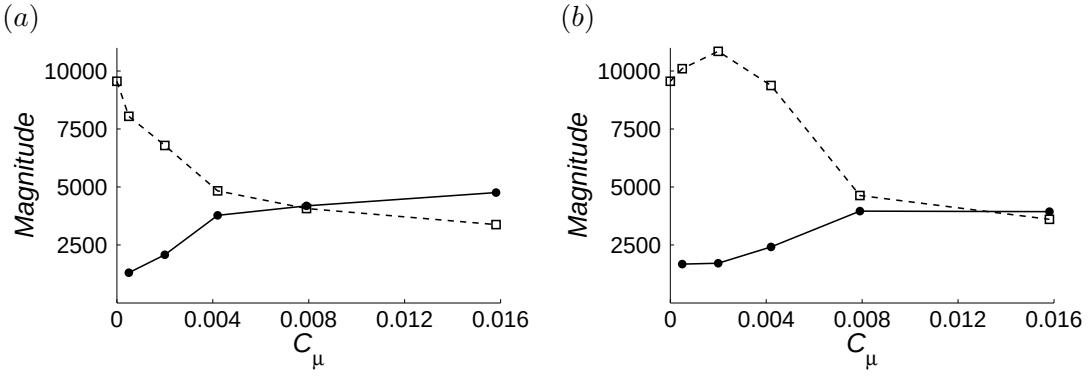

FIGURE 5.7: Mode A (thick lines, solid circles) and mode N (dashed line, open squares) magnitudes from DMD analysis at varying momentum coefficient C_μ for (a) $St_{act} = 0.11$ and (b) $St_{act} = 0.30$.

Figure 5.7 shows the results of DMD conducted for both the $St_{act} = 0.11$ and $St_{act} = 0.30$ momentum coefficient sweeps. As expected, the magnitude of modes A and N are dictated by the momentum coefficient. For the optimum actuation frequency case, $St_{act} = 0.11$, the prevalence of mode A grows substantially while mode N diminishes over the range $2 \times 10^{-3} < C_\mu < 4 \times 10^{-3}$, while for the higher actuation frequency case, $St_{act} = 0.30$, the equivalent range is $4 \times 10^{-3} < C\mu < 8 \times 10^{-3}$. This confirms that the

flow response to momentum coefficient depends on actuation frequency: the actuation frequencies having more effect require less momentum input to reach their optimum state.

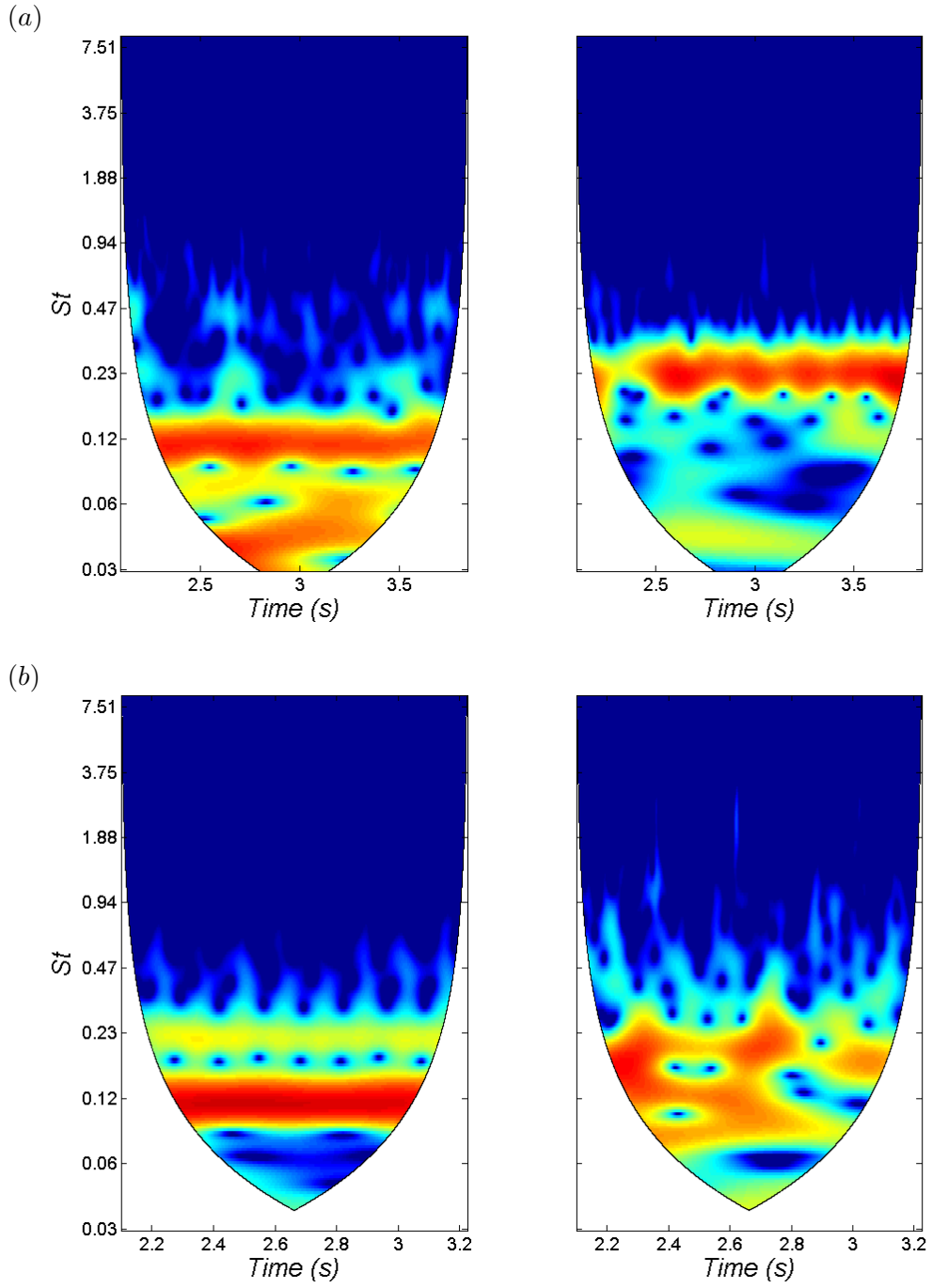

FIGURE 5.8: Wavelet analysis on the drag (left) and lift (right) signals for $St_{act} = 0.11$ at (a) $C_\mu = 5 \times 10^{-4}$ and (b) $C_\mu = 1.6 \times 10^{-2}$.

The results also confirm that simply increasing the prevalence of mode A and di-

minishing mode N is not all that is required for optimal drag reduction: at the higher momentum coefficients, the magnitudes of both mode A and N are similar for both $St_{act} = 0.11$ and $St_{act} = 0.30$ but the drag reduction is much greater for the former. The difference, as explained in § 4.8.2, is the larger vortices generated by $St_{act} = 0.11$, which magnify the effect of the mode.

The above conclusions are supported by wavelet analysis, which shows in Figure 5.8(a) an increasing prevalence of the actuation frequency in the drag signal with increasing momentum coefficient. This analysis also shows that the first harmonic of the actuation frequency, $2St_{act}$, appears in the signal at higher momentum coefficients (this will be discussed further in § 5.2), while low frequency fluctuations are diminished. The presence of the natural frequency in the lift signal is confirmed to be less consistent at higher momentum coefficients (Figure 5.8(b)).

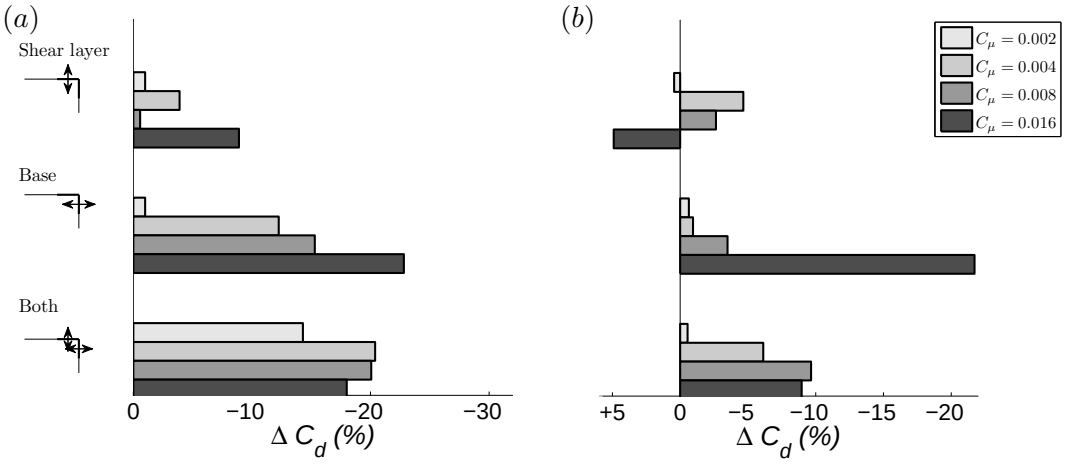

FIGURE 5.9: Drag reduction for different actuation configurations for (a) $St_{act} = 0.11$ and (b) $St_{act} = 0.30$.

5.2 Orientation configurations

The above results were obtained for actuation from all four rear-corner slots — two imparting flow perpendicular to the freestream immediately upstream of the separation point (*shear-layer* actuation), and two on the extremities of the rear face imparting flow parallel to the freestream (*base* actuation). This approach, initially employed to mimic the 45 deg actuation of the previous experimental results of Pastoor *et al.* (2008), also allows the effect of each actuation orientation configuration to be tested individually.

This was explored by testing each configuration with an increasing momentum co-

efficient ($C_\mu = 2 \times 10^{-3}, 4 \times 10^{-3}, 8 \times 10^{-3}$ and 1.6×10^{-2}), and comparing with the both-slots case, which shall hereafter be termed *dual* actuation. While running these tests for all of the actuation frequencies originally tested under dual actuation would be ideal, given the resources required a representative subset was chosen. The different jet configurations were tested with actuation at the optimum frequency, $St_{act} = 0.11$, and at a higher frequency case, $St_{act} = 0.30$ (as was the case above in section 5.1). This allows for an understanding of the mechanisms involved in both shear-layer and base actuation configurations to be developed, which in turn gives a greater insight into dual actuation. Incrementing the momentum coefficient for each configuration will also aid in developing further insight into the mechanisms of each configuration.

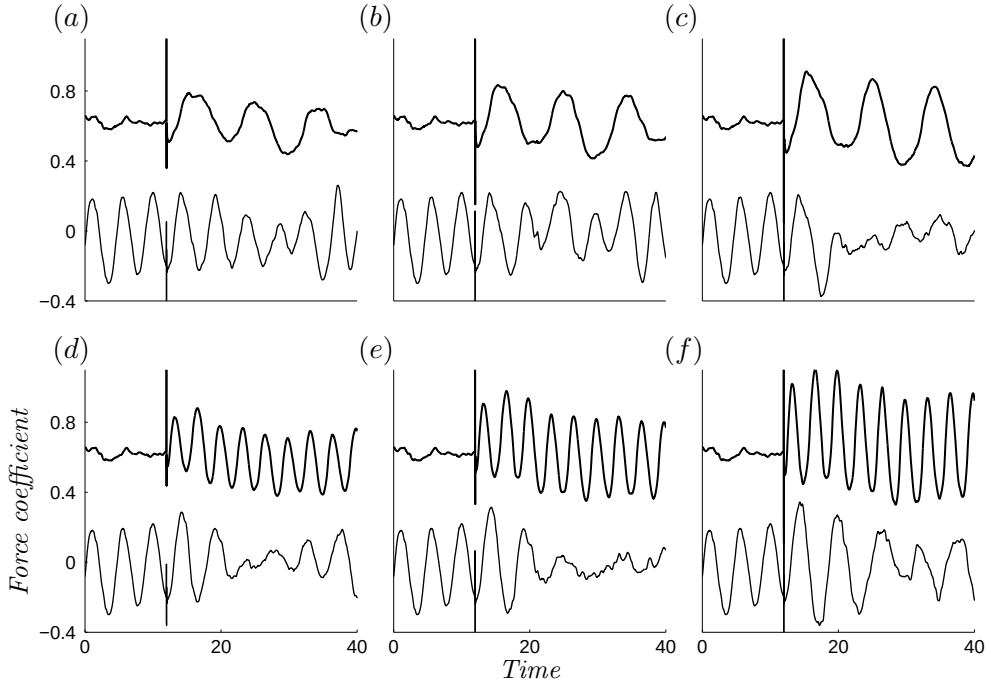

FIGURE 5.10: Drag (thick lines) and lift (thin lines) signals for shear-layer actuation cases at (a) $St_{act} = 0.11, C_\mu = 4 \times 10^{-3}$, (b) $St_{act} = 0.11, C_\mu = 8 \times 10^{-3}$, (c) $St_{act} = 0.11, C_\mu = 1.6 \times 10^{-2}$, (d) $St_{act} = 0.30, C_\mu = 4 \times 10^{-3}$, (e) $St_{act} = 0.30, C_\mu = 8 \times 10^{-3}$, (f) $St_{act} = 0.30, C_\mu = 1.6 \times 10^{-2}$.

The results for $St_{act} = 0.11$, shown in Figure 5.9(a), indicate that base actuation is significantly more successful at reducing drag than shear-layer actuation for all C_μ, but not as successful as dual-actuation for $2 \times 10^{-3} \leq C_\mu \leq 8 \times 10^{-3}$. For base actuation at $C_\mu = 1.6 \times 10^{-2}$, however, the greatest drag reduction of all the cases is observed — an impressive 24%.

For $St_{act} = 0.30$, the results of which are shown in Figure 5.9(b), the success of

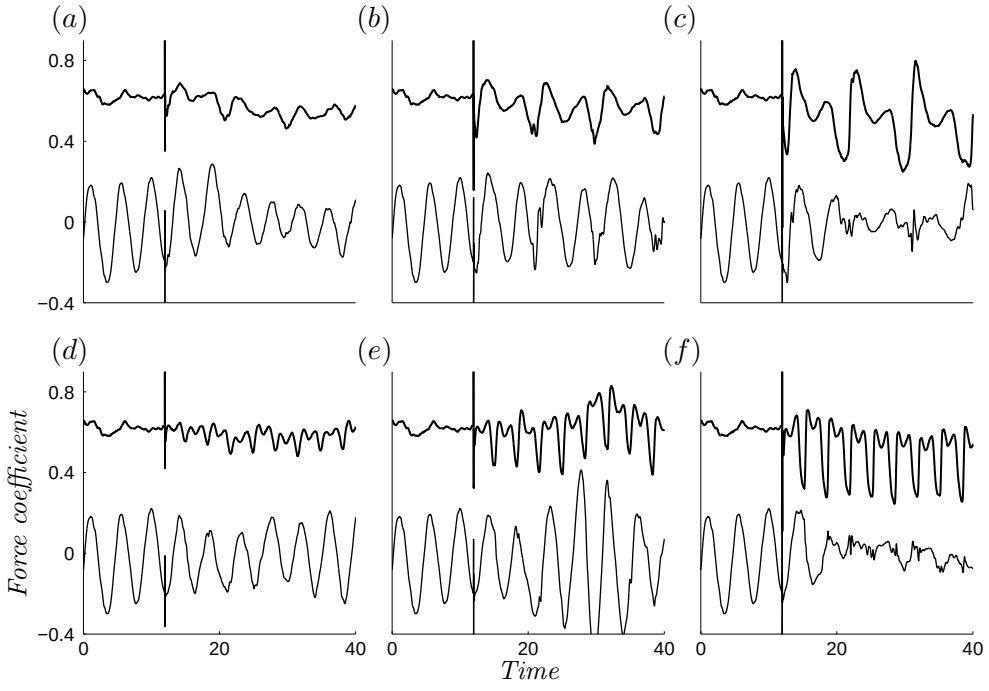

FIGURE 5.11: Drag (thick lines) and lift (thin lines) signals for base actuation cases at (a) $St_{act} = 0.11, C_\mu = 4{\times}10^{-3}$, (b) $St_{act} = 0.11, C_\mu = 8{\times}10^{-3}$, (c) $St_{act} = 0.11, C_\mu = 1.6{\times}10^{-2}$, (d) $St_{act} = 0.30, C_\mu = 4 \times 10^{-3}$, (e) $St_{act} = 0.30, C_\mu = 8 \times 10^{-3}$, (f) $St_{act} = 0.30, C_\mu = 1.6 \times 10^{-2}$.

base actuation at a large momentum coefficient is once again observed. However, base actuation is not as successful at lower momentum coefficients. The opposite trend is observed for shear-layer actuation, where moderate success occurs at $4 \times 10^{-3} \geq C_\mu \leq 8 \times 10^{-3}$, but an increase in drag occurs at $C_\mu = 1.6 \times 10^{-2}$.

These results suggest the three configurations impact the wake in different ways. Below, the drag and lift signals, wake contours and dynamic mode decomposition are used to analyse each configuration individually to develop an understanding of the different underlying mechanisms.

5.2.1 Flow Statistics

The shear-layer configuration returns a similarly smooth drag signal to the dual actuation case, with a locked-on signal even at the low momentum coefficient $C_\mu = 2 \times 10^{-3}$. Figure 5.10 shows the increasing amplitude of the drag signal oscillations with increasing momentum coefficient. In fact, the growth of the PSD magnitude at the actuation frequency in the drag signal appears to be linear, as shown in Figure 5.12(a). Figure 5.12(b) shows the decay of the Strouhal frequency's dominance in the lift signal is not exactly linear, however the decreasing trend is clear.

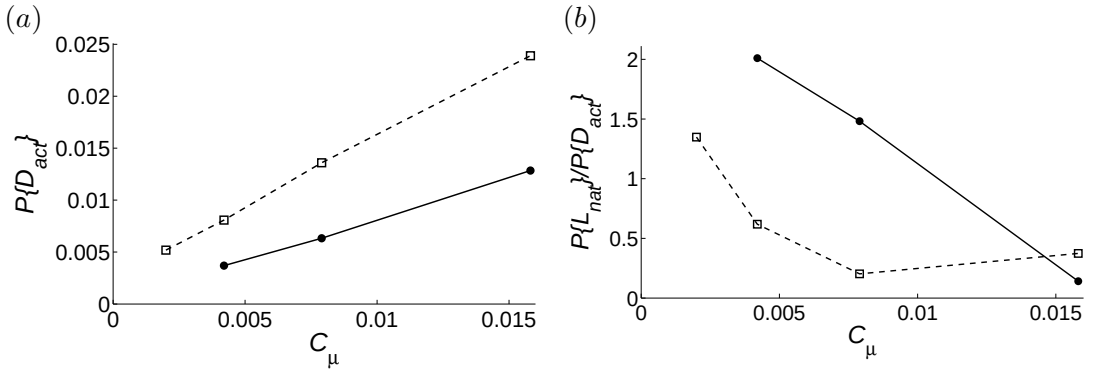

FIGURE 5.12: Shear-layer actuation: (a) Relationship between the actuation frequency magnitude in the drag signal spectra $P\{D_{act}\}$ and momentum coefficient C_μ. (b) Relationship between the ratio $P\{L_{nat}\}/P\{D_{act}\}$ (where $P\{L_{nat}\}$ is the Strouhal frequency magnitude in the lift spectra) and C_μ. For both plots, the solid lines with closed circles represent $St_{act} = 0.11$, while the dashed line with open squares represent $St_{act} = 0.30$.

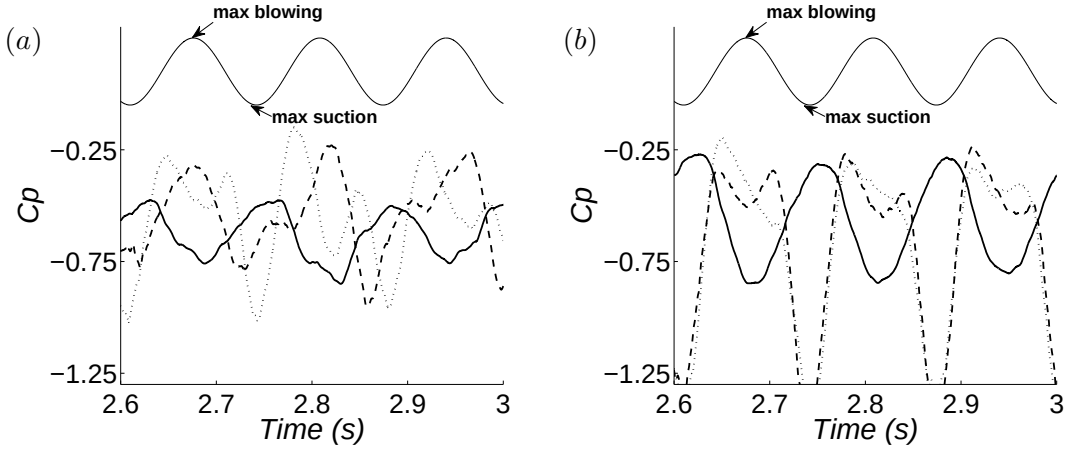

FIGURE 5.13: Pressure signals for shear-layer actuation at $St_{act} = 0.11$ with (a) $C_\mu = 4{\times}10^{-3}$ and (b) $C_\mu = 1.6 \times 10^{-2}$. The dotted and dashed lines represent the upper and lower slot pressure signals respectively. The base pressure (thick solid line) and actuation signal (thin line) are also plotted.

Interestingly, however, this locked-on drag response does not result in a large drag reduction, even at higher momentum coefficients. An analysis of the upper and lower slot pressure signals reveals a rather complicated wake response is taking place. These signals are *not* locked on to the actuation signal, yet they also appear to fluctuate in a pattern related to the actuation frequency. This is clearly seen in Figure 5.13, which shows the pressure signals for $C_\mu = 4 \times 10^{-3}$ and 1.6×10^{-2}. In both cases, and especially the former, the unity of the signals is disrupted during the blowing phase.

The base actuation configuration also shows this behaviour in the slot pressure signals. However, here the secondary frequency appears in the base pressure signal also. At the maximum momentum coefficient $C_\mu = 1.6 \times 10^{-2}$, the secondary frequency is

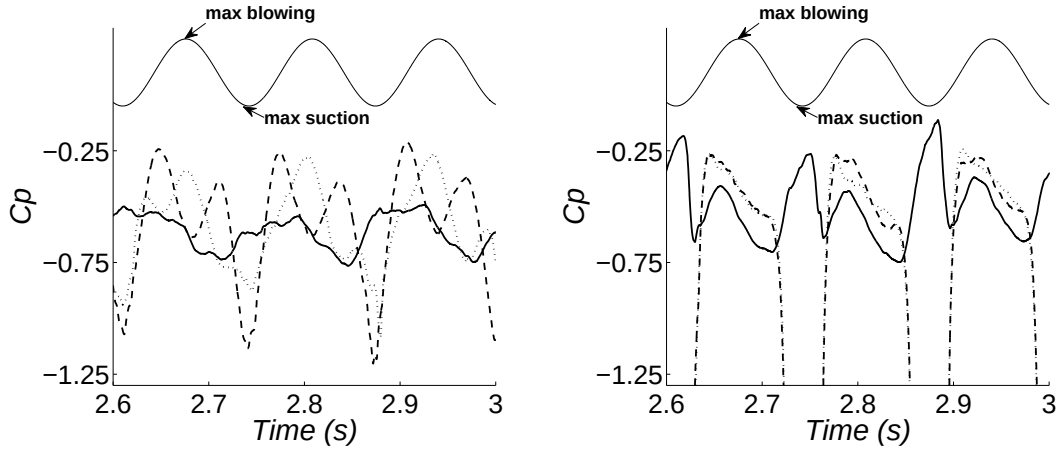

FIGURE 5.14: Pressure signals for base actuation at $St_{act} = 0.11$ with (a) $C_\mu = 4 \times 10^{-3}$ and (b) $C_\mu = 1.6 \times 10^{-2}$. The dotted and dashed lines represent the upper and lower slot pressure signals respectively. The base pressure (thick solid line) and actuation signal (thin line) are also plotted.

very apparent in the base pressure signal (Figure 5.14), while the upper and lower slot signals indicate near constant in-phase flow. This distinct "double dip" shape in the base pressure signal is also evident in the drag signals (Figure 5.11). However, despite this new base pressure response, a large drag reduction is obtained. This indicates that the cross correlation between the upper and lower pressure signals is the vital statistic determining drag reduction success, and the shape of the base pressure signal is inconsequential. Figure 5.15 confirms what can be seen by eye in Figures 5.13 and 5.14: shear-layer actuation is less successful at achieving in-phase flow at the rear separation points than base actuation.

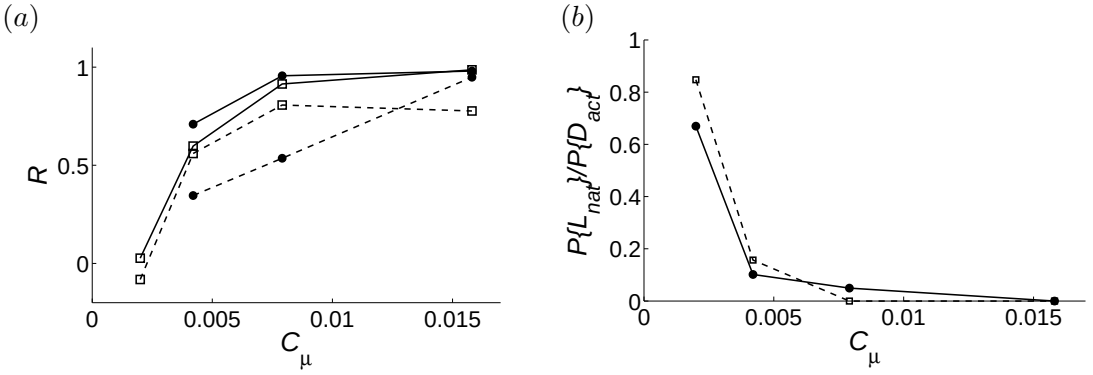

FIGURE 5.15: (a) Cross-correlation coefficient R between upper and lower slot pressure signals. Closed circles represent $St_{act} = 0.11$ and open squares represent $St_{act} = 0.30$. Solid lines represent base actuation and dashed lines represent shear-layer actuation. (b) Momentum coefficient against $P\{L_{nat}\}/P\{D_{act}\}$, the ratio of the natural frequency peak to the actuation frequency peak in the upper slot pressure signal for shear-layer actuation (dashed line) and base actuation (solid line) at $St_{act} = 0.30$.

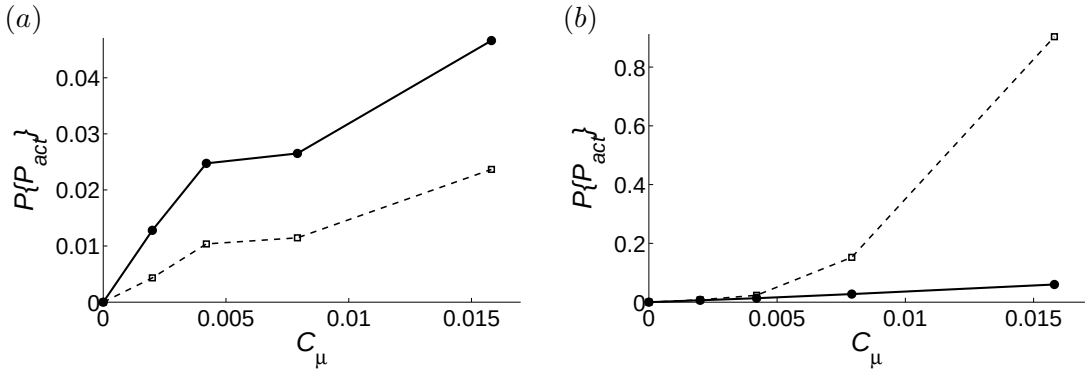

FIGURE 5.16: Magnitude of spectral peak at St_{act} from base pressure signal (solid lines, filled circles) and from upper slot pressure signal (dashed lines, open squares) against momentum coefficient C_μ at $St_{act} = 0.30$ for (a) shear-layer actuation and (b) base actuation.

5.2.2 Dynamic behaviour

Figure 5.17 shows the development of vortices in the base pressure signal for the most successful case – base actuation with $C_\mu = 1.6 \times 10^{-2}$ – helping determine the cause of the "double dip" in the base pressure signal discussed above. The peaks occur either side of the maximal blowing phase of actuation. The first (point 1), which occurs when suction switches to blowing, is due to the development of synchronous vortices directly behind the base surface (as opposed to the dual and shear-layer actuation which creates the vortices above/below the base surface). The vortices begin to form during the suction phase of actuation – for base actuation, this results in high vorticity, as the shear layers are forced to turn inward immediately after separation.

As the vortices move into the wake, the drag coefficient drops slightly (point 2). However, at this point, the blowing reduces, allowing the two opposite-signed vortices to grow even further, lowering the pressure in this region. This coincides with the second peak (point 3). Once suction begins, diffusion and cross-annihilation of the synchronous vortices causes rapid recovery in the pressure, leading to a trough in the drag signal just after the point of maximum suction (point 4).

This appears to be the desired base pressure response. The "double dip" indicates that sufficient vorticity has collected in the synchronous vortices to dominate the wake. The dual actuation case, in fact, also shows a mild "double dip" for the maximum momentum coefficient case. This is expected, as it is a combination of the shear-layer and base actuation configurations.

In the shear-layer actuation case, the suction is not able to direct the flow any further past the lower and upper surfaces. The result is a delayed development of the

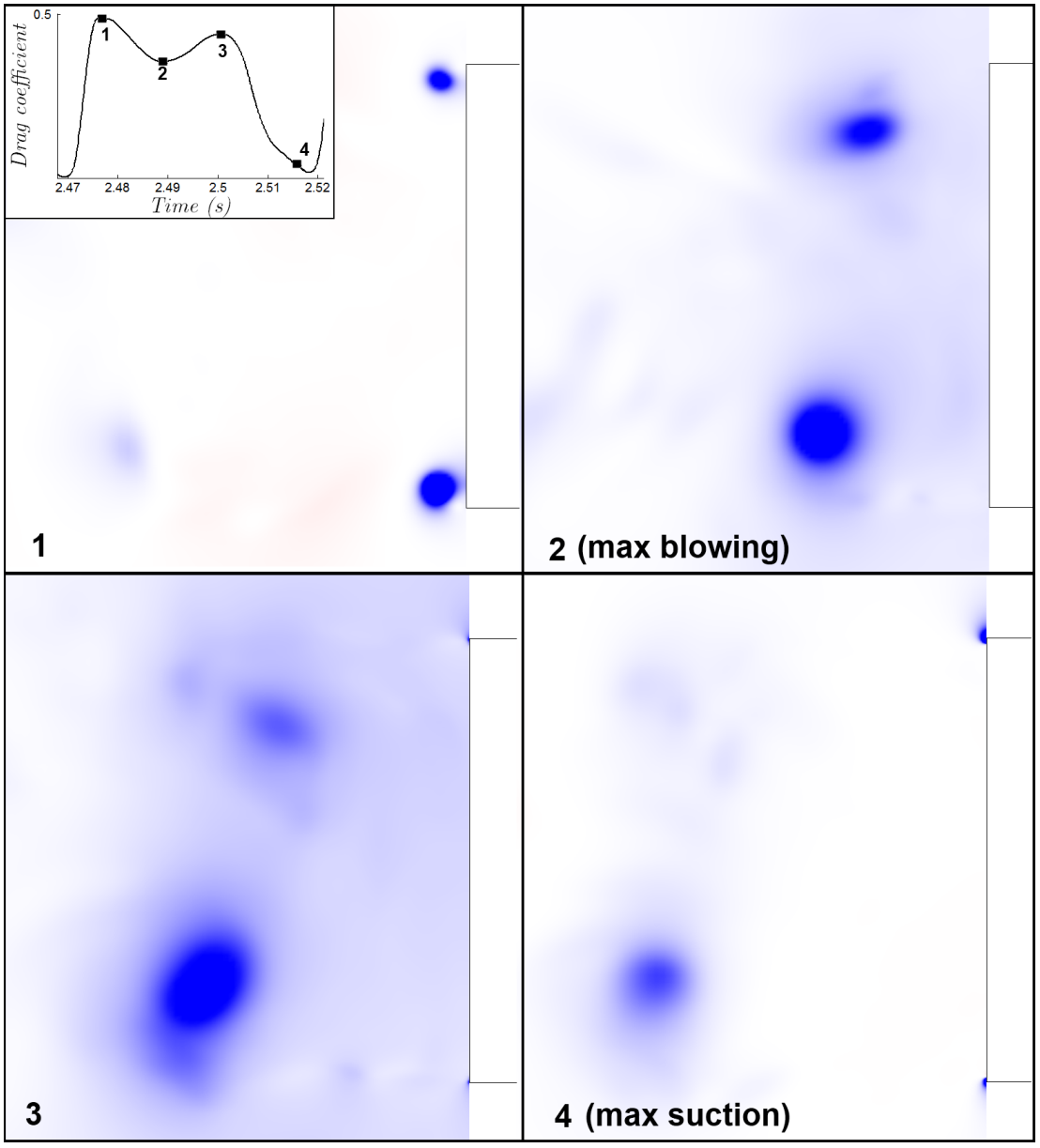

FIGURE 5.17: Centreplane pressure contours of a typical cycle for base actuation at $St_{act} = 0.30$ and $C_\mu = 1.6 \times 10^{-2}$. Upper left inset shows evolution of drag coefficient with time, with the location of each numbered snapshot indicated.

synchronous vortices, which are far weaker and much less able to influence the flow.

As the momentum coefficient increases, so does the height of the first peak, due to increased vorticity in the initial vortices. At lower actuation frequencies, the forming synchronous vortices are allowed more time to collect more vorticity. At higher actuation frequencies, more energy is required to achieve this threshold.

Phase-averaged vorticity contours further reveal the nature of these different mechanisms. For the shear-layer actuation configuration (Figure 5.18), alternately shed

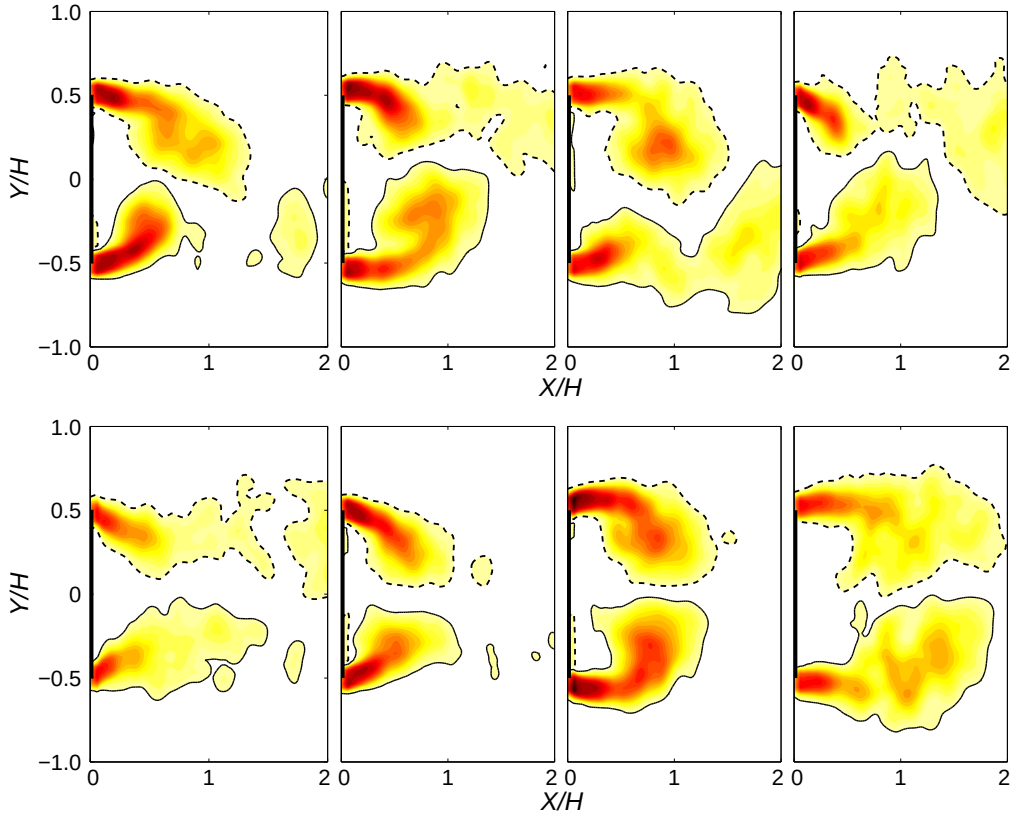

FIGURE 5.18: Phase-averaged vorticity contours for shear-layer actuation at $St_{act} = 0.11$ with $C_\mu = 4 \times 10^{-3}$ (top) and $C_\mu = 1.6 \times 10^{-2}$ (bottom). Left most snapshot coincides with maximum suction (minimum drag) in cycle.

vortices are still observed in the wake at $C_\mu = 4 \times 10^{-3}$, although the asymmetry is less pronounced than the natural case. At $C_\mu = 1.6 \times 10^{-2}$, synchronous vortices are evident, although they noticeably extend further above and below the wake than observed in the dual actuation case. In the base actuation case (Figure 5.19), the flow appears to change little throughout the cycle at $C_\mu = 4 \times 10^{-3}$. This again suggests that base actuation is successful at disrupting the natural instability. At $C_\mu = 1.6 \times 10^{-2}$, the synchronous vortices are very pronounced, as discussed above, and do not extend above and below the wake as observed for the shear-layer actuation case.

Dynamic Mode Decomposition is again used to provide further insight into the flow. The technique is particularly useful here, with the actuation frequency held constant and thus minimising the potential areas for discrepancy between cases (the ratio of actuation frequency to sampling frequency, and number of timesteps required for each decomposition, for example, are no longer issues).

Immediately apparent in Figure 5.20 is the lower mode magnitudes recovered for

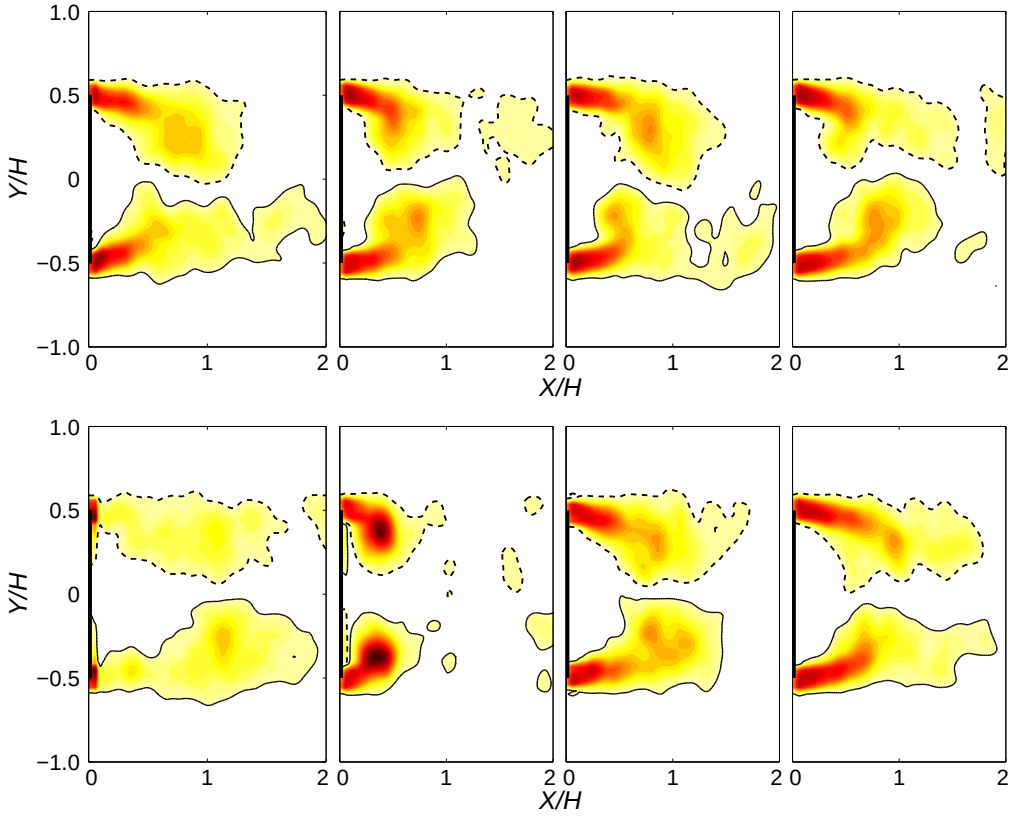

FIGURE 5.19: Phase-averaged vorticity contours for base actuation at $St_{act} = 0.11$ with $C_\mu = 4 \times 10^{-3}$ (top) and $C_\mu = 1.6 \times 10^{-2}$ (bottom).

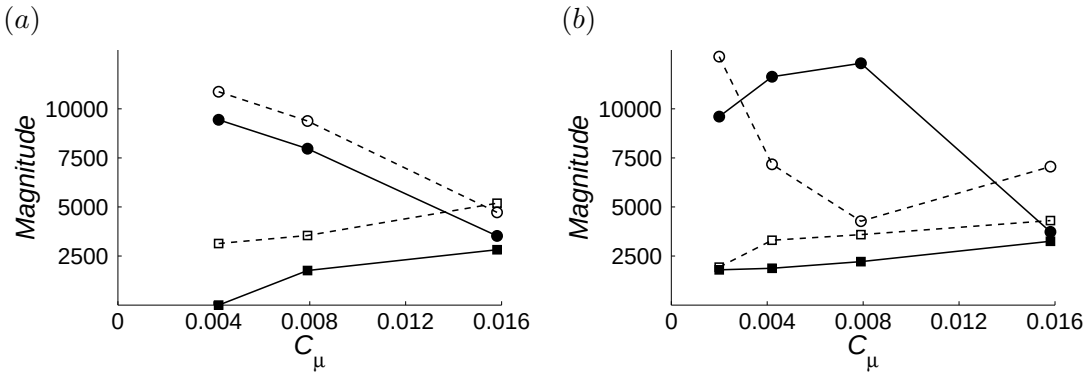

FIGURE 5.20: DMD mode magnitudes for (a) $St_{act} = 0.11$ (b) $St_{act} = 0.30$. Filled markers represent base actuation, while open markers represent shear-layer actuation. Circles are mode N, squares mode A.

the base actuation configurations at $St_{act} = 0.11$. While mode A is less prevalent (it does not even appear at $C_\mu = 4 \times 10^{-3}$), this configuration does reduce the magnitude of mode N noticeably. For $St_{act} = 0.30$, mode N is not reduced at $C_\mu \leq 8 \times 10^{-3}$, and drag reduction is negligible. At $C_\mu = 1.6 \times 10^{-2}$, however, the mode N magnitude drops significantly and a sizeable drag reduction results. This once again shows that

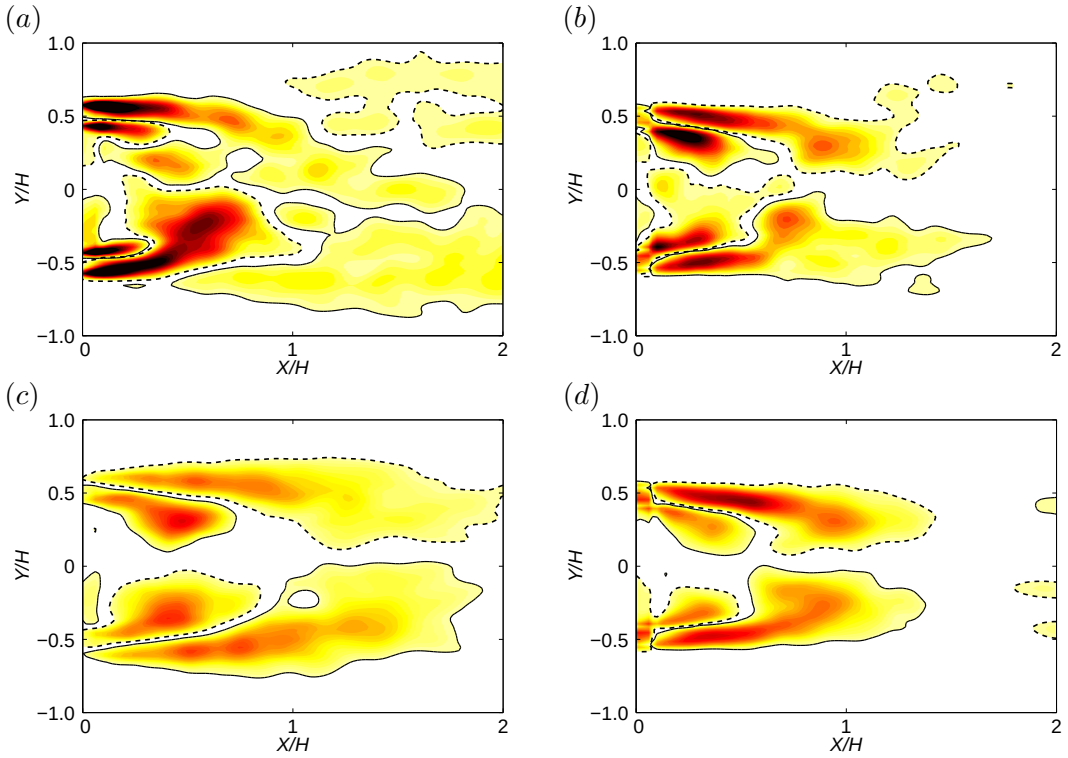

FIGURE 5.21: Mode A spanwise vorticity at $St_{act} = 0.11$ for (a) shear-layer actuation at $C_\mu = 8 \times 10^{-3}$, (b) base actuation at $C_\mu = 8 \times 10^{-3}$, (c) shear-layer actuation at $C_\mu = 1.6 \times 10^{-2}$, (d) base actuation at $C_\mu = 1.6 \times 10^{-2}$. Maximum/minimum contour levels for (a) and (b) are half those of (c) and (d).

reducing the prevalence of mode N coincides with greater drag reduction.

Furthermore, as shown in Figure 5.21, mode A has a different structure depending on the actuation configuration used. For base actuation, the synchronous vortices are more tightly compacted, with the shear layers bent inward. This causes greater mixing, and a less turbulent wake at $1 < X/H < 2$. In the shear-layer actuation case, the shear layers are angled slightly outward, which results in more spread out structures and less interaction. This narrower shape of mode A, coupled with the lower mode N magnitude, appear to explain why base actuation is so effective despite returning a lower mode A magnitude.

These trends, however, do not explain the large jump in drag reduction for base actuation at the highest momentum coefficient, $C_\mu = 1.6 \times 10^{-2}$. This boost in drag reduction is likely due to an additional mode (called AA) at a frequency of $2St_{act}$, which is apparent at this momentum coefficient at both $St_{act} = 0.11$ and $St_{act} = 0.30$ (see Figure 5.22). This mode features a similar shape to mode A, but with smaller structures. The mode is, as one would expect, therefore also present in the dual actuation cases at

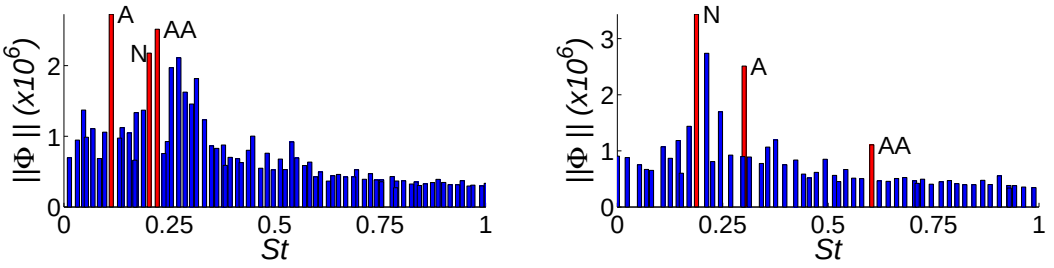

FIGURE 5.22: Mode A spanwise vorticity at $St_{act} = 0.11$ and $C_\mu = 1.6 \times 10^{-2}$ for (a) shear-layer actuation and (b) base actuation.

$C_\mu = 1.6 \times 10^{-2}$, but does not appear in any of the shear-layer actuation cases.

As mode AA occurs at exactly double the frequency of mode A, the two can be superimposed to gain further understanding of the final wake mechanism. This quasi-mode $A*$ is shown in Figure 5.23(c). The result is a stronger pair of synchronous vortices forming, resulting in greater cross-annihilation and a subsequent period of lower vorticity in the wake.

This new mode is also likely responsible for the suppression of the natural frequency and the extremely low magnitude of mode N in the wake at $C_\mu = 1.6 \times 10^{-2}$, in both the dual and base actuation cases. Its presence in only these two configurations also confirms that base and shear-layer actuation impact the wake in different ways. It is unclear whether this mode is actually present at the lower C_μ values but too weak to be detected by DMD, or if it only is triggered above a certain threshold value. The former seems plausible, due to the presence of the harmonic frequency in the base pressure signals for all base actuation cases.

Wavelet analysis, the plots of which are located in Appendix B (Figures 6-9), provides further evidence of the different mechanisms discussed in this chapter. Easily identifiable in the drag signal is the lack of activity at the actuation frequency harmonic $2St_{act}$ for the shear-layer actuation cases, while the base actuation cases show a high energy in this region. This is a result of the "double dip" behaviour observed in the drag and base pressure signals, and discussed above. Furthermore, St_{act} is noticeably subdued in the base actuation cases, underlining the weaker synchronous shedding created by the configuration.

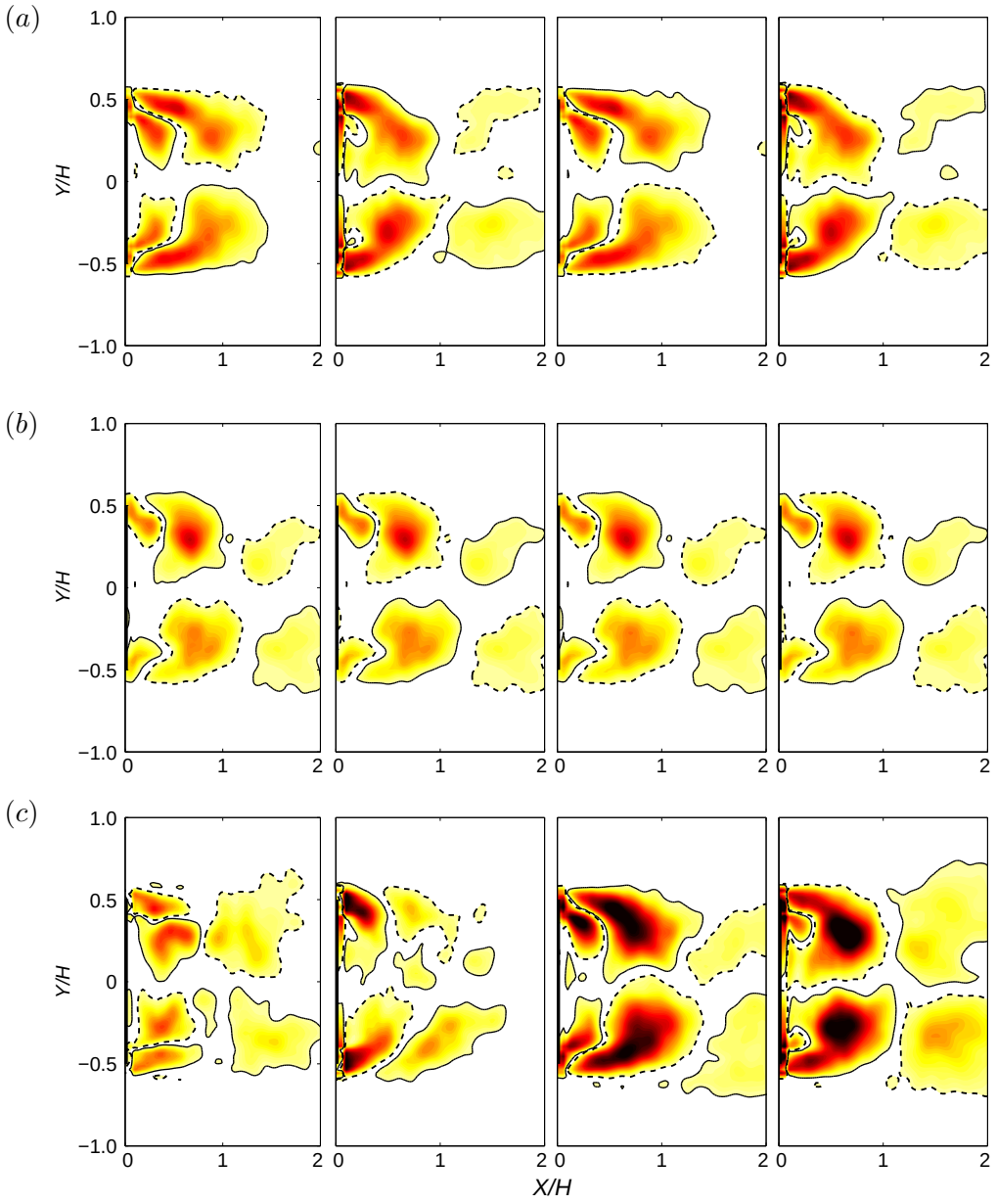

FIGURE 5.23: Vorticity contours for base actuation at $St_{act} = 0.11$. One complete actuation cycle is plotted at four points in time (from left to right). (a) Mode A (b) Mode AA (c) Quasi-mode $A*$, the superposition of modes A and AA.

5.3 Summary

The first section of this chapter shows that the success of actuation improves with increasing momentum coefficient until a certain threshold is reached, above which the drag reduction does not improve (and for $St_{act} = 0.11$ actually decreases). The results also suggest this threshold is higher for the less optimum cases. The reason for higher

drag at lower momentum coefficients is a propensity for the upper and lower shear layers to fall out of phase, as shown by a lower correlation between the upper and lower slot pressure signals.

The second section shows that the shear-layer and base actuation configurations achieve drag reduction through essentially different mechanisms. Shear-layer actuation is more successful at creating synchronous vortices in each separating shear layer, however the vortices influence the wake less, resulting in a more asymmetric wake. Base actuation, on the other hand, is more successful at disrupting the natural instability, due to the direct interaction of the actuator velocities with the wake. When combined, it appears the two mechanisms contribute to each other's success further, as the total drag reduction for four-slot actuation at $C_\mu = 8 \times 10^{-3}$ is significantly greater than the sum of the drag reduction obtained for separate shear-layer or base actuation at $C_\mu = 4 \times 10^{-3}$.

The momentum coefficient threshold for four-slot actuation, however, does not appear to be the same for shear-layer and base actuation configurations, and the latter may offer the greatest potential for drag reduction provided enough input energy is available. Its success at high momentum coefficients is due to the presence of an additional mode, AA. This mode, occurring at double the frequency of mode A, is shown to contribute to the loss of a sinusoidal response in the system, while enhancing the synchronous vortex shedding mechanism through exaggerating the periods of high and low vorticity in the wake. This explains the large drag reduction obtained for both actuation frequencies tested with base actuation at $C_\mu = 1.6 \times 10^{-2}$.

In the next chapter the body is moved towards the ground, a scenario more representative of a ground vehicle. The effect this has on the natural flow and actuation success is investigated.

Chapter 6

Effect of ground proximity

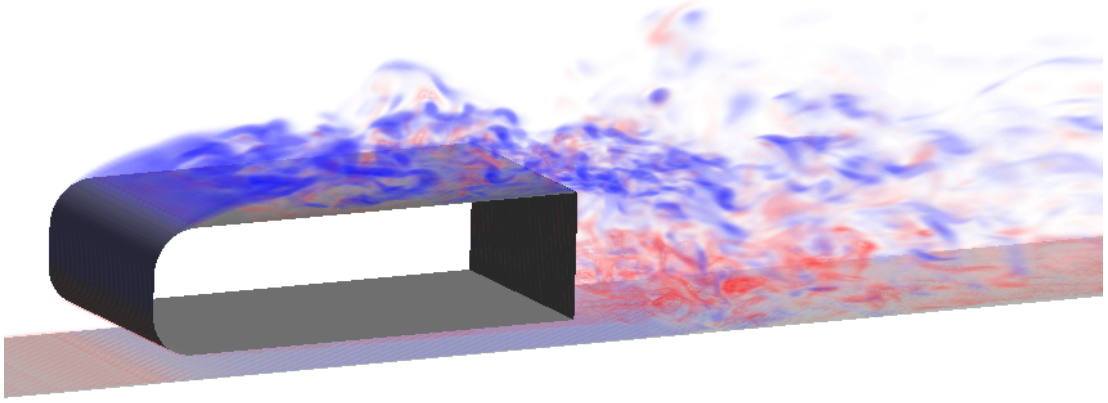

FIGURE 6.1: A snapshot of a perspective view of the instantaneous absolute spanwise vorticity for the natural flow over the body $0.2H$ above ground. The flow is characterised by separation over the upper leading edge, while staying attached underneath. The blue-white-red colour map depicts spanwise vorticity from negative (clockwise) to positive (counter-clockwise) levels.

6.1 Natural flow statistics

To better approximate the upper and lower shear layers at the rear of a truck, the effect of ground clearance on both the natural and actuated flow was also explored. The ground clearance used was $0.2H$, mimicking a standard truck height, while a moving ground (at the velocity of the inlet flow) was also employed to recreate a typical road with no boundary layer. Further details on the setup can be found in §2.8.

In §1.3.4 the ground proximity effect for bluff body flows was introduced, with the previous literature suggesting a lower drag and less coherent vortex shedding would be expected with decreasing ground clearance. Indeed, these traits were observed here,

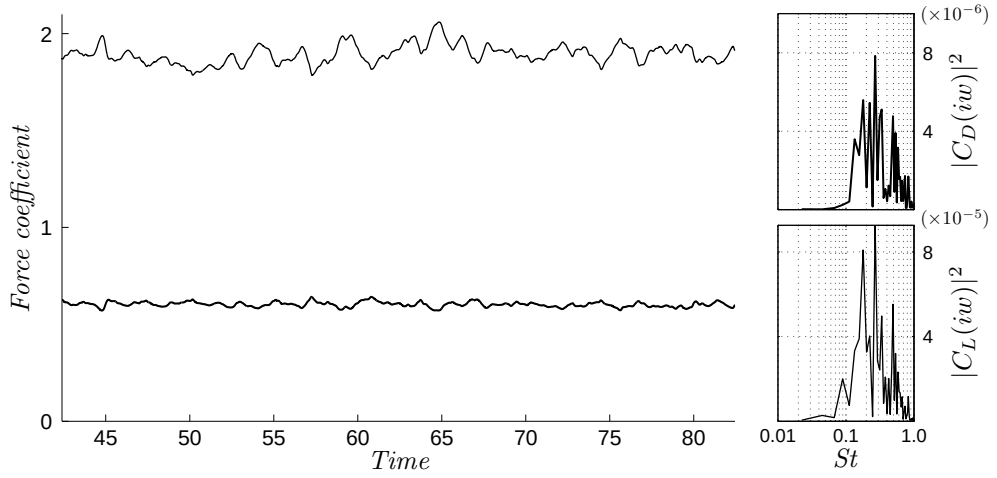

FIGURE 6.2: Time history of drag (thick line) and lift (thin line) signals for natural flow with ground clearance of $0.2H$. The frequency spectrum for each signal is displayed on the right. The drag spectra amplitude (top) is displayed at a scale one order of magnitude lower than the lift spectra amplitude (bottom). The lift coefficient has a mean value of 1.86 – the reason for this high value is apparent in the time-averaged velocity and pressure contours discussed in §6.1.1.

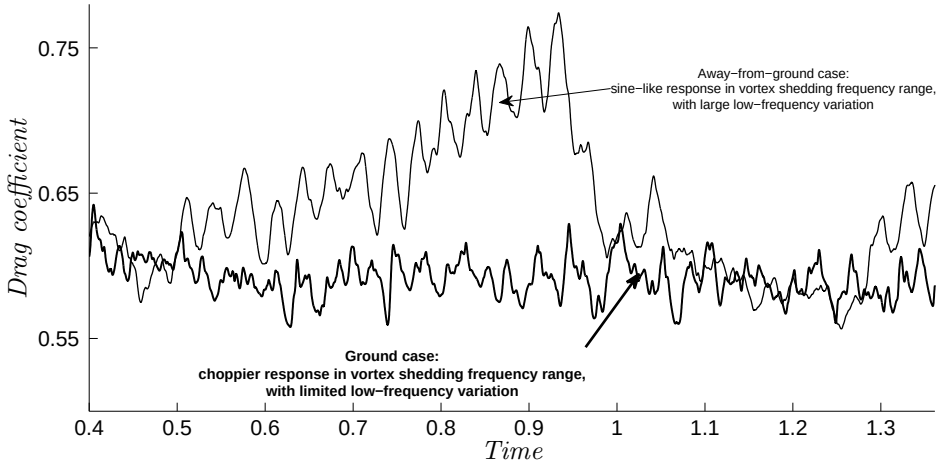

FIGURE 6.3: Time history of drag signals for natural flow with ground clearance of $0.2H$ (thick line) and away-from-ground (thin line).

along with many other noteworthy changes to the natural flow that are outlined in this chapter.

The low-frequency meandering of the drag observed in the away-from-ground case is shown in Figures 6.2 and 6.3 to be subdued in the ground proximity case, with the drag coefficient hovering around the mean value of 0.60 at all times. The higher frequency fluctuations related to the von Kármán instability, on the other hand, appear less consistent than the away-from-ground case. The PSD confirms this, with no single

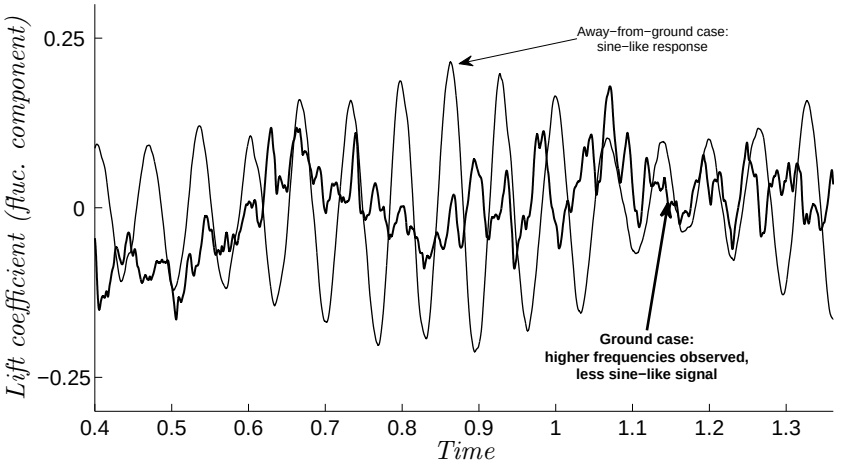

FIGURE 6.4: Time history of fluctuating lift ($C_L - \overline{C_L}$) signals for natural flow with ground clearance of $0.2H$ (thick line) and away-from-ground (thin line).

dominant frequency peak observed. The peak magnitude here is an order of magnitude lower than that observed for the corresponding frequency in the away-from-ground case, while the areas under the peaks of each case are similar. The same differences occur in the lift signal, with irregular and higher frequency oscillations observed (Figure 6.4). This all suggests that for the ground proximity case, the vortex shedding mechanism is less coherent than in the away-from-ground case.

Ground	C_d	$C_{L,rms}$*	C_{pb}	St_D	$P\{D_{max}\}$	St_l	$P\{L_{max}\}$	t_{total}
No	0.72	0.29	-0.51	0.44	$1.2 \times 10^{-}2$	0.22	$2.8 \times 10^{-}5$	367 (5.38 s)
Yes	0.60	1.86*	-0.38	0.27	$7.8 \times 10^{-}6$	0.27	$9.3 \times 10^{-}5$	83 (1.37 s)

TABLE 6.1: Natural flow statistics for away-from-ground case (first line) and ground proximity case (second line). * for the away-from-ground case this value is $C_{L,rms}$, for the ground case $C_{L,ave}$

6.1.1 Natural time-averaged flow structure and topology

The time-averaged flow-field is significantly affected by the ground plane. Most striking are the changes upstream of the rear face. Separation occurs over the upper edge, with re-attachment occuring $2.26H$ downstream of the leading edge, 41% greater than for the away-from-ground case. No separation occurs over the lower edge, with the flow underneath the body somewhat resembling a steady channel flow, complete with laminar boundary layer. In fact, to be more specific, this region is a *Coutte* flow scenario, where one surface is moving at the freestream velocity (here, the ground plane), while

the other surface is stationary (here, the lower body surface). Such scenarios result in an almost linear streamwise velocity profile, $U(y) = U_\infty \frac{y}{h} + \frac{1}{2\nu}\frac{dp}{dx}(y^2 - hy)$. When the pressure gradient is small, as is the case here, the first term is much larger than the second, which results in a near-constant shear stress throughout the region. While the mass flow rate in this "Couette" region (referred to as the channel region hereafter) remains constant as the rear edge is approached, the peak velocity slightly increases due to a growing boundary layer along the body's lower surface.

The disparity at the front of the body leads to an asymmetric pressure profile, with the stagnation point occurring below the centrepoint of the nose. Furthermore, a large band of negative pressure appears in the separated region above the body. This all results in the high average lift coefficient of 1.86.

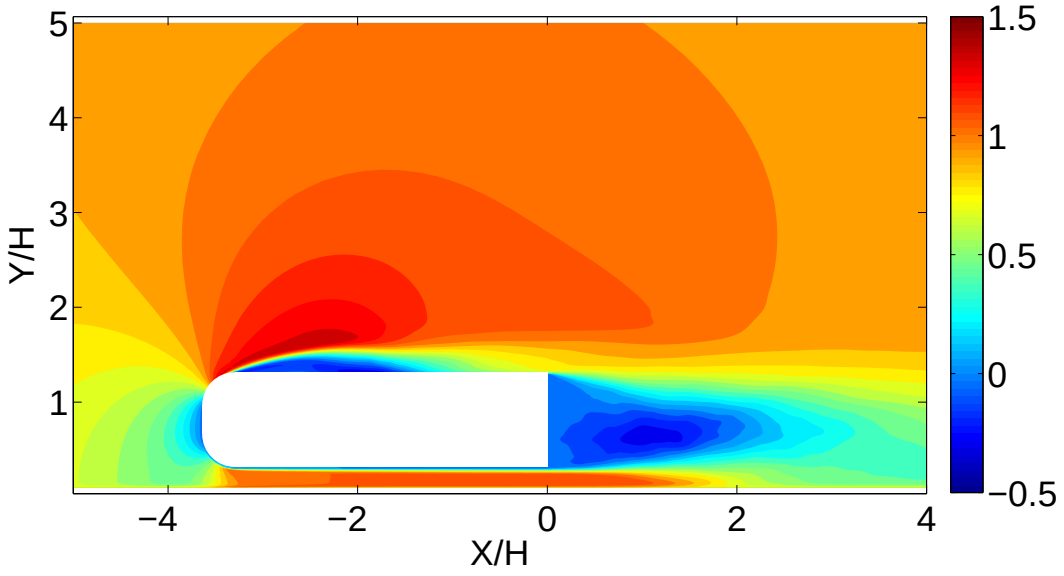

FIGURE 6.5: Time-averaged u velocity along the centreplane.

6.1.2 Boundary layer

While the away-from-ground flow case features two identical boundary layers, here there are three boundary layers, each with a unique profile. The upper surface boundary layer is turbulent, and thicker than that observed in the away-from-ground case due to the greater region of separation over the upper front edge. The lower surface boundary layer is laminar and has a displacement thickness of $0.024H$ and momentum thickness $0.010H$. The ground boundary layer is less typical – normally a surface moving at the freestream velocity features no boundary layer. However, here the fluid velocity

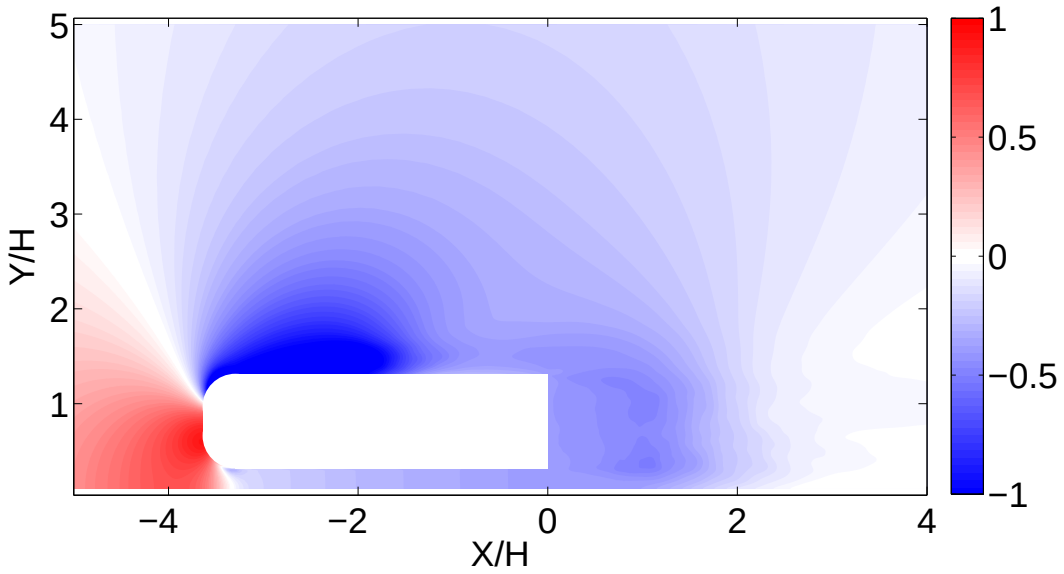

FIGURE 6.6: Time-averaged pressure coefficient contour through the centre plane.

reaches $1.15U_\infty$ at the lower rear edge (it is worth repeating here that U_∞ is the *corrected* freestream velocity) due to the slight pressure gradient between front and back, resulting in a difference in velocity between ground plane and the fluid in the centre of the channel. Thus, while Morton (1984) showed that no vorticity is generated at a surface moving in its own plane steadily, here a vorticity is generated due to the pressure gradient. This will be shown to influence the wake dynamics in §6.2.

The upper surface turbulent boundary layer has a momentum thickness of $0.5H$, and a displacement thickness of $0.58H$, all considerably larger than the boundary layer thickness of the away-from-ground case (which featured values of $0.019H$ and $0.025H$ respectively). This is due to the greater separation length over the upper leading edge, which leaves less room for the detached turbulent structures to decay and the re-attached flow to establish a traditional boundary layer profile.

6.1.3 Wake

In the wake region the asymmetry of the time-averaged flow is less pronounced in the velocity and pressure contour plots. The dead-water region of the wake seems to occur halfway between the upper body surface and the ground plane, rather than halfway between the upper and lower body surfaces. Of further note is the perseverance of the flow from the lower channel beyond into the wake region.

Time-averaged streamlines (Figure 6.8) and vectors provide a clearer look at the

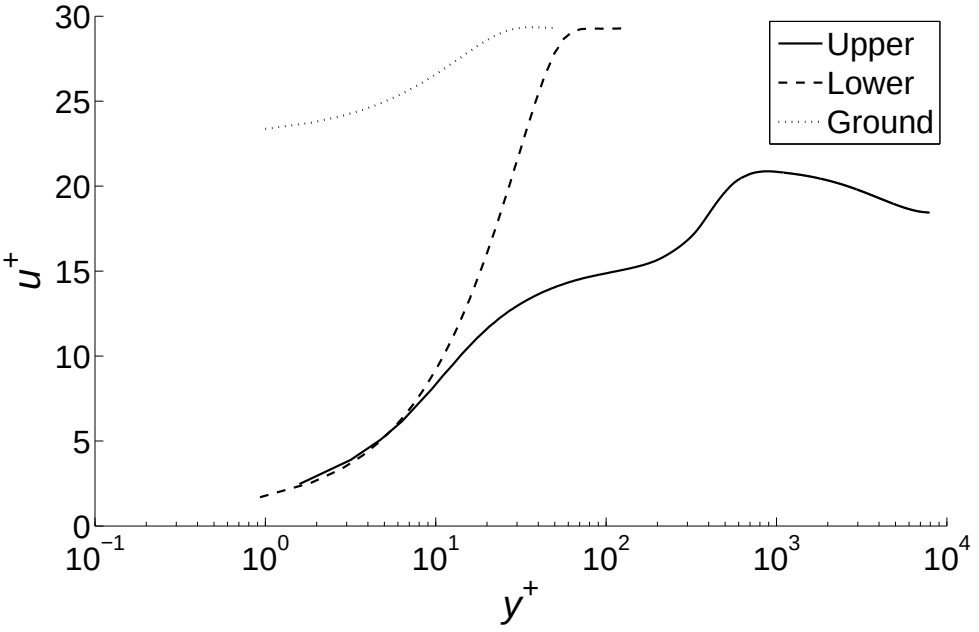

FIGURE 6.7: Spanwise- and time-averaged boundary layer profile $X/H = -0.1$ (i.e. 0.1 upstream of the rear).

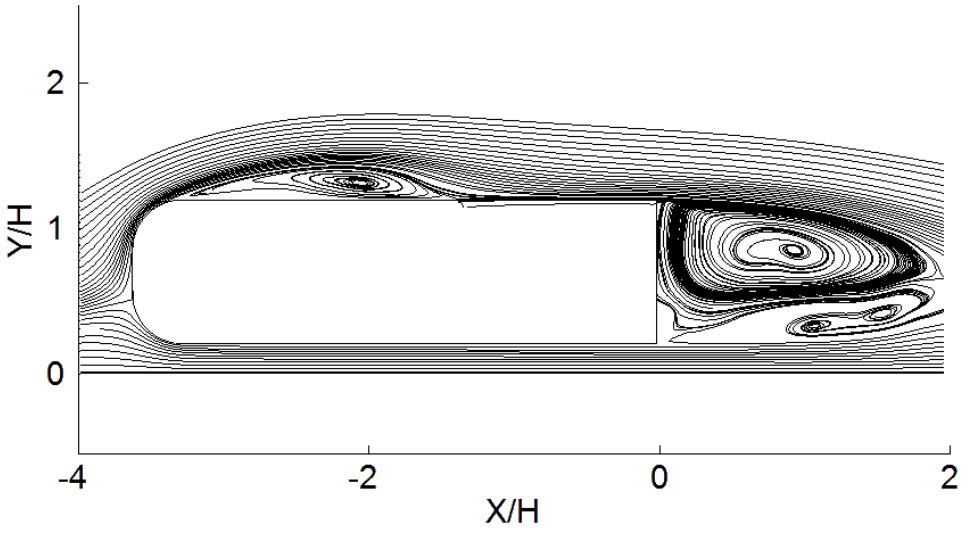

FIGURE 6.8: Time-averaged velocity streamlines through the centre plane.

asymmetry in the wake. The upper recirculation region dominates the wake, with the lower recirculation region narrower and far less pronounced. The centre of this lower recirculation region is further downstream than that of the upper ($1.34H$ compared to $0.95H$). The strong reverse flow region that results from these two opposing recirculation zones, and which normally occurs at the centreline of the wake, is pushed much lower in this case. This results in a region of minimal flow activity just downstream of

the lower rear separation point, and upward travelling flow along the remainder of the rear face.

The Reynolds stresses in the wake, shown in Figure 6.9 are also noticeably different in the presence of ground. $\langle u'u' \rangle$ and $\langle v'v' \rangle$ feature a very similar distribution, and are significantly less intense than for the away-from-ground case (Figure 4.10). The $\langle u'v' \rangle$ component is at a similar level to the away-from-ground case, but does not feature the small oppositely-signed pocket regions near the base. The separatrix (mean separation line) extends $1.85H$ downstream, compared to $0.95H$ for the away-from-ground case.

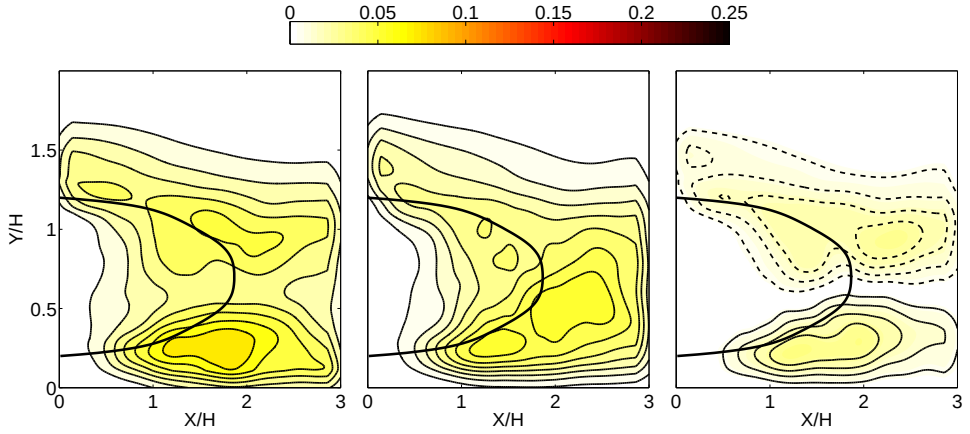

FIGURE 6.9: Reynolds stress averages along the centreplane in the wake. From left to right: $\langle u'u' \rangle / U_\infty^2$, $\langle v'v' \rangle / U_\infty^2$, $\langle u'v' \rangle / U_\infty^2$. Dashed contour lines indicate negative magnitudes. Thick line indicates separatrix (mean separation line).

Figure 6.10 shows that the wake features an altogether higher pressure, with two low pressure regions vertically aligned a distance of $X \approx H$ behind the rear. This indicates that the upper and lower shear layers do not interact nearly as much as the away-from-ground case, which shows only one large low pressure region (Figure 4.11). Closer to the body, an asymmetry in the pressure profile develops, with a lower pressure observed on the upper half of the rear face (Figure 6.10).

In conclusion, the main differences of the ground proximity time-averaged wake, when compared to the away-from-ground wake, are a higher pressure throughout, lower Reynolds stresses, a longer wake length, and the introduction of asymmetry.

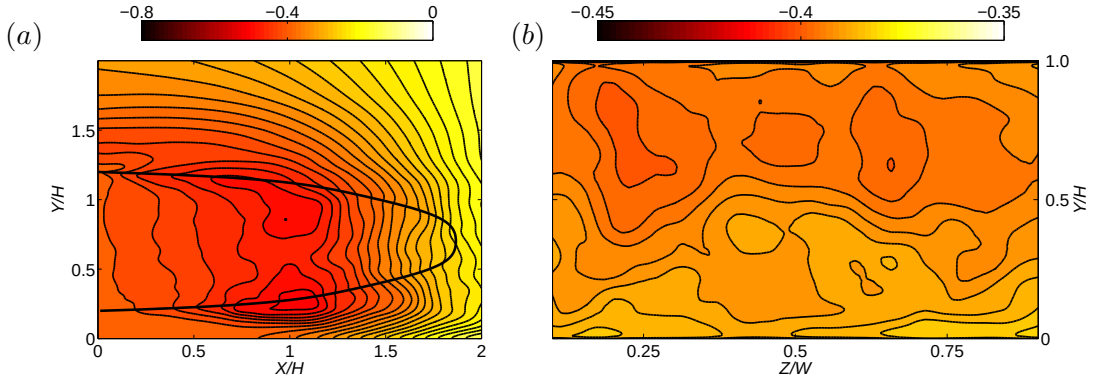

FIGURE 6.10: (a) Time-averaged pressure coefficient along centreplane in wake and (b) on the rear base surface over $0.1 < Z/W < 0.9$. Thick line represents separatrix.

6.2 Natural transient flow characteristics

6.2.1 The von Kármán and Kelvin-Helmholtz instability modes

In addition to the time-averaged differences discussed above, an analysis of the transient results reveals that the dynamics in the wake are also significantly different from the away-from-ground case. The drag and lift signal analysis presented above suggested the prevalence of vortex shedding in the wake is significantly diminished, and the velocity monitors add further evidence. No clear frequency peaks are observed in either upper or lower positioned monitor points (Figure 6.11). Observation of the actual flow field confirms this: no visible vortex shedding is observed.

6.2.2 Dynamic Mode Decomposition

Dynamic mode decomposition confirms this absence of strong vortex shedding in the wake. The Ritz and mode magnitude plots, Figures 6.12 (a) and (b) respectively, show no dominant dynamic mode appears in the decomposition. The two highest magnitude modes are shown in Figure 6.13, and reveal numerous turbulent structures in the near wake with little coherent spatial structure. Some structure does appear further downstream, however, for both cases. This is especially true for the second mode, where alternate-signed paired regions of vorticity at $X/H > 1$ are observed, and appear to be spaced apart at a regular interval. This, coupled with the lack of structure in the near-wake, reveals that the presence of the ground plane does impose some regular dynamic behaviour on the flow, while limiting the vortex shedding.

However, it must not be forgotten that these dynamic modes are very weak, and the mean mode superimposed with unstructured turbulent structures is the overwhelming

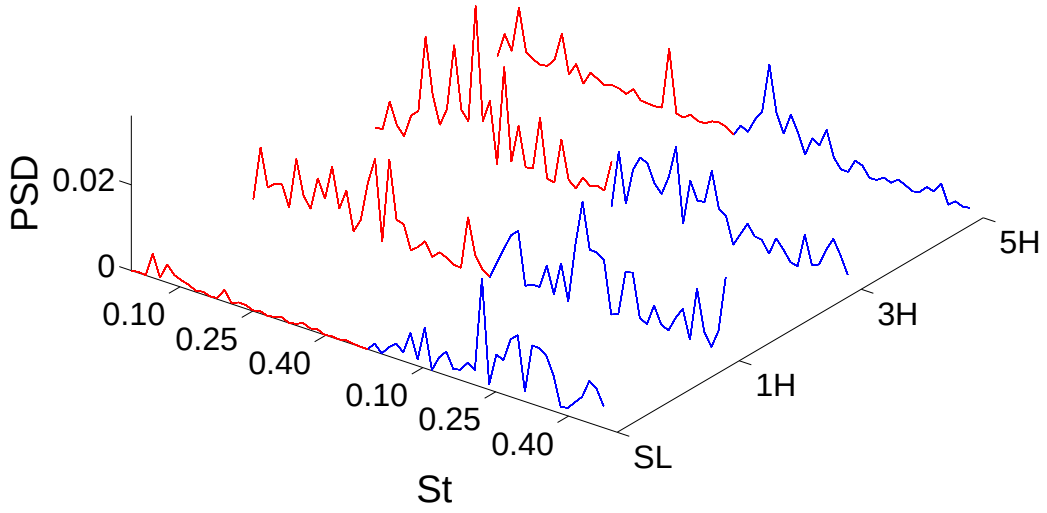

FIGURE 6.11: Spectra of velocity monitors in shear layer, 1H, 3H and 5H downstream of rear. The red line represents the lower-wake monitors, while the blue line represents the upper-wake monitors. See § 2.5 for exact locations of monitor points

.

modus operandi of the flow. The mean mode, pictured in Figure 6.12(c), is very strong, and also reveals some new insights to the flow. Two regions of opposite sign vorticity appear on the ground plane. These seem to affect the lower shear layer, which has a high vorticity at separation but does not extend as far downstream as the upper shear layer.

6.3 Actuated flow statistics

For the body in ground proximity, actuation was applied in the same manner as that described in §4, this time after 36 non-dimensional time units (0.58 seconds) of natural flow. The actuation proved far less successful at reducing drag, with minimal changes observed in the mean drag for all actuation frequencies. Figure 6.14 shows that, like in the away-from-ground case, the drag signal locks-on to the actuation signal almost immediately. In fact, the amplitude of the drag signal is even larger than that observed in the away-from-ground case. For the case shown, $St_{act} = 0.22$, the average drag signal amplitude is 0.21 for the former and 0.16 for the latter.

However, the lift signal responds in a completely different manner to the response observed in the away-from-ground case, where it remained oscillating at the natural

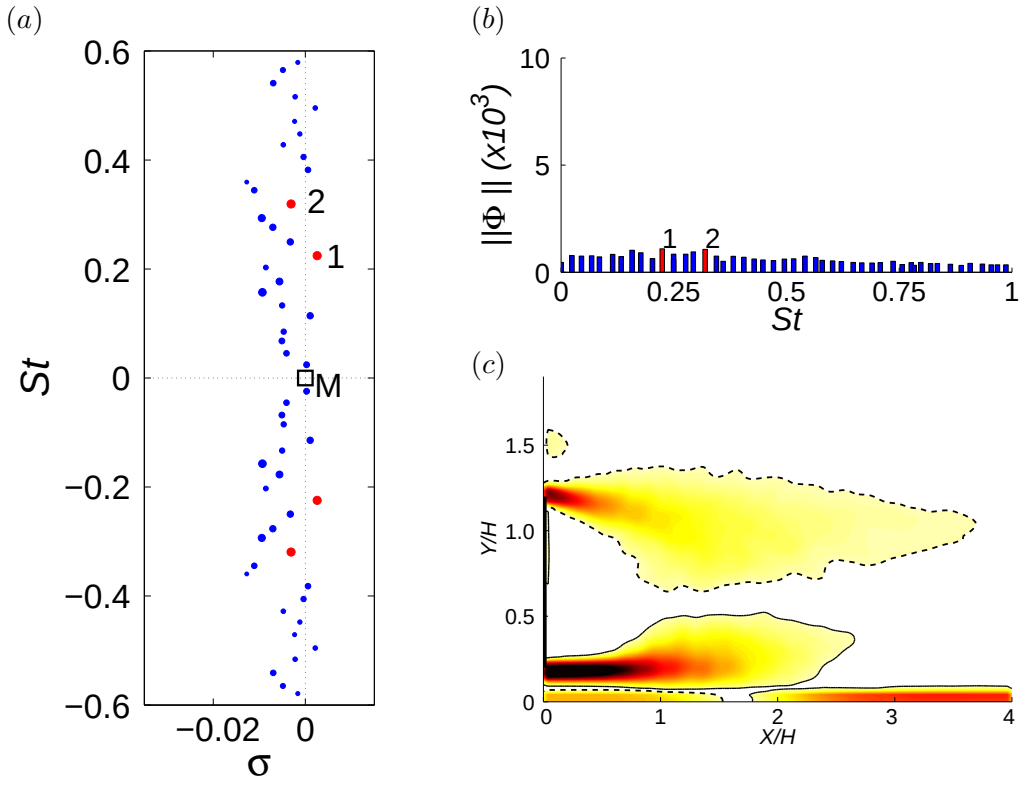

FIGURE 6.12: Natural flow dynamic mode decomposition for ground proximity case: (a) spectrum showing the growth rate (σ) of each mode. The red dots are the most relevant modes, with the size of each dot showing its relative magnitude. The mean mode (M) is indicated with an open square. Modes 1 and 2 occur at $St = 0.22$ and $St = 0.32$ respectively, but are very weak; (b) The relative magnitude of each mode is plotted against frequency; and (c) vorticity contours for the mean mode.

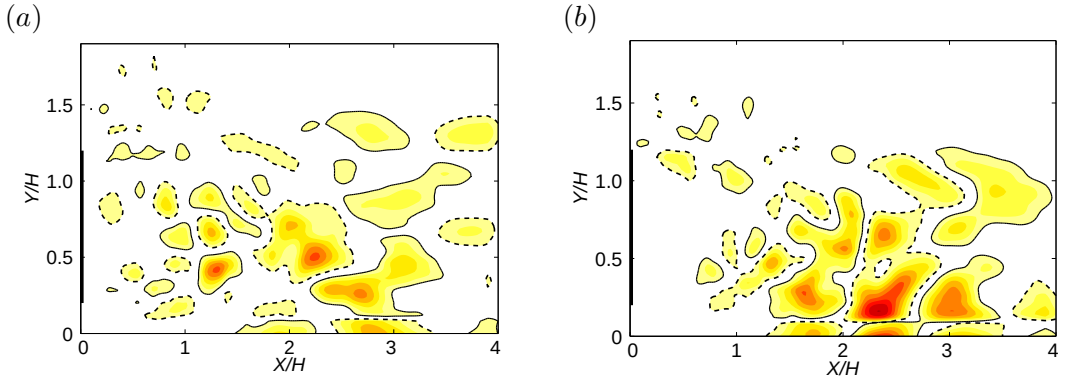

FIGURE 6.13: (a) Vorticity contours of the highest magnitude dynamic mode, which occurs at a frequency of $St = 0.22$. (b) Vorticity contours of the second highest magnitude dynamic mode, which occurs at a frequency of $St = 0.32$.

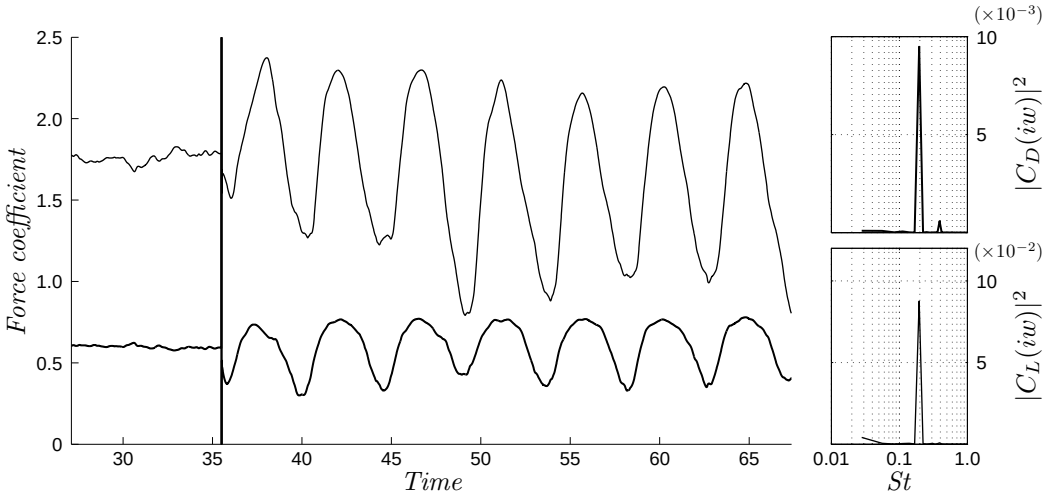

FIGURE 6.14: Time history of drag (lower line) and lift (upper line) signals for $St_{act} = 0.195$. The frequency spectrum for each signal is displayed on the right. The drag spectra amplitude (top) is displayed at an order of magnitude lower than the lift spectra amplitude (bottom). Both signals return a distinct peak at the actuation frequency of 0.195. The discontinuity at $t = 36$ corresponds to the switch from unforced to forced flow.

Strouhal frequency but with less coherence. Here the lift signal locks-on to the actuation frequency for all cases, oscillating at large amplitudes, and the mean lift coefficient drops. A slight lag occurs, with the lift signal $15 - 35°$ behind the drag signal (the lag reduces as actuation frequency increases).

The signals shown in Figure 6.14 are representative of all cases. However, the amplitude of the drag signals grows slightly with increasing actuation frequency, while the amplitude of the lift signal decreases significantly. This is represented in Figure 6.15(b), which displays the spectral peaks of both signals. Once again, as was observed for the away-from-ground case, the lowest frequency case $St_{act} = 0.04$ shows small high frequency oscillations superimposed on the locked-on signals.

Despite the lock-on of both drag and lift signals, Figure 6.15(a) shows that the actuation has little impact on the mean drag value. The only case that appears to offer any drag reduction is the lowest frequency case, $St_{act} = 0.04$. However, the drag reduction obtained for this case is still well below that of the away-from-ground tests. This case shows a high natural frequency peak in the lift signal spectra, and a low actuation frequency peak in the drag spectra – in the away-from-ground case these measures would correspond to the worst performing run.

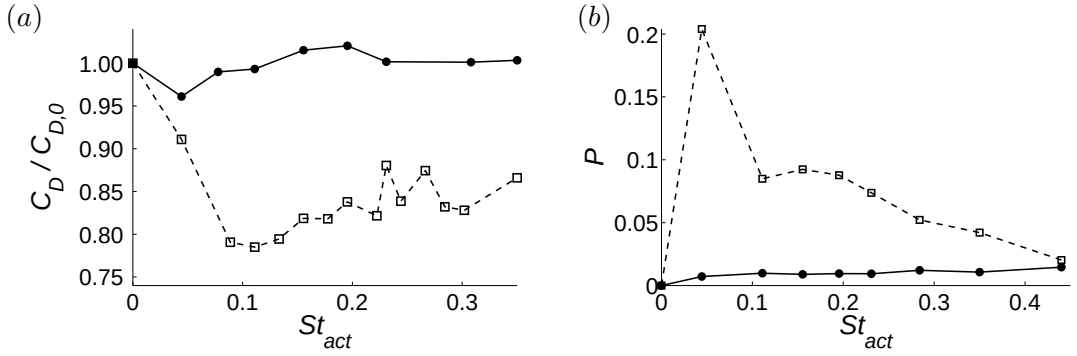

FIGURE 6.15: (a) Numerical results for mean drag at different actuation frequencies. Thick line (filled dots) represents ground proximity with body $0.2H$ above ground plane; dashed line (open squares) represents away-from-ground case. (b) Magnitude of actuation frequency spectral peaks for drag signal ($P\{D_{act}\}$, closed circles) and for lift signal ($P\{L_{nat}\}$, open squares).

6.3.1 Effect of momentum coefficient

In an attempt to find a successful drag reduction case, the momentum coefficient was doubled to $C_\mu = 0.016$ for the case with $St_{act} = 0.35$. This proved to have the opposite of the desired effect, returning no change in the drag at all, compared to a 2.0% drag reduction at $C_\mu = 0.008$.

Finally, a case was tested with an asymmetric momentum coefficient set up: $C_\mu = 4 \times 10^{-3}$ for the upper slots combined, and $C_\mu = 8 \times 10^{-3}$ for the lower slots combined (leaving a total $C_\mu = 0.12$). The idea behind this was to generate larger vortices in the lower shear layer, so that they were closer in size to the upper layer vortices. This was indeed achieved by introducing this configuration, however the result was a drag increase of 2.0%. As expected, evening the size of the upper and lower vortices has no beneficial effect on the drag, as the natural case features minimal vortex shedding in the first place. It appears likely that there is no more sophisticated method of periodic forcing capable of having a beneficial effect on drag for shear layers influenced by the ground effect. These results in particular do not offer any new insights into the ground proximity flow and its potential for control. As such, they will not be explored in further detail.

6.4 Actuated time-averaged flow structure and topology

The time-averaged properties of the case $St_{act} = 0.195$, which produced results typical of all actuation cases, are analysed here to gain further insight into the actuated flow. The mean separation line indicates a shorter wake under actuation—the opposite of

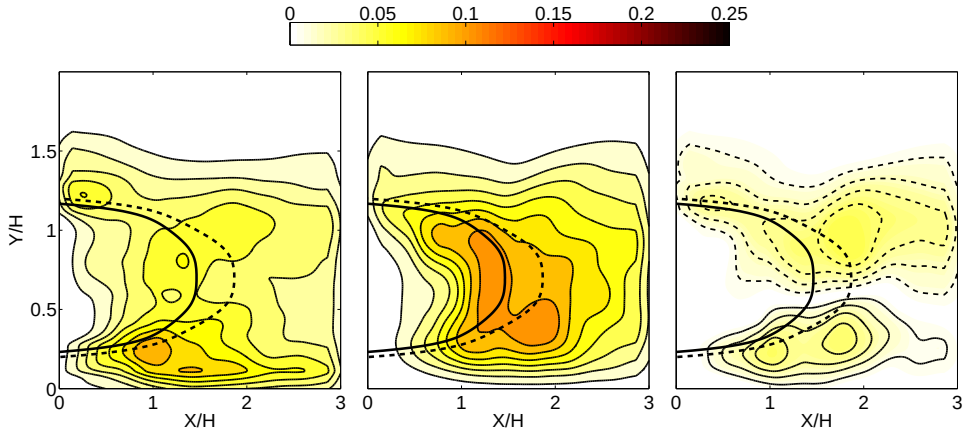

FIGURE 6.16: Reynolds stress averages along the centreplane in the wake for $St_{act} = 0.195$. From left to right: $\langle u'u' \rangle / U_\infty^2$, $\langle v'v' \rangle / U_\infty^2$, $\langle u'v' \rangle / U_\infty^2$. Dashed contour lines indicate negative magnitudes. Thick line indicates separatrix (mean separation line), dashed thick line indicates separatrix of unforced case.

what occurred away from ground. The Reynolds stresses, pictured in Figure 6.16, are slightly larger than observed in the natural case. The vertical velocity normal stress, $\langle v'v' \rangle$, experiences the largest increase, with a region of high energy fluctuations appearing at the centre of the mean separation line. The increased diffusion through these higher Reynolds stresses increases the curvature of the streamlines, leading to the shorter recirculation zone.

The wake time-averaged pressure contours, Figure 6.17, have a very similar topology to the natural case. However, here the minimum pressure regions are pushed closer to the base – for the natural case they were located around $X/H = 1$, whilst here they are at around $X/H = 0.8$. Once again, this is the opposite of what was achieved for actuation away from ground, where the minimum pressure regions were pushed further downstream. Furthermore, the asymmetry of the base pressure profile in the natural ground case seems to be exaggerated by actuation. The lower half of the base has a time-averaged pressure similar to the natural case ($C_P \approx -0.39$), however, the upper half is markedly reduced, especially at the upper extremities, where C_P approaches -0.60.

6.5 Actuated flow dynamic behaviour

Velocity monitors in the wake reveal the lower shear layer is influenced more by actuation than is the upper separating shear layer. This is due to the greater turbulent fluctuations that occur in the upper shear layer, compared to the laminar lower shear

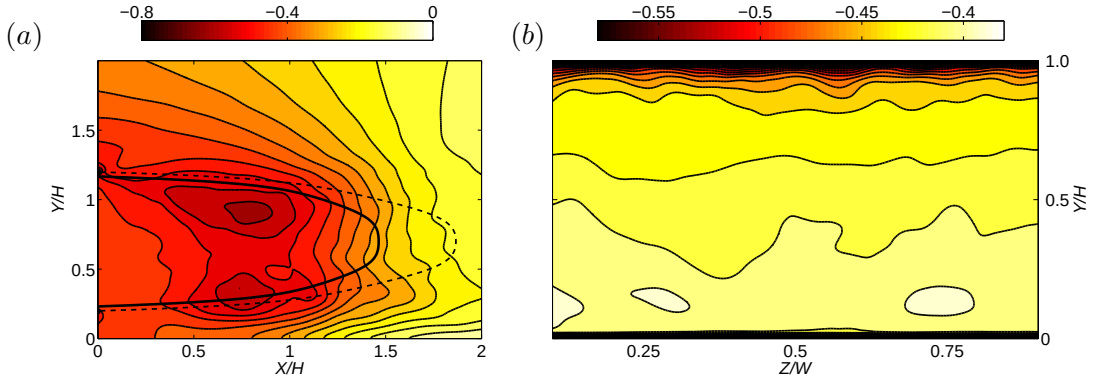

FIGURE 6.17: Time-averaged pressure coefficient along centreplane in wake (a) and on rear base surface over $0.1 < Z/W < 0.9$ (b) for $St_{act} = 0.195$. Thick line represents separatrix, dashed thick line indicates separatrix of unforced case.

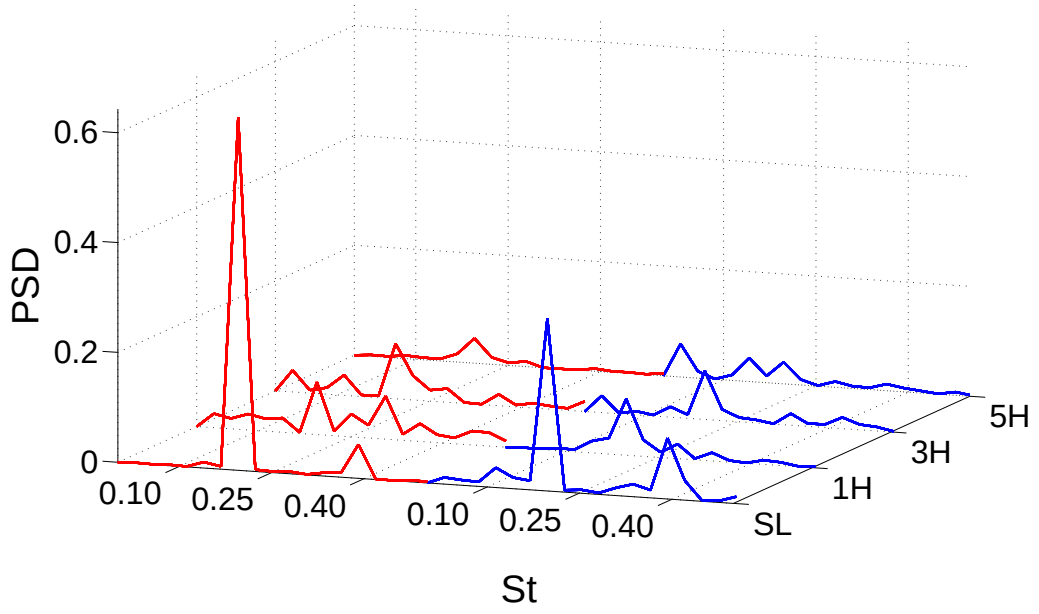

FIGURE 6.18: Spectra of velocity monitors in shear layer, 1H, 3H and 5H downstream of rear for $St_{act} = 0.195$. The red line represents the lower-wake monitors, while the blue line represents the upper-wake monitors. All peaks occur at St_{act}. See § 2.5 for exact locations of monitor points.

layer. The spectra, therefore, return higher peaks for the bottom signals, as shown in Figure 6.18.

6.5.1 Phase averaging

The phase-averaged vorticity contours reveal the local maximum points in the drag and lift signals occur when the upper vortex is in the near wake, at $X/H \approx 0.7H$, while the local minimum points occur when the upper vortex has travelled further downstream to

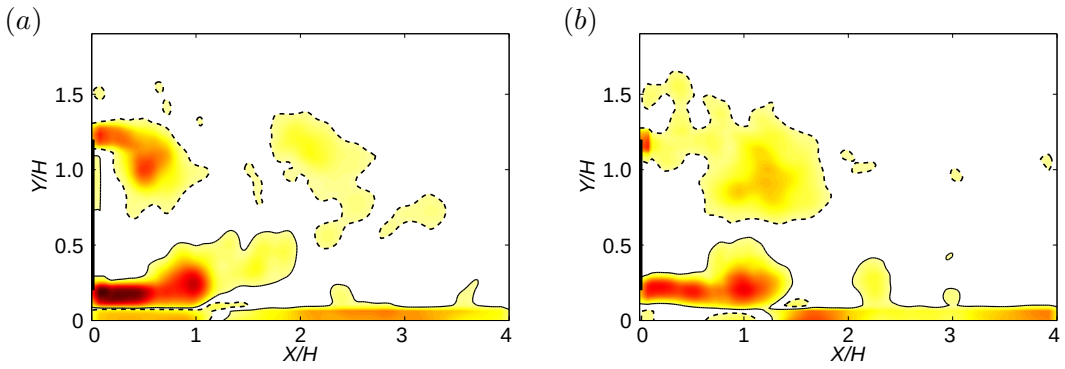

FIGURE 6.19: Phase averaged spanwise averaged vorticity contours for $St_{act} = 0.195$ at drag signal (a) peaks and (b) troughs.

$X/H \approx 1.3$. The lower vortex shows a reduction in the vorticity between the maximum and minimum signal values, however, no change in position appears to be involved. The lower vortex generated by actuation appears to stagnate around $X/H = 1$, while only the upper convects further downstream.

The dominance of the upper vortex reveals why the lift signal locks in to the actuation signal. In the away-from-ground case, the symmetric vortices are shed simultaneously, and there is therefore little net force imparted on the body in the vertical direction. Here, the motion of the upper vortex dictates the oscillations of the lift signal (and, of course, the drag signal). This causes very large oscillations in the lift signal; however, the oscillations are not large enough to create negative lift on the body at any point in time.

6.5.2 Dynamic Mode Decomposition

For the natural ground case, dynamic mode decomposition revealed no dominant dynamic modes in the wake. Applying actuation does, as expected, produce a dominant dynamic mode evident in the Ritz and mode magnitude plots of Figure 6.20. Figure 6.21 shows the mode shares similarities with mode A of the away-from-ground flow: namely, opposite-signed vortices are concurrently produced in the upper and lower shear layers. However, the vortices created here are not symmetric – the upper vortices are noticeably larger in size than the lower. Furthermore, an extra region of vorticity is observed on the ground plane. This complicates the evolution of the vortex pairs, resulting in a more intricate wake. Figure 6.22 shows this evolution over half an actuation cycle, allowing the mechanism to be analysed further. It can be seen that as the upper vortex grows, it moves towards the centre of the wake. This does not occur for

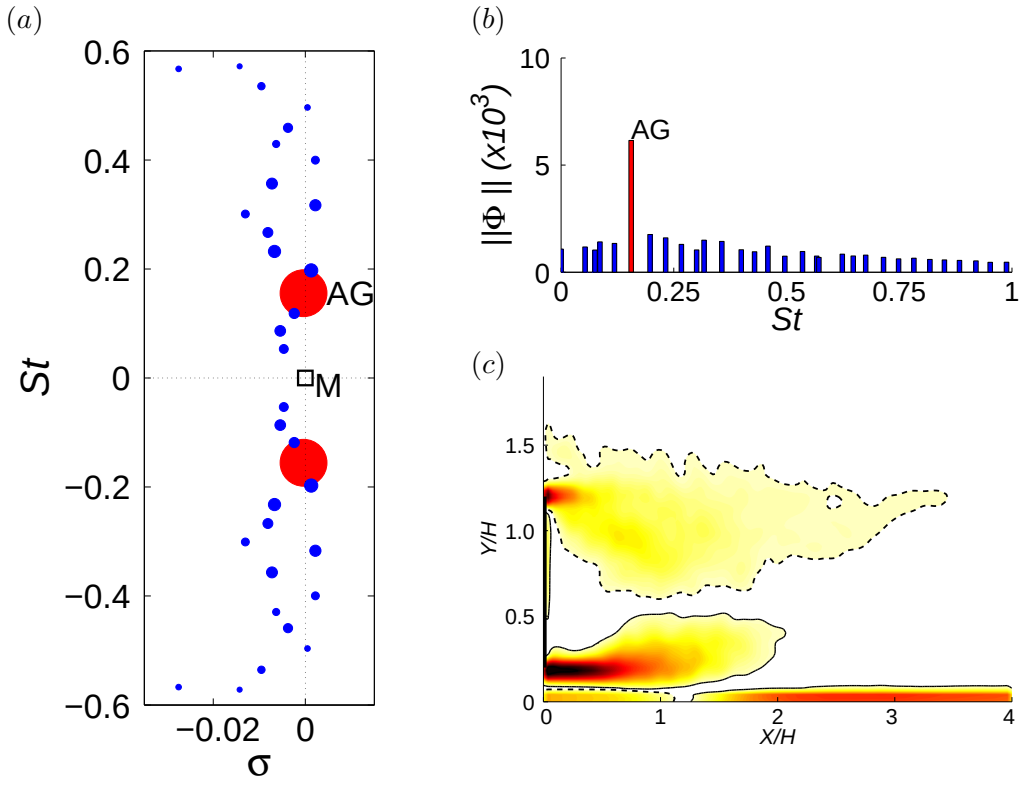

FIGURE 6.20: Dynamic mode decomposition for $St_{act} = 0.155$: (a) spectrum showing the growth rate (σ) of each mode. The red dots are the most relevant modes, with the size of each dot showing its relative magnitude. The mean mode (M) is indicated with an open square. Mode AG occurs at the actuation frequency, $St_{act} = 0.155$; (b) The relative magnitude of each mode is plotted against frequency; and (c) vorticity contours for the mean mode.

the lower vortex, which grows in the streamwise direction rather than vertically towards the centre. The result is an uneven pair of vortices travelling downstream—the upper large vortex resembling that created in the away-from-ground actuation, and the lower a thin, horizontally-aligned region above the ground. This structure is observed for all actuation cases, with the vortices becoming smaller at the higher actuation frequencies.

The results suggest that the less coherent vortex shedding which occurs for natural flow in the presence of ground is the major reason why this form of actuation, which attempts to mitigate vortex shedding, is ineffective. In the case of ground proximity, the upper and lower shear layers are no longer identical – the ground plane develops its own vorticity which interferes with the lower shear layer, while the upper shear layer is thicker and more turbulent due to the leading edge separation over the upper half of the body. This physical disparity reduces the propensity of the upper and lower shear layers to interact and roll-up into one another.

Wavelet analysis, which can be seen in Appendix B (Figure 10), confirms the above

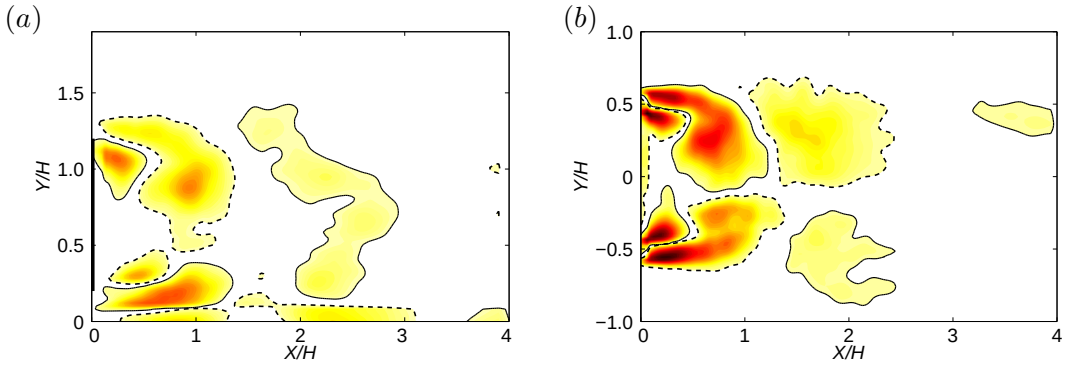

FIGURE 6.21: Vorticity contours at $St_{act} = 0.155$ for the first unsteady Koopman mode in (a) the ground proximity case (mode AG) and (b) the away-from-ground case (mode A).

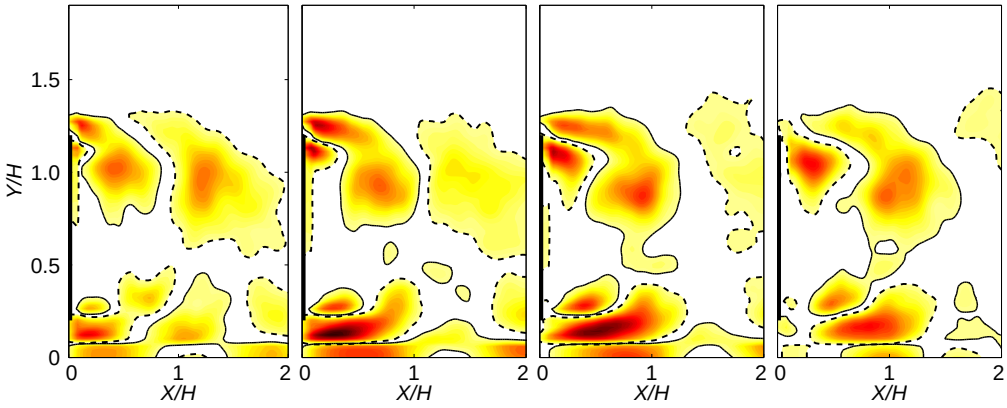

FIGURE 6.22: $St_{act} = 0.155$: Vorticity contours of half a cycle of first unsteady Koopman mode (mode AG). The second half of the cycle continues as above, but with opposite signed vorticity.

findings: no dominant frequency is present in either the drag or lift signals for natural flow, while under actuation both the drag and lift signals lock-on to the actuation frequency.

6.6 Summary

The results presented in this chapter highlight a striking influence of ground proximity on the natural flow. The results overwhelmingly suggest that actuation is unlikely to yield notable drag reduction for bluff body shear layers in the presence of ground, i.e. those behind the upper and lower rear edges of a truck-trailer. It appears that the limited interaction of the shear layers renders the current technique of producing synchronous vortices much less effective.

Chapter 7

Conclusions

7.1 Summary of results

This chapter contains a brief summary of the conclusions of the thesis. The reader is directed to individual results chapters for more detailed discussions on the conclusions.

This thesis has presented analysis and numerical investigation of open-loop periodic wake control at the rear edges of a D-shaped bluff body, with an eye to its potential for drag reduction on heavy vehicles. This first required the replication and verification of experimental work on a simplified model in the absence of ground, with the numerical method allowing for new insights on the flow to be developed. Actuation at angles perpendicular and parallel to the freestream was also tested. Finally, the effect of ground proximity was studied, with the body moved $0.2H$ above a moving ground plane.

In chapter 3 focus was placed on the influence of actuation frequency, with an optimum actuation frequency of $St_{act} = 0.11$ being found, slightly lower than the $St_{act} = 0.15$ found experimentally by Pastoor *et al.* (2008) for a similar but not identical setup. The numerical approach undertaken provided new perspectives on the wake mechanisms in both the natural and actuated flows. Actuation was seen to create a new mode in the wake, mode A, characterised by the creation of synchronous vortices in the upper and lower shear layers. The natural shedding mode, mode N, was also observed in all actuation cases, but was less prevalent for the more successful forcing frequencies.

A hypothesis on the success of lower actuation frequencies was also presented. Dynamic mode decompositions showed a lower ratio of mode A vortex circulation to mode N vortex circulation existed for the higher actuation frequency cases. This suggests the higher actuation frequencies do not allow the synchronous vortices enough time to

develop a sufficient size to impact the wake, which results in a less symmetrical near wake.

In chapter 5 the influence of momentum coefficient C_μ and actuation orientation was explored. The former was shown to influence the period of time the upper and lower shear layers spent in-phase, with a threshold value existing below which the upper and lower shear layers are unable to maintain in-phase flow for significant periods of time. This threshold value changes depending on the actuation frequency, with optimal cases having a lower threshold.

The actuation orientation was tested by isolating the shear-layer and base actuation configurations, with the findings suggesting each affects the wake in different ways, and that these mechanisms are beneficial to one another when operating in unison. The base actuation case is more effective at disrupting the natural instability, and appears to offer greater potential at this Reynolds number. Further investigation of these mechanisms is recommended, especially at higher actuation frequencies.

Chapter 6 covered the effect of ground proximity on the natural and actuated flow. The results showed that the presence of ground suppressed the von Kármán shedding mechanism, resulting in a lower drag coefficient. The drag reduction delivered by actuation was negligible, due to the technique's large reliance on the 2D nature of the von Kármán shedding process. This also raises doubt that the actuation technique would work at higher Reynolds numbers, such as those encountered by trucks, where the von Kármán mechanism is thought to be weaker.

7.2 Scope of results

While the above conclusions offer many new insights into bluff body aerodynamics and flow control, they cannot be directly applied to actual truck-trailers, which are three-dimensional bluff bodies and which operate at higher Reynolds numbers. They do, however, allow us to propose some new hypotheses on the suitability of the actuation technique on truck-trailers. It appears that actuation is more likely to be successful if applied to the rear side edges of a trailer, where the opposite shear layers do not experience a ground proximity effect, as opposed to the upper and lower rear edges, where the shear layers do. This idea is illustrated in Figure 7.1.

The flow behind a three-dimensional body is likely more complex than this hypothesis suggests, but it is a useful starting point. Recommended work towards realising

whether this hypothesis is valid is outlined below, in the recommendations section.

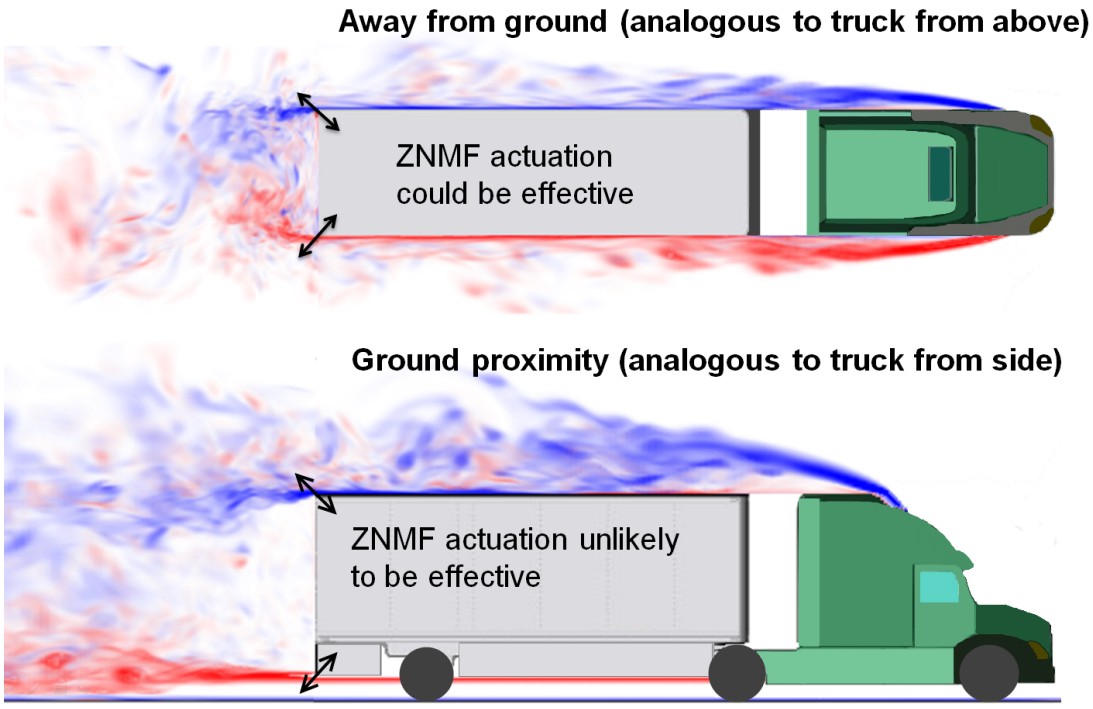

FIGURE 7.1: Schematic of possible effect of Zero Net Mass Flux (ZNMF) actuation at side and upper/lower rear edges of a truck-trailer. The blue/red colours indicate regions of instantaneous vortices from the results presented in this thesis (the top image uses natural flow from the away from ground case, while the bottom image uses natural flow from the ground proximity case).

7.3 Recommendations

The numerical results presented in this thesis are currently being experimentally verified at Monash University. The experimental technique being used also allows for much higher Reynolds numbers to be tested, which is vital in determining whether the technique has potential on truck-trailers. Preliminary results reveal that the method does continue to yield drag reduction at Reynolds numbers of up to 600,000, with shear-layer actuation proving more effective at the higher Reynolds numbers than was shown here. However, these tests have not been replicated in ground proximity. This remains a necessity, and is a strongly recommended area for future work.

The method of control analysed in this thesis is relatively new, having first been explored only in the last decade. Thus, this research is but one link in a long chain of necessary work required to optimise the method for potential heavy-vehicle drag reduction. The research has shown the large difference that exists between opposite

shear layer interaction behind a body in freestream and a body in ground proximity. The next step requires full characterisation of a flow with both of these scenarios, i.e. an Ahmed-style three-dimensional body in ground proximity (upper and lower shear layers are influenced by the ground, and side shear layers are not). Work in this area has recently been published (Grandemange *et al.* 2013), which suggests a complex interaction of the four shear layers and corner vortices exists and recommends further analysis. Importantly, this experimental study focussed largely on dynamic features of the wake, which should be a point of emphasis for future work (as opposed to the sole exploration of time-averaged features).

Furthermore, it appears that most three-dimensional rounded leading-edge bluff body studies are conducted in ground proximity, in an attempt to approximate vehicle flow, while most two-dimensional studies are conducted away from ground. There appears to be a gap in the literature of two-dimensional bodies in ground proximity (which this thesis attempts to partially address) and three-dimensional bodies away from the ground. The author feels the latter could also potentially offer new insights into the flow of truck-trailers, as necessary information may be missed by jumping two levels in complexity (from two-dimensional bodies away from ground to three-dimensional bodies near to ground) rather than by stepping up complexity one level at a time.

Of course, in addition to characterisation of the natural flow for these cases, open-loop periodic actuation should also be attempted from the rear edges, with testing on a full-scale truck-trailer the ultimate goal.

Appendix A

The attached CD

The attached CD contains a collection of movie files showing the spanwise vorticity development in the wake with time. Dual, shear layer and base actuation at $St_{act} = 0.11$ are included for the away-from-ground case, in addition to the natural flow case. For the ground proximity case, the natural flow and dual actuation at $St_{act} = 0.11$ are included.

The vorticity is spanwise averaged from 7 equidistant planes through the domain. Accompanying the vorticity contours in these movies are two signal plots - the upper left plot is the rear base pressure signal, while the upper right is the lift signal. This aids in understanding the relationship between the wake dynamics and the forces experienced by the body.

An electronic copy of this text is also available on the disc.

Appendix B

Wavelet analysis plots

The wavelet plots were generated using a collection of MATLAB scripts developed by Aslak Grinsted of the United Kingdom National Oceanography Centre. Further information on these scripts can be found at http://noc.ac.uk/using-science/crosswavelet-wavelet-coherence.

Figures B.1-B.5 relate to Chapter 4, Figures B.6-B.9 to Chapter 5 and Figure B.10 to Chapter 6.

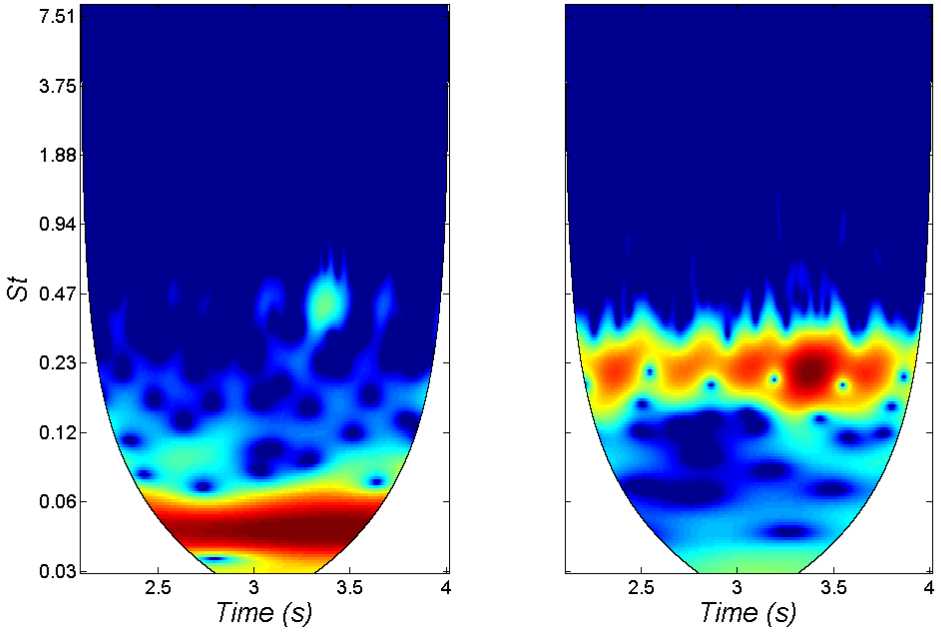

FIGURE B.1: Wavelet analysis on the drag (left) and lift (right) signals for actuation at $C_\mu = 8 \times 10^{-3}$ and $St_{act} = 0.04$.

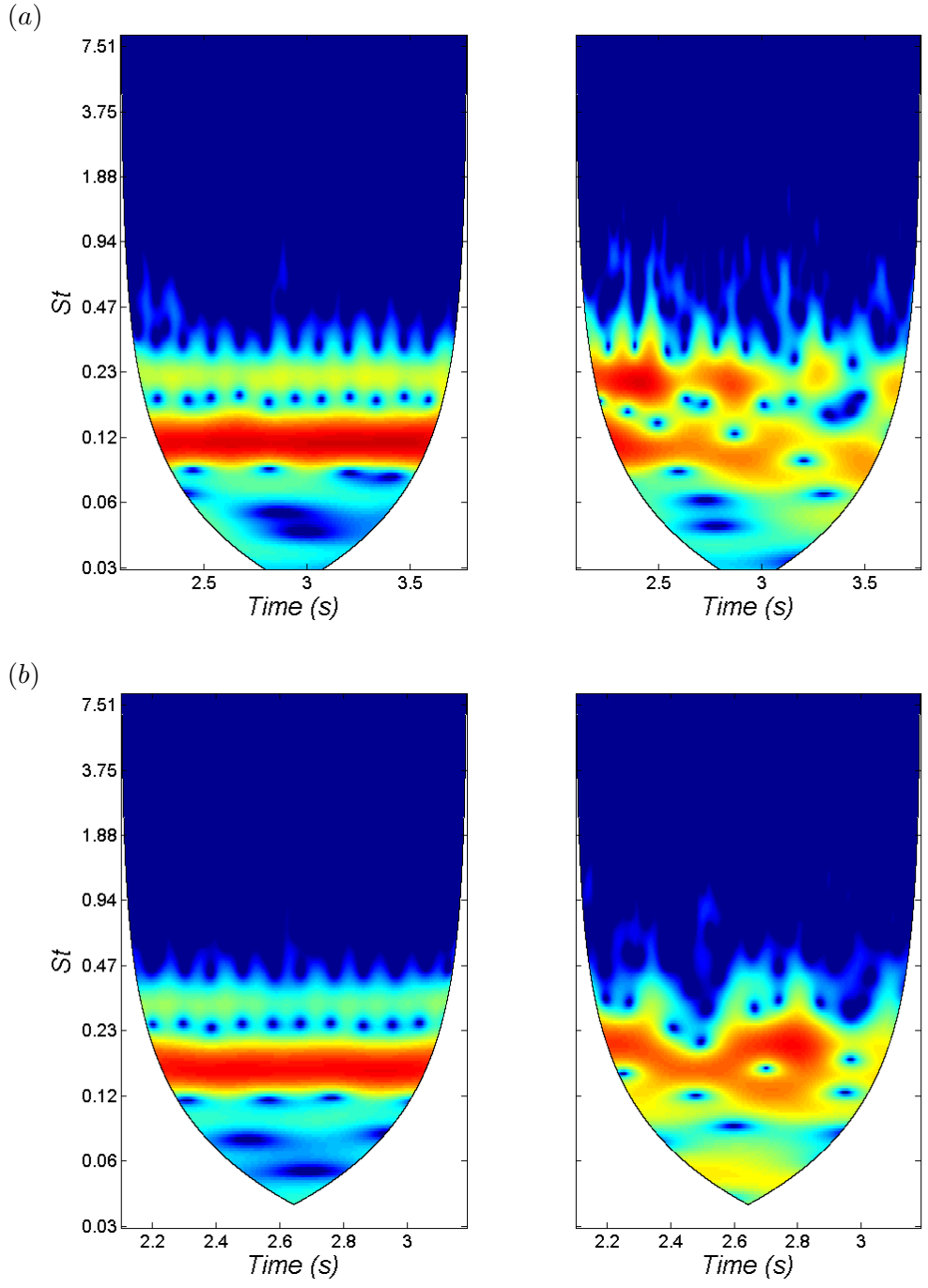

FIGURE B.2: Wavelet analysis on the drag (left) and lift (right) signals for actuation at $C_\mu = 8 \times 10^{-3}$ and (a) $St_{act} = 0.11$, (b) $St_{act} = 0.155$.

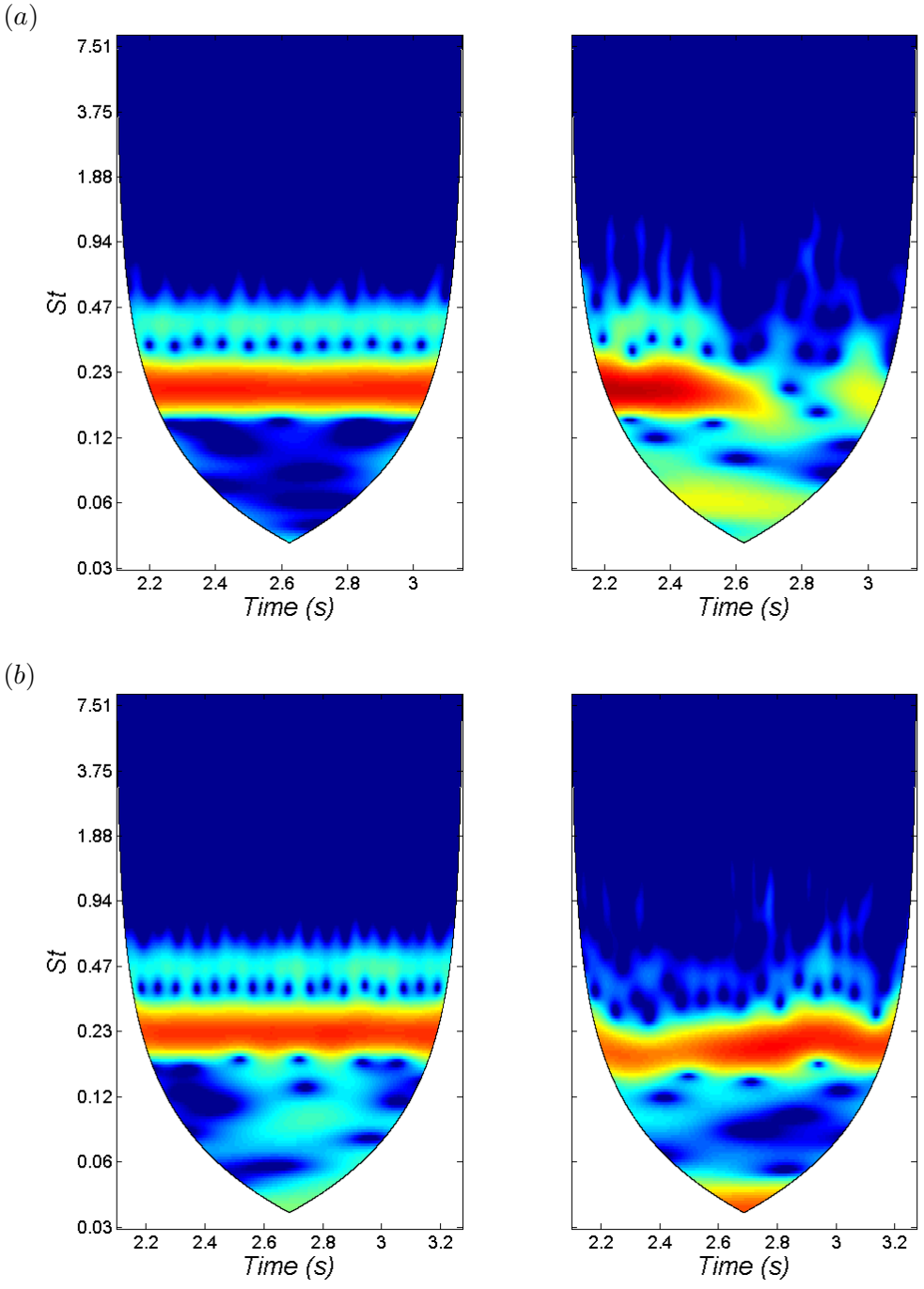

FIGURE B.3: Wavelet analysis on the drag (left) and lift (right) signals for actuation at $C_\mu = 8 \times 10^{-3}$ and (a) $St_{act} = 0.195$, (b) $St_{act} = 0.23$

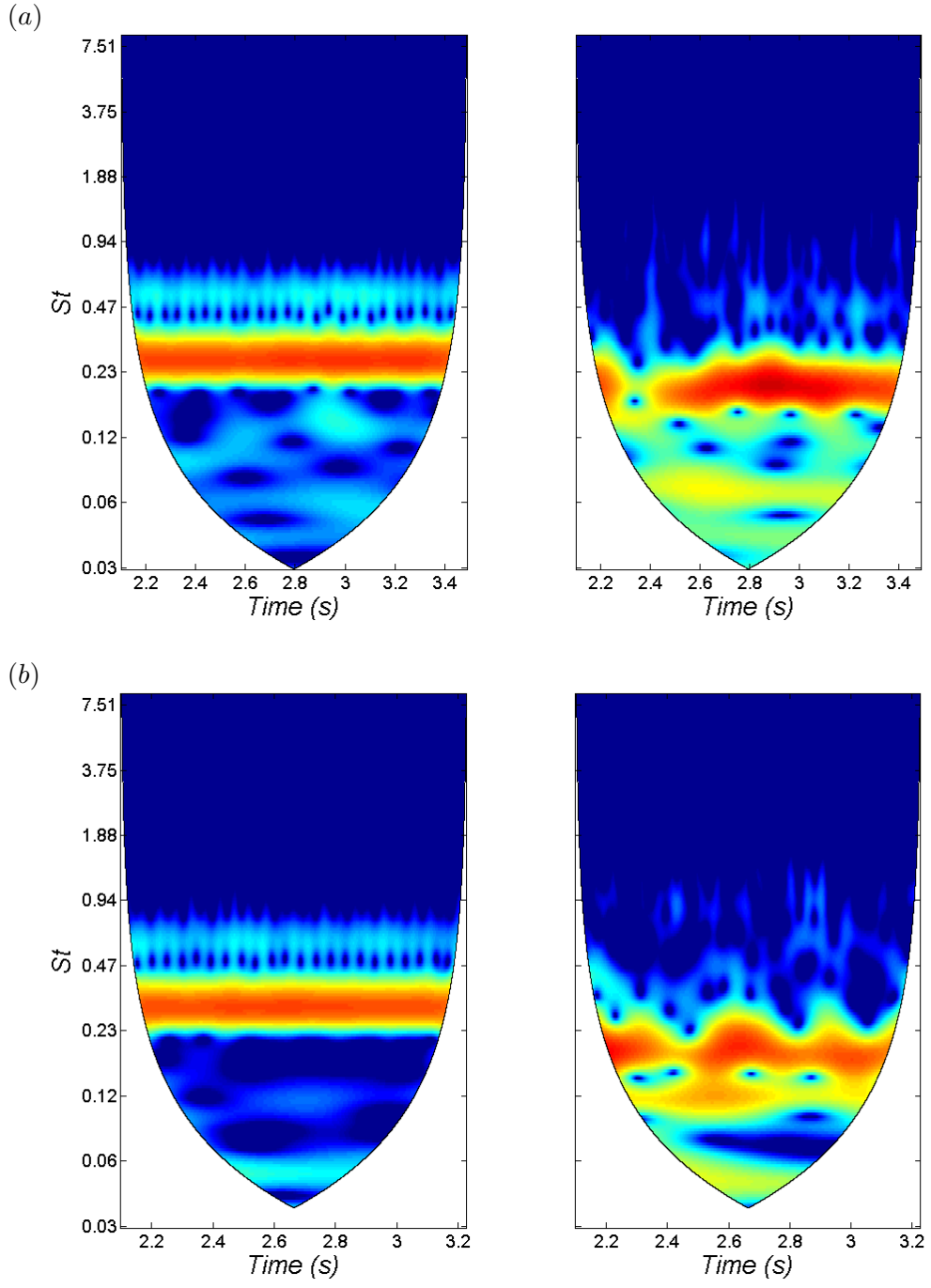

FIGURE B.4: Wavelet analysis on the drag (left) and lift (right) signals for actuation at $C_\mu = 8 \times 10^{-3}$ and (a) $St_{act} = 0.265$, (b) $St_{act} = 0.30$

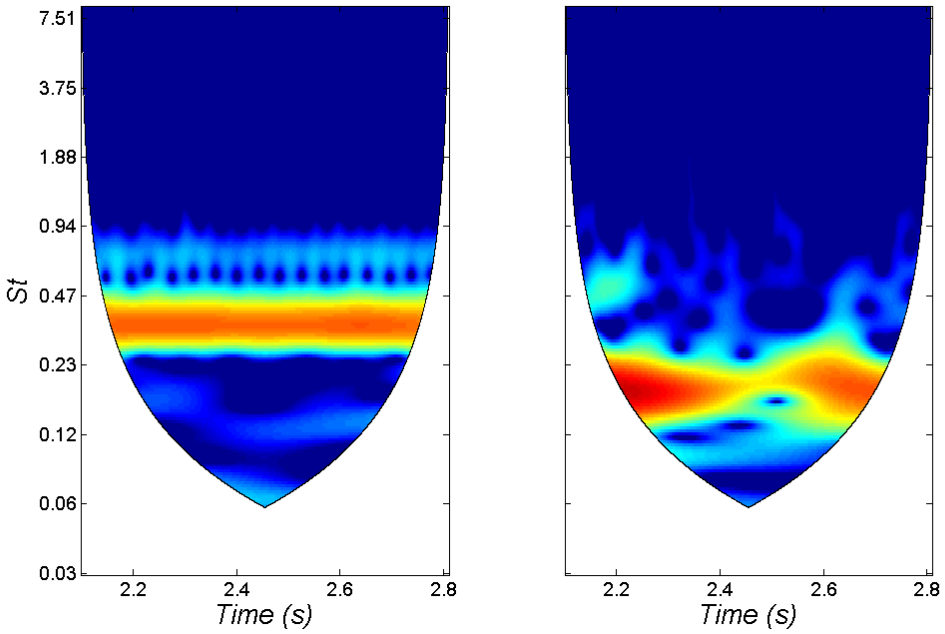

FIGURE B.5: Wavelet analysis on the drag (left) and lift (right) signals for actuation at $C_\mu = 8 \times 10^{-3}$ and $St_{act} = 0.35$

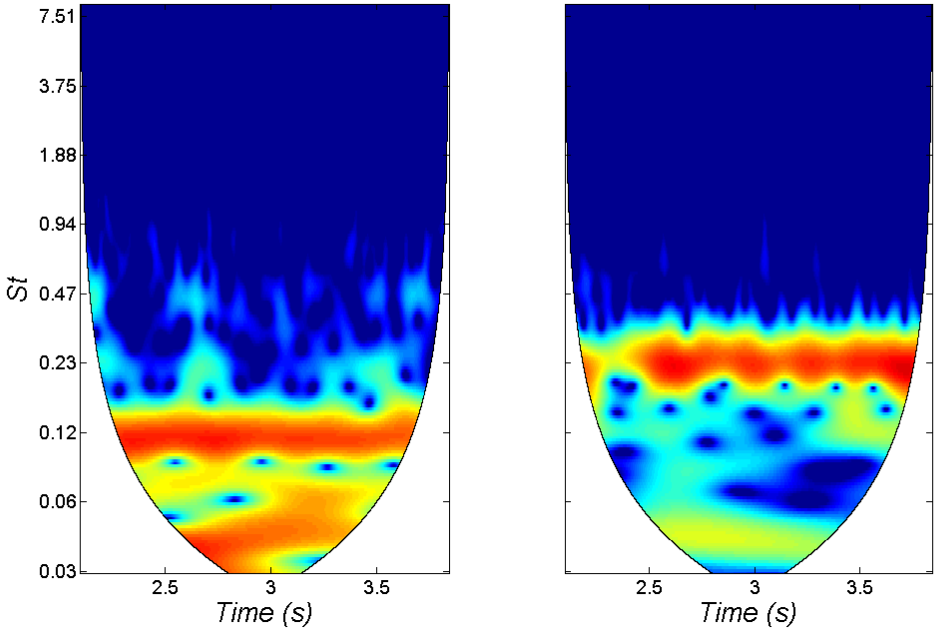

FIGURE B.6: Wavelet analysis on the drag (left) and lift (right) signals for actuation at $St_{act} = 0.11$ and $C_\mu = 5 \times 10^{-4}$.

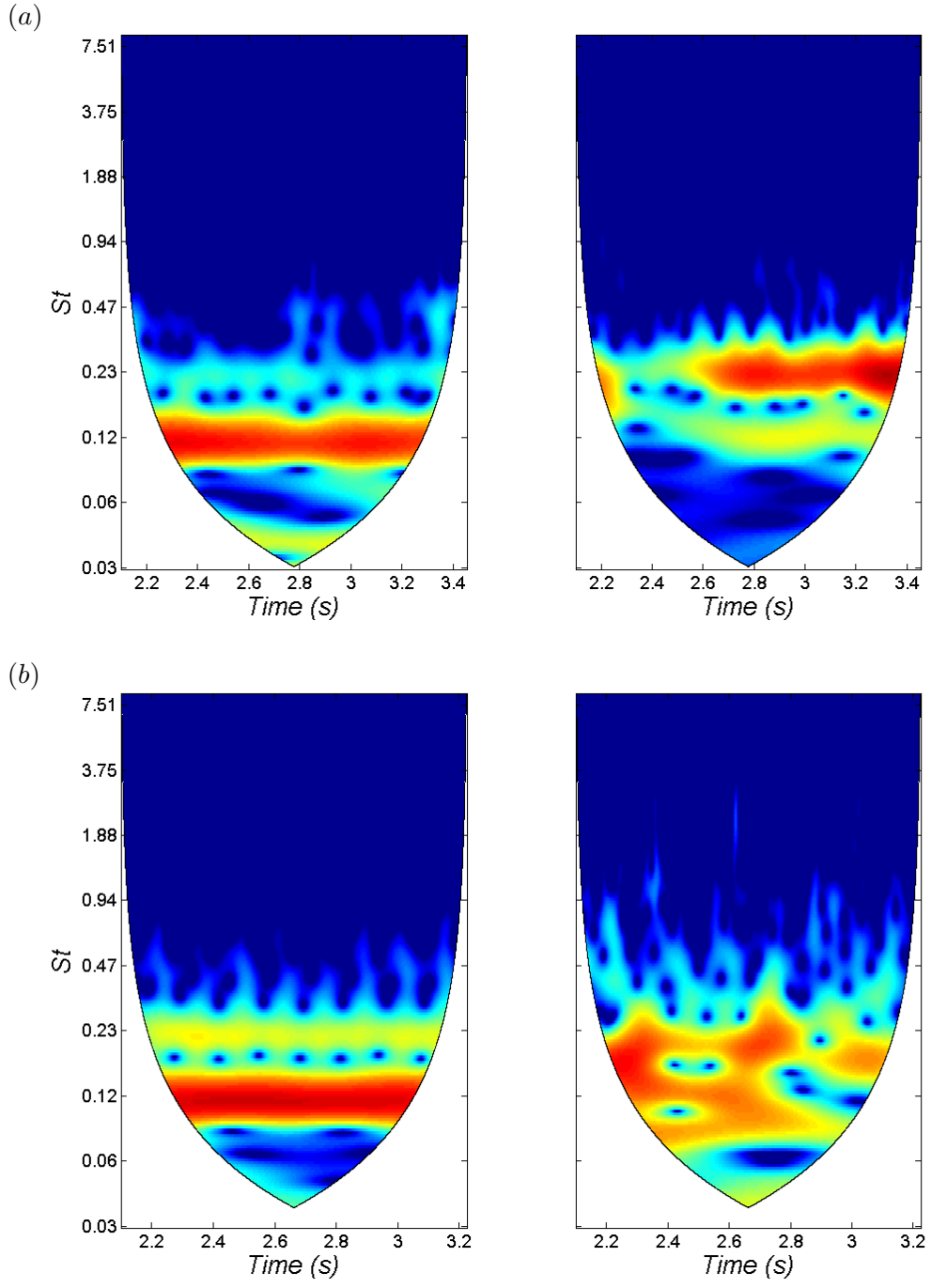

FIGURE B.7: Wavelet analysis on the drag (left) and lift (right) signals for actuation at $St_{act} = 0.11$ and (a) $C_\mu = 2 \times 10^{-3}$, (b) $C_\mu = 1.6 \times 10^{-2}$

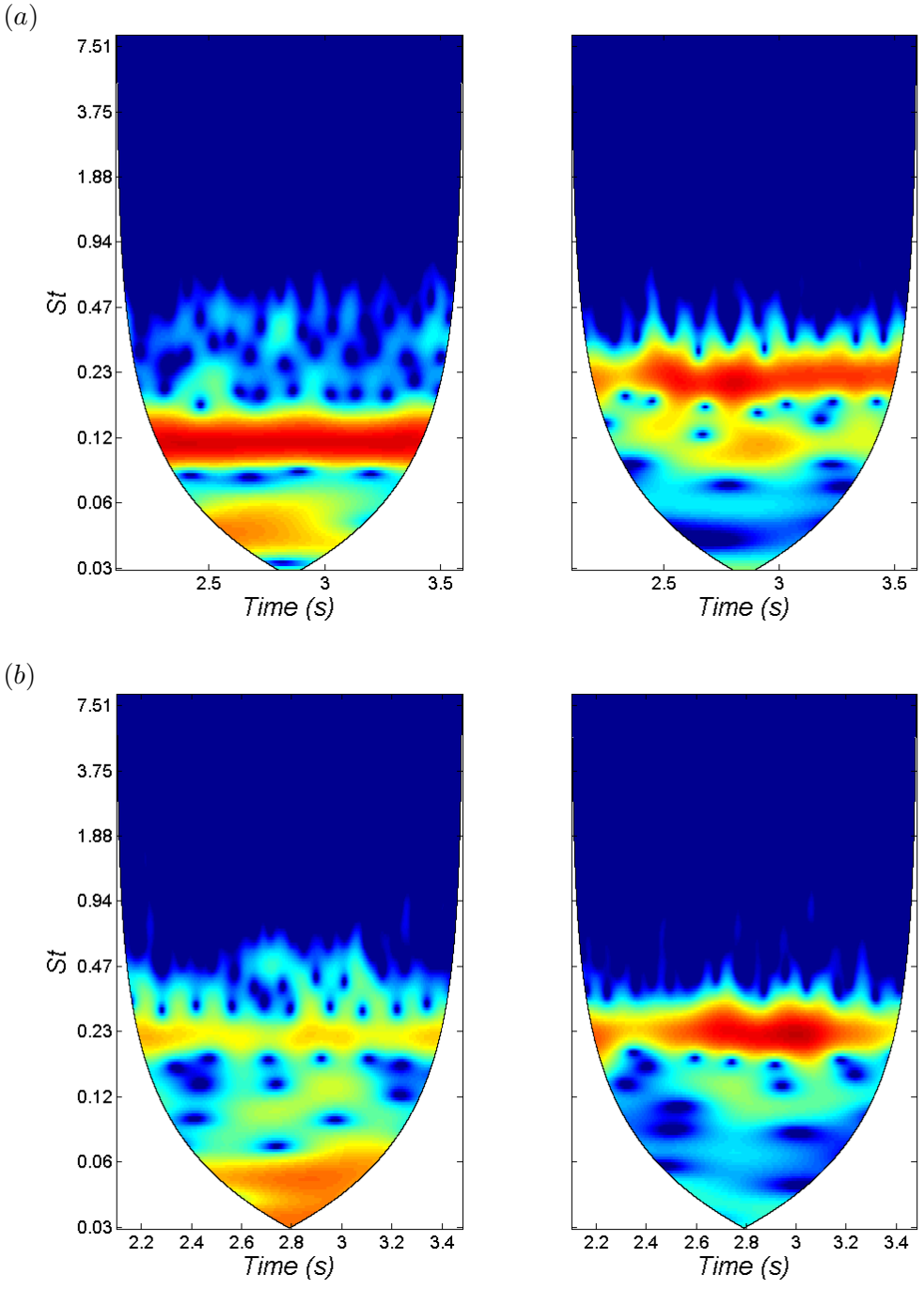

FIGURE B.8: Wavelet analysis on the drag (left) and lift (right) signals for $St_{act} = 0.11$ and $C_\mu = 4 \times 10^{-3}$ with (a) shear layer actuation and (b) base actuation.

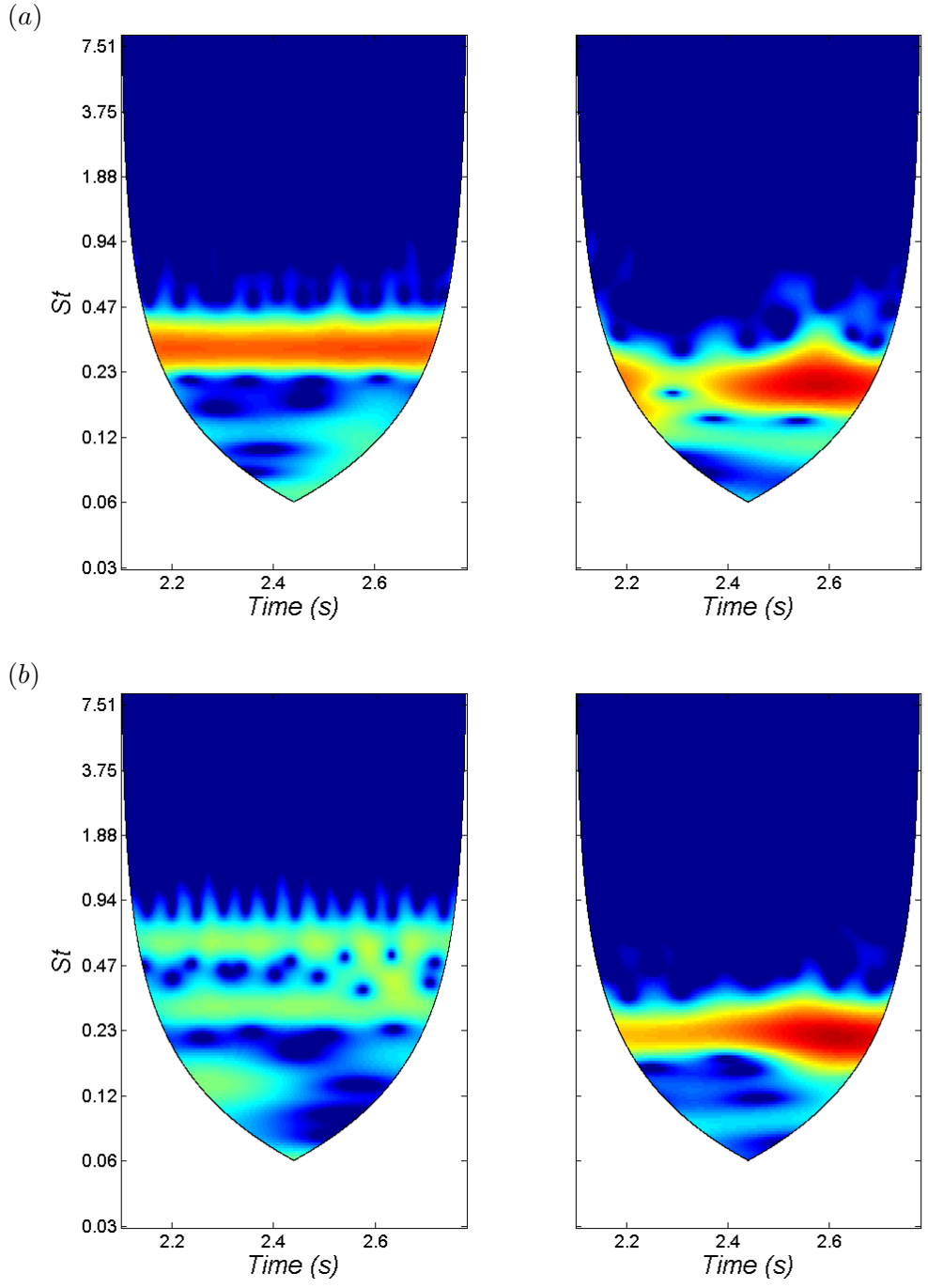

FIGURE B.9: Wavelet analysis on the drag (left) and lift (right) signals for $St_{act} = 0.30$ and $C_\mu = 4 \times 10^{-3}$ with (a) shear layer actuation and (b) base actuation.

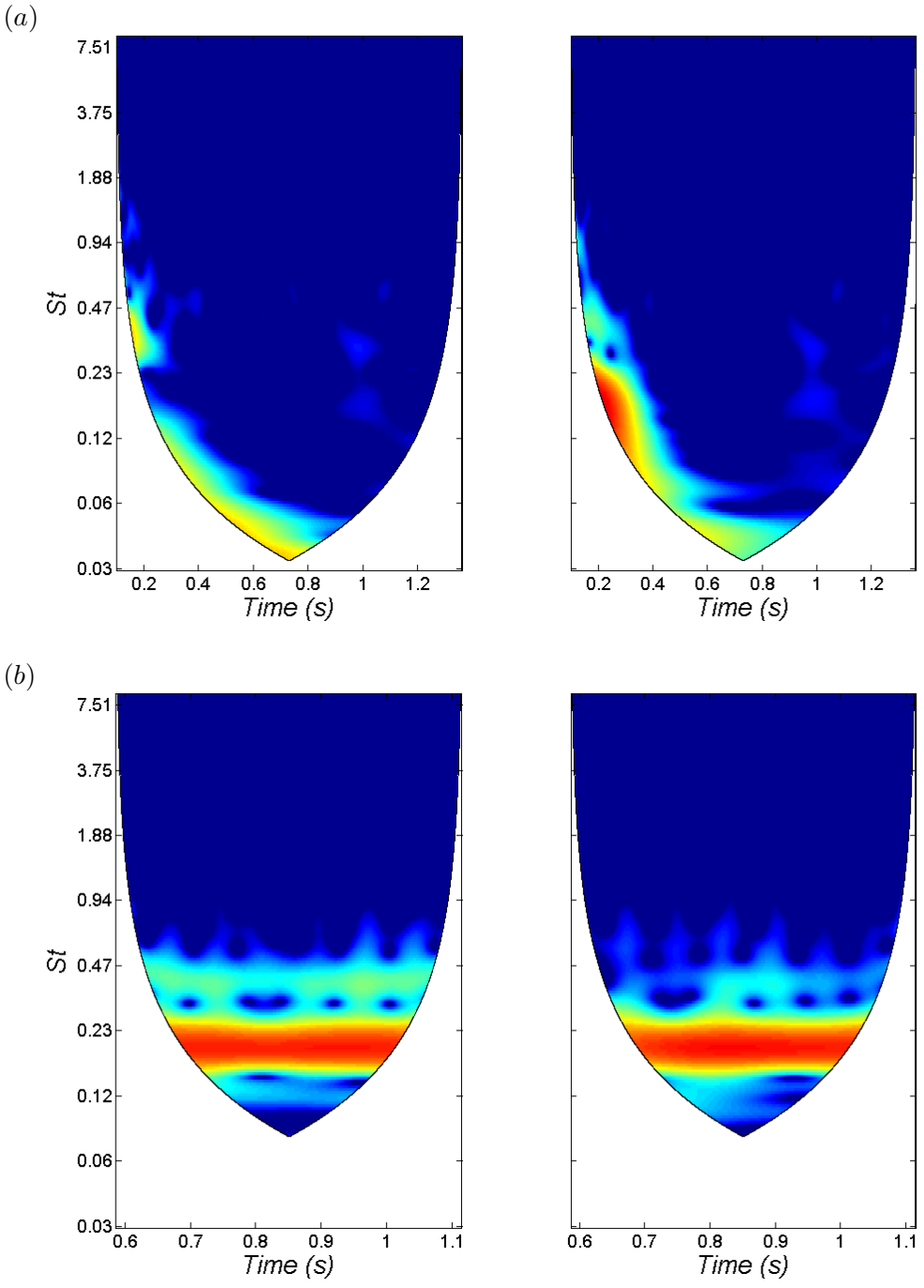

FIGURE B.10: Wavelet analysis on the drag (left) and lift (right) signals in ground proximity for (a) natural flow and (b) $St_{act} = 0.195$.

Bibliography

Ahmed, S. & Ramm, G. 1984 Some salient features of the time averaged ground vehicle wake. *SAE Technical Paper No. 840300* .

Almeida, O., Mansur, S. S. & Silveira-Neto, A. 2008 On the Flow Past Rectangular Cylinders: Physical Aspects and Numerical Simulation. *Thermal Engineering* **7(1)**, 55–64.

Anderson, E. & Szewczyk, A. 1997 Effects of a Splitter Plate on the near wake of a circular cylinder in 2D and 3D flow configurations. *Exp. Fluids* **23**, 161–174.

Arcas, D. R. & Redekopp, L. G. 2004 Aspects of wake vortex control through base blowing/suction. *Phys. Fluids* **16(2)**, 452–456.

Bayraktar, I., Landman, D. & Baysal, O. 2001 Experimental and Computational Investigation of Ahmed Body for Ground Vehicle Aerodynamics. *SAE Technical Paper 2001-01-2742* .

Bearman, P. W. 1965 Investigation of the Flow Behind a 2D Model with a Blunt Trailing Edge and Fitted with Splitter Plates. *J. Fluid Mech.* **21**, 241–255.

Bearman, P. W. 1967 The Effect of Base Bleed on the Flow behind a Two-Dimensional Model with a Blunt Trailing Edge. *Aeronaut. Q.* **18**, 207–224.

Bearman, P. W. 1997 Near wake flows behind two- and three-dimensional bluff bodies. *J. Wind Eng. Ind. Aerodyn.* **71**, 33–54.

Beaudoin, J., Cadot, O., Aider, J. & Wesfreid, J. 2006 Drag reduction of a bluff body using adaptive control methods. *Phys. Fluids* **18**, NA.

Bloor, M. 1964 The transition to turbulence in the wake of a circular cylinder. *J. Fluid Mech.* **19**, 290–304.

Brun, C., Aubrun, S., Goossens, T. & Ravier, P. 2008 Coherent Structures and their Frequency Signature in the Separated Shear Layer on the Wides of a Square Cylinder. *Flow, Turbulence & Combustion* **81**, 97–114.

Chapman, D. R. 1979 Computational aerodynamics development and outlook. *AIAA J.* **12**, 1293–1313.

Cherry, N. J., Hillier, R. & Latour, M. E. 1984 Unsteady measurements in a separated and reattaching flow. *J. Fluid Mech.* **11**, 13–46.

Choi, H., Jeon, W. P. & Kim, J. 2008 Control of Flow Over a Bluff Body. *Annu. Rev. Fluid Mech.* **40**, 113–139.

Choi, H. & Moin, P. 1993 Effects of the Computational Time Step on Numerical Solutions of Turbulent Flow. *J. Comp. Physics* **113**, 1–4.

Cooley, J. W. & Tukey, J. W. 1965 An Algorithm for the Machine Computation of the Complex Fourier Series. *Math. Comp.* **19**, 297–301.

Darekar, R. & Sherwin, S. 2001 Flow past a square-section cylinder with a wavy stagnation face. *J. Fluid Mech.* **426**, 263–295.

Davidson, L. 2009 Large Eddy Simulations: how to evaluate resolution. *Int. J. Heat Fluid Flow* **30(5)**, 1016–1025.

Davidson, L. 2010 How to evaluate the resolution of an LES of recirculating flow. In *Quality and Reliability of Large-Eddy Simulation II Vol. 16*, pp. 269–286. Springer.

Delaunay, Y. & Kaiktsis, L. 2001 Control of circular cylinder wakes using base mass transpiration. *Phys. Fluids* **13**, 3285–3302.

Djilali, N. & Gartshore, I. S. 1991 Turbulent flow around a bluff rectangular plate. Part I: Experimental Investigation. *J. Fluids Eng.* **113**, 51–59.

Duell, E. G. & George, A. R. 1999 Experimental Study of a Ground Vehicle Body Unsteady Near Wake. *SAE Technical Paper 1999-01-0812* .

Dusek, J., Gal, P. L. & Fraunie, P. 1994 A numerical and theoretical study of the first Hopf bifurcation in a cylinder wake. *J. Fluid Mech.* **264**, 59–80.

Dyk, M. V. 2002 *An album of Fluid Motion*. The Parabloic Press, Stanford.

Farell, C., Guven, O., Carrasquel, S. & Patel, V. C. 1977 Effect of Wind-Tunnel Walls on the Flow Past Circular Cylinders and Cooling Tower Models. *J. Fluids Eng.* **99(3)**, 470–479.

George, W. K. 2007 Is there a universal log law for turbulent wall-bounded flows? *Phil. Trans. R. Soc. A* **365**, 789–806.

Germano, M., Piomelli, U., Moin, P. & Cabot, W. H. 1991 A dynamic subgrid-scale eddy-viscosity model. *Phys. Fluids* **3(7)**, 1760–1765.

Gerrard, J. H. 1966 The mechanics of the formation region of vortices behind bluff bodies. *J. Fluid Mech.* **25**, 401–413.

Ghosal, S. & Moin, P. 1995 The Basic Equations for the Large Eddy Simulation of Turbulent flows in Complex Geometry. *J. Comp. Physics* **118**, 24–37.

Goupillaud, P., Grossman, A. & Morlet, J. 1984 Cycle-Octave and Related Transforms in Seismic Signal Analysis. *Geoexploration* **23**, 85–102.

Graftieaux, L., Michard, M. & Grosjean, N. 2001 Combining PIV, POD and vortex identification algorithms for the study of unsteady turbulent swirling flows. *Meas. Sci. Technol.* **12**, 1422–1429.

Grandemange, M., Gohlke, M. & Cadot, O. 2013 Turbulent wake past a three-dimensional blunt body. Part 1. Global modes and bi-stability. *J. Fluid Mech.* **722**, 51–84.

Griffin, O. 1981 Universal Similarity in the Wakes of Stationary and Vibrating Bluff Structures. *J. Fluids Eng.* **103(1)**, 52–58.

Hackett, J. E., Wilsden, D. J. & Lilley, E. E. 1979 *Estimation of Tunnel Blockage from Wall Pressure Signatures: A Review and Data Correlation*. Lockheed-Georgia Company.

Hazarika, B. K. & Hirsch, C. 1994 Behaviour of Separation Bubble and Reattached Boundary Layer around a Circular Leading Edge. *ASME Paper No. 94-GT-385* .

Henning, L., Pastoor, M., King, R., Noack, B. R. & Tadmor, G. 2007 Feedback Control Applied to the Bluff Body Wake, Vol. 95. In *Active Flow Control*, pp. 369–390. Springer.

Herry, B. B., Keirsbulck, L., Labraga, L. & Paquet, J.-B. 2011 Flow Bistability Downstream of Three-Dimensional Double Backward Facing Steps at Zero-Degree Sideslip. *J. Fluids Eng.* **133(5)**, 054501.

Ho, C. M. & Nosseir, N. S. 1981 Dynamics of an Impinging Jet. Part I: The Feedback Phenomenon. *J. Fluid Mech.* **105**, 119–142.

Hourigan, K., Thompson, M. C. & Tan, B. T. 2001 Self-sustained oscillations in flows around long blunt plates. *J. Fluid. Struct.* **15**, 387–398.

Howard, R. & Pourquie, M. 2002 Large Eddy Simulation of an Ahmed reference model. *J. Turbul.* **3(1)**.

Huerre, P. & Monkewitz, P. 1990 Local and global instabilities in spatially developing flows. *Annu. Rev. Fluid Mech.* **22**, 473–537.

Hwang, J. Y., Yang, K. S. & Sun, S. H. 2003 Reduction of flow-induced forces on a circular cylinder using a detached Splitter Plate. *Phys. Fluids* **15**, 2433–2436.

Hwang, R. R. & Sue, Y. C. 1997 Numerical Simulation of Shear Effect on Vortex Shedding Behind a Square Cylinder. *I. J. Numer. Meth. Fluids* **25**, 1409–1420.

Jiang, X. & Lai, C. H. 2010 *Numerical Techniques for Direct and Large-Eddy Simulations*. CRC Press.

von Kármán, T. & Rubach, H. 1912 Über den mechanismus des flüussigkeits-und luftwiderstandes. *Phys. Z.* **13**, 49–59.

Khalighi, B., Chen, K. & Iaccarino, G. 2012 Unsteady Aerodynamic Flow Investigation Around a Simplified Square-Back Road Vehicle with Drag Reduction Devices. *J. Fluids Eng.* **134(6)**, 061101.

Khalighi, B., Zhang, S., Koromilas, C., Balkanyi, S. R., Bernal, L. P., Iaccarino, G. & Moin, P. 2001 Experimental and Computational Study of Unsteady Wake Flow behind a bluff body with a Drag Reduction Device. *SAE Technical Paper No. 2001-01B-207* .

Khor, M., Sheridan, J. & Hourigan, K. 2010 Power-Spectral density estimate of the Bloor-Gerrard instability in flows around circular cylinders. *Exp. Fluids* **50**, 527–534.

Kim, J., Hahn, S., Kim, J. S., Lee, D. K. & Choi, H. 2004 Active control of turbulent flow over a model vehicle for drag reduction. *J. Turbul.* **5**, 19.

Kim, M. & Geropp, D. 1998 Experimental investigation of the ground effect on the flow around some two-dimensional bluff bodies with moving-belt technique. *J. Wind Eng. Ind. Aerodyn.* **74-76**, 511–519.

Kiya, M. & Abe, Y. 1999 Turbulent elliptic wakes. *J. Fluid. Struct.* **13**, 1041–1067.

Krajnovic, S. 2009 Large eddy simulation of flows around ground vehicles and other bluff bodies. *Phil. Trans. R Soc. A* **367**, 2917–2930.

Krajnovic, S. & Davidson, L. 2002 Large-Eddy Simulation of the Flow Around a Bluff Body. *AIAA Journal* **40(5)**, 927–936.

Krajnovic, S. & Davidson, L. 2005a Flow around a simplified car, part 1: Large Eddy Simulation. *J. Fluids Eng.* **127**, 907–918.

Krajnovic, S. & Davidson, L. 2005b Flow around a simplified car, part 2: Understanding the flow. *J. Fluids Eng.* **127**, 919–928.

Krajnovic, S. & Fernandes, J. 2011 Numerical simulation of the flow around a simplified vehicle model with active flow control. *Int. J. Heat Fluid Flow* **32**, 192–200.

Kwon, K. & Choi, H. 1996 Control of laminar vortex shedding behind a circular cylinder using splitter plates. *Phys. Fluids* **8**, 479.

Lee, D. & Yamamoto, A. 1994 Wavelet Analysis: Theory and Applications. *Hewlett-Packard Journal* pp. 44–52.

Lehmkuhl, O., I. Rodríguez, R. Borrell, C. D. P.-S. & Oliva, A. 2000 Control of global instability in a nonparallel near wake. *J. Fluid Mech.* **404**, 345–378.

Leu, T. & Ho, C. 2000 Control of global instability in a non-parallel near wake. *J. Fluid Mech.* **404**, 345–378.

Lilly, D. K. 1992 A proposed modification of the Germano subgrid-scale closure method. *Phys. Fluids A* **4(3)**, 633–635.

Maddox, S., Squires, K., Wurtzler, K. & Forsythe, J. 2003 Detached-Eddy Simulation of the Ground Transportation System. *J. Turbul.* **3(57)**, 1–21.

Mannini, C., Weinman, K., Soda, A. & Schewe, G. 2009 Three-dimensional numerical simulation of flow around a 1:5 cylinder. *EACWE 5 Proceedings, Italy* .

Maskell, E. C. 1963 A Theory of the Blockage Effects on Bluff Bodies and Stalled Wings in a Closed Wind Tunnel. *ARC R&M* **3400**.

Menter, F. & Kuntz, M. 2004 Adaption of Eddy-Viscosity Turbulence Models to Unsteady Separated Flows Behind Vehicles. In *The Aerodynamics of Heavy Vehicles: Trucks, Buses and Trains*, pp. 339–352. Springer.

Mercker, E. 1986 A Blockage Correction for Automotive Testing in a Wind Tunnel with Closed Test Section. *J. Wind Eng. & Ind. Aerodyn.* **2-3**, 149–167.

Michalke, A. 1965 On spatially growing disturbances in an inviscid shear layer. *J. Fluid Mech.* **23**, 521–544.

Mills, R., Sheridan, J. & Hourigan, K. 2001 Response of base suction and vortex shedding from rectangular prisms to transverse forcing. *J. Fluid Mech.* **461**, 25–49.

Mills, R. H. 1998 Vortex interaction in flows over bluff bodies. PhD thesis, Monash University, Australia.

Minguez, M., Pasquetti, R. & Serre, E. 2008 High-order Large-Eddy Simulation of flow over the Ahmed body car model. *Phys. Fluids* **20**, 095101.

Morton, B. R. 1984 The Generation and Decay of Vorticity. *Geophys. Astrophys. Fluid Dyn.* **28**, 277–308.

Nakaguchi, H., Hashimoto, K. & Muto, K. 1968 An experimental study of aeroydnamic drag of rectangular cylinders. *J. Japan Soc. Aero. Space Sci.* **16**, 1–5.

Nakamura, Y. 1996 Vortex shedding from bluff bodies and a Universal Strouhal number. *J. Fluid. Struct.* **10**, 159–171.

Nakamura, Y. & Hirata 1989 Critical geometry of oscillating bluff bodies. *J. Fluid Mech.* **208**, 375–393.

Nakamura, Y. & Nakashima, M. 1986 Vortex excitation of prisms with elongated rectangular, H and T cross-sections. *J. Fluid Mech.* **163**, 149–169.

Nakamura, Y., Ohya, Y. & Tsuruta, H. 1991 Experiments on vortex shedding from flat plates with square leading and trailing edges. *J. Fluid Mech.* **222**, 437–447.

Noack, B. R., Tadmor, G. & Morzynski, M. 2004 Low-Dimensional Models for Feedback Flow Control. Part I: Empirical Galerkin models. *AIAA Flow Control Conference* **2**, 1–11.

Obasaju, E. D. 1983 An Investigation of the Effects of Incidence on the Flow Around a Square Section Cylinder. *Aero. Quarterly* **34**, 243–259.

Okajima, A. 1982 Strouhal number of rectangular cylinder. *J. Fluid Mech.* **123**, 379–398.

Okajima, A., Ueno, H. & Sakai, H. 1992 Numerical simulation of laminar and turbulent flows around rectangular cylinders. *Int. J. Num. Meth. Fluids* **15**, 999–1012.

Österlund, J., Johansson, A., Nagib, H. & Hites, M. 2000 A note on the overlap region in turbulent boundary layers. *Phys. Fluids* **12**, 1.

Ozono, S. 1999 Flow control of a vortex shedding by a short splitter plate asymmetrically arranged downstream of a cylinder. *Phys. Fluids* **11**, 2928.

Pankajakshan, R., Mitchell, B. & Whitfield, D. L. 2008 Full-Scale Simulations of Drag Reduction Devices for Class 8 Trucks. *University of Tennessee SimCenter* .

Park, H., Lee, D., Jeon, W., Hahn, S. & Kim, J. 2006 Drag reduction in flow over a two-dimensional bluff body with a blunt trailing edge using a new passive device. *J. Fluid Mech.* **563**, 389–414.

Pastoor, M., Henning, L., Noack, B. R., King, R. & Tadmor, G. 2008 Feedback shear layer control for bluff body drag reduction. *J. Fluid Mech.* **608**, 161–196.

Petrusma, M. S. & Gai, S. L. 1994 The effect of geometry on the base pressure recovery of the segmented blunt trailing edge. *Aeronaut. J.* **98**, 267–274.

Pope, S. 2004 Ten questions concerning the large-eddy simulations of turbulent flows. *New J. Physics* **35**, 1–24.

Prasad, A. & Williamson, C. H. K. 1997 The instability of the shear layer separation from a bluff body. *J. Fluid Mech.* **333**, 375–402.

Protas, B. & Wesfreid, J. E. 2002 Drag force in the open-loop control of the cylinder wake in the laminar regime. *Phys. Fluids* **14(2)**, 810–826.

Provansal, M., Mathis, C. & Boyer, L. 1987 Bénard-von Kármán instability: transient and forced regimes. *J. Fluid Mech.* **182**, 1–22.

Pun, C. W. & O'Neill, P. L. 2007 Unsteady flow around a Rectangular Cylinder. *Australasian Fluid Mechanics Conf.* **16**, 1449–1456.

Reynolds, O. 1895 On the Dynamical Theory of Incompressible Viscous fluids and the Determination of the Criterion. *Phil. Trans. R. Soc. Lond.* **186**, 123–164.

Robinson, S. K. 1991 Coherent motions in the turbulent boundary layer. *Annu. Rev. Fluid Mech.* **23**, 601–39.

Rockwell, D. & Naudascher, E. 1978 Review: Self-sustaining oscillations of flow past cavities. *J. Fluids Eng.* **100**, 152–165.

Rockwell, D. & Naudascher, E. 1979 Self-sustained oscillations of impinging free shear layers. *Annu. Rev. Fluid Mech.* **11**, 67–94.

Rockwell, D. & Naudascher, E. 1994 *Flow-Induced Vibration - An Engineering Guide*. Rotterdam Editor: A. Balkema.

Rodriguez, O. 1991 Base drag reduction by the control of three-dimensional unsteady vortical structures. *Exp. Fluids* **11**, 218–226.

Roshko, A. 1954 On the drag and shedding frequency of bluff cylinders. *NACA Technical Note* **3169**.

Roshko, A. 1955 On the wake and drag of bluff bodies. *J. Aeronaut. Sci.* **22**, 124.

Roshko, A. 1961 Experiments on the flow past a circular cylinder at very high Reynolds number. *J. Fluid Mech.* **10**, 345–356.

Roshko, A. & Lau, J. C. 1965 Some observations on transition and reattachment of a free shear layer in incompressible flow. *Proc. Heat Transfer & Fluid Mech. Inst.* pp. 157–167.

Rowley, C. W., Mezic, I., Bagheri, S., Schlatter, P. & Henningson, D. S. 2009 Spectral analysis of nonlinear flows. *J. Fluid Mech.* **641**, 115–127.

Schlichting, H. & Gersten, K. 2000 *Boundary Layer Theory*. Springer.

Schmid, P. J. 2010 Dynamic mode decomposition of numerical and experimental data. *J. Fluid Mech.* **656**, 5–28.

Scotti, A., Meneveau, C. & Fatica, M. 1997 Dynamic Smagorinsky model on anisotropic grids. *Phys. Fluids* **9(6)**, 1856–1858.

Singh, S. P. & Mittal, S. 2004 Energy Spectra of Flow Past a Circular Cylinder. *Int. J. CFD* **18(8)**, 671–679.

Spohn, A. & Gillieron, P. 2002 Flow Separations Generated by a Simplified Geometry of an Automotive Vehicle. In *Proc. IUTAM Symp. on Unsteady Separated Flows, Toulouse, France*.

Stankiewicz, W., Morzynski, M., Noack, M. & Thiele, F. 2005 Stability properties of a 2D flow around an Ahmed Body. In *Proc. Math. Mod. & Analysis, Trakai, Lithuania*, pp. 129–134.

Tanner, M. 1972 A method of reducing the base drag of wings with blunt trailing edges. *Aeronaut. J.* **23**, 15–23.

Taylor, Z. 2011a Features of the turbulent flow around symmetric elongated bluff bodies. *J. Fluid. Struct.* **27(2)**, 250–265.

Taylor, Z. 2011b Vortex shedding from elongated bluff bodies. PhD thesis, The University of Western Ontario, Canada.

Thompson, M. C. & Hourigan, K. 2005 The shear-layer instability of a circular wake. *Phys. Fluids* **17**, 021702.

Tombazis, N. & Bearman, P. W. 1997 A study of three-dimensional aspects of vortex shedding from a bluff body with a mild geometric distrubance. *J. Fluid Mech.* **330**, 85–112.

Tritton, D. J. 1988 *Physical Fluid Dynamics, 2nd Edition*. Oxford Science Publications.

UK Dept Transport 2010 *Aerodynamics for Efficient Road Freight Operations*. Queens Printer and Controller of HMSO.

University, B. 2012 Numerical simulations of turbulent combustion and combustion engines—brunel university, london.

Vino, G., Watkins, S., Mousley, P., Watmuff, J. & Prasad, S. 2005 Flow structures in the near-wake of the Ahmed model. *J. Fluid. Struct.* **20**, 673–695.

Wassen, E., Eichinger, S. & Thiele, F. 2010 Simulation of Active Drag Reduction for a Square-Back Vehicle. *Active Flow Control II (Notes on Numerical Fluid Mechanics and Multidisciplinary Design)* **108**, 241–255.

Wei, T. & Smith, C. R. 1986 Secondary vortices in the wake of circular cylinders. *J. Fluid Mech.* **169**, 513–533.

Williamson, C. 1996 Vortex dynamics in the cylinder wake. *Annu. Rev. Fluid Mech.* **28**, 477–539.

Wood, C. 1964 The effect of base bleed on a periodic wake. *J. R. Aeronaut. So.* **68**, 477–482.

Wu, J., Sheridan, J., Hourigan, K. & Soria, J. 1996 Shear Layer Vortices and Longitudinal Vortices in the Near Wake of a Circular Cylinder. *Exp. Therm. Fluid Sci.* **12**, 169–174.

Yao, Y. F. & Sandham, N. D. 2002 Direct Numerical Simulation of turbulent trailing-edge flow with base flow control. *AIAA Journal* **40(9)**, 1708–1716.

Yoon, J. 2005 Control of flow over a circular cylinder using wake disrupter. Master's thesis, Seoul Natl. Univ., Korea.

Zdravkovich, M. M. 1996 *Flow around Circular Cylinders, Vols 1 and 2*. Oxford: Oxford University Press.